

Characterisation of Advanced Porous Materials

Mohd Ayub Sulong

Thesis submitted for the Degree of Doctor of Philosophy

The University of Newcastle, Australia

Faculty of Engineering and Built Environment

School of Engineering

Centre for Mass and Thermal Transport in Engineering Materials



August 2015

Declaration

Statement of Originality

I hereby certify that this thesis contains no material which has been accepted for the award of any other degree or diploma in any university or other tertiary institution and, to the best of my knowledge and belief, contains no material previously published or written by another person, except where due reference has been made in the text. I give consent to this copy of my thesis when deposited in the University Library, being made available for loan and photocopying subject to the provisions of the Copyright Act 1968.

Thesis by Publication

I hereby certify that this thesis is submitted in the form of a series of published papers of which I am a joint author. I have included as a part of this thesis a written statement from each co-author; and endorsed by the Faculty Assistant Dean (Research Training), attesting to my contribution to the joint publications.

Mohd Ayub Sulong

Statement of Contribution

A written statement has been obtained from the following co-authors attesting my contribution to joint publications included as part of this thesis. Statements summarising and clearly identifying the nature and extent of the intellectual input by myself are included as part of this thesis.

Dr. Thomas Fiedler

Prof. Irina V Belova

Prof. Graeme E Murch

Prof. Andreas Öchsner

Assoc. Prof. Dr Matej Vesenjak

Prof. Aldo R Boccaccini

Dr. Vincent Mathier

Prof. Yoshikazu Higa

Mr. Mehdi Taherishargh

Mr. Chris Younger

Dedication

To my father, Sulong Omar
This journey would not be possible without him.

Acknowledgements

I am very grateful to my lead supervisor Dr. Thomas Fiedler who tirelessly guided me through this degree. His advice and assistance on cellular metals proved to be invaluable throughout this journey. His dedication and hard work towards getting the job done is inspirational. I would also like to thank my other supervisors Prof. Irina Belova, Prof. Graeme Murch and Prof. Andreas Öchsner for their continuous assistance and invaluable guidance. I am grateful to them for making a strong point about this venture, which is to be less dependent academically.

I am very thankful to the faculty and staff members in the Faculty of Engineering and Built Environment, School of Engineering. Special thanks to Ms. Lea Petrovic, Ms. Katherine Harrison and Ms. Rachel Hambleton for their generous help during my time at the University of Newcastle. I also would like to acknowledge helpful lab technicians, Mr. Mitch Gibbs, Mr. Dean Ferry, Mr. Peter Garfoot and Ian Clarke.

To the entire members of the Centre for Mass and Thermal Transport in Engineering Materials, past, present, interns and visitors — Prof. Zi-Kui Liu and wife, Dr. Alex Evteev, Dr. Elena Levchenko, Dr. Christoph Veyhl, Mr. Taherishargh, Mrs. Momenzadeh, Mr. Ahmed, Mrs. Paul, Mr. Sarder, Mr. Sowa and my friends.

I would like to personally thank Universiti Teknologi Malaysia (UTM) and Ministry of Higher Education (MOHE) for providing the SLAI scholarship that has made the start of this degree possible. I acknowledge direct and indirect assistance from all of my friends here in Newcastle. I wish you all the best in your careers and life.

Finally, I wish to convey my sincere thanks to my wife, children and family members for their motivation, moral support and patience on this path.

List of publications

Peer reviewed scientific publications included as part of this thesis

This thesis is based on the following papers, listed in the following sequence within the present manuscript.

1. T Fiedler, MA Sulong, V Mathier, IV Belova, C Younger, GE Murch, "Mechanical properties of aluminium foam derived from infiltration casting of salt dough." *Computational Materials Science* 81 (2014): 246-248.
2. Taherishargh, M, MA Sulong, IV Belova, GE Murch, T Fiedler, "On the particle size effect in expanded perlite aluminium syntactic foam." *Materials and Design* 66 (2015): 294-303.
3. M.A. Sulong, M. Taherishargh, I.V. Belova, G.E. Murch, T. Fiedler, "On the mechanical anisotropy of aluminium perlite syntactic foam." *Computational Materials Science* 109 (2015): 258-265.
4. M.A. Sulong, M. Vesenjak, I.V. Belova, G.E. Murch, T. Fiedler, "Compressive properties of Advanced Pore Morphology (APM) foam elements." *Materials Science and Engineering: A* 607 (2014): 498-504.
5. M Vesenjak, MA Sulong, L Krstulović-Opara, V Mathier, T Fiedler, "Dynamic compression of aluminium foam derived from infiltration casting of salt dough." *Mechanics of Materials* (2015).
6. M.A. Sulong, I.V. Belova, A.R. Boccaccini, G.E. Murch, T. Fiedler, "A model of the mechanical degradation of foam replicated scaffolds." *Under review in Journals of Materials Science*

I warrant that I have obtained, where necessary, permission from the copyright owners to use any part of my own published work in which the copyright is held by another party.

Additional publication

1. T Fiedler, MA Sulong, M Vesenjak, Y Higa, IV Belova, A Öchsner, GE Murch, "Determination of the thermal conductivity of periodic APM foam models." *International Journal of Heat and Mass Transfer* 73 (2014): 826-833.

Conference contributions

1. MA Sulong, V Mathier, I Belova, G Murch and T Fiedler, "Compressive Properties of Corevo® Foam under Uni-Axial Loading Based on Experimental and Numerical Analysis." *Applied Mechanics and Materials*. Vol. 597. 2014. 3rd International Conference on Advanced Materials Design and Mechanics (ICAMDM) May 23-24, 2014, Singapore.
2. MA Sulong, I Belova, T Fiedler, G Murch and A Öchsner: On the Elastic-Plastic Properties of Syntactic Perforated Hollow Sphere Structures, In: Cellmat 2012, 7th International Conference on Porous Metals and Metallic Foams, Nov 7-9, 2012, Dresden, Germany. (Poster presentation)

Table of Content

Declaration	ii
Statement of Contribution	iii
Dedication	iv
Acknowledgements	v
List of publications	vi
Table of Content	viii
Abstract	ix
List of Symbols	x
Chapter 1	Introduction
	1
	1.1 Hypotheses
	4
Chapter 2	Literature Review
	6
	2.1 Advanced porous materials
	6
	2.1.1 Cellular metals
	6
	2.1.2 Tissue engineering scaffolds
	8
	2.2 Manufacturing
	10
	2.2.1 Fabrication technique of cellular metals
	10
	2.2.2 Production of tissue engineering scaffolds
	14
	2.3 Applications
	15
	2.3.1 Multi-functional cellular metals
	15
	2.3.2 Tissue engineering scaffolds in applications
	17
	2.4 Limitations
	19
Chapter 3	Mechanical properties of aluminium foam derived from infiltration casting of salt dough
	20
Chapter 4	On the particle size effect in expanded perlite aluminium syntactic foam
	24
Chapter 5	On the mechanical anisotropy of aluminium perlite syntactic foam
	35
Chapter 6	Compressive properties of advanced pore morphology foam elements
	44
Chapter 7	Dynamic compression of aluminium foam derived from infiltration casting of salt dough
	52
Chapter 8	A model of the mechanical degradation of foam replicated scaffolds
	78
Chapter 9	Conclusions and Outlook
	99
	9.1 Engineering material charts
	99
	9.2 Discussions
	101
	9.3 Conclusions
	103
	9.4 Outlook
	103
References	105
Appendix	111
	viii

Abstract

Advanced porous materials are a new group of materials where the desired properties can be controlled and even tailored. These interesting materials offer a vast field of applications, thanks to their multi-functional abilities. Several types of advanced porous structures including cellular metals and ceramic porous materials are the focus of the present investigation. Corevo[®] foam and perlite metallic syntactic foam are investigated in this thesis and manufactured from infiltration casting. In addition, advanced pore morphology foam elements are addressed that are fabricated using thermal expansion of a thin wire-shaped precursor. Ceramic porous structures specially developed (via foam replication) for tissue engineering scaffolds are also studied within the scope of this work. Given the similarity of the geometrical structure of all these materials, the same mechanical characterisation approaches are adopted to assess their mechanical properties. The materials properties are determined for quasi-static and dynamic compression for both small and large strain deformation. Numerical simulations are performed by making use of the highly accurate models obtained from micro-computed tomography data. Where possible, numerical results are verified by the findings of experimental testing. Detailed analysis is included in each chapter elaborating the result from the numerical simulations and the compressive loading test. Versatile tools such as electron microscopy, image based geometry analyser software and IR-thermal imaging are utilised to assist the study. The results show that all cellular metals investigated in this thesis exhibit the characteristic stress-strain curve of metallic foams. This means that a linear slope is found in the beginning of the compression loading, this is followed by a long plateau region indicating energy absorption capability and ends with a steep slope at the end representing the densification. Corevo[®] foam exhibits a significant amount of mechanical anisotropy in casting direction under quasi-static compressive loading. The degree of mechanical anisotropy is considered mild for perlite metallic syntactic foam in the casting direction under the same loading condition. Foam materials (Corevo[®] and advanced pore morphology foam element) characterised under dynamic loading show a strain-rate dependence property. Last, but not least, a possible extension of the present research is proposed at the end of this thesis in the Conclusions and Outlook section.

List of Symbols

Greek letters

Symbol	Description
ε_{pl}	Plastic strain
ε_u	Ultimate yield strain
ρ_{Al}	Aluminium density
ρ_P	Perlite particle density
ρ_{TiO_2}	Titania density
ρ_s	Perlite particle's solid part density
σ_0	Initial yield stress
$\sigma_{0.2}$	0.2% offset yield stress
σ_{max}	Maximum compressive stress
σ_{pl}	Plateau stress
σ_u	Ultimate yield stress
σ_{ys}	Yield stress
ϕ_{Al}	Calculated aluminium volume fraction
ϕ_{Res}	Resorbed volume fraction
$\phi_{TiO_2}^*$	Titania volume fraction in original scaffold before resorption
Δu_{\parallel}	Average length change in parallel direction
Δu_{\perp}	Average length change in perpendicular direction
ρ	Density
ε	Strain tensor
η	Energy absorption efficiency
ν	Poisson's ratio
χ	Degree of anisotropy
ϕ	Diameter

Arabic letters

Symbol	Description
A_0	Initial surface area
F_N	Nodal force
S_i	Specific internal surface area
V_{Al}	Matrix volume fraction
V_{Cyl}	Cylinder volume
V_{Prism}	Rectangular prismatic volume
V_{TiO2}	Calculated titania volume
V_{TiO2}^*	Titania volume in original scaffold before resorption
V_m	Metal volume
V_p	Perlite particle volume
V_{sf}	Syntactic foam volume
d_{max}	Maximum diameter
d_{min}	Minimum diameter
l_0	Initial side length
l_{col}	Column strut length
m_s	Mass of combined perlite particles
m_{sf}	Mass of syntactic foam
p	Porosity
p^*	Porosity of original scaffold before resorption
h, H	Height, Height of cylinder
C	Strain rate sensitivity
D	Diameter of cylinder
E	Young's modulus
T	Tangent modulus
W	Absorbed energy
d	Diameter
dF	Change in force
dy	Change in $-y$ displacement
k	Effective stiffness
l	Length
m	Mass
n	Power law relation coefficient
t	Time
u	Macroscopic deformation

IUPAC and ASTM nomenclature

Symbol	Description
A1100	Ductile aluminium alloy
A201	Aluminium alloy
A356	Al; Si(7.2%);Mg(0.4%), Aluminium alloy billets
A357	Al; Si(7%);Mg(6%), Aluminium alloy billets
A6061	Hardened aluminium alloy
Al ₂ O ₃	Alumina
SiC	Silicon carbide
TiH ₂	Titanium dihydride
TiO ₂	Oxygen(2-);Titanium(4+), Titania or Titanium dioxide

Abbreviations

Abbreviation	Description
3D	Three Dimensional
APMS	Advanced Pore Morphology Structure
ASTM	American Society for Testing Materials
CCD	Charge-Coupled Device
CoV	Coefficient of Variance
CT	Computed Tomography
DIC	Digital Image Correlation
EP	Expanded Perlite
ESA	European Space Agency
FEA	Finite Element Analysis
HVN	Vickers Hardness Number
IR	Infra-Red
ISO	International Organisation for Standardisation
IUPAC	International Union of Pure and Applied Chemistry
MHSS	Metallic Hollow Sphere Structure
MST	Mean Strut Thickness
NURBS	Non-Uniform Rational B-Spline
PDLLA	Poly(D,L-lactide)
PGA	Polyglycolide
PLA	Polylactic Acid
QS	Quasi-Static
RAM	Random Access Memory

Continuation of abbreviations	
Abbreviation	Description
RVE	Representative volumetric element
SEM	Scanning Electron Microscope
Std. Dev.	Standard Deviation
MSF	Metallic Syntactic Foam
STL	Stereolithography

Chapter 1

Introduction

Porous materials in nature have evolved to achieve structural optimisation. They accommodate the need for having lightweight yet strong structures. Structures existing in nature such as bones, cork, wood and honeycombs are perfect examples to showcase this concept. These structures have inspired engineers to develop new materials to suit various needs of applications. Advanced porous materials are a group of materials that can be tailored to provide multi-functional properties. They can be manufactured via many different ways and by using a wide range of base materials. Examples that are investigated in the scope of this thesis are cellular metals and tissue engineering scaffolds.

Cellular metals are a category of advanced porous materials which were discovered over eight decades ago where a very first patent was documented in French (Banhart, 2013). These engineered materials are distinguished from traditional dense metals by their combination of specific mechanical and physical properties. Metallic cellular structures in general can be grouped into two main classes: open-cell and closed-cell types (Jee *et al.*, 2000). One outstanding feature of these materials is their ability to absorb large amounts of strain energy at a relatively low stress level due to their highly porous structure (Öechsner and Augustin, 2009). Cellular metals are used in engineering applications such as lightweight sandwich panels, automotive crash absorbers and industrial machine vibration dampers (Pannert *et al.*, 2009).

Materials with porous structures also have been developed in biomedical research. The main applications in this field are tissue engineering scaffolds. A tissue engineering scaffold is implanted inside the human body to support the regrowth of damaged or missing tissue. During this process the structure has to match the stiffness and strength of the surrounding tissue in order to support the mechanical stresses during the ingrowths (Xie *et al.*, 2010, Boccaccini *et al.*, 2006). Depending on the type of tissue that is intended to re-grow, the base material and geometry of the scaffold can be adjusted to match the required mechanical properties. To date, a number of bio-inert and biodegradable tissue engineering scaffolds have been designed to fulfil these specific requirements. Inorganic, ceramic-based scaffolds such as titania, alumina, and calcium phosphates are among available examples reported in the literature (Mohamad Yunos *et al.*, 2008). Organic, polymer based scaffolds, for instance, polyglycolic acid (PGA), polylactic acid (PLA), or co-polymers polylactic-co-glycolic acid (PLGA) are also used to synthesise a highly porous scaffolds (Chen and Boccaccini, 2006, Baker *et al.*, 2009, Torres *et al.*, 2007).

The detailed investigation of the mechanical properties of advanced porous materials will provide an important contribution to engineering and materials science. In the present study Corevo[®] foam, perlite-metallic syntactic foam (perlite-MSF), advanced porous morphology structure (APMS) and titania biomaterial scaffolds are investigated by means of numerical simulations and/or experimental tests. Most of the samples are characterised mechanically for

the first time. For engineering applications of cellular metals, the precise knowledge of their mechanical properties such as stiffness, strength and energy absorption capability is crucial. This research is required in order to advance the knowledge of cellular metals. The same is true for the materials used for biomedical applications: characterisation of general mechanical properties for tissue engineering scaffolds is very important in order to match the targeted surrounding bone (or soft tissue) structure.

The investigations presented in this thesis are done either by means of experimental tests or numerical analysis. Wherever possible, both methods are combined to obtain an independent validation of the results. The advantages of experimental tests include the direct assessment on intended samples and time saving. However, there are two major disadvantages of the experimental approach: (i) observations are usually limited to the surface of samples and no information on internal deformation mechanisms can be obtained and (ii) destructive testing prevents the repeated investigation of identical samples. Undoubtedly, experimental tests are very crucial in determining the suitability of metallic foams for specific usage. The additional computational analysis of the material further allows the overcoming of the limitations of experimental testing without the increased cost and time requirements. It should be emphasised here that experimental testing on cellular metals permits the sample to be used only once. This limitation makes the investigation of anisotropic behaviour of cellular foams difficult by means of experimental testing. In contrast, computational analysis based on virtual 3D models of the real sample is non-destructive and the investigation can be repeated for loading in different spatial directions. This repetitive nature of simulation allows the anisotropic material behaviour (for example, of cellular metals) to be explored. Numerical simulations also allow parametric studies to be conducted. This means a controlled variation of a single parameter (i.e. hardening modulus) is possible since a single numerical model can be used repeatedly. The limitations of computational analysis are: long computation times; and the need for validation by means of the experimental test to ensure the reliability of the results. It is worth mentioning that the combination of experimental testing and numerical analysis adopted in several investigations in this thesis provides a more extensive insight.

The main focus of this thesis will be on the mechanical characterisation of metallic foams which are assessed by quasi-static and dynamic loading modes. The general mechanical properties for advanced porous structure such as Young's modulus, yield stress, plateau stress and energy absorption are characterised within the scope of this thesis.

The thesis begins with an Introduction (Chapter 1) which provides a general overview of the topic of this thesis. That Chapter elaborates the link between papers gathered in the following Chapters of this manuscript. The following Chapter 2 presents a general literature review on advanced porous structures that is supplemented by more specific information in the beginning of the subsequent Chapters. Chapter 2 addresses the topics manufacturing, application and limitations of advanced porous materials.

Chapters 3-5 focus on the mechanical characterisation of cellular metals manufactured by infiltration casting, i.e. Corevo[®] foam and perlite-metallic syntactic foam (perlite-MSF). The

difference between these two materials originates in the physical properties and geometry of the filler particles used. Corevo[®] foam has filler particles (salt particles) with visible edges and perlite-MSF with a more rounded geometry. Chapters 3-5 also cover the mechanical characterisation of the metallic foams using quasi-static loading. Quasi-static compression is the simplest and thus most efficient test on most engineering materials and allows the determination of Young's modulus, Poisson's ratio and the initial yield stress. Some properties that are unique to cellular metals are the plateau stress and densification strain and can further be determined by these compression tests. The mechanical properties of Corevo[®] foam are discussed in Chapter 3 and perlite-MSF is studied in Chapter 4. In Chapter 4 the effects of particle size on the mechanical response of the cellular metal is investigated. Chapter 4 discusses the mechanical characterisation of perlite-MSF based on experimental tests and is extended using computational analysis in the subsequent Chapter 5. The investigation also employs computational simulation to study the mechanical anisotropy of perlite-MSF. Strain hardening first observed in experimental testing in Chapter 4 is investigated numerically by making use of a reverse engineering method.

The thermal expansion of pre-cursor method is an alternative approach to produce metallic porous structures. The cellular metals formed by using this approach (i.e. APMS) allow the close control of their physical properties such as the amount of porosity, average pore size, pore shape, pore distribution and degree of pore coalescence (Vesenjak *et al.*, 2013, Vesenjak *et al.*, 2011, Baumeister *et al.*, 2007) at increased cost due to a more complex manufacturing process. This motivates the investigation of the mechanical properties of APMS under compressive loading presented in Chapter 6. The Chapter combines the results of quasi-static and dynamic analyses of the material. The dynamic analysis enables the study of possible strain rate sensitivity. The strain rate sensitivity of metallic foams is defined as the material's stress-strain characteristics that are dependent on the rate (or speed) of loading. Dynamic analysis provides this information by compressing the sample at a high compression velocity. The deformation mechanism is usually somewhat different from the one found in quasi-static loading. This is chiefly due to inertia effects and base material strain rate sensitivity. As a result, the initial plastification observed in the scope of our investigation tends to be concentrated at the interface of the sample with moving pressure stamp.

Chapter 7 discusses the dynamic analysis of Corevo[®] metallic foam. The heat generated due to plasticity during dynamic loading is captured by an IR thermograph camera to identify areas of high plastic deformation. The use of infrared cameras during the compression test provides an important insight of major deformation behaviour of the cellular metals which is unavailable to the naked eye. However, the analysis with IR thermograph is limited to the outer surface of the sample. Therefore, the additional deformation analysis of the internal deformation mechanism is performed using computational analysis of the same material.

In Chapter 8, a *ceramic* cellular structure is considered. This tissue engineering scaffold is made of titania and intended for application in bone-remodelling. The ceramic cellular structure is different to cellular *metals* because of its different base material. However, the porous structure (morphology) is very similar to cellular metals with a comparable porosity.

This enables the characterisation of the material using a similar approach for computational analysis as for cellular metals. Numerical models are generated from the μ CT data to capture the complex geometry of the scaffold. The geometry data is further modified to simulate surface erosion due to immersion in body fluid and predict the resulting change in mechanical properties.

Finally, conclusions and a brief outlook are presented at the end of this manuscript in Chapter 9.

Section 1.1 Hypotheses

In this section, the hypotheses in the scope of this thesis are presented. These hypotheses are addressed chapter by chapter in order to cover all the important research questions that lead to the investigations conducted in the thesis.

In Chapter 3, it is proposed that open-cell type cellular metals will have a layer-wise failure mechanism. This hypothesis is tested by careful monitoring of the propagation of the plastification regions. This is achieved by means of numerical modelling with the use of a highly precise reconstructed 3D model from a μ CT scanner. This approach is very beneficial because of the ease of the virtual analysis and obtaining results coming from it.

The investigation conducted in Chapter 4 aims to answer the question: Does the filler particle size affect the general mechanical properties of metallic foams? At present, several papers in the literature have already indicated that the size of filler particles in ceramic and polymeric based foams directly affects its mechanical properties (Juhasz, 2004) and (Cho, Joshi and Sun, 2006).

Chapter 5 starts with the proposition that there is a significant difference between the amount of load that can be supported by thin struts or weak cell walls parallel to the loading direction compared with other directions. This research question has also arisen due to anisotropic behaviour of mechanical properties obtained in Chapter 3. The samples in Chapter 3 and Chapter 5 are different in terms of filler particles' type and chemical composition of matrices used. However, their cellulous structures and manufacturing route are nearly identical.

In the following Chapter 6, we postulate that a single APM foam has a uniform plastic deformation throughout the structure. The investigations in this chapter are also directed to answer the question: Are the mechanical properties of single APM foams affected if the outer skin is removed?

In Chapter 7, we wish to probe whether the mechanical behaviour gained from quasi-static loading for open-type metallic foam is significantly different from dynamic loading counterparts. Thermal imaging is used in the investigation to locate the deformation concentration during the impact test. The research question is: Does inertia affect the plastic deformation of metallic foam derived from infiltration casting? This is answered at the end of this research.

Finally, in Chapter 8 we assume that if a tissue engineering scaffold is gradually eroded in simulated body fluid (SBF), then its mechanical properties also characteristically disintegrate. This relationship (in functional form) between the immersion time and effective mechanical properties is investigated. Results of this study are certainly valuable for future tissue engineering development.

Chapter 2

Literature review

This Chapter provides an extensive literature review that covers the general properties, manufacturing, applications and limitations of advanced porous materials. The mechanical characterisation of advanced porous materials such as cellular metals and tissue engineering scaffolds under compressive loading is the ultimate objective of this work. The results of the present study allow the mechanical behaviour of advanced porous materials subjected to compressive loading in technological applications to be predicted. Chapter 2 can also be used as a reference point whenever the materials investigated in this work are compared to existing porous materials reported by other researchers.

2.1 Advanced porous materials

Advanced porous materials are a class of materials known for their low densities and excellent strength-to-weight ratio. They demonstrate a wide variety of specific mechanical and physical properties (Ashby *et al.*, 2000) that make them different from traditional dense metals. To date, cellular metals have been used in a number of applications discussed in Section 2.3, thanks to a broad selection of different base materials to choose from. For example, aluminium honeycomb sandwich structure was replaced by Aluminium Foam Sandwich (AFS) to build two cone-shaped adaptors (Schwingel *et al.*, 2007) for the European ‘Ariane 5’ rocket that must be very light but exhibit sufficient strength to support the huge weight of the vehicle.

In the biomedical research field, a new generation of tissue engineering scaffolds are being designed to aid cell growth whilst giving the structural support from the imposed load (Hollister, 2005, Adachi *et al.*, 2006). These scaffolds constitute another sub-class of advanced porous materials. Various biodegradable tissue engineering scaffolds are being investigated for application in real life bone regeneration (Hutmacher *et al.*, 2004, Rezwan *et al.*, 2006, Novak *et al.*, 2009).

2.1.1 Cellular metals

The word ‘cell’ originates from the Latin word *cella* meaning enclosed space. This word was coined by British scientist, Robert Hooke in the 1660s when he investigated cork and found pores which he called “cells” under his hand-crafted microscope (Gibson *et al.*, 2010). Figure 2.1 shows the microscope drawn and invented by Robert Hooke and a sample of a cork tree’s bark. The concept of cellular metals emerged in 1983 (Ashby and Medalist, 1983). Later, in the early 21st century, these ground-breaking materials have been further studied in terms of cost-efficient manufacturing methods and multi-functionality. Several prominent researchers in this field, for example, Gibson and Ashby, introduced a universal framework for the characterisation of cellular metals (i.e. relative density, plateau stress and densification strain) that serves as reference point for the present researchers (Ashby *et al.*, 2000, Gibson and Ashby, 2001).

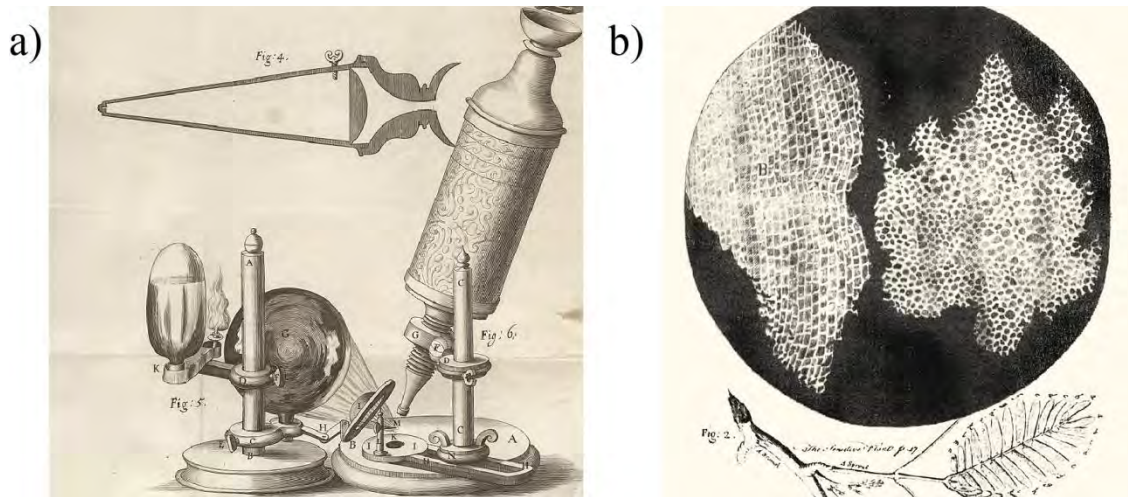


Figure 2.1: a) Classic microscope invented by Robert Hooke b) Pore structure of cork under Hooke's microscope (Both images are adapted from the *Micrographia* book, 1961).

Gas-filled voids or low-density spacer materials are introduced within the metallic matrix to produce lightweight cellular metals. There are two main categories of cellular metals, namely open-cell and closed-cell types (Jee *et al.*, 2000). Open-cell type cellular metals have the geometry of a sponge, where a fluid like water can easily pass through the material. Closed-cell cellular metals are similar to foams such as polystyrene foam that contains trapped air bubbles. In both cases, the pore geometry may vary in terms of its size, spatial morphology, and shape (Banhart, 2001, Degischer and Kriszt, 2002, Öchsner and Augustin, 2009).

Despite the significant physical differences of pores in open- and closed-cell type cellular metals, the characteristic compressive stress-strain curves remain similar. A comparison between Alporas[®] (closed-cell type) and M.Pore[®] (open-cell type) compressive stress-strain curves can be seen in Figure 2.2 (Bastawros *et al.*, 2000, Vesenjak *et al.*, 2012). Overall, the curves obtained from compression loading tests can be divided into three distinctive regions. These three regions can be easily identified by separating the initial (quasi-linear) region denoted by a circle, notably long plateau stress (shaded middle) curve and rapidly ascending densification stress at the end (Coty *et al.*, 2008). The similarity of the compressive curves for both types of cellular metals is chiefly due to the existence of hollow voids within the material's matrix. This unique physical feature allows the material to absorb a significant amount of energy during compressive loading whilst undergoing large macroscopic deformation and without losing its structural integrity. The combined volume fraction of voids (commonly referred to as porosity) determines the strength of the material and its ability to absorb energy from the compressive stress before densification occurs.

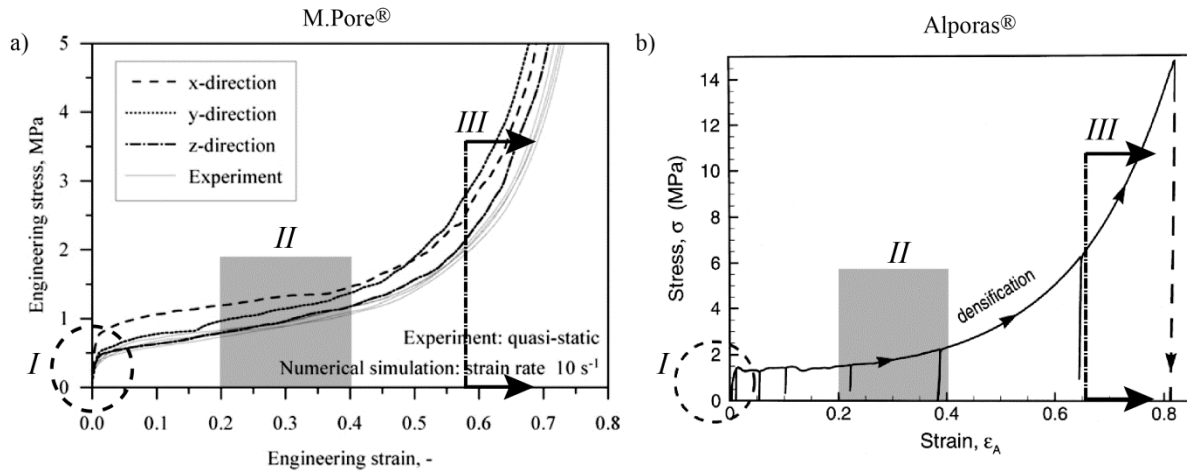


Figure 2.2: Compressive loading stress-strain curves for a) open-cell type, b) closed-cell type cellular metals. Images adapted from published literature (Vesenjak *et al.*, 2012, Bastawros *et al.*, 2000)

By introducing pores into solid materials (via foaming or particles inclusion) the properties change drastically. For example, metallic and ceramic foams can reach densities as low as 10^2 kg/m^3 compared with 10^4 kg/m^3 for solid metals and ceramics (Ashby *et al.*, 2000, Gibson and Ashby, 1997). This significantly reduced density allows the design of light yet strong and stiff structures which is difficult to achieve using solid materials. The extended range of possible densities is not the only change of properties made possible by the foaming of a solid material. Other properties that can be tailored are Young's modulus (Badiche *et al.*, 2000, Yu *et al.*, 2012), yield strength (Amsterdam *et al.*, 2008, Bart-Smith *et al.*, 1998) and thermal conductivity (Babscán *et al.*, 2003, Solórzano *et al.*, 2009). As a result, a new range of properties can be adjusted to suit specific engineering applications. Further attractive properties of cellular metals that have been reported in the literature are vibration damping (Merkel *et al.*, 2009), acoustic absorption (Öechsner and Augustin, 2009) and versatile thermal properties (Babscán *et al.*, 2003, Hosseini *et al.*, 2009). The large internal surface areas created by the internal pores further enable their use as catalysts or heat exchangers.

2.1.2. Tissue engineering scaffolds

Advanced biomaterials are designed to support the natural recovery mechanisms of the human body. To this end, 3rd generation tissue engineering scaffolds are being developed which support cell growth, are biocompatible and are slowly degradable at the same time (Rezwan *et al.*, 2006, Tiainen *et al.*, 2012). As a result, revision surgeries can be avoided. Given that the scaffold material is biodegradable, the potential risk imposed by permanent medical prostheses can be avoided as well (Quadbeck *et al.*, 2010). Figure 2.3 shows the geometry of a ceramic based tissue engineering scaffold that has been re-generated from micro-computed tomography (μCT) data. The resorbed and unresorbed titania scaffolds are illustrated in the Figure to show the surface degradation of the material in body fluids.

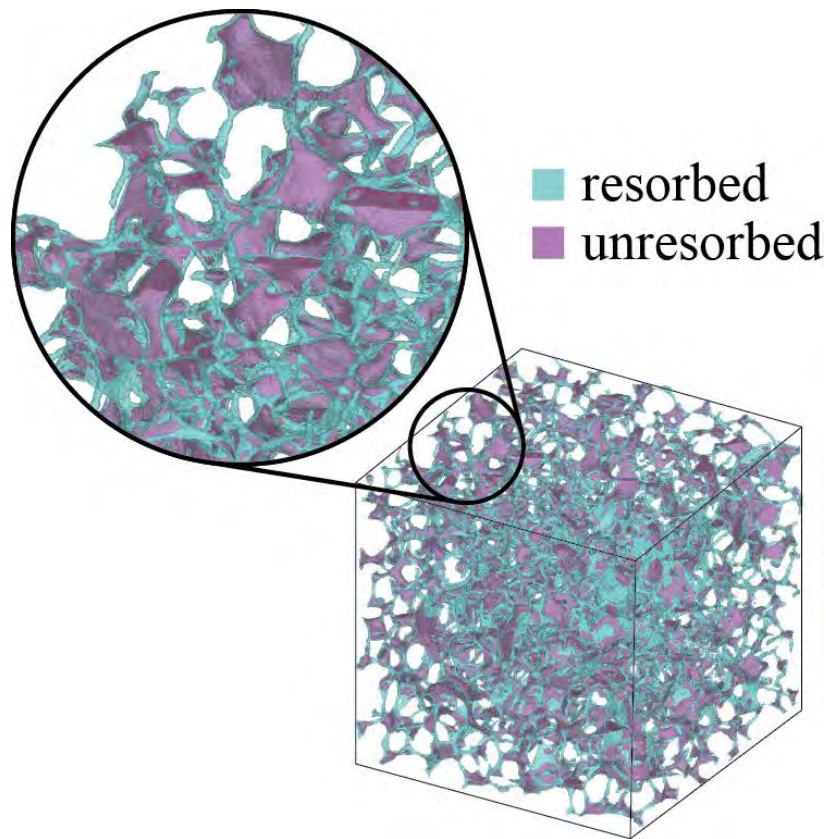


Figure 2.3: Titania biomaterial scaffold generated from μ CT data

Biodegradable scaffolds are intended for use in bone-regeneration. This is a new concept of tissue engineering to replace the traditional practice of synthetic implants introduced in the early 1990's which has limitations from tissue grafting (Xie *et al.*, 2010). Biodegradable polymers can be grouped into 4 classes: 1) natural-based poly-saccharides materials (i.e. starch, chitosan), 2) proteins (i.e. soy, collagen, silk) 3) Polyglycolide (PGA), 4) Poly(D,L-lactide) (PDLLA) (Rezwan *et al.*, 2006). Alternatively, tissue engineering scaffolds can be made of ceramics such as bioactive glass (Bioglass[®]), alumina (TiO_2) and calcium phosphates (Mohamad Yunus *et al.*, 2008). Bioactive glass and ceramic scaffolds are known to have a low compression load resistance and high brittleness. In addition, it was shown by (Gutwein and Webster, 2002) and by (Webster *et al.*, 2001) that the bioactive materials with bioinert particulates such as TiO_2 and Al_2O_3 show a lack of bone bonding when the particulate form is in bulk or micrometer-size. However, an enhanced cell integration is observed when the particulate inclusions are nano-sized (Savaiano and Webster, 2004)

Tissue engineering scaffold degradation has been addressed in previous research. Experimental studies have used magnetic resonance and computed tomography imaging to monitor *in vivo* implant resorption (Torio-Padron *et al.*, 2011, Kłodowski *et al.*, 2014). However, the high cost, risk and time requirements associated with these techniques limit their applicability for extensive studies. This inhibitor can be overcome by the additional use of numerical models. Han and Pan (2009) developed a mathematical model of the simultaneous crystallization and biodegradation of biopolymers such as PGA and PLA. They extended a previous phenomenological model Wang *et al.* (2008) by considering the

formation of a crystalline phase that retards the reaction. The models combine a set of coupled reaction-diffusion equations that were solved for simple geometries using a finite element method. In Sanz-Herrera and Boccaccini (2011) addressed the degradation of bioactive glasses for tissue engineering scaffolds. The reaction of bioactive glasses with body fluid results in hydroxyapatite being formed on the surface of the scaffold. The growing hydroxyapatite layer introduces a diffusion barrier that decreases the reaction rate over time. The complete set of equations that constitute their model was solved using a finite element method representing the geometry as voxels.

2.2 Manufacturing

In the manufacturing of cellular metals, perhaps the major impediment faced is the materials' stochastic geometry. The complex and irregular character of the internal structure of cellular metals may cause the mechanical properties to be unreliable and prevent their usage in safety-relevant applications. Furthermore, the development of advanced tissue engineering scaffolds is based on the motivation to combine mechanical support with value added properties such as improved bioactivity and controlled degradation ability. In the following sub-sections, the existing manufacturing methods for cellular metals and advanced tissue engineering scaffolds are discussed.

2.2.1 Fabrication technique of cellular metals

Owing to the rapid development of manufacturing processes, many types of cellular metals can be manufactured. In recent years, not only have a variety of novel manufacturing processes appeared, but also an improvement in the quality of the product and a reduction of the relatively high cost for foamed metals can be seen. There are nine different production processes of metal foams that have been identified (Ashby *et al.*, 2000). Figure 2.4 illustrates a list of existing manufacturing routes for cellular metals. The properties of cellular metals are influenced by the properties of the used metal, their relative density, pore sizes and the cell morphology. Cellular metals demonstrate a variety of outstanding specific mechanical and physical properties such as considerable energy absorption (Evans *et al.*, 1998) and high specific stiffness (Ashby *et al.*, 2000). Cellular metals also exhibit a low specific weight, reduced electrical conductivity, good mechanical damping, reduced flammability, good recyclability and good machinability (Baumeister *et al.*, 1997).

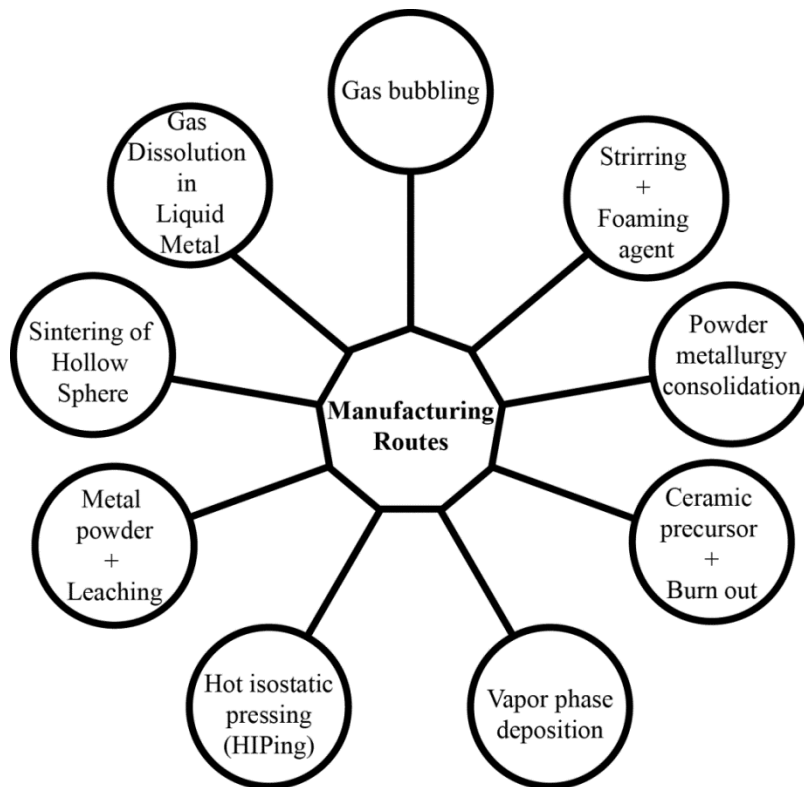


Figure 2.4: Identified manufacturing routes of cellular metals. Many of these methods are implemented in commercially established cellular materials (Ashby *et al.*, 2000).

APM foam elements. In 2005, Stöbener *et al.* investigated a new concept of metal foam components production (Stöbener *et al.*, 2005b). The resulting cellular material is called Advanced Pore Morphology (APM, see Figure 2.6) foam and it has been developed based on an improvement of the powder metallurgical FOAMINAL[®] process that was introduced earlier by Baumeister (1990).

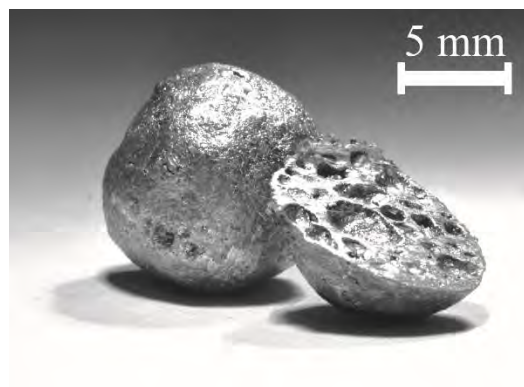


Figure 2.6: A photograph of APM foam elements.

The FOAMINAL[®] process is known to produce successfully near net-shaped parts and three-dimensional (3D) sandwich panels with a foamed core layer. In (Hohe *et al.*, 2012), an AlSi7 aluminum alloy was prepared in powder metallurgy precursor form with TiH₂ added as foaming agent. Foaming was activated by the heating of the precursor. This process usually takes place within a mould cavity. During the foaming process furnace temperatures up to 800 °C are used depending on matrix alloys and the presence of stabilizing ceramic particles. As a result, the foaming mould has to bear high thermal loads in each foaming cycle (Lehmhus *et al.*, 2009). A new process route proposed by Stöbener and Rausch (2009) in APM foaming eliminates the need for expensive moulds. The manufacturing procedure consists of powder compaction (by the CONFORM[®] process) and rolling of the AlSi7 alloy with TiH₂ foaming agent to obtain expandable precursor material. The wire-shaped precursor material (diameter $\varnothing = 3$ mm) is then cut into small granulates (length $l = 2$ mm) (Stöbener and Rausch, 2009), which are expanded into sphere-like foam elements (see Figure 2.6) due to the thermal decomposition of the TiH₂ foaming agent in a continuous belt furnace. This is driven by internal gas pressure, surface tension and the formation of an oxide skin. Three sizes of APM foam elements have been manufactured so far with diameters 5, 10, and 15 mm and foam element densities varying from 0.5-1.0 kg/m³ (IFAM, 2007, Lehmhus *et al.*, 2009). Structures assembled by APM foam elements exhibit two types of porosity: (i) the inner porosity in single APM foam elements (approx. 70%) and (ii) the outer porosity between many APM foam elements which depends on the size of the APM elements and their arrangement (Stöbener *et al.*, 2005a). Detailed information on the automated production of APM foam elements can be found in the literature (Stöbener and Rausch, 2009).

Corevo[®] foams. Corevo[®] foam is sometimes referred to as salt foam and is a new type of cellular material. This new material belongs to the class of open-cell type cellular metals. A photograph of Corevo[®] foam is shown in Figure 2.7. This lightweight structure is fabricated by means of infiltration casting method. The pores in the final product are filled with salt dough which acts as a placeholder before they are dissolved. Depending on the size of the salt dough pellets which can be selected from 2mm-10mm interval, broad range of porosities (65-85%) can be achieved.

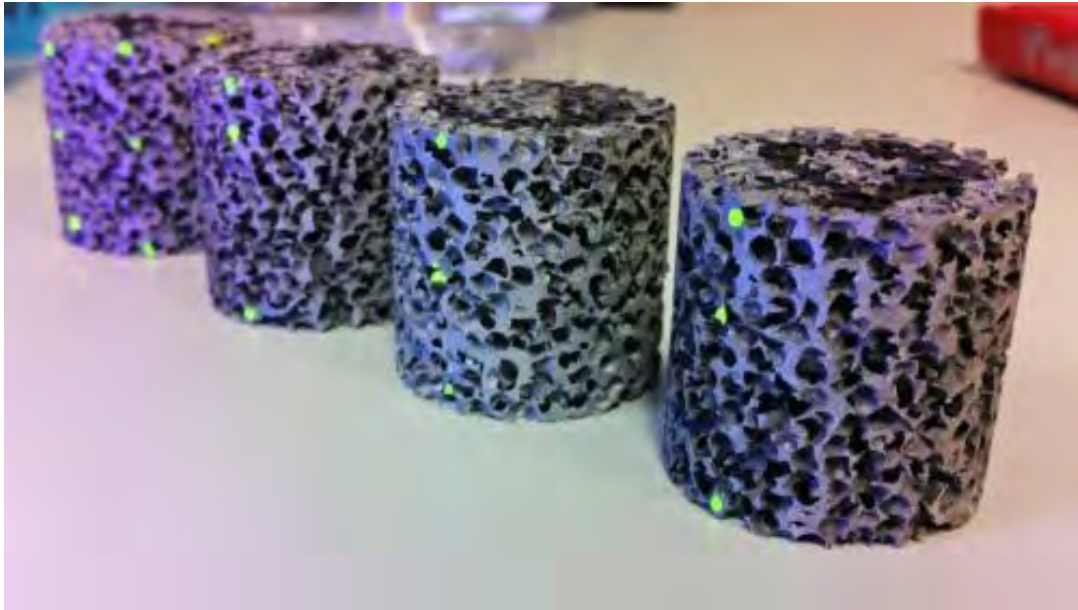


Figure 2.7: Light photographs of Corevo[®] foam samples

Perlite-MSF. A new type of metallic cellular foam material was introduced recently using low-cost expanded perlite (EP) particles as a filler material making use of the infiltration casting manufacturing technique. A reconstructed 3D model based on micro-computed tomography data of this syntactic foam is shown in Figure 2.8. The metallic matrix of the foam is made of A356 aluminium alloy. The manufacturing process includes the counter gravity infiltration of molten aluminium into a packed bed of perlite particles. The production cost of perlite-MSF is relatively low compared with other MSFs due to its inexpensive raw materials (filler particles and matrix) without the need of prolonged holding time in the furnace (>20 minutes) (Taherishargh *et al.*, 2014). Perlite particle size ranging from 1-5.6 mm can be used during the manufacturing process and this defines the final porosity of the foam. To achieve a homogeneous filler particle distribution, the mould is vibrated at controlled time intervals. The molten aluminium is injected through a small orifice from the bottom to the top of a graphite mould. A stainless steel mesh is positioned on top of the mould to hold the mixture of aluminium melt and (buoyant) perlite particles in place. Finally, the mould is cooled to room temperature before the sample is removed.

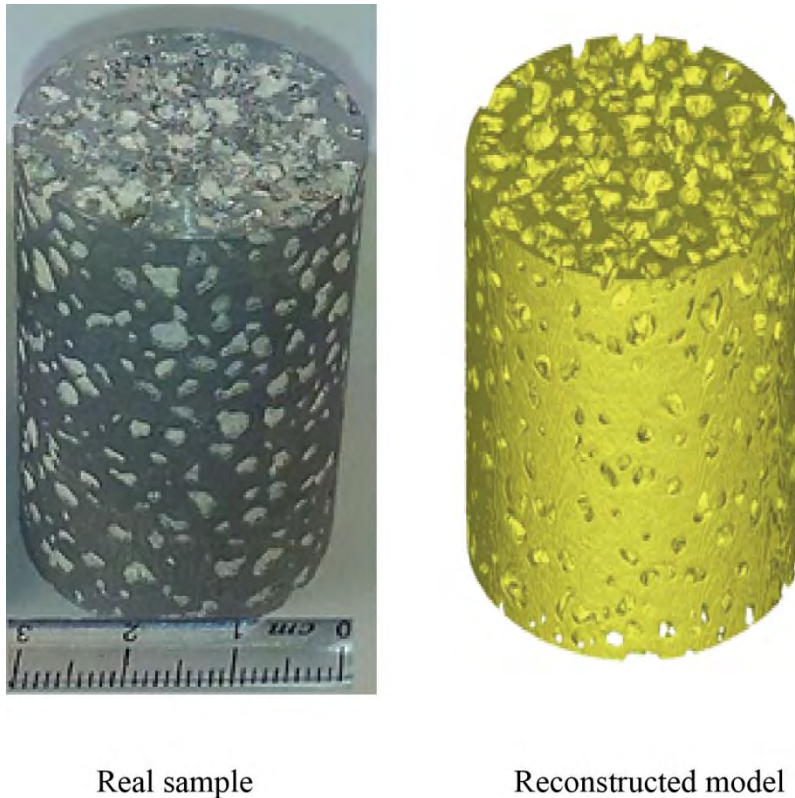


Figure 2.8: Perlite-MSF original sample and a virtual model (of another sample) reconstructed using μ CT data

2.2.2 Production of tissue engineering scaffolds

To date, the most effective methods to manufacture tissue engineering scaffolds are robocasting (Russias *et al.*, 2007), sol-gel synthesising (Menon, 2009), thermally induced phase separation (Torres *et al.*, 2007) and the foam replication method (Fu *et al.*, 2009). Details of some of these methods are described in this section.

Robocasting. Robocasting is a technique used to manufacture an object layer-by-layer, often with the help of computer-aided design (CAD) (Hutmacher *et al.*, 2004). In this technique, the three-dimensional (3D) printer's inkjet in the form of aqueous paste is deposited on top of the previous layer through a small orifice of a nozzle (Yeong *et al.*, 2004). The porosity of the horizontal XY plane is controlled by adjusting the neighbouring filaments. The vertical Z space is created by extruding subsequent layer of filaments over previous layer of filaments. One of the restrictions of this rapidly increasing biomaterial scaffolds production method is the limited range of materials that can be transformed into aqueous paste while retaining their bioactivity. Biomaterial scaffolds containing bioactive glass manufactured using robocasting method have been reported in (Russias *et al.*, 2007), but the information on production of bioactive glass scaffolds using similar methods is very limited. Recently, bioactive glasses from the 6P53B group have been used in robocasting methods to produce glass scaffolds that exhibit a compressive strength comparable to human cortical bone (~ 136 MPa) (Fu *et al.*, 2011b).

Sol-gel processing. Sol-gel synthesis is another technique to fabricate bioactive glass scaffolds. Scaffolds produced by the sol-gel method have a few advantages such as a hierarchical pore morphology and good process control (Menon, 2009, Uchida *et al.*, 2003, Fu *et al.*, 2011a). Hierarchical pores positively promote the response of human cells towards the scaffold. The likely explanation for this behaviour is that the scaffold structure successfully mimics the hierarchical nature of tissues and physiological environment (Fu *et al.*, 2011a). In spite of many good characteristics found in scaffolds derived from sol-gel method, their structures have a relatively low strength (0.3-2.3 MPa) (Jones *et al.*, 2006) and consequently this scaffold material can only be exploited in low load-bearing tissue areas.

Foam replication. The foam replication method was first used to produce macro-porous ceramics (Karl and Somers, 1963), before it was adapted to successfully create porous glass scaffolds. The chief advantage of the foam replication method is its ability to produce highly porous glass scaffolds with an open and interconnected porosity of up to 95% (Fu *et al.*, 2011a). Scaffolds that can be produced with the foam replication method include various base materials such as silicate (Vitale-Brovarone *et al.*, 2009), borosilicate (Fu *et al.*, 2010) and borate bioactive glass (Fu *et al.*, 2009). However the challenge of biomaterials produced by this technique is their relatively low mechanical strength compared to trabecular bone. Post-processing of glass scaffolds produced by foam replication such as coating with porous poly(D,L-lactide) PDLLA (Novak *et al.*, 2009, Gerhardt *et al.*, 2007) or carbon nanotubes can be used to improve the strength of the glass scaffold. It has been reported that PDLLA coated glass scaffolds are seven times stronger than their uncoated counterparts (Novak *et al.*, 2009). This strengthening mechanism could be attributed to the filling of micro-cracks in the thin struts by the PDLLA slurry (Fiedler *et al.*, 2014). The present study focuses on scaffolds manufactured using the foam replication method. The resulting scaffolds exhibit porosities $p > 90\%$ and an average pore size of 300 μm .

2.3 Applications

Both cellular metals and tissue engineering scaffolds are able to fulfil several functions. This ability is useful when optimisation is needed to comply with demanding working conditions. For example, cellular metals can be used to sustain a relatively high temperature of exhaust smoke emitted directly from an internal combustion engine when applied as a silencer or catalyst (Tritt, 2004, Merkel *et al.*, 2009). The new generation of biomedical scaffolds can not only be exploited as medical prostheses, but the same structure can also be a catalyst for cell growth during the patient's healing process (Glorius *et al.*, 2011, Li *et al.*, 2009).

2.3.1 Multi-functional cellular metals

High strength-to-weight ratio structures. Some industries, for example aerospace, demand materials that are simultaneously lightweight and strong. Similarly, modern motor vehicles benefit from the use of lighter materials. The use of such design materials reduces the energy consumption and facilitates the acceleration of the vehicle. Other examples of metal foams used in lightweight structures are robotic arms, milling machine tables (Baumeister *et al.*, 2004) and laser head mountings (Hipke *et al.*, 2007). Another interesting application is the

development of cone 3936 for Ariane 5 as shown in Figure 2.9. The cone structure of European Space Agency (ESA) rocket is built using aluminium foam sandwiches (AFS). The cone structure is an assembly of 12 segments (see Figure 2.9b) with an integrated flange used to hold them in position (Schwingel *et al.*, 2007). The cone structure has been tested at the prototype stage where around half of the limit load during launch was used. Sound agreement was found between the predictions made by numerical simulations and the static test. The cone structure with aluminium foam core can be seen as a promising candidate for future lightweight rocket construction.

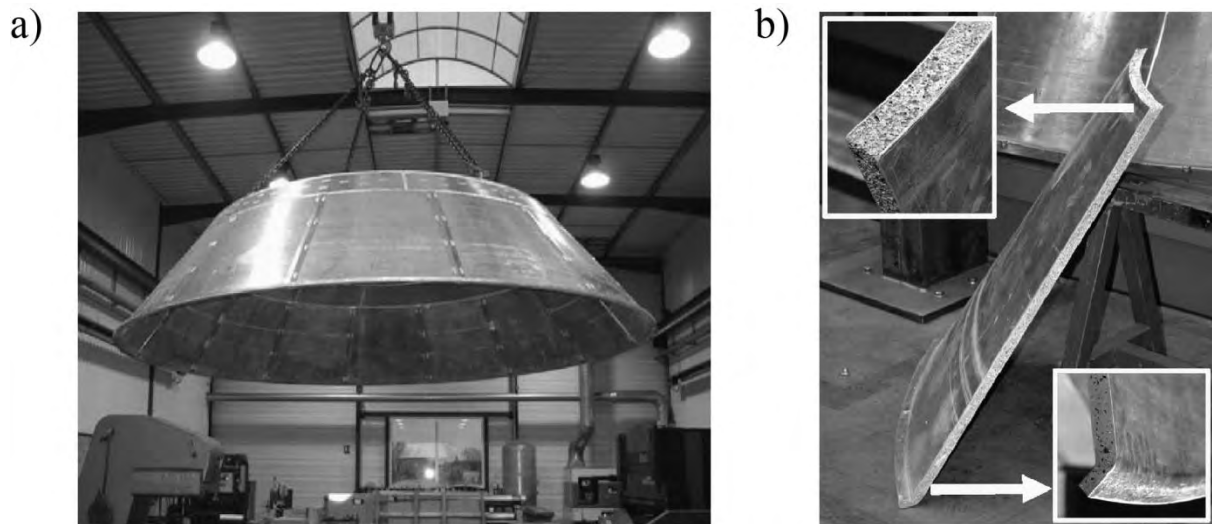


Figure 2.9: Cone prototype constructed for the body of Ariane 5 rocket, a) assembled AFS segments, b) close-up view of foam sandwiched by aluminium sheets (Image adapted from Schwingel *et al.*, 2007).

Energy absorption. Another important property of cellular metals is their ability for controlled collapse under high loads. This is due to the ability of the material to be compressed at a constant stress level within the stress plateau until the densification point is reached. A huge amount of energy can be absorbed by the unique structure of these metallic porous materials.

This is the perfect property for sacrificial components in modern vehicle design, for example a crash impact absorber. The cellular metals may be fitted to a vehicle and designed to collapse in order to protect passengers (Banhart and Weaire, 2002). Due to the cell wall structure in metal foams, a high compression load can be effectively absorbed by means of plastic deformation. Unlike polymer foams where energy is stored elastically and released after unloading, the absorbed energy in metallic foams is permanently converted into plastic deformation and thermal energy. One of the metal foam examples that are already commercially used is Alulight®. This closed-cell type of cellular metals is currently used in a side skirt crash absorber for luxury vehicles (Hipke *et al.*, 2007).

Thermal applications. Cellular metals can be used in a wide range of heat transfer related applications especially where lightweight structures that retain strength and toughness are needed. Unlike polymer foams that are broadly used due to their low thermal conductivity (e.g.: polystyrene hot-drink cups) metallic foams are ideal for heat transfer enhancement. Open-cell metals can be used in applications such as cryogenic heat exchangers, heat exchangers for airline equipment, coal combustors, heat sinks for high-powered electronic devices, heat shielding for aircraft exhaust, compact heat exchangers, liquid heat exchangers, air-cooled condenser-cooling towers and regenerators for thermal engines (Lu *et al.*, 1998).

Structural vibration damping. The low density of most cellular metals makes the material suitable for adding to components where excessive vibrations occur. Inside the porous structure of cellular metals mechanical vibrations are transformed into thermal energy thus reducing the vibration energy. As a rule of thumb, the smaller the pores within a cellular metal, the better vibrations can be absorbed (Raju *et al.*, 2007). Examples for the application in vibration damping are a high speed cutting machine and machine arm (Baumeister and Weise, 2000, Baumeister and Molitor, 2009). The vibrational behaviour of hollow sphere structures (HSS), a closed-cell type of cellular metal, has been addressed by Merkel *et al.* 2009. A good correlation between numerical and experimental frequency results was found.

Sound absorption. The unique structure of metal foams allows them to attenuate sound waves and acoustic energy by transforming them into heat energy. For this reason, open-cell metallic sponges are able to act as an acoustic absorber. For sound absorption (i.e. such as in a theatre), cellular metals absorb sound waves once they enter the pore cavities. However, the dimension of the cavities must be compatible with the wave length of the sound to enable them to penetrate into the porous material. In this application, the multi-functional properties of the metal foam add further advantages. The metal is durable to the most adverse work conditions such as high temperature, humidity and vibrations (Stöbener *et al.*, 2003) and non-combustible. An example for an industrial application is a gear wheel equipped with aluminium foam components. The cellular structure of metal foam in the gear provides two benefits: 1) Noise emission is reduced by the hybrid gear and 2) The total weight of the gear wheels is lowered by 25%.

2.3.2 Tissue engineering scaffolds in applications

Ceramic biomaterials have been widely applied in biomedical implant such as dental and orthopaedic implants (Boccaccini *et al.*, 2005). Tissue engineering scaffolds which also fall under ceramic biomaterial category, are fabricated to act as a bone graft (Hollister, 2005). Over a decade of development, the tissue engineering scaffolds have been improved to become bioactive and biodegradable. This improvement indeed is useful since the commonly practiced revision surgery need not be executed. Besides the cost being significantly decreased by avoiding revision surgery, the biodegradable scaffolds also reduce adverse risk to human health caused by permanent bone implants.

In developing this artificial bone, collaboration between powder metallurgy (PM) material engineers and clinical experts produces a material that is biodegradable. Open-cell cellular

materials made of Fe0.6P alloy has been successfully implanted in the femur of adult sheep and shows good biocompatibility and no inflammatory response of the surrounding bone tissue (Quadbeck *et al.*, 2010). Another research team at Fraunhofer IFAM in Germany investigated the same open-cell cellular structure but using Ti6Al4V alloy. The resulting bone implant matched the strength of real bone tissue and most importantly allows bone cells and blood vessels to grow inside the cellulous structure (Stephani, 2010, Muñoz-Bonilla *et al.*, 2013).

Titania scaffolds belong to the ceramic tissue engineering sub-group. Titania scaffolds derived from the foam replication method can reach an overall porosity of up to 85%. Furthermore, the microstructure of this material is similar to that of human trabecular bone (Fu *et al.*, 2008). Titania scaffolds are designed to act as a temporary support for the bone tissue regeneration. Titania scaffolds have been proven to be applicable for such application and a large number of studies have been reported on *in vivo* implantation in laboratory animals such as rabbits (Kłodowski *et al.*, 2014, Liu *et al.*, 2004), minipigs (Tiainen *et al.*, 2012), rats (Meretoja *et al.*, 2007, Midha *et al.*, 2013) and humans (Fu *et al.*, 2008). Several factors including biocompatibility, cell attachment ability and size of the pores determine the suitability of the scaffold to serve its ultimate purpose.

2.4 Limitations

In spite of having the ability to combine multiple functions into a single material, cellular metals and tissue engineering scaffolds are restricted by some factors. These limitations often stem either from lack of research or unknown parameters (i.e. pore coalescence, precise degree of bioactivity, etc.) (Boomsma and Poulikakos, 2001, Yeong *et al.*, 2004). However, these challenges become the driving force for engineers and material scientists alike to probe into the problems and develop viable solutions. As a result, further improvement can be accomplished.

Cellular metals. The scattering of material parameters represents an essential limiting factor for the large-scale industrial usage of cellular metals. Their stochastic geometry results in unpredictable mechanical properties. However, this problem can be overcome by finding ways to control the pore structure during the manufacturing process. By increasing control over the pore creation in cellular metals, it will allow better homogeneity of its morphology and topology (pore size distribution, pore shape and cell wall geometry) (Markaki and Clyne, 2001, Vesenjak *et al.*, 2008). As a result, a better control of these important parameters will allow a close control of the mechanical properties. Some researchers solve this problem by introducing a method where homogeneous metallic hollow spheres are assembled to form a metallic foam (Augustin and Hungerbach, 2009). A related approach is the use of a precursor heat expansion which consists of a mixture made up of metal powder and a powdered blowing agent (Stöbener *et al.*, 2005a) to create APM foam elements. Another important challenge for cellular metals to enter the mainstream market is the reduction of their high manufacturing cost.

Tissue engineering scaffolds. Numerous investigations have been reported in the literature showing that tissue engineering scaffolds can be manufactured using a variety of different base materials. Nevertheless, there are still a few aspects that hinder the advance of these innovative materials. First, the mechanical integrity of biomaterial scaffolds is frequently found to be below targeted application requirements. To compromise, an initially fragile tissue engineering scaffold usually needs a second treatment such as surface coating (Novak *et al.*, 2009, Meng *et al.*, 2009) or the incorporation of enforcement particles within the biomaterial scaffold (Rezwan *et al.*, 2006). Secondly, the tissue engineering scaffolds always suffer from inadequate structural design. The need for highly porous scaffolds (~90% porosity) (Novak *et al.*, 2009) to accommodate the cell growth impedes the optimisation of mechanical properties. Thirdly, a disadvantage is caused by the complexity of experimental tests with biological tissues which requires a long characterisation period (Kokubo and Takadama, 2006). This difficulty constrains the speed of acquiring essential data. Lastly, the adhesion of cells or degree of bioactivity within the implant is hindered by unsuitable scaffold surfaces which reduce the effective new cell growth (Liu *et al.*, 2004, Rohanová *et al.*, 2011). This is yet another challenge for tissue engineering scaffolds researchers and to date, several proposed methods (i.e. heat treatment) have already been reported in the literature.

Chapter 3

Mechanical properties of aluminium foam derived from infiltration casting of salt dough

Chapter 3 investigates the mechanical properties of Corevo[®] aluminium foam under quasi-static compression. This Chapter showcases the combined experimental and numerical testing approach that is further applied in the following Chapters 4, 5 and 6. The quasi-static mechanical characterisation of aluminium foam structure derived from infiltration casting of salt dough is discussed in this Chapter.

The effective elastic gradient (Young's modulus equivalent), Poisson's ratio, initial yield stress and 0.2% offset yield stress are determined experimentally and numerically. The complex internal geometry of the sample is successfully captured by means of micro-computed tomography (μ CT) imaging approach. The investigations are made using the numerical model and further test the mechanical anisotropy of the material. The numerical simulation also provides additional insight on the distribution of the plastic deformation within the material's meso-structure. To introduce compressive loading (performed on a total of four samples), appropriate boundary conditions are prescribed on the surfaces of the numerical models. Mechanical behaviour that is typical for cellular metals (e.g. initial elastic gradient followed by a plateau stress and densification) is found with a noticeable elastic anisotropy. Mechanical anisotropy is observed for Young's modulus and the initial yield stress, markedly in the direction that is parallel to the casting direction. Sound agreement between experimental and numerical results was found. The numerical analysis indicated that initial plasticity tends to occur in thin struts of the meso-structure which are parallel to the macroscopic loading direction.

The findings from this investigation enhance the knowledge of the compressive properties of open-cell type cellular metals under quasi-static loading. Results presented in this Chapter also add more information on cellular metals derived from infiltration casting.

This investigation has been published online and accepted for print publication by the journal Computational Materials Science.

T Fiedler, MA Sulong, V Mathier, IV Belova, C Younger, GE Murch, "Mechanical properties of aluminium foam derived from infiltration casting of salt dough." *Computational Materials Science* 81 (2014): 246-248.

Reprint license has been obtained from Elsevier.

Copyright © 2015 Elsevier



Mechanical properties of aluminium foam derived from infiltration casting of salt dough



T. Fiedler^{a,*}, M.A. Sulong^a, V. Mathier^b, I.V. Belova^a, C. Younger^a, G.E. Murch^a

^a The University of Newcastle, School of Engineering, Callaghan, NSW 2308, Australia

^b Constellium Innovation Cells, EPFL Quartier de l'Innovation E, CH-1015 Lausanne, Switzerland

ARTICLE INFO

Article history:

Received 7 June 2013

Received in revised form 1 August 2013

Accepted 11 August 2013

Available online 15 September 2013

Keywords:

Cellular metal

Mechanical properties

Compressive testing

Finite element method

ABSTRACT

This paper addresses the mechanical properties of Corevo[®] aluminium foam. The effective Young's modulus, Poisson's ratio, and material yield stress are determined. To this end, samples are tested using uni-axial compressive testing. In addition, micro-computed tomography data of the complex material geometry are obtained and converted into finite element calculation models. The numerical analysis further enables the testing of mechanical material anisotropy and plastic deformation within the material's meso-structure.

© 2013 Elsevier B.V. All rights reserved.

Cellular metals combine a range of attractive properties. Due to their high porosity they are relatively light whilst maintaining a high level of strength [1]. Furthermore, they can be used for the damping of structural and acoustic vibrations [2]. Their versatile thermal properties make them especially attractive for use in thermal conductivity enhancement [3] or heat exchangers [4]. Finally, cellular metals exhibit controlled deformation behaviour under compressive loading making them optimum materials for plastic energy absorption applications [5,6]. Corevo[®] aluminium foam is a novel type of cellular metal consisting of an aluminium matrix and an interconnected pore network. In this paper and for the first time, its mechanical properties are characterised using experimental and numerical methods.

Corevo[®] foam is manufactured by a replication process based on salt dough as a spacer material [7]. Salt dough pellets are manufactured with sizes ranging from 2 to 10 mm (dictating the final pore size of the foam) and compressed into a preform (the compression step dictates the final foam porosity ranging from 70% to 80%). Aluminium is then infiltrated inside the preform by a low pressure die casting process. After this step, the salt is rinsed away to obtain the final foam. This process is quite versatile, allowing for foam parts with various shapes and sizes as well as the integration (one shot during casting or by integration of external elements at the preform stage) of dense metal parts.

Finite element analysis of models based on micro-computed tomography (μ CT) data is now an established tool for the numerical analysis of cellular metals and their complex meso-structures

[8,9]. It enables mechanical testing of materials without destroying samples, the study of anisotropy, strain rate dependency and the visualisation of stresses within the material [10]. Furthermore, geometric modifications of the models enable the virtual study of material defects or the improvement of materials [11].

Fig. 1 shows a light photograph and μ CT reconstruction of one of the tested cylindrical Corevo[®] foam samples. A total of four cylindrical samples have been used for the mechanical characterisation of Corevo[®] aluminium foam. These samples are analysed using experimental and numerical testing to determine their effective Young's modulus, Poisson's ratio and yield strength.

A total of four samples have been tested in the experimental analysis. Prior to uni-axial compression, samples 2 and 3 were scanned using μ CT imaging for additional numerical analysis. The voxel size in both scans was 36.25 μ m. All samples exhibited a cylindrical shape (diameter and height $d = h = 25$ mm). The masses m of each sample are listed in Table 1. The sample porosity p was calculated in two steps. First, the metal volume V_m was obtained by dividing the mass by the density of the aluminium alloy (i.e. $\rho_{Al} = 2670$ kg/m³ [12]). The combined volume of the pores is then the metal volume V_m subtracted from the cylinder volume $\pi \cdot d^2 \cdot h / 4$. Subsequent normalisation of the pore volume with the cylinder volume yields the porosity p . For samples 2 and 3 where μ CT data were available the specific internal surface area S_i was determined. In the first step the μ CT data was segmented by identifying the metallic phase using the software ImageJ. The segmentation threshold was adjusted iteratively until the segmented metal volume corresponded to the calculated metal volume V_m . Next, a fine STL surface mesh was generated that encloses the segmented metal volume using the commercial software Mimics 10. The area of

* Corresponding author. Tel.: +61 24921 6188; fax: +61 24921 6946.

E-mail address: Thomas.Fiedler@newcastle.edu.au (T. Fiedler).

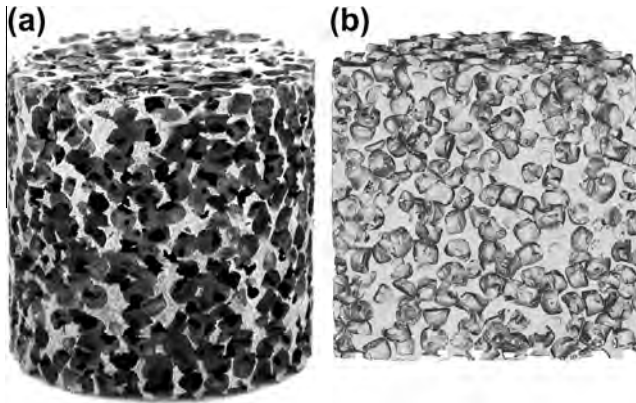


Fig. 1. Corevo® aluminium foam cylinder ($d = h = 25$ mm): (a) photograph of sample #3 and (b) μ CT reconstruction of sample #3 sliced along its centre.

Table 1
Samples' characteristics.

Nr	m (g)	p (%)	S_i (mm ² /mm ³)
#1	9.165	71.7	–
#2	8.900	72.6	1.48
#3	8.970	72.4	1.49
#4	8.875	72.6	–

the surface mesh was divided by the cylinder volume in order to calculate the specific internal surface area S_i . The values indicated homogenous geometric properties of the samples considered.

Compressive testing was performed on a Shimadzu 50 kN uni-axial testing machine. The speed of the machine crosshead was 0.5 mm/min (quasi-static compression). Compressive forces F were measured using a 50 kN load cell. Displacements u were obtained using a novel optical measurement system that provides superior accuracy (resolution 3.4 μ m) at small displacements and machine crosshead displacement data at large displacements. Images were recorded with a frequency of 1 s^{−1}. The force–displacement curve obtained was transformed into engineering stress–strain data using the initial cylindrical cross section A_0 and height h_0 , i.e. $\sigma = F/A_0$ and $\varepsilon = \Delta u/h_0$. A total of four specimens were tested with the results being shown in Fig. 2. The effective Young's modulus (z -direction) is identical to the initial slope of the stress–strain curve. The corresponding values are $E_1 = 7.15$ GPa, $E_2 = 6.52$ GPa, $E_3 = 5.38$ GPa, and $E_4 = 6.29$ GPa where the subscript indicates the sample ID. Furthermore, the 0.2% offset yield strength $\sigma_{0.2}$ was

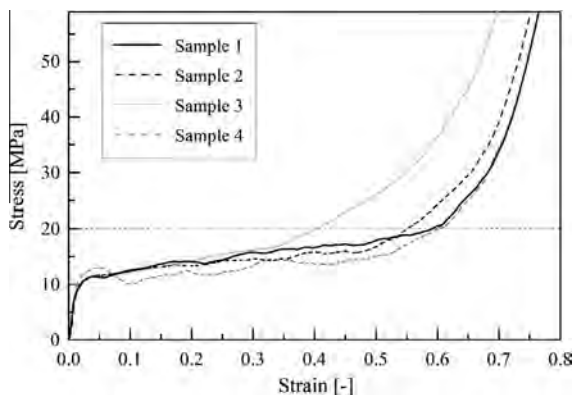


Fig. 2. Stress–strain data of the experimental measurement.

determined and similar values were found for all samples ($\sigma_{0.2,1} = 11.2$ MPa, $\sigma_{0.2,2} = 11.0$ MPa, $\sigma_{0.2,3} = 11.2$ MPa, and $\sigma_{0.2,4} = 12.4$ MPa). The densification strain was defined as the strain where stress first exceeds 20 MPa. The corresponding values are $\varepsilon_{d1} = 0.59$, $\varepsilon_{d2} = 0.55$, $\varepsilon_{d3} = 0.43$, and $\varepsilon_{d4} = 0.60$. It is interesting to note that the onset of densification occurs earlier in sample 3.

Segmented micro-computed tomography data were converted into high resolution finite element calculation models that accurately capture the complex meso-structure of the material. In the first step, two non-intersecting cubes with a side length of 10 mm were extracted from each of the two cylindrical μ CT data sets of samples 2 and 3. Mixed meshes containing tetrahedral, pentahedral and hexahedral elements exhibit minimum element distortion and thus superior numerical accuracy [13] and were used in the present analysis. Preliminary mesh refinement analysis indicates a minimum of 710,000 nodes per model for numerical convergence. Analogous to the experimental testing, uni-axial compressive loading was simulated. To this end, a time-dependent compressive boundary condition was prescribed at one surface of a cube whilst the opposing surface was constrained in its normal direction. By alternating the orientation of these planes, material anisotropy was tested. All other surfaces remained unconstrained. For the subsequent calculation of Poisson's ratio, averaged displacements of the nodes within the free surfaces were used. The chemical composition of the metallic base material corresponds to AIS7G06. Accordingly, the following base material properties were used in the numerical analysis: Young's modulus $E = 72.4$ GPa, Poisson's ratio $\nu = 0.33$, and initial yield stress $\sigma_0 = 241$ MPa. Plastic hardening was modelled using a tangent modulus $T = 2.3$ GPa to match the ultimate yield stress $\sigma_u = 310$ MPa at $\varepsilon_u = 0.03$ [12].

A user-supplied subroutine was applied to log the total nodal reaction force F and nodal displacement Δu . Based on these values and identical to the procedure used in experimental testing, engineering stresses σ and strains ε were calculated. The numerical stress–strain data were used to extract the effective material properties of Corevo® aluminium foam. Fig. 3 shows the effective Young's modulus and initial yield stress. Young's modulus ranges from 3.4 to 7.7 GPa and a distinct elastic anisotropy was found. The effective Young's modulus was relatively consistent in the x and y -directions. However, in the casting (i.e. z) direction distinctly higher values were found. Especially the extracted cubes #2b and #3a showed excellent agreement with experimental results. The initial yield stress (see Fig. 3b) is the macroscopic stress at the instant when plasticisation first occurs within the numerical calculation model. The material property follows the anisotropy found for Young's modulus. This material property can only be determined in numerical analysis and limits the range of purely elastic deformation.

Poisson's ratio ν (see Table 2) was calculated by dividing the average length change Δu_{\perp} perpendicular to the loading direction by the average length change Δu_{\parallel} parallel to the loading direction, i.e. $\nu = -\Delta u_{\perp}/\Delta u_{\parallel}$. The orientation of Poisson's ratio is indicated by its subscripts with the first subscript indicating the loading direction and the second subscript the transverse direction. The results are summarised in Table 1 and show values between 0.17 and 0.36. Minimum values are found for compression in the x or y -directions and transverse deformation in the z -direction, i.e. ν_{xz} and ν_{yz} . This can be explained by the relatively high Young's modulus in the z -direction (see Fig. 3a).

Furthermore, finite element analysis allows the visualisation of the deformation mechanism within the material's meso-structure. Fig. 4 shows the distribution of equivalent plastic strain at a macroscopic compression of 10%. It can be observed that plastification is concentrated in thin struts parallel to the loading direction. This behaviour is observed for all (i.e. x , y , and z) loading directions.

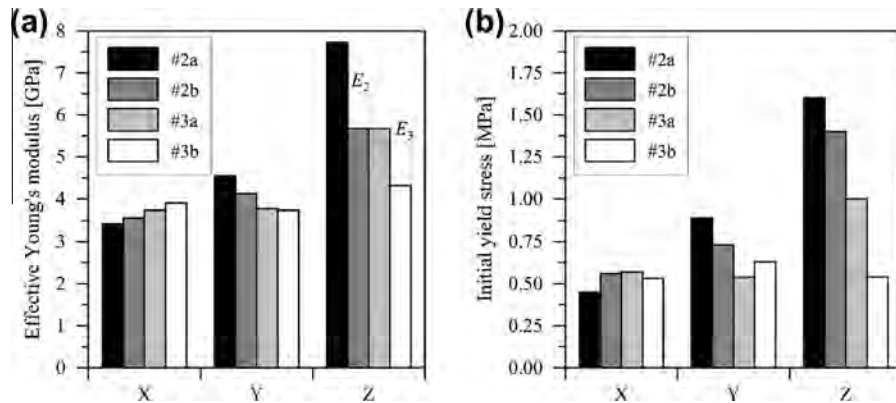


Fig. 3. Results of the finite element analyses: (a) effective Young's modulus and (b) initial yield stress.

Table 2
Poisson's ratio.

	#1	#2	#3	#4	Average
ν_{xy}	0.31	0.26	0.31	0.30	0.30
ν_{xz}	0.17	0.18	0.18	0.20	0.18
ν_{yx}	0.36	0.32	0.31	0.30	0.32
ν_{yz}	0.19	0.17	0.20	0.19	0.19
ν_{zx}	0.32	0.26	0.23	0.30	0.28
ν_{zy}	0.24	0.25	0.32	0.30	0.28

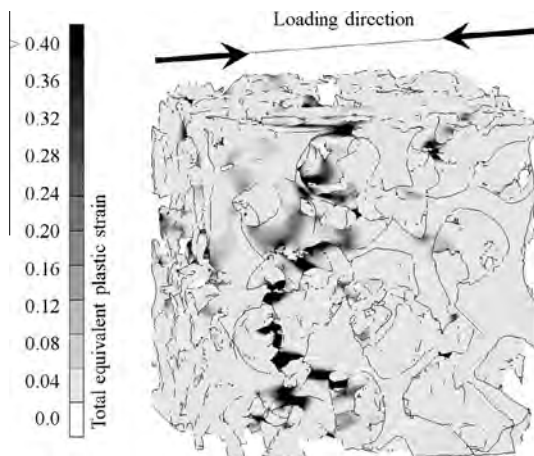


Fig. 4. Distribution of equivalent plastic strain (sample #2a).

This paper addressed the mechanical properties of Corevo® aluminium foam. Combined experimental and numerical analysis al-

lowed the determination of the effective Young's modulus, Poisson's ratio, initial yield strength and 0.2% offset yield strength. The elastic anisotropy was found with Young's modulus ranging from an average of 3.9 GPa in the x-y plane to 5.9 GPa in the z-direction. Similar behaviour was found for the initial yield stress (x-y plane 0.6 MPa and 1.14 MPa in the z-direction). Good agreement between experimental and numerical results for Young's modulus was found. Experimental analysis further indicated values of the 0.2% offset yield strength between 11.0 MPa and 12.4 MPa. The densification strain (i.e. the strain where 20 MPa is first exceeded) was found to range from 0.43 to 0.60. Finally, numerical analysis indicates that initial plasticisation was concentrated in thin struts of the meso-structure parallel to the macroscopic loading direction.

References

- [1] M.F. Ashby, A. Evans, N.A. Fleck, L.J. Gibson, J.W. Hutchinson, H.N.G. Wadley, *Metal Foams: A Design Guide*, Elsevier Science, Burlington, 2000.
- [2] J. Banhart, J. Baumeister, M. Weber, *Mater. Sci. Eng. A* 205 (1996).
- [3] T. Fiedler, A. Öchsner, I.V. Belova, G.E. Murch, *Forum* 273–276 (2008) 222.
- [4] J. Tian, T.J. Lu, H.P. Hodson, D.T. Queheillalt, H.N.G. Wadley, *Int. J. Heat Mass Transfer* 50 (2007).
- [5] M. Vesenjak, Z. Ren, T. Fiedler, A. Öchsner, *J. Compos. Mater.* 43 (2009) 2491.
- [6] S. Tanaka, K. Hokamoto, S. Irie, T. Okano, Z. Ren, M. Vesenjak, S. Itoh, *Measurement* 44 (2011).
- [7] Y. Conde, J.F. Despois, R. Goodall, A. Marmottant, L. Salvo, C.S. San-Marchi, A. Mortensen, *Adv. Eng. Mater.* 8 (2006).
- [8] C. Veyhl, I.V. Belova, G.E. Murch, T. Fiedler, *Mater. Sci. Eng. A* 528 (2011) 4550.
- [9] O. Caty, E. Maire, S. Youssef, R. Bouchet, *Acta Mater.* 56 (2008) 5524.
- [10] M. Vesenjak, C. Veyhl, T. Fiedler, *Mater. Sci. Eng. A* 541 (2012) 105.
- [11] T. Fiedler, I.V. Belova, G.E. Murch, *Scripta Mater.* 67 (2012) 120–125.
- [12] J. Holt, *Structural Alloys Handbook*, CINDAS, Purdue University, West Lafayette, 1996.
- [13] C. Veyhl, I.V. Belova, G.E. Murch, A. Öchsner, T. Fiedler, *Finite Elem. Anal. Des.* 46 (2010) 371.

Chapter 4

On the particle size effect in expanded perlite aluminium syntactic foam

Chapter 4 addresses a different type of cellular metal manufactured by infiltration casting. The difference to the material in the previous Chapter is a different spacer material, i.e. expanded perlite particles instead of salt dough. These expanded perlite particles have a very low density and thus may remain in the structure without noticeably increasing its weight. However, they are very weak compared to the metallic matrix and cannot bear a significant load. The material investigated in this Chapter can be categorised as a “syntactic foam”. Syntactic foams are defined as a cellular material containing hollow inclusions (often but not always of a near spherical shape) surrounded by a matrix material (Couteau and Dunand, 2008).

The present Chapter focuses on the effect of different filler particle sizes on the geometry of the syntactic foam and its mechanical properties. Samples are made using A356 aluminium alloy. Infiltration casting is used to manufacture the syntactic foam by using expanded perlite (EP) as filler material. The investigation addresses two main objectives:

- 1) the influence of EP particle size on microstructural, geometrical, and mechanical properties of the foams and
- 2) the effect of heat treatment on the mechanical response of perlite-MSF foam.

To this end, EP particles with three different size ranges are used for sample preparation and all samples undergo a T6 heat-treatment. The mechanical properties elastic gradient, yield stress, plateau stress, and energy absorption are examined in this Chapter. The findings indicate that when inspected under an electron microscope, samples containing smaller particles have a refined cell wall micro-structure with small dendritic arms. The filler particle size is further found to directly affect the homogeneity of the foam’s cell-wall geometry. Foam structures with smaller particles exhibit a superior mechanical response, chiefly due to its more uniform and refined grain cell-wall microstructure compared to bigger particle size sample counterparts.

Results from this investigation contribute significantly to the understanding of cellular metals manufactured from infiltration casting methods. The mechanical response of the material is influenced markedly by filler particle size and heat treatment.

This investigation has been published online and accepted for print publication by the journal *Materials and Design*.

Taherishargh, M, MA Sulong, IV Belova, GE Murch, T Fiedler, "On the particle size effect in expanded perlite aluminium syntactic foam" *Materials and Design* 66 (2015): 294-303.

Reprint license has been obtained from Elsevier.

Copyright © 2015 Elsevier



On the particle size effect in expanded perlite aluminium syntactic foam



M. Taherishargh*, M.A. Sulong, I.V. Belova, G.E. Murch, T. Fiedler

Centre for Mass and Thermal Transport in Engineering Materials, Discipline of Mechanical Engineering, University of Newcastle, University Drive, Callaghan, NSW 2308, Australia

ARTICLE INFO

Article history:

Received 11 September 2014

Accepted 26 October 2014

Available online 4 November 2014

Keywords:

Syntactic foam

Expanded perlite

Cell size

Mechanical properties

Thickness

ABSTRACT

Packed beds of expanded perlite (EP) particles with three different size ranges (1–1.4, 2–2.8, and 4–5.6 mm) have been infiltrated with molten Al to produce EP/A356 Al syntactic foam. A T6 heat treatment was applied to the foams. The effects of EP particle size on microstructural, geometrical, and mechanical properties of the foams were investigated. The EP particle size determines the number of cells across the sample diameter (7–25). It also influences the microstructural characteristics of the cell-wall alloy and the homogeneity of the cell-wall geometry. Enhanced microstructural characteristics and a greater geometrical homogeneity of the cell-wall in the case of smaller EP particles result in superior mechanical properties. The compressive deformation becomes more uniform by decreasing the EP particle size resulting in smoother and steeper stress–strain curves. As a result, these foams exhibit higher plateau stresses and improved energy absorption. The number of cells across the sample diameter does not have a significant effect on the mechanical properties of the samples considered.

© 2014 Elsevier Ltd. All rights reserved.

1. Introduction

Metallic foams are characterized structurally by their cell type (open or closed), porosity, cell shape, and cell size [1–3]. Such structural properties can be tailored by utilizing hollow or porous particles to introduce the porosity in case of metallic syntactic foams [4–7]. It has been shown that the mechanical response of the metallic foams under compression depends on the structural characteristics. There has been good agreement on the effect of density and cell shape on the mechanical properties. It is now well accepted that the plateau stress and energy absorption of the metallic foams depends on density [1,8–12] and cells geometry [3]. In the case of metallic syntactic foams, the density and cell shape cannot always be varied freely since they depend on the filler particles' morphology and density [13]. However, the cell size can be controlled easily by the filler particle size. Studies have shown that reducing the particles' size enhances the mechanical properties of syntactic foams containing high strength hollow spheres [4,14–17]. The explanation is in the fact that the wall thickness to diameter ratio is higher in the case of smaller particles [4,14,15,18]. However, there are some contradictions on the effect of cell size on the mechanical properties of foams containing no filler materials. Some researchers reported that the mechanical properties of the foams improve as the cell size decreases [11,12,19], while others have shown that there is an optimum cell size at

which the foam has superior mechanical properties [9,20,21]. Interestingly, some reports have shown that decreasing the cell size reduces the plateau stress and the energy absorption of the foams [1,22,23].

In a previous study, we introduced expanded perlite (EP), a natural porous volcanic glass, as a new filler material which offers lower density and cost for metallic syntactic foams [13]. However, unlike other porous filler materials [24–26] EP does not have a direct strengthening effect in EP/A356 Al syntactic foam. These foams show mechanical behaviour similar to metallic foams that contain no filler material because of the low mechanical strength of EP. Heat treatment proved to be an efficient process to improve the mechanical properties of the EP/A356 syntactic foam [27]. While changing the particles' size could be a good approach to tailor mechanical properties, this has not been reported in the case of syntactic foams containing low strength porous filler particles. In the present study, we report on an investigation of the effect of EP particle size on mechanical properties of heat-treated EP/A356 syntactic foam.

2. Experiment

2.1. Foam preparation

Syntactic foams composed of A356 aluminium alloy and EP particles were synthesised by a counter gravity infiltration process. The A356 aluminium alloy with a composition of 7.2 wt% Si, 0.4 wt% Mg, 0.1 wt% Ti, 0.12 wt% Fe, and the balance aluminium,

* Corresponding author. Tel.: +61 432620029.

E-mail address: Mehdi.Taherishargh@uon.edu.au (M. Taherishargh).

provided by the supplier (Hayes Metals), was used as the matrix. According to their product specification, the EP particles have the composition of 75 wt% SiO₂, 14 wt% Al₂O₃, 3 wt% Na₂O, 4 wt% K₂O, 1.3 wt% CaO, 1 wt% Fe₂O₃, 0.3 wt% MgO, 0.2 wt% TiO₂ with traces of heavy metals. The EP particles were sieved to 3 size ranges (1–1.4 mm, 2–2.8 mm, 4–5.6 mm) and thus have a 40% size increase within and between the groups. The sieving process was done by a vibrating machine with frequency of 50 Hz. The sieves with the standard ASTM mesh sizes were used (ASTM No. 18, 14, 10, 7, 5, and 3.5 corresponding to 1, 1.4, 2, 2.8, 4, and 5.6 mm openings). A detailed description of the infiltration process along with the set-up configuration can be found in [13]. The samples underwent a T6 heat treatment comprising a solution treatment at 540 °C for 16 h followed by water quenching. Subsequent aging was performed at 160 °C for 10 h.

The exact height (*h*) and diameter (*d*) of the cylindrical samples were measured using a digital calliper and the foam volume was calculated. The density of samples was calculated by dividing the sample mass by this volume.

2.2. Microstructural observations

Sections were cut from some of the foam samples with a silicon carbide disc cutter. Standard grinding was performed manually using 180-, 240-, 320-, 600-, and 1200-grit silicon carbide papers on disc rotating with speed of 240 rpm. Subsequent polishing with 0.5 µm and 0.05 µm diamond powder suspended in distilled water resulted in mirror-like surfaces. The microstructure of the cell walls was investigated using an Olympus BX60 M optical microscope.

2.3. µCT observations

µCT scans were prepared from samples containing small, medium and large EP particles. All images were captured using an Xradia MicroXCT-400 machine with a Hamamatsu L8121-03 X-ray source with a constant voxel size of 35.32 µm. The selected acceleration voltage was 140 kV with a current of 70 µA.

2.4. Compression test

Compression tests were conducted according to the ISO-13314 standard [28]. Five cylindrical samples for each particle size were prepared to generate statistically significant data. The compression tests were conducted on a uni-axial computer-controlled 50 kN Shimadzu testing machine with the crosshead speed 3 mm/min corresponding to a strain rate of 10^{−3} s^{−1}. Both ends of the samples were ground and lubricated by a silicon lubricant to reduce the friction between the samples surface and loading platens. The load and cross-head displacements were recorded by the data acquisition software Trapezium2. The engineering stress–strain data was then calculated based on the initial sample cross-section and height.

3. Results

3.1. Samples porosity and µCT observations

Fig. 1 shows the syntactic foams with small sized particles (SP), medium sized particles (MP), and large sized particles (LP) and a constant diameter of 30 mm. The dense packing and uniform distribution of the EP particles throughout the sample is a result of the 5-step filling and vibration of the mould [13]. Most of the surface particles were removed from the pores during the machining

and surface grinding due to the weak bonding between the EP particles and Al matrix.

It has been shown that the surface and internal pores of EP particles are not infiltrated by molten Al [13]. Accordingly, the volume fraction of EP particles (*F_p*) can be calculated as:

$$F_p = \left(\frac{V_{sf} - ((m_{sf} - m_p) / \rho_{Al})}{V_{sf}} \right) \quad (1)$$

where *V_{sf}* is the foam volume, *m_p* is the combined perlite mass, *m_{sf}* is the syntactic foam mass, and *ρ_{Al}* is the density of aluminium (2.68 g/cm³ according to the mixing rule). Also, the density of EP particles (*ρ_p*) can be calculated as:

$$\rho_p = \frac{m_p}{V_{sf} - ((m_{sf} - m_p) / \rho_{Al})} \quad (2)$$

The total porosity of syntactic foam (*F_{TP}*) is then obtained as:

$$F_{TP} = F_p \times \left(1 - \frac{\rho_p}{\rho_s} \right) \quad (3)$$

where *ρ_s* is the density of the solid part of the perlite particles (2.79 g/cm³) [13]. Table 1 shows the density data of the Ø30 mm samples with different EP particle sizes. The standard deviations of density are 0.04, 0.018, and 0.008 mm for SP, MP, and LP foams respectively. Accordingly, the SP foams exhibit the highest scattering of density. This scatter decreases significantly as the particle size increases. The smaller particles create a higher fraction of narrow regions between neighbouring particles which require a higher pressure for effective infiltration with molten metal [29]. However, based on the lower density of small EP particles (see EP particle density in Table 1), one can assume that they have a lower strength which makes them more susceptible to collapse at high pressures. Accordingly, small variations in infiltration pressure may either result in incomplete infiltration or the collapse of EP particles thus causing the relatively high scatter of density in the SP samples.

Micro-computed tomography (µCT) data was obtained for one additional sample of each particle size. In the first step of the µCT analysis the raw µCT data of each sample was segmented. To this end, the perlite volume fractions of the scanned samples were determined using Eq. (1). In an iterative process a grey-scale threshold was then adjusted until the volume fraction of the µCT matches this reference value [30]. As a result, voxels can be attributed to either the perlite particles (black voxels) or the metallic phase (white voxels). It should be mentioned here that perlite appears transparent in the µCT data due to its low density and wall thickness.

In the following, the geometrical characteristics of the foam structure are evaluated based on the µCT data. The uniformity of the aluminium phase, i.e. the material distribution between the struts and joints is analysed. A set of segmented images with 600 × 600 × 600 voxels and a voxel side length of 35.32 µm was loaded into the open-source software ImageJ [31]. The calculations were performed using the BoneJ plugin [32]. This plugin calculates the local thickness by determining the diameter of the largest sphere which can be grown inside the segmented (aluminium) phase [32,33]. A summary of the analyses is shown in Table 2. As expected, the average value of the local thickness decreases as the EP particles size decreases. Furthermore, the coefficient of variation (CoV) of the local thicknesses was determined. A high coefficient of variation indicates a strong deviation of the local thickness. This can be caused by (a) struts with differing diameters and (b) by a conical shape where struts narrow towards their centre. Accordingly, the CoV predominantly quantifies the uniformity of the aluminium phase. The values of the CoV in Table 2 indicate that the strut thickness is more uniform in SP samples (0.36) compared with MP (0.40) and LP (0.51) samples.

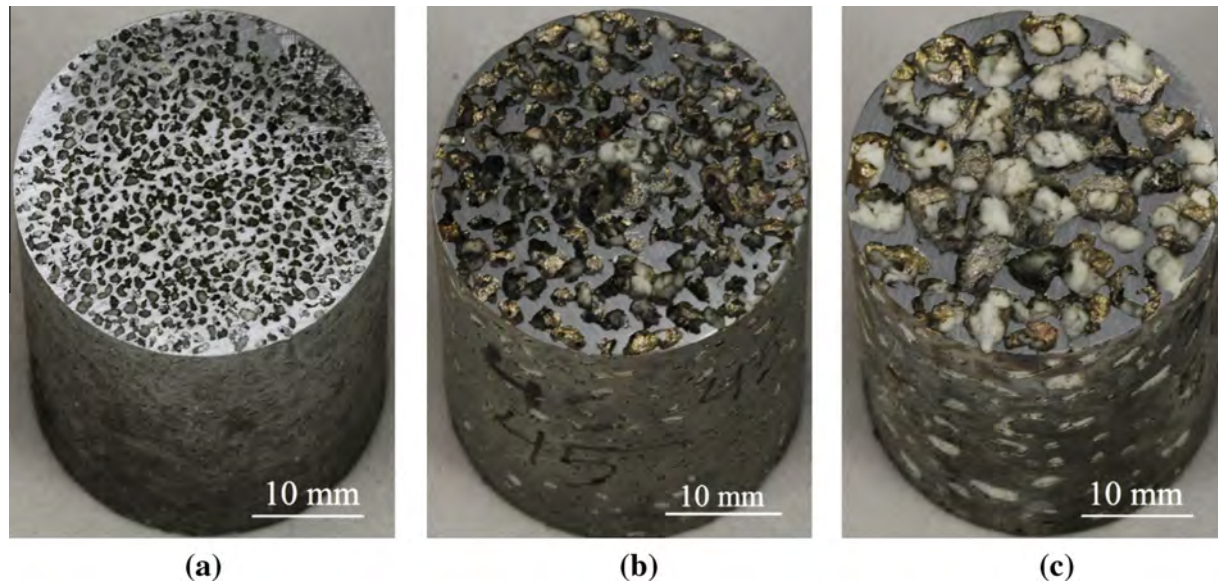


Fig. 1. Representative cross section of EP/A356 syntactic foam with EP particle sizes of (a) 1–1.4 mm (SP), (b) 2–2.8 mm (MP), and (c) 4–5.6 mm (LP).

Table 1

Density and porosity data of Ø30 mm samples containing EP particles with size range of 1–1.4 mm (SP), 2–2.8 mm (MP), and 4–5.6 mm (LP).

Samples	EP mass (g)	Foam mass (g)	Foam volume (cm ³)	Foam density (g/cm ³)	EP volume fraction (%)	EP particle density (g/cm ³)	Total porosity (%)
SP1	3.11	35.08	34.22	1.03	65.15	0.14	61.88
SP2	3.08	35.75	33.17	1.08	63.25	0.15	59.92
SP3	3.04	37.73	34.30	1.10	62.26	0.14	59.08
SP4	3.03	37.63	34.03	1.11	62.06	0.14	58.86
SP5	3.01	38.67	34.03	1.14	60.89	0.15	57.72
MP1	3.22	35.73	33.87	1.05	64.19	0.15	60.78
MP2	3.23	36.30	34.06	1.07	63.78	0.15	60.38
MP3	3.47	36.93	34.09	1.08	63.37	0.16	59.73
MP4	3.23	36.85	34.03	1.08	63.14	0.15	59.74
MP5	3.35	37.72	34.30	1.10	62.61	0.16	59.11
LP1	4.22	36.87	33.87	1.09	64.03	0.19	59.57
LP2	4.19	37.46	34.01	1.10	63.50	0.19	59.08
LP3	4.07	36.89	33.61	1.10	63.57	0.19	59.23
LP4	4.13	36.91	33.21	1.11	63.17	0.20	58.71
LP5	4.22	38.37	44.48	1.11	63.12	0.19	58.75

Table 2

Analysis of the μ CT images in BoneJ.

Samples	LP	MP	SP
Particle size range (μ m)	4000–5600	2000–2800	1000–1400
Mean strut thickness (μ m)	965.9	694.9	377.3
Standard deviation (σ)	14.01	7.96	3.89
Coefficient of variation (CoV)	0.51	0.40	0.36

Fig. 2 shows the cell-wall thickness distribution in samples using the *thickness* command of ImageJ/BoneJ. The bright yellow colour is assigned to the highest local wall thickness of each sample and the dark blue corresponds to the lowest wall thickness, respectively. For better comparison, sections of foams with small and medium EP particles are magnified to have the same relative cell size as the LP foam. One can see that the frequency of occurrence of bright yellow and dark blue colour (i.e. very large and very low local wall thicknesses) decreases as the cell size decreases. Moreover, the colour map shifts to shades of orange indicating a more uniform wall thickness close to the mean value. In combination with the CoV this indicates a more homogeneous wall thickness distribution in the struts of SP foams.

3.2. Cell wall microstructure

Fig. 3 shows the microstructure of the cell-wall in SP and LP foams. The microstructure of the A356 alloy consists of aluminium-rich primary and secondary dendritic arms. A eutectic phase comprising the aluminium rich phase and silicon flakes forms between the dendritic arms during the solidification. Heat treatment changes the morphology of silicon particles from flakes to a near spherical shape and blurs the interdendritic boundaries [27]. In the following, untreated samples (as cast) are examined for a better illustration of the microstructure.

Cavities are the most common defect found in Al–Si alloys [34]. The microstructure of the LP foams is replete with small and big cavities while only small cavities are scarcely observed in the case of SP foams (see Fig. 3a and b). The main sources of such cavities are the shrinkage accompanying the solidification in combination with insufficient liquid metal feeding [27]. As can be seen, the cavities, marked with arrows, are mainly distributed at the central areas of the nodes. Solidification starts at the particles surfaces and proceeds with the dendrites oriented in the corresponding easy growth directions. Upon solidification, the molten metal is fed to the nodes via struts to compensate the solidification shrinkage. μ CT observations showed that the ratio between the thinnest

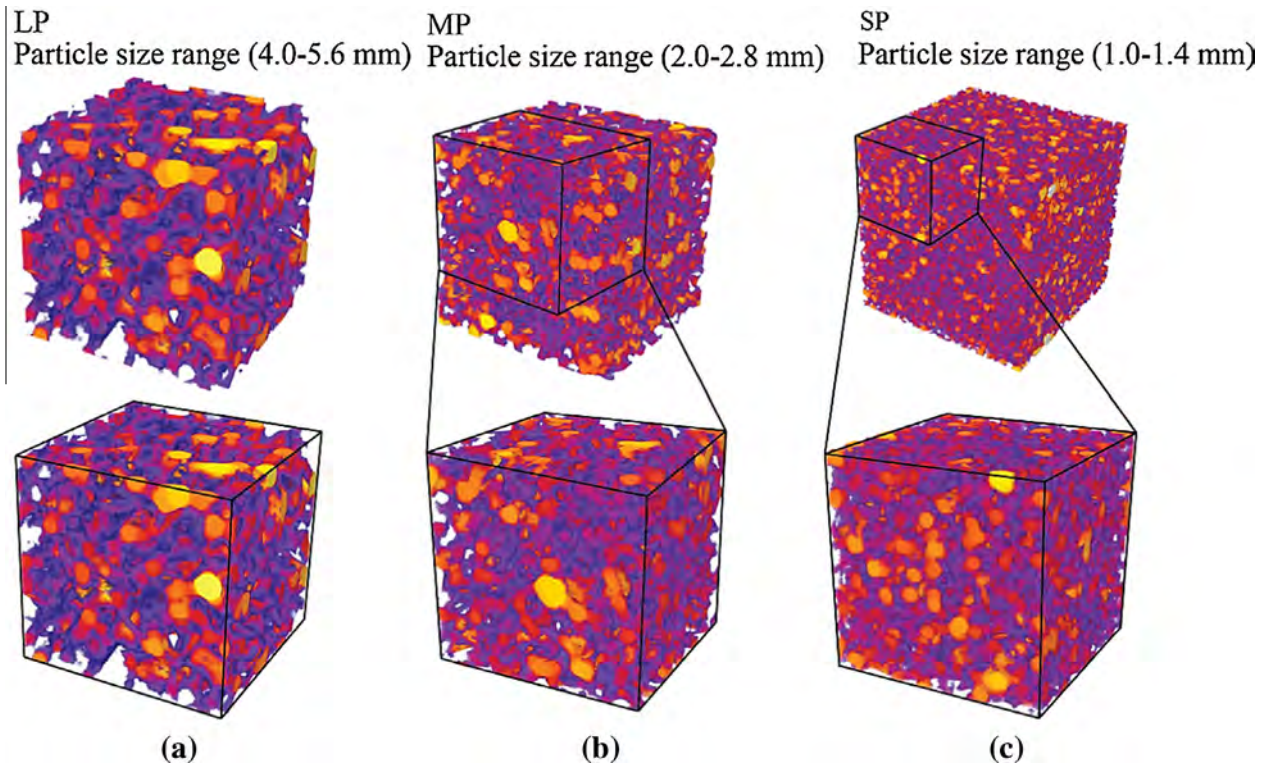


Fig. 2. Wall thickness distribution within the samples. The dark blue and bright yellow colours are assigned to the areas with the thinnest and thickest cell walls respectively. (For interpretation of the references to colour in this figure legend, the reader is referred to the web version of this article.)

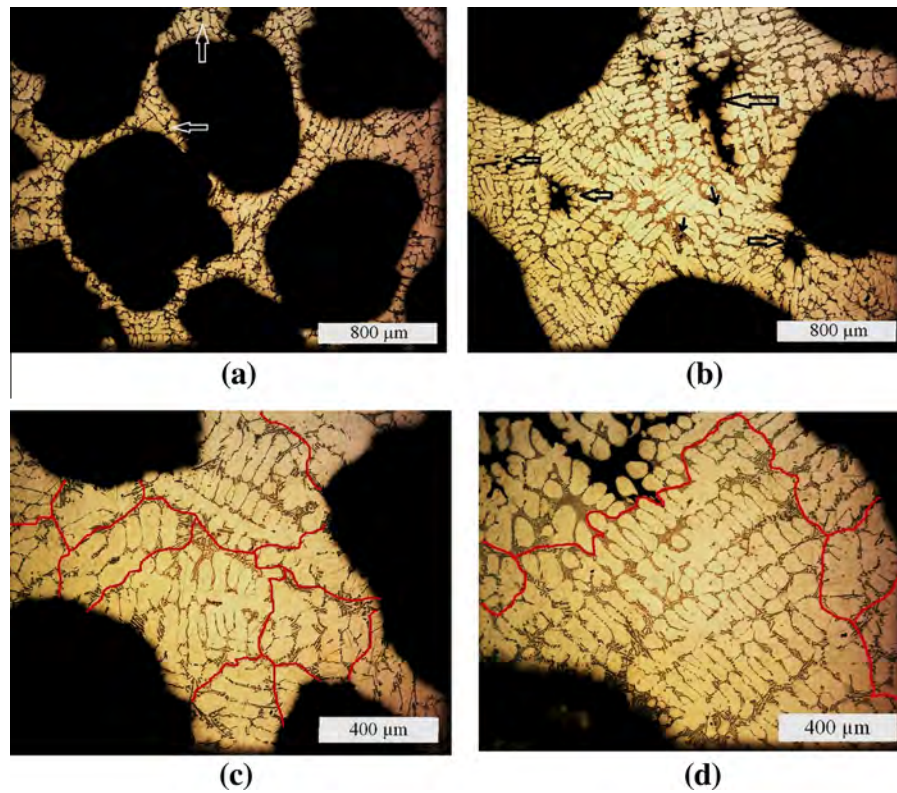


Fig. 3. Optical micrographs of cell walls in (a) and (c) SP foam; (b) and (d) LP foam.

part (the struts) and the nodes is higher in the case of foams containing larger particles. Therefore, the struts are likely to solidify earlier and block the feeding channels to the nodes. Improper melt feeding results in the formation of large cavities at the final stages of solidification, mainly in central areas of nodes in the LP samples.

Comparing Fig. 3c and d, one can see that the grain structure of the aluminium matrix changes from large columnar dendritic grains (LP) to relatively fine equiaxed dendrites (SP) as the particle size decreases. The structure is called columnar if the dendrites' growth is oriented in a preferential direction, whereas equiaxed dendrites are growing in all spatial directions [35]. During solidification, solid nuclei form at the surface of EP particles and start to grow. Growth occurs more rapidly in direction parallel to the heat flow direction i.e. normal to the EP particles surface. Less favourably-oriented crystals grow more slowly and tend to get pinched off by the more rapid growth of their neighbours. Several dendrites of similar orientation can form a grain. The approximate grain boundaries in SP and LP foams are marked in Fig. 3c and d. The grain size is smaller in the case of SP foams. The reason could be the higher curvature of the surface of the smaller particles and accordingly more simultaneous solidification directions. In addition, the higher total surface area of the smaller particles results in more nucleation sites.

3.3. Compression stress strain curves

In the following section the relative cell size, i.e. the ratio of cell size to sample diameter is addressed. According to the numerical study in [36], the effective stiffness and strength of a foam decreases as the relative cell size increases. In order to address this effect in the present study, two *small* SP and MP foams each with a diameter of 15 mm and a height of 22 mm were fabricated. In this way, the small MP foams (diameter 15 mm) have a similar relative cell size as the LP foams with normal size (diameter 30 mm). Fig. 4 shows a Ø30 mm LP sample and Ø15 mm MP sample of similar relative cell size. Similarly, the Ø15 mm SP samples have almost the same relative cell size as the Ø30 mm MP foams. The crosshead speed used for the compression test of the small samples was 1.5 mm/min in order to achieve the same strain rate used for the Ø30 mm samples.

Fig. 5 shows the quasi-static stress–strain curves of the samples. All of the EP/A356 syntactic foams show the classical

foam stress–strain curves comprising three main regions: the elastic region, the plateau at which the stress remains approximately constant over a large strain interval and densification where the stress increases rapidly. However, comparing Fig. 5a–c, it can be seen that the curves become smoother and steeper as the particle size decreases. This is attributed to a more uniform deformation behaviour which will be discussed below. Moreover, a slight increase in density resulted in higher stresses for all samples. The curves of the Ø15 mm samples are close to the ones of Ø30 mm foams of the same particle size (SP or MP). It appears that the effect of the relative particle size can be disregarded for the samples considered. However, the Ø15 mm samples exhibit slightly stronger stress oscillations compared to the corresponding Ø30 mm samples. The explanation is a smaller volume (containing a lower number of struts) where localised deformation (e.g. the buckling of a single strut) has a stronger impact on the macroscopic stress.

3.4. Compression characteristics

The compressive stress–strain response of the samples changes significantly with the EP particle size. This can be related to the strain hardening behaviour of the foams which has been the focus of some research recently [37–41]. Strain hardening occurs in the plastic region. For quantification, the strain-hardening exponent n of the foam is obtained by fitting a power-law relation [41] (i.e. $\sigma = K \epsilon^n$) to the true stress–true strain curves. In the present study, the n value was measured as the slope of a linear regression analysis of the true stress–strain data on a logarithmic scale ($\log \sigma = \log K + n \log \epsilon$) between 10% and 40% strain.

Fig. 6 shows the change of the coefficient n with respect to foam density and EP particle size. The n value increases considerably with decreasing particle size. In addition, the strain hardening exponent of the MP samples increase linearly with density. Interestingly, the n value of the SP foams decreases slightly as the density increases. Some researchers reported that strain hardening is sensitive to the foam density [40] while others found no correlation between hardening and foam density [41]. Based on our results, it seems that the dependency of the coefficient n on density is influenced by the cell size.

Fig. 7 shows the mechanical properties of the foam samples. All values have been derived from the stress strain curves using the ISO 13314 standard [28]. The plateau stress (σ_{pl}) is the mean stress between 20% and 40% of macroscopic strain. First, the sample with the minimum density was compressed for each size batch (SP, MP, and LP) and its plateau stress was measured. The remaining samples were unloaded at 70% and reloaded at 20% of the corresponding plateau stress. Their elastic gradient was obtained as the secant line of the resulting hysteresis loop. Alternatively, the quasi-elastic gradient (QE) can be determined as the approximate stress–strain gradient in the elastic region. The 1% offset yield stress (σ_y) was determined using this QE. The absorbed energy was calculated using the integral:

$$W = \int_0^{50\%} \sigma d\epsilon \quad (4)$$

where ϵ is the macroscopic strain. The energy absorption efficiency was obtained as:

$$\eta = \frac{W}{\sigma_{\max} \epsilon_{50\%}} \quad (5)$$

in which σ_{\max} is the maximum stress up to a strain of 50%. Finally, the plateau end strain ϵ_{ple} is obtained from the first intersection of the stress–strain data with 1.3 times the plateau stress of the corresponding sample.

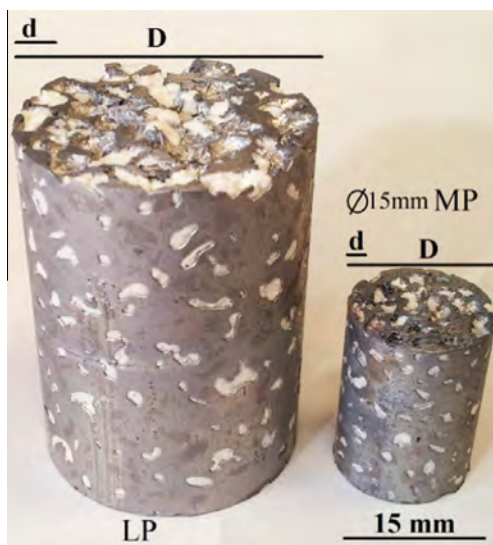


Fig. 4. Ø30 mm LP and Ø15 mm MP samples which have the similar relative cell size 1/7 (i.e. the ratio of average cell size diameter d to the sample diameter D).

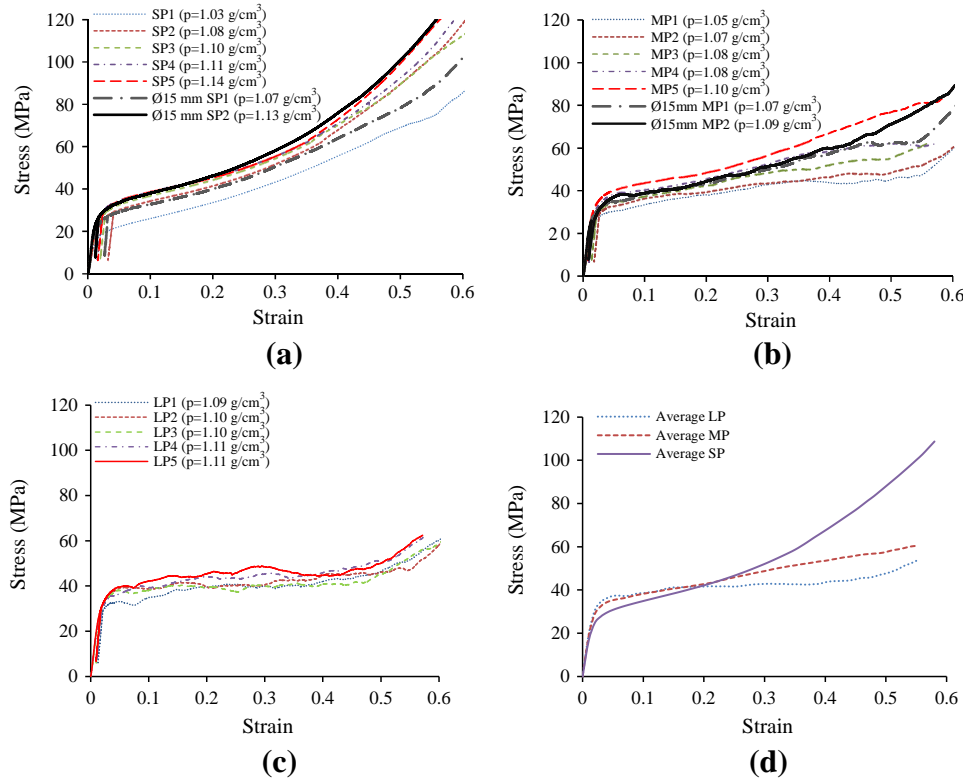


Fig. 5. Stress strain curves of (a) Ø30 mm and Ø15 mm SP foams, (b) Ø30 mm and Ø15 mm MP foams, (c) Ø30 mm LP foams, and (d) average stress strain curves.

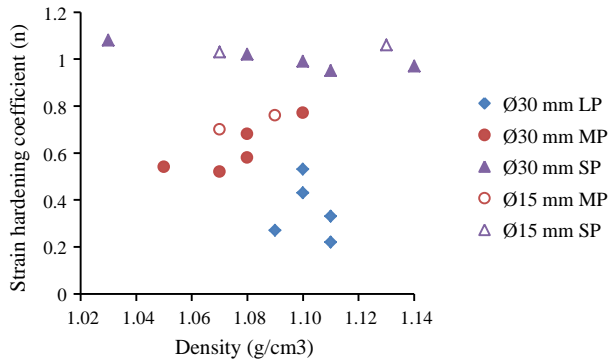


Fig. 6. Strain hardening exponent of Ø30 mm and Ø15 mm foam samples with respect to the foams density.

Regardless of particle size all mechanical properties except the energy absorption efficiency and plateau end strain increase with density (see Fig. 7a–d). The same observation has been broadly reported in the literature for a variety of metallic foams [8,40,42–45]. The SP foams have the minimum and MP foams have the highest elastic gradient at a given density (see Fig. 7a). The same trend is observed for the 1% offset yield stress (see Fig. 7b).

The plateau stress and the energy absorption are often considered as the most important mechanical properties of metal foams. The degree to which the foam deviates from a constant plateau stress is quantified by the energy absorption efficiency [40]. It can be observed that σ_{pl} and W are considerably lower in the case of LP foams while these foams show the highest energy absorption efficiency even at higher densities. This is due to their relatively constant plateau stress over a wide range of strain (see Fig. 5c). At low densities, the plateau stress of SP foams exceeds the value of MP foams. However, the SP foams show significantly lower

energy absorption efficiency and plateau end strain due to the relatively high gradient of the plateau. Interestingly, the plateau stress of SP foams shows less sensitivity to the density in comparison to MP and LP foams. Fig. 7c shows that σ_p of MP and LP foams increases with similar slopes which are distinctly higher than that of SP foams.

Furthermore, the similarity of the mechanical characteristics of Ø15 mm (unfilled markers) and corresponding Ø30 mm (filled markers) samples is apparent from the graphs. This underlines the limited effect of the relative particle size on the mechanical properties of the foams.

4. Discussion

The mechanical properties of metallic foams depend on density, the properties of the cell wall material, and the cell geometry [36]. The effect of density on mechanical properties of metallic foams is often expressed using a power law relation [11,15,46]:

$$\frac{\sigma_{pl}}{\sigma_{ys}} = C \left(\frac{\rho}{\rho_s} \right)^\gamma \quad (6)$$

where σ_{ys} is the yield stress of solid material, ρ and ρ_s are foam density and the density of solid material respectively, and C and γ are fitting parameters. As shown in Fig. 7, the plateau stress of all foams increases with the foam density. Elastic stiffness, energy absorption, and 1% offset yield stress show a similar behaviour. The yield stress and density of heat-treated A356 alloy are 256 MPa and 2.78 g/cm³ respectively [27]. Applying Eq. (4), γ has the value of 2.4, 6.5, and 7.6 in the case of SP, MP, and LP foams.

In the case of EP/A356 syntactic foam, the microstructure and geometry of cells are determined by the EP filler material. Smaller EP particles yield a refined cell-wall microstructure with a smaller grain size, fewer defects and an equiaxed dendritic morphology. In addition, the size of the EP particles affects the geometrical

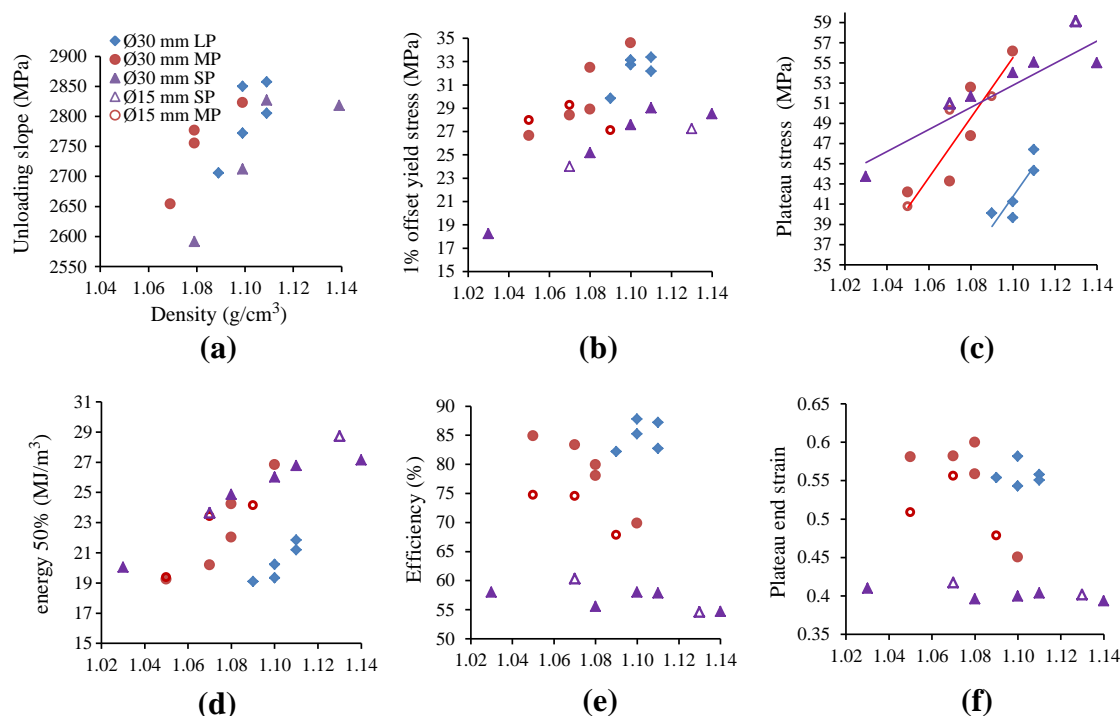


Fig. 7. Mechanical characteristic of EP/A356 LP, MP, and SP foams VS density; (a) unloading slope, (b) 1% offset yield stress, (c) plateau stress, (d) absorbed energy 50%, (e) energy absorption efficiency, and (f) plateau end strain.

properties of the foam in two ways: (i) smaller particles result in a lower relative cell size which is equal to higher number of cells for a constant sample diameter and (ii) the material distribution between the struts and nodes change with the EP particle size. Each of these parameters may have different effects on the mechanical properties of the syntactic foams.

4.1. Relative size effect

According to the literature [47], the number of cells across the sample diameter is an important parameter since the individual response of cells during compression loading is influenced by their location in the material. Compared to the cells located near surfaces, cells in the bulk experience more constrained deformation [47]. According to the results of a numerical study conducted by Tekoglu et al., increasing the relative cell size decreases the stiffness and strength of the metallic foam. According to these authors, the reason is a higher area fraction of weak boundary layers located at the stress-free (i.e. no normal stresses) surfaces. The lower deformation resistance of cells in these areas accelerates the formation of localized deformation bands and results in a lower plastic strength. However, they found that the compressive properties are widely size-independent for specimens in which the relative cell size is less than 1/8 [36]. Jeon and Asahina reported the same fact for a relative cell size of less than 1/6 [48]. A theoretical evaluation of Nieh et al. showed that the relative cell size has a negligible effect on mechanical properties while the cell shape and the density play major role [49]. Our experimental findings are in good agreement with these reports. We showed that the relative cell size has a negligible effect on the mechanical properties of EP/A356 syntactic foam (see Figs. 5d–7). Otherwise, one could expect that Ø15 mm MP samples would show a mechanical behaviour closer to the Ø30 mm LP samples since they both have the same relative cell size (almost 1/7). However, they replicated the behaviour of Ø30 mm MP samples containing the same particles but with a different relative cell size (i.e. 1/13). Analogously, the

Ø15 mm SP foams replicated the mechanical properties of the Ø30 mm SP samples (the corresponding relative cell sizes are 1/13 and 1/26, respectively). Accordingly, the influence of other parameters like the cell-wall microstructure, material distribution between the struts and nodes, and cell shape uniformity seem to be more important for their mechanical behaviour.

4.2. Elastic properties

Both the unloading modulus and the 1.0% offset yield stress first increase and then decrease with increasing cell size. In metallic foams localised plastic deformation already occurs at early stages of compressive loading. Thus it is usually not possible to derive the initial yield stress from the stress–strain graph. Alternatively, the 1.0% offset yield stress is used and provides an approximate limit for the ‘elastic’ deformation of the foams.

The μ CT data of the syntactic foam samples shows that the uniformity of the cell wall thickness decreases with increasing EP particles size (see Table 2 and Fig. 2). A higher coefficient of variation of the cell-wall thickness in the case of larger EP particles means that the ratio between the average thickness of the thin struts to the thick joint areas increases with an increase in EP particle size. This geometrical characteristic affects the resistance of the structure to elastic deformation. Simulation results presented in [50] indicate that the stiffness of unit cell structures increases with increasing the ratio between the joint solid fraction and the strut up to a critical point after which it drops. According to the authors, the moment of inertia of ligaments near the joint, at which the bending moment is a maximum, increases as the thickness of the joint increases. This yields a higher elastic stiffness of unit cells. However, upon further increasing of the joint thickness and decreasing of strut thickness, the decrease in the moment of inertia at the middle of struts dramatically decreases the stiffness of the structure and additional thickness of the joint does not have a significant effect on stiffness. This reduces the overall stiffness of the structure. In good agreement with this study, the highest elastic

values are found for MP samples with strong joints and sufficiently large struts that have the highest resistance to elastic bending.

4.3. Plastic properties

The higher gradient of the stress plateau of SP foam results in a higher plateau stress, energy absorption (see Fig. 7), and a higher strain hardening exponent (see Fig. 6). However, the energy absorption efficiency decreases (see Fig. 7) because σ_{\max} grows more rapidly than the absorbed energy. The higher slope and smoothness of the stress–strain curves of the samples with smaller particles (see Fig. 5) indicate more uniform deformation behaviour. To pursue a better understanding of the deformation behaviour one SP and LP foam sample was bisected prior to compression. One side of the samples was truncated in the radial direction by 8 mm (diameter 30 mm) to see the behaviour of the cells during compression. Fig. 8 shows photographs of the samples at various stages of compression and the corresponding stress–strain curves. Fig. 8a (I) and (III) correspond to the SP and LP samples respectively. For a

better comparison, a section of the images of SP samples is magnified (see Fig. 8a (II)). The deformation is quite uniform for the SP foam while the LP foam shows a localised deformation.

At the beginning of plastic deformation, localized deformation bands initiate at single cells and grow across the entire cross section by cell distortions in the form of bending or buckling. Further deformation of cells is reduced due to strain hardening of the cell wall. Instead, stress concentrations are transmitted to the neighbouring cells which are still within the elastic region and new deformation bands nucleate and grow progressively in different areas [39,46,47]. This is a well-accepted mechanism for deformation of metallic foams. In the case of SP foam, multiple deformation bands form throughout the sample after initiation of plastic deformation. This is because of successive stress transmission due to cell-walls strain hardening. Upon further deformation, the progressive strain hardening of the deformation bands and the impingement of struts on one another [39] result in a steady increase of foam strength (see Fig. 8b). This can explain the high strain hardening coefficient n in the case of SP foams (see Figs. 6 and 8b).

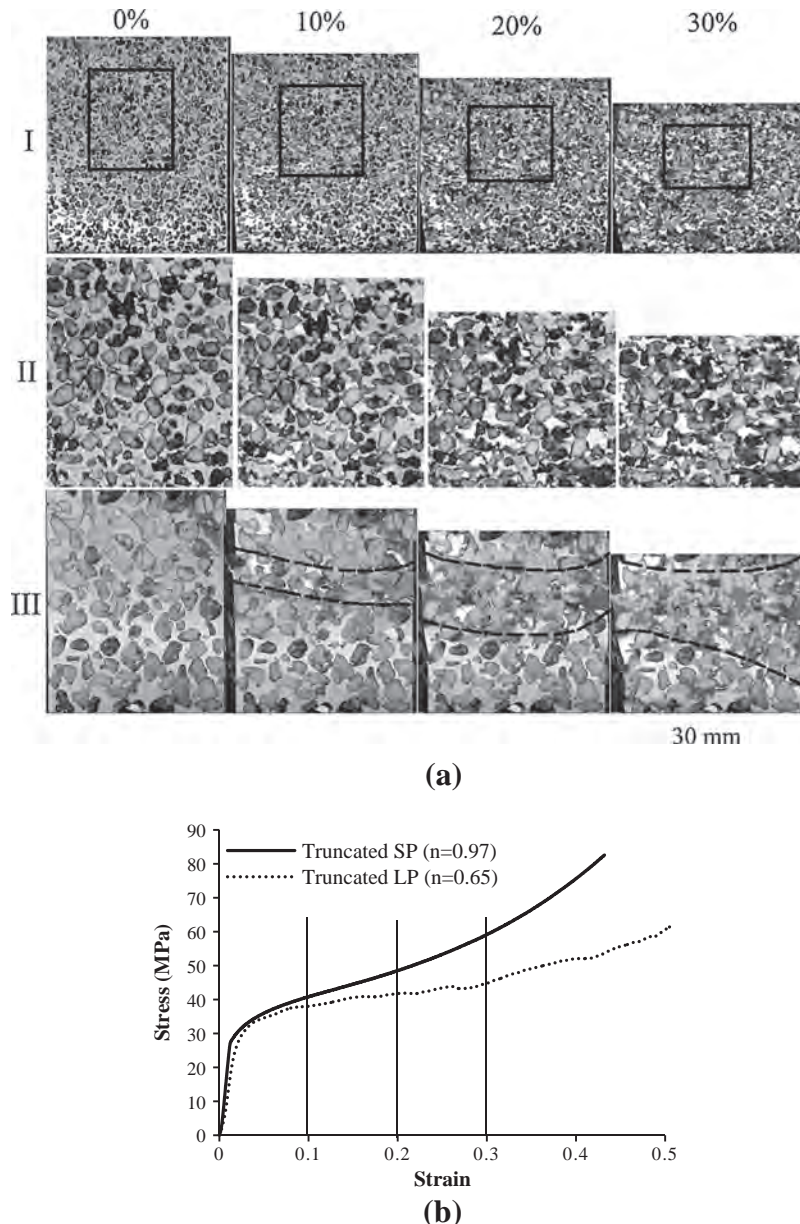


Fig. 8. (a) Compressive deformation of (I) truncated SP foam and (III) truncated LP foam; (II) magnified section showed with black rectangular in (I) and (b) the corresponding stress–strain curves of SP and LP foams.

Moreover, the curve is smooth because of simultaneous activity of multiple deformation bands. In contrast, the LP foams deform by continuous formation and collapse of discrete bands of cells. As can be seen in Fig. 8a (III), the deformation is localized in a band at 10% strain while the other regions of the foam remain largely undeformed. Upon collapse of this layer, a second band is formed and collapses (i.e. at the 20% and 30% strain). This behaviour continues until all of the undeformed cells are consumed. The result of this localised deformation bands is a stress strain curve with distinct oscillations in the plateau regime. As different bands have approximately the same strength, the compressive strength of the foam remains relatively constant until all the cells are collapsed. This is a likely explanation for the relatively constant plateau stress of LP foams and their lower overall n values (see Figs. 6 and 8b).

One can deduce that the plastic deformation of the foams is controlled by the strain hardening of the cell struts and nodes [39]. The hardening and deformation behaviour of the cell struts depends on both the microstructure of the material and the geometry of the cells, i.e. the material distribution between the struts and the nodes [39]. These parameters are influenced by the EP particle size. The microstructure of the cell walls changes from a columnar dendritic structure with large grains to an equiaxed dendritic structure with considerably smaller grains (see 2.2). The equiaxed grain structure has more isotropic macroscopic mechanical properties [35]. In addition, a small grain structure has a higher resistance to deformation and hence a higher mechanical strength [51]. Moreover, it was shown that cell-wall imperfections i.e. micro-shrinkages decreases considerably as the EP particle size decreases. These imperfections have deleterious effects on the mechanical properties of the A356 alloy [34]. Accordingly, one can say that the smaller EP particles result in stronger cell walls with higher strain hardening ability.

From a geometrical point of view, the cross-sectional area of cell struts varies along the length increasing closer to the cell nodes. As a consequence the nodes contain a significant portion of the material. Mangipudi et al. numerically investigated the strain hardening behaviour of irregular cell wall [39]. According to the authors, the yielding and the formation of the plastic hinge initiate at a location away from but close to the nodes. At low strains, a large fraction of struts near the nodes becomes plastic. Further yielding of the strut depends on the hardening behaviour of the material [39]. In the case of foams with smaller EP particles, the hardening capacity of the cell wall material is higher because of a refined microstructure and fewer defects. This leads to effective hardening of the solid material causing higher stresses in plastic regions and yielding of neighbouring elastic areas. Because of the lower difference between the thickness of struts and nodes of foams containing smaller EP particles (see Table 2 and Fig. 2), the plastic hinges can more easily spread to a large portion of strut and node. In contrast, foams with larger particles exhibit a lower strain hardening capacity of the cell wall material and a higher difference between the thickness of struts and nodes (see Table 2 and Fig. 2). This results in a limited spread of plastic hinge and a higher stress concentration at thin struts. Accordingly, one can say that failure occurs at the thin struts while a large portion of the nodes is still mostly in the elastic regime. This means that less solid material participates in plastic deformation of foams containing larger EP particles which can explain the comparably lower plateau stress.

5. Conclusions

EP/A356 aluminium syntactic foams were fabricated via infiltration of a packed bed of EP particles with three different size ranges. The effects of EP particle size on microstructural, geometri-

cal and mechanical characteristics of heat treated syntactic foams were investigated. The results presented in this study indicate:

- (1) Smaller EP particles resulted in a refined cell wall microstructure with smaller dendritic grains and less defects. This results in higher strength and hardenability of the cell-wall. The homogeneity of the cell geometry also increases as the EP particle size decreases.
- (2) The compressive stress-strain curves of all foams comprise three regimes of elastic deformation, plateau and densification. The elastic properties, e.g. stiffness and the 1% offset yield stress increase first and then decrease as the EP particles size decreases.
- (3) More uniform geometry of cells and higher mechanical strength of cell wall material result in more effective strain hardening in the case of smaller EP particles. This causes more uniform plastic deformation with multiple active deformation bands. As a result, the foams with smaller EP particles show smoother and steeper stress-strain curve and a higher plateau stress and energy absorption capacity.
- (4) The number of cells across the sample diameter (minimum of 7 in the present study) has a negligible effect on the mechanical properties of syntactic foams.

References

- [1] Jiang B, Wang Z, Zhao N. Effect of pore size and relative density on the mechanical properties of open cell aluminum foams. *Scr Mater* 2007;56(2):169–72.
- [2] Jiang B, Zhao NQ, Shi CS, Li JJ. Processing of open cell aluminum foams with tailored porous morphology. *Scr Mater* 2005;53(6):781–5.
- [3] Bekoz N, Oktay E. Effects of carbamide shape and content on processing and properties of steel foams. *J Mater Process Technol* 2012;212(10):2109–16.
- [4] Santa Maria JA, Schultz BF, Ferguson JB, Rohatgi PK. Al–Al₂O₃ syntactic foams – Part I: Effect of matrix strength and hollow sphere size on the quasi-static properties of Al–Al₂O₃/Al₂O₃ syntactic foams. *Mater Sci Eng A* 2013;582(0):415–22.
- [5] Orbulov IN. Compressive properties of aluminium matrix syntactic foams. *Mater Sci Eng A* 2012;555:52–6.
- [6] Orbulov IN, Majlinger K. Description of the compressive response of metal matrix syntactic foams. *Mater Des* 2013;49:1–9.
- [7] Majlinger K, Orbulov IN. Characteristic compressive properties of hybrid metal matrix syntactic foams. *Mater Sci Eng A* 2014;606:248–56.
- [8] Ramamurthy U, Paul A. Variability in mechanical properties of a metal foam. *Acta Mater* 2004;52(4):869–76.
- [9] Xia XC, Chen XW, Zhang Z, Chen X, Zhao WM, Liao B, et al. Effects of porosity and pore size on the compressive properties of closed-cell Mg alloy foam. *J Magn Alloys* 2013;1(4):330–5.
- [10] Bekoz N, Oktay E. Mechanical properties of low alloy steel foams: dependency on porosity and pore size. *Mater Sci Eng A* 2013;576:82–90.
- [11] Jinnapat A, Kennedy A. Characterisation testing of open cell Al foams manufactured by molten metal infiltration of porous salt bead preforms: effect of bead size. *Metals (Basel, Switz)* 2012;2(2):122–35.
- [12] Wen CE, Yamada Y, Shimojima K, Chino Y, Hosokawa H, Mabuchi M. Compressibility of porous magnesium foam: dependency on porosity and pore size. *Mater Lett* 2004;58(3–4):357–60.
- [13] Taherishargh M, Belova IV, Murch GE, Fiedler T. Low-density expanded perlite–aluminium syntactic foam. *Mater Sci Eng A* 2014;604:127–34.
- [14] Balch DK, Dunand DC. Load partitioning in aluminum syntactic foams containing ceramic microspheres. *Acta Mater* 2006;54(6):1501–11.
- [15] Wu GH, Dou ZY, Sun DL, Jiang LT, Ding BS, He BF. Compression behaviors of chemosphere-pure aluminum syntactic foams. *Scr Mater* 2007;56(3):221–4.
- [16] Kiser M, He MY, Zok FW. Mechanical response of ceramic microballoon reinforced aluminum matrix composites under compressive loading. *Acta Mater* 1999;47(9):2685–94.
- [17] Palmer RA, Gao K, Doan TM, Green L, Cavallaro G. Pressure infiltrated syntactic foams—process development and mechanical properties. *Mater Sci Eng A* 2007;464(1–2):85–92.
- [18] Orbulov IN, Ginzler J. Compressive characteristics of metal matrix syntactic foams. *Compos A Appl Sci Manuf* 2012;43(4):553–61.
- [19] Jeon YP, Kang CG, Lee SM. Effects of cell size on compression and bending strength of aluminum-foamed material by complex stirring in induction heating. *J Mater Process Technol* 2009;209(1):435–44.
- [20] Cao Xq, Wang Zh, Ma Hw, Zhao Lm, Yang Gt. Effects of cell size on compressive properties of aluminum foam. *Trans Nonferrous Met Soc China* 2006;16(2):351–6.

- [21] Xu ZG, Fu JW, Luo TJ, Yang YS. Effects of cell size on quasi-static compressive properties of Mg alloy foams. *Mater Des* 2012;34:40–4.
- [22] Tuncer N, Arslan G, Maire E, Salvo L. Investigation of spacer size effect on architecture and mechanical properties of porous titanium. *Mater Sci Eng A* 2011;530(1):633–42.
- [23] Yu H, Guo Z, Li B, Yao G, Luo H, Liu Y. Research into the effect of cell diameter of aluminum foam on its compressive and energy absorption properties. *Mater Sci Eng A* 2007;454–455:542–6.
- [24] Tao XF, Zhang LP, Zhao YY. Al matrix syntactic foam fabricated with bimodal ceramic microspheres. *Mater Des* 2009;30(7):2732–6.
- [25] Zhao Y, Tao X, Xue X. Manufacture and mechanical properties of metal matrix syntactic foams. Pittsburgh, PA; 2008.
- [26] Zhang LP, Zhao YY. Mechanical response of Al matrix syntactic foams produced by pressure infiltration casting. *J Compos Mater* 2007;41(17):2105–17.
- [27] Taherishargh M, Belova IV, Murch GE, Fiedler T. On the mechanical properties of heat-treated expanded perlite–aluminium syntactic foam. *Mater Des* 2014;63:375–83.
- [28] ISO, Mechanical testing of metals – Ductility testing – Compression test for porous and cellular metals. In: 13314, Switzerland; 2011.
- [29] Garcia-Cordovilla C, Louis E, Narciso J. Pressure infiltration of packed ceramic particulates by liquid metals. *Acta Mater* 1999;47(18):4461–79.
- [30] Toriwaki J, Yonekura T. Euler number and connectivity indexes of a three dimensional digital picture. *Forma* 2002;17:183–209.
- [31] Schneider CA, Rasband WS, Eliceiri KW. NIH Image to ImageJ: 25 years of image analysis. *Nat Methods* 2012;9:671–5.
- [32] Doube M, Klosowski MM, Arganda-Carreras I, Cordelières FP, Dougherty RP, Jackson JS, et al. BoneJ: free and extensible bone image analysis in ImageJ. *Bone* 2010;47(6):1076–9.
- [33] Hildebrand T, Rüeggsegger P. A new method for the model-independent assessment of thickness in three-dimensional images. *J Microsc* 1997;185(1):67–75.
- [34] Ammar HR, Samuel AM, Samuel FH. Effect of casting imperfections on the fatigue life of 319-F and A356-T6 Al–Si casting alloys. *Mater Sci Eng A* 2008;473(1–2):65–75.
- [35] Reinhart G, Mangelinck-Noël N, Nguyen-Thi H, Schenk T, Gastaldi J, Billia B, et al. Investigation of columnar–equiaxed transition and equiaxed growth of aluminium based alloys by X-ray radiography. *Mater Sci Eng A* 2005;413–414:384–8.
- [36] Tekoğlu C, Gibson LJ, Pardoën T, Onck PR. Size effects in foams: experiments and modeling. *Prog Mater Sci* 2011;56(2):109–38.
- [37] San Marchi C, Mortensen A. Deformation of open-cell aluminum foam. *Acta Mater* 2001;49(19):3959–69.
- [38] Mukherjee M, Kolluri M, Garcia-Moreno F, Banhart J, Ramamurty U. Strain hardening during constrained deformation of metal foams – effect of shear displacement. *Scr Mater* 2009;61(7):752–5.
- [39] Mangipudi KR, van Buuren SW, Onck PR. The microstructural origin of strain hardening in two-dimensional open-cell metal foams. *Int J Solids Struct* 2010;47(16):2081–96.
- [40] Kolluri M, Karthikeyan S, Ramamurty U. Effect of lateral constraint on the mechanical properties of a closed-cell Al foam: I. Experiments. *Metall Mater Trans A* 2007;38A(9):2006–13.
- [41] Amsterdam E, de Vries JHB, De Hosson JTM, Onck PR. The influence of strain-induced damage on the mechanical response of open-cell aluminum foam. *Acta Mater* 2008;56(3):609–18.
- [42] Luong DD, Strbik OM, Hammond VH, Gupta N, Cho K. Development of high performance lightweight aluminum alloy/SiC hollow sphere syntactic foams and compressive characterization at quasi-static and high strain rates. *J Alloys Comp* 2013;550:412–22.
- [43] Tao X, Zhang L, Zhao Y. Compressive response of Al matrix syntactic foam manufactured by liquid sintering. *Mater Sci Technol (MS&T)* 2008. Pittsburgh, PA.
- [44] Sugimura Y, Meyer J, He MY, Bart-Smith H, Grenstedt J, Evans AG. On the mechanical performance of closed cell Al alloy foams. *Acta Mater* 1997;45(12):5245–59.
- [45] Li K, Gao XL, Subhash G. Effects of cell shape and cell wall thickness variations on the elastic properties of two-dimensional cellular solids. *Int J Solids Struct* 2005;42(5–6):1777–95.
- [46] Mu Y, Yao G, Luo H. Effect of cell shape anisotropy on the compressive behavior of closed-cell aluminum foams. *Mater Des* 2010;31(3):1567–9.
- [47] Bastawros AF, Bart-Smith H, Evans AG. Experimental analysis of deformation mechanisms in a closed-cell aluminum alloy foam. *J Mech Phys Solids* 2000;48(2):301–22.
- [48] Jeon I, Asahina T. The effect of structural defects on the compressive behavior of closed-cell Al foam. *Acta Mater* 2005;53(12):3415–23.
- [49] Nieh TG, Higashi K, Wadsworth J. Effect of cell morphology on the compressive properties of open-cell aluminum foams. *Mater Sci Eng A* 2000;283(1–2):105–10.
- [50] Zargarian A, Esfahanian M, Kadkhodapour J, Ziaei-Rad S. Effect of solid distribution on elastic properties of open-cell cellular solids using numerical and experimental methods. *J Mech Behavior Biomed Mater* 2014;37:264–73. <http://dx.doi.org/10.1016/j.jmbbm.2014.05.018>.
- [51] Zhang LY, Jiang YH, Ma Z, Shan SF, Jia YZ, Fan CZ, et al. Effect of cooling rate on solidified microstructure and mechanical properties of aluminium–A356 alloy. *J Mater Process Technol* 2008;207(1–3):107–11.

Chapter 5

On the mechanical anisotropy of aluminium perlite syntactic foam

This Chapter is an extension of Chapter 4 and addresses the mechanical properties of perlite-metallic syntactic foam. The main difference is that Perlite-MSF samples are investigated by means of computation simulation as opposed to the experimental tests presented in Chapter 4. The versatility of the finite element method enables the determination of the stress distribution inside the material and the detailed investigation of deformation mechanisms. In addition, unlike in destructive experimental testing, the virtual samples can be repeatedly compressed in multiple directions permitting the characterisation of the foam's mechanical anisotropy.

Directional analysis conducted in this Chapter reveals a weak mechanical anisotropy of perlite-MSF. Micro-computed tomography (μ CT) imaging is used in order to capture the complex internal morphology of the material. The effective material properties are found to be slightly higher if the loading direction is parallel to the casting direction. The deformation mechanism analysis revealed that plastic deformation tends to accumulate in thin struts that are parallel to the loading direction. Interestingly, this coincides with the deformation mechanism found for Corevo[®] foams observed previously in Chapter 2. The so-called layer-wise collapse mechanism found in this numerical investigation is in line with observations reported in the experimental test.

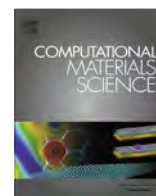
In summary, aluminium perlite syntactic foam has characteristic stress-strain curves typical for cellular metals. In addition, a mild mechanical anisotropy is found. The analysis given in this Chapter provides another important insight towards the development of cellular metals manufactured from infiltration casting approach. The general mechanical properties obtained from quasi-static compression of the material are certainly vital for its future development.

This investigation has been published online and accepted for print publication by the journal *Computational Materials Science*.

M.A. Sulong, M. Taherishargh, I.V. Belova, G.E. Murch, T. Fiedler, "On the mechanical anisotropy of aluminium perlite syntactic foam." *Computational Materials Science* 109 (2015): 258-265.

Reprint license has been obtained from Elsevier.

Copyright © 2015 Elsevier



On the mechanical anisotropy of the compressive properties of aluminium perlite syntactic foam



M.A. Sulong^{a,b,*}, M. Taherishargh^a, I.V. Belova^a, G.E. Murch^a, T. Fiedler^a

^a Centre for Mass and Thermal Transport in Engineering Materials, School of Engineering, The University of Newcastle, Callaghan 2308, Australia

^b Universiti Teknologi Malaysia, Faculty of Mechanical Engineering, 81310 Skudai, Johor, Malaysia

ARTICLE INFO

Article history:

Received 3 June 2015

Accepted 17 July 2015

Keywords:

Mechanical anisotropy

Micro computed tomography

Finite element analysis

Syntactic foam

ABSTRACT

A novel metallic syntactic foam is produced using a counter-gravity infiltration casting method. To this end, expanded perlite particles are combined with an aluminium alloy matrix. This enables close control of geometry at a relatively low production cost. The mechanical properties of the material are studied using finite element analysis. Numerical calculation models are generated directly from micro-computed tomography in order to capture their complex internal geometry. For verification purposes, numerical results are compared with experimental measurements of similar samples where available. But in contrast to experimental testing the numerical analysis is non-destructive and hence allows the repeated testing of samples in multiple loading directions. Thus, material anisotropy can be investigated for the first time. To this end, the quasi-elastic gradient, the 1% offset yield stress and the plateau stresses are obtained from virtual compression tests in three perpendicular directions (one coincides with the casting direction). Results indicate a weak anisotropy of the mechanical properties.

© 2015 Elsevier B.V. All rights reserved.

1. Introduction

Metallic syntactic foams (MSF) are made by combining light-weight filler particles with a metallic matrix [1]. Due to the relatively low strength of commonly used filler materials, metallic syntactic foams often exhibit mechanical properties similar to cellular metals. Their most important characteristic is an excellent energy absorption at a constant and controlled stress level [2,3]. Furthermore, cellular metals and MSF exhibit a high strength-to-weight ratio [4], damp vibrations [5] and have versatile thermal properties [6]. The density of MSF is higher compared to cellular metals at the same level of porosity [1] due to the additional mass introduced by the filler particles. However, MSF exhibit both superior elastic stiffness and strength [7,8]. In MSF the embedded filler particles can be hollow or porous [8]. The bulk material porosity and mechanical properties of these structures strongly depend on the filler material. The most common metal matrix material studied is aluminium and its alloys with various filler materials such as silicon carbide (SiC) spheres [1], fly ash cenosphere [9,10] and alumina (Al₂O₃) particles [11].

* Corresponding author at: Centre for Mass and Thermal Transport in Engineering Materials, School of Engineering, The University of Newcastle, Callaghan 2308, Australia. Tel.: +61 (0)2 4921 6804; fax: +61 (0)2 4921 6946.

E-mail address: mohdayub.sulong@newcastle.edu.au (M.A. Sulong).

Al/Ceramic spheres MSF have been tested using both static and dynamic compression tests. Results were acquired for two types of ceramic spheres obtained from different suppliers (Envirospheres Pty Ltd., Australia and Omega Minerals Ltd., Germany). Experimental tests include Al/Ceramic sphere foams with four different aluminium volume fractions. Higher matrix volume fraction (aluminium volume fraction, $V_{Al} = 0.6$) sample has shown higher plateau strength and energy absorption under static compression loading when compared to a lower matrix volume fraction sample ($V_{Al} = 0.32$). Al/Ceramic spheres MSF reveal that their plateau stress and energy absorption capability mostly depend on the volume fraction of the aluminium matrix [12]. The mechanical properties of the ceramic spheres only have a minor impact on the properties of the bulk material. This was attributed to the fact that Al is stronger than the porous ceramic spheres. It was found that higher Al volume fractions in the foam structure leads to improved mechanical response of the structure, such as plateau stress due to denser Al matrix network. Another MSF material is developed by Luong et al. using aluminium alloy A356 filled with silicon carbide hollow spheres (SiC) [1]. They reported that the compressive and plateau strengths were higher compared to aluminium/fly ash cenosphere metallic syntactic foam under uni-axial loading [9,10,13]. The compressive strengths of Al/SiC foams was recorded at 160 MPa, however for the Al/fly ash cenosphere this parameter was found to be only 75 MPa [10].

Several types of metallic syntactic foams (MSF) are usually manufactured using pressure infiltration casting, see, for example [1,7,8,12,14]. The work by Zhang and Zhao [12] describes the manufacturing of an aluminium matrix foam made by the infiltration of porous ceramic spheres [12]. The ceramic spheres studied were synthetically made using ceramic fine powder (particle size: 1–10 μm) which can be tailored into a variety of sphere sizes [15–18]. Rohatgi et al. [14] reported that a high volume fraction and uniform distribution of particles was achieved using infiltration casting method when fly ash filler materials is used in A356 aluminium alloy matrix. A new type of metallic cellular foam material was introduced recently using low-cost expanded perlite (EP) particles as a filler material making use of the infiltration casting manufacturing route (see Fig. 1). This new type of metallic cellular foam is referred to as perlite-MSF (perlite-metallic syntactic foam) in the following parts of this manuscript. The production cost of perlite-MSF is relatively low compared to other MSF due to its inexpensive filler and matrix material. A thorough review on the production process can be found in the manuscript [19]. Investigations have shown that the mechanical properties of perlite-MSF can be improved by reduction of the EP particle size and T6 treatment [20]. The investigation in [19] further indicates a higher plateau stress and energy absorption of perlite-MSF for decreasing particle size ($d = 1.0 \dots 1.4 \text{ mm}$) due to changes in the aluminium micro-structure and a more uniform geometry of cells compared to larger EP particles ($d = 4.0 \dots 5.6 \text{ mm}$). This is in contrast with the work done by Castro et al. [7] which involved alumina spheres (as a filler materials) infiltrated with two types of aluminium alloys (i.e.: ductile A1100 and hardened A6061). Static and dynamic impact loading tests showed that the use of smaller size alumina spheres ($d = 1 \text{ mm}$) does not increase the energy absorbed by the metallic syntactic foam compared to larger alumina spheres ($d = 2.5 \text{ mm}$) [8]. The investigation in [8] however is using A201 aluminium alloy as a matrix in their sample. In comparison with the mechanical properties of the other MSF the dynamic compression testing of perlite-MSF revealed more efficient energy absorption in high speed compression [21]. An

increase in compression resistance in high impact loading was ascribed to the filler particles (i.e.: perlite) which entrapped air. High impact loading caused the pressure of this entrapped air within the perlite particles to increase resulting in a higher macroscopic compressive resistance (see Fig. 2).

In the present paper, the mechanical characterisation of perlite-MSF under quasi-static compression is performed numerically for the first time. Numerical models were generated using micro-computed tomography (μCT) imaging in order to capture the complex internal morphology of the material. Finite element analysis of these models then allows the computation of stress distribution and the detailed study of deformation mechanisms. Furthermore, unlike in destructive experimental testing the virtual samples can be compressed in multiple directions enabling the characterisation of mechanical anisotropy. Mechanical anisotropy in the present work is defined as the dependence of the mechanical properties on the compressive loading direction.

2. Finite element analysis (FEA)

Micro-computed tomography (μCT) data of perlite-MSF samples has been obtained in order to capture accurate three-dimensional models of their complex meso-structure. Due to their low density, the perlite particles appear transparent and only the aluminium phase is visible. In total, three foam samples from the same production batch with a medium perlite particle size (diameter $d = 2.0\text{--}2.8 \text{ mm}$) were scanned using the μCT imaging approach. A voxel length of $35.32 \mu\text{m}$ was used that ensures capturing all relevant geometrical detail. The masses m , heights H and diameters D of the scanned samples are listed in Table 1. The numerical models in the present study are cubic sub-volumes with the side length of $l = 21.15 \text{ mm}$ that have been sliced from the scans of the cylindrical samples.

A model of a cellular structure must be sufficiently large to form a representative volumetric element (RVE) that exhibits the same properties as the complete structure [3]. Simulation of larger volumes unnecessarily increases the computational cost and should therefore be avoided. According to previous studies [1,2] the minimum side length over pore diameter ratio (l/d) for RVEs of cellular metals is 6–8. The numerical models of this study have a side length of $l \approx 21.15 \text{ mm}$ (see Table 2) and the pore (particle) size



Fig. 1. Photograph of A356/perlite metallic syntactic material.

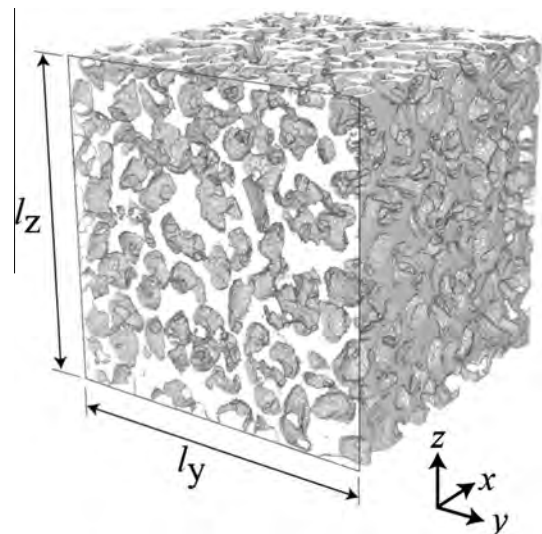


Fig. 2. Optical micrograph of perlite-MSF on the frontal-yz plane of sample A, showing coexisting small and large pores with interconnected morphology.

Table 1
Physical parameters of perlite-MSF for medium (M) particle size samples.

Characteristics for group M samples used in analysis			
Samples	A	B	C
Foam mass, m_s (g)	16.89	16.59	16.01
Diameter, D (mm)	30.70	30.70	30.70
Height, H (mm)	43.75	43.60	43.50
Porosity, p (%)	61.22	61.07	62.22

is between 2.0 mm and 2.8 mm. Accordingly, the l/d ratio is in the range of 7.6–10.5 and meets the criteria for a RVE.

Perlite-MSF can be manufactured using different expanded perlite particle sizes. Accordingly, samples can be classified as containing small (S), medium (M) and large (L) particles. The corresponding particle diameter ranges are $d = 1.0 \dots 1.4$ mm (S), $d = 2.0 \dots 2.8$ mm (M) and $d = 4.0 \dots 5.6$ mm (L). Previous investigation on perlite-MSF has shown that the particle size affects the mechanical properties of the metallic strut material [19]. It was found that the particle size alters the microstructure of the metallic struts resulting in changing mechanical properties of the aluminium alloy. In the numerical simulations, this effect is reproduced by modifying the material model based on the simulated particle size according to findings in [19]. It should be noted that the samples with smaller particles exhibit a slightly decreased variation of strut thickness which could affect mechanical properties. However, in the scope of this work the effect of these minor geometric changes is disregarded. To minimize the geometric error introduced by this simplification, all μ CT scans are performed on medium (M) samples. In total, three mesh models are created from group M samples.

2.1. Modelling approach

2.1.1. Geometric discretisation

Prior to the generation of the numerical calculation model the μ CT data has to be segmented. By using the aluminium volume fraction as a reference, the μ CT data is processed using grey-value thresholding. The threshold is iteratively adjusted until the calculated aluminium volume fraction ϕ_{Al} of the sample coincides with the segmented volume fraction of the virtual model. The target volume fraction ϕ_{Al} is calculated as the total volume of the aluminium matrix divided by the cylinder volume that encloses the sample i.e. $\phi_{Al} = V_{Al}/V_{Cyl}$. The enclosing cylinder volume is simply $V_{Cyl} = \pi \times D^2 \times H/4$ using the values listed in Table 1. The total volume of the aluminium matrix V_{Al} is the inverse volume of the packed perlite particles (i.e.: $V_{Al} = V_{Cyl} - V_p$) and the volume of perlite particles V_p can be calculated using the following equation;

$$V_p = V_{Cyl} - ((m_s - m_p)/\rho_{Al})$$

The mass of the syntactic foam m_s is obtained by direct weighing of samples. Variable m_p is the combined mass of perlite particles in the mould prior to infiltration casting. Finally, the density of A356 aluminium alloy $\rho_{Al} = 2520$ kg/m³ is taken from literature [22]. The porosity in the present work is defined as the inverse of

Table 2
Mesh parameters for numerical models.

Sample	Al. volume fraction, ϕ_{Al}	Side length x, l_x (mm)	Side length y, l_y (mm)	Side length z, l_z (mm)	Number of elements
A	0.388	21.156	21.151	21.156	2415k
B	0.389	21.149	21.150	21.159	2589k
C	0.378	21.151	21.149	21.157	2450k

the aluminium matrix volume fraction ($p = 1 - \phi_{Al}$) which is of course identical to the perlite particle volume fraction. It should be mentioned here that this definition of porosity does not account for solid perlite (approx. 6% of a particle [19]) and possibly micro-porosity in the aluminium alloy matrix. As a result of the segmentation, the greyscale μ CT images are converted into a set of bitmaps. Next, a stereolithography (STL) surface mesh is generated from the segmented images. The STL surface mesh needs to contain a sufficient number of triangles to avoid the loss of geometric details. To this end, a minimum of 9.7 million elements were used in all surface meshes. The surface mesh is then transformed into a volume mesh using the commercial meshing software Sharc Harpoon using an automated meshing algorithm. A so-called ‘mixed mesh’ model is created which contains hexahedral, pentahedral and tetrahedral elements. Mixed mesh models of complex geometries tend to have a superior numerical accuracy due to lower element distortion [23]. A total of five models with 811k, 985k, 1488k, 2415k and 3011k elements are prepared for a mesh sensitivity study for sample A. The quasi-elastic gradient is used for the mesh sensitivity study and the model with 2415k elements is found to give a good convergence. The error margin of the selected model is around 3.8% compared to the model with maximum number of elements. Fig. 3 shows a comparison between a coarse and a fine volume mesh. The mesh parameters for the final numerical models used in the present work are summarised in Table 2.

2.1.2. Boundary conditions

All simulations are conducted using the commercial finite element software MSC.Marc®. Quasi-static mechanical compression is simulated in order to investigate the effective mechanical properties of the syntactic foam. Fig. 4 shows the boundary conditions used in all simulations. A time-dependent displacement boundary condition is imposed on one surface of the cubical numerical model to introduce compressive loading. A zero displacement boundary condition is assigned to its opposite surface to represent a stationary pressure stamp. Contact between all surfaces is assumed to be frictionless. By alternating the orientation of the compression and fixed planes, material anisotropy can be tested as well.

2.1.3. Material model

The perlite-MSF matrix material is A356 aluminium. Literature provides the following material properties for this alloy: Young’s modulus $E = 75$ GPa [24], Poisson’s ratio $\nu = 0.35$ [24], and yield stress $\sigma_{y0} = 230$ MPa (ideal plasticity is assumed) [25]. This material model was used in one initial simulation and plotted together with averaged experimental data in Fig. 5b. It can be seen that this material model overestimates the stiffness within the elastic range (see Fig. 5b). However, the use of a decreased value for the modulus $E^* = 14$ GPa shows a sound agreement with the experimental data and is thus used in all subsequent simulations. Similar deviations have been previously observed in numerical simulations of cellular metals and required a recalibration of Young’s modulus to obtain a good fit with experimental tests. Studies include the numerical analysis of metallic hollow sphere structures [26,27], sintered metallic fibre structures [28] and open-cell metal foam [29]. The accepted reason for this apparent decrease of elastic stiffness is micro-plasticity that occurs at small strains and reduces the material stiffness. Therefore, E^* should no longer be considered as an elastic constant but as an effective fitting parameter that successfully reproduces the base material behaviour.

The perlite particle size affects the formation of the aluminium micro structure during casting and changes its mechanical properties [19]. The direct experimental determination of these mechanical properties is difficult to achieve since the cooling rate during

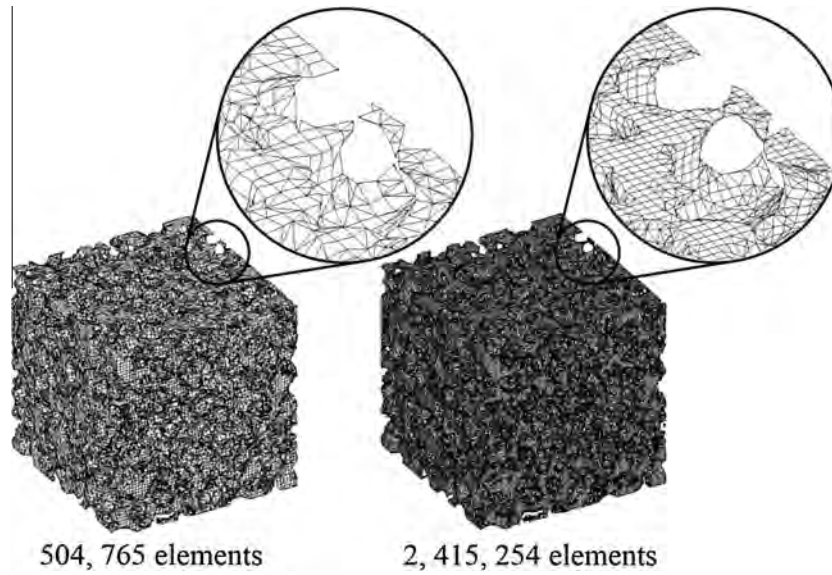


Fig. 3. Mesh models of perlite-MSF numerical model, sample A. A magnified mesh is shown for the coarse (left) and fine (right) models.

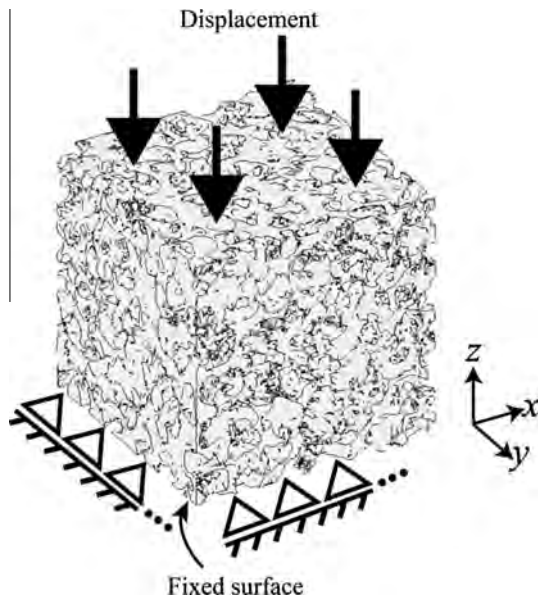


Fig. 4. Schematic diagram of boundary conditions applied to the numerical model.

solidification must be precisely replicated to obtain the same micro-structure in solid samples. A more efficient approach is therefore numerical analysis. To this end the hardening behaviour of the aluminium alloy is described as a general parabolic function of plastic strain ε_{pl} , i.e. $\sigma_y(\varepsilon_{pl}) = \sigma_{y0} \cdot [a \cdot \varepsilon_{pl}^2 + b \cdot \varepsilon_{pl} + c]$, where $\sigma_{y0} = 230$ MPa [25] is the initial yield stress of A356 alloy. The three fitting parameters a , b and c are systematically modified until the solution of the numerical model approximates the experimental data for the corresponding particle size with a good accuracy. The obtained hardening behaviour for each particle size is shown in Fig. 5 for one sample (sample A) and is used in all subsequent simulations for the corresponding particle sizes.

2.1.4. Evaluation

For each simulation time-step, a user subroutine logs the nodal reaction forces F_N and average nodal displacements Δu of all nodes where the compressive boundary condition is prescribed. The

engineering stress σ is calculated as the sum of nodal reaction forces F_N divided by the initial surface area A_0 of the cubic model i.e. $\sigma = \sum F_N / A_0$. The engineering strain is calculated by dividing the average nodal displacement Δu by the initial side length l_0 of the numerical model i.e. $\varepsilon = \Delta u / l_0$. Once the engineering stresses and strains are obtained, the quasi-elastic gradient, the 1.0% offset yield stress and the plateau stress are determined following the ISO 13314 [30] standard. The plateau stress is calculated as the arithmetic mean of the engineering stresses between 20% and 30% compressive strain.

3. Results and discussions

Fig. 5 allows the comparison of stress–strain curves for numerical and experimental testing. Numerical simulation results are plotted as dashed lines and the thick solid lines represent the experimental data taken from [19]. In all experimental tests, the samples were compressed in casting (z) direction and experimental samples contained small (S), medium (M) or large (L) sized perlite particles. After the calibration of the material model (see Fig. 6) an excellent agreement between numerical and experimental measurements is achieved.

A major advantage of numerical simulation over experimentation is the ability to repeatedly test a virtual model without destroying it. We use this in the present work to investigate the mechanical anisotropy of perlite-MSF. In order to avoid excessive computation times, the anisotropy study is limited to MSF containing medium sized EP particles. The results are shown in Fig. 7 where samples are represented by colour (blue, magenta and cyan for sample A, B and C respectively) and loading directions are indicated by different line types. It can be seen that the stresses in the casting direction (i.e.: the z -dir.) are slightly higher compared to the perpendicular x - and the y - directions.

It is difficult to quantify mechanical anisotropy by observing Fig. 7 alone. Therefore, the quasi-elastic gradient, the plateau stress and the 1% offset yield stress are determined for each virtual compression test. Using this data, a set of bar charts is created in Fig. 8a–c that allows the directional comparison of material properties. The mechanical properties are similar for samples A and B whereas distinctly lower values are obtained for sample C. This can be explained by the higher porosity of the sample (see Table 1). In addition to the graphical representations, the ratio χ

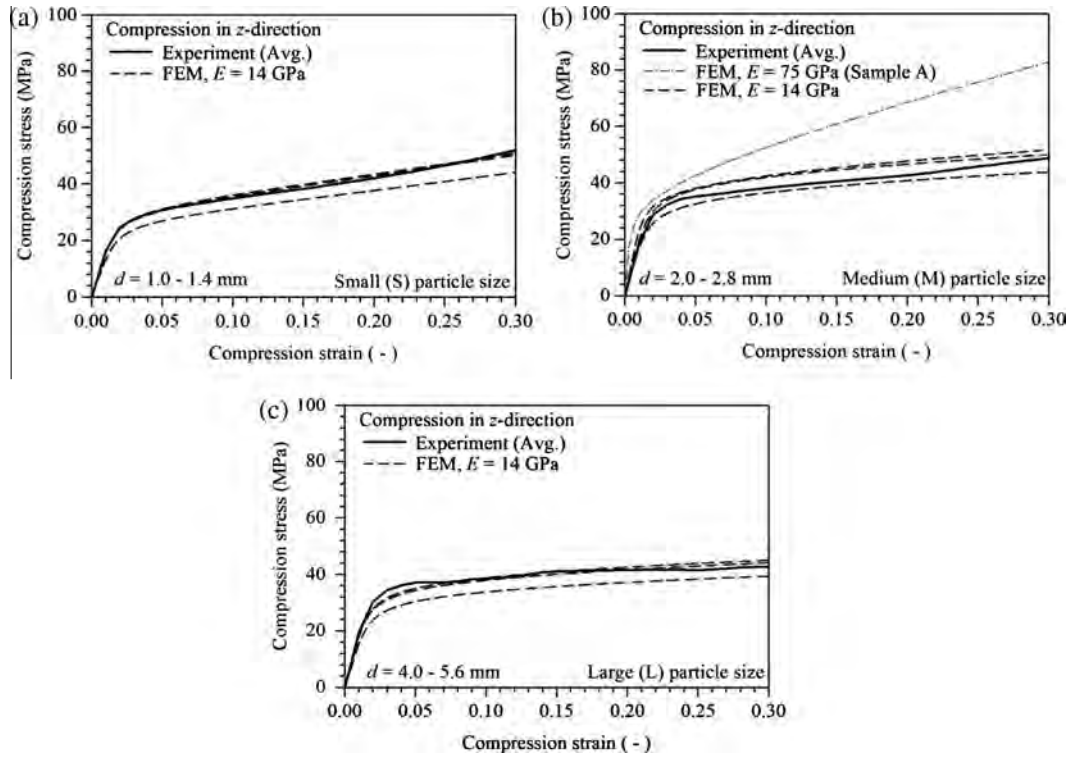


Fig. 5. Stress-strain curves for perlite-MSF obtained by numerical simulation and by quasi-static compression test [19] with different perlite particle sizes: (a) small, $d = 1.0$ – 1.4 mm, (b) medium, $d = 2.0$ – 2.8 mm and (c) large, $d = 4.0$ – 5.6 mm.

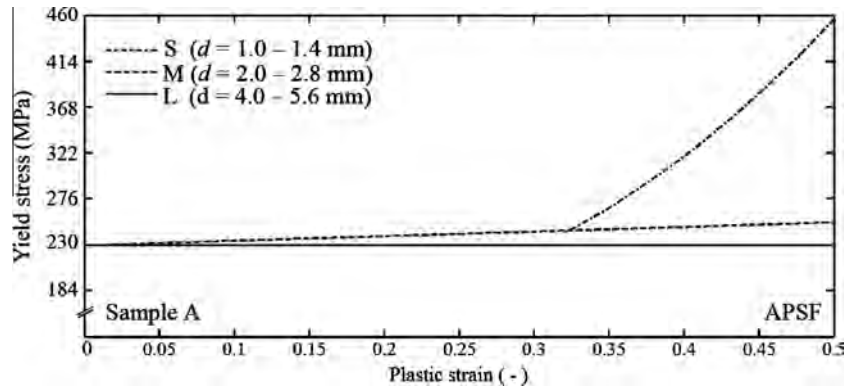


Fig. 6. Hardening modulus model for perlite-MSF sample A with three different particle sizes, $d = 1.0$ – 1.4 mm for particle size (S), $d = 2.0$ – 2.8 mm for particle size (M), and $d = 4.0$ – 5.6 mm particle size (L).

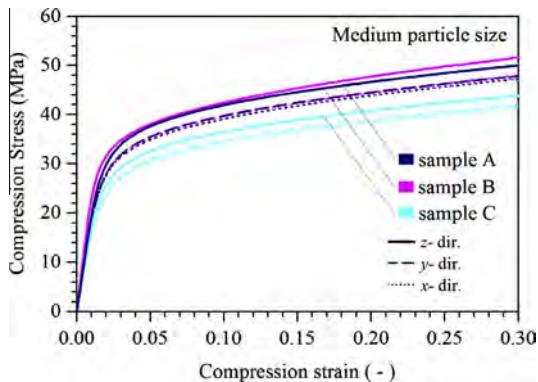


Fig. 7. Stress-strain curves for different loading directions.

of the minimum and maximum value of each mechanical property is determined to quantify the degree of anisotropy. A ratio χ close to 1 indicates isotropic behaviour whereas low values are evidence of a strong anisotropy.

The quasi-elastic gradients are shown in Fig. 8a and their values range from 1585 MPa to 2463 MPa. The maximum value belongs to sample B and loading in z-direction (i.e. parallel to the casting direction) and the minimum value corresponds to the sample C and loading in y-direction. Elastic anisotropy is clearly observed and for all samples the highest elastic gradient coincides with the casting direction. This can be attributed to a slight variation of perlite particles distribution within the samples due to a gravitational filling process described in [31]. It can be postulated that this variation of perlite particles distribution may create slightly thicker struts that are aligned in the casting direction. The anisotropy ratio χ of the quasi-elastic gradient is 0.93, 0.76 and 0.91

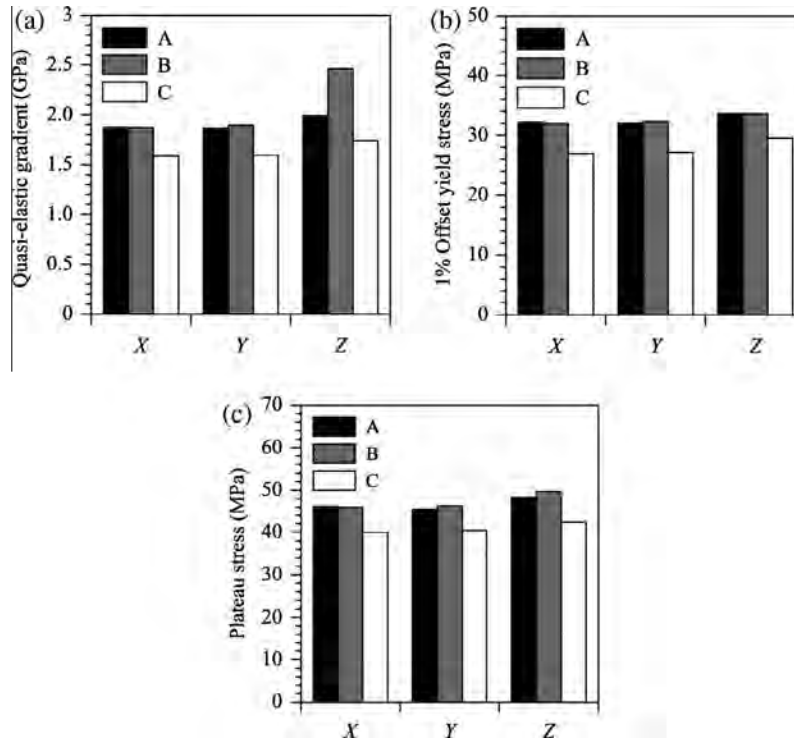


Fig. 8. Effective material properties for different loading directions: (a) quasi-elastic gradient, (b) 1% offset yield stress, (c) plateau stress.

Table 3

Anisotropy ratio of mechanical properties for medium perlite-SMF samples.

Sample	Anisotropy ratio		
	Quasi-elastic gradient	1% offset yield stress	Plateau stress
A	0.93	0.95	0.94
B	0.76	0.94	0.93
C	0.91	0.91	0.94

for samples A, B and C respectively (see Table 3). This ratio for sample B is much lower than of the other two samples. This may be likely explained as the existence of unevenly distributed strut thickness as a result of manual multiple-step filling procedure during the manufacturing process [31].

The values of the 1% offset yield stress are shown in Fig. 8b. Analogous to the elastic behaviour, the 1% offset yield stress is highest in the casting direction. Absolute values of the 1% offset yield stress are between 29.5 MPa to 33.6 MPa and the anisotropy ratio χ for sample A, B and C is 0.95, 0.94 and 0.91 respectively (see Table 3). These values are close to unity indicating only a weak anisotropy of the plasticity properties. This observation is further supported by results for the plateau stress shown in Fig. 8c ($\chi \geq 0.93$). In summary, slightly stronger mechanical properties are observed in the casting direction (i.e. z-) and weaker in the corresponding normal directions (i.e. x- and y). This observation shows that perlite-MSF exhibit systematic slight mechanical anisotropy. It should be noted that this anisotropy is weak compared to other metallic foams [29,32]. The anisotropy behaviour of plateau stress of the m.pore[®] aluminium foam has been investigated in [29] and was found to be 0.49, indicating stronger anisotropy compared to the present material. The anisotropy ratio for the plateau stress of AlSi7Mg Alporas-like metallic foam was reported in [33] as $\chi = 0.59$.

3.0.1. Deformation analysis

Using numerical analysis, the plastic deformation in perlite-MSF for different material models (S, M and L perlite particle sizes) can be analysed in great detail.

In order to correlate plastic deformation with geometric features a geometric analysis was conducted. To this end, the strut thickness distribution of the micro-computed tomography data was calculated using the BoneJ plugin [34]. The results are shown for a thin slice of sample B in Fig. 9a where dark colour indicates thin struts. Fig. 9b shows the corresponding distribution of equivalent plastic strain. One can observe that plasticity originates at such thin struts before moving to similar adjacent features. The localised plasticity has a tendency to occur in thin struts that are parallel to the loading direction. A magnified thin strut undergoing local buckling is shown in Fig. 9b. Localised plastic deformation initiates at low strains ($\varepsilon = 0.1$) and precedes strut buckling occurring at larger macroscopic strain $\varepsilon \approx 0.2 \dots 0.3$. This mechanism of plastic deformation was first described in [19,20] based on sample surface observations during compressive testing.

An identical plastic collapse mechanism is observed for models S and L making use of numerical post-script data (see Fig. 10). In Fig. 10a, a cross-sectional view through the center of the cube shows the internal plastic failure. The black arrows indicate the loading direction used in numerical simulations. Subsequent images of the plastic deformation propagation for the macroscopic compressive strain $\varepsilon = 0.1, 0.2$ and 0.3 , are shown together with their respective oblique view (for $\varepsilon = 0.2$). Analogous to the deformation mechanism described above, plasticity starts to accumulate in thin struts at low strains ($\varepsilon = 0.1$) and subsequently this leads to a localised buckling.

For material model S (see Fig. 10a), the number of collapse bands is relatively high compared to the results of the M and L material models (see Figs. 9 and 10b). In the case of small filler particles, more thin struts undergo plastic deformation at the same level of macroscopic strain (i.e. $\varepsilon = 0.3$). This behaviour is identical

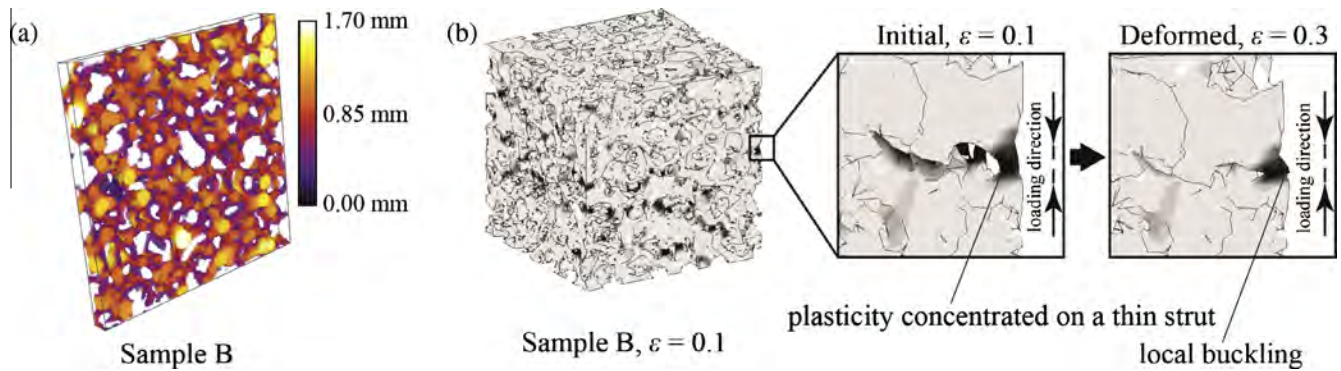


Fig. 9. Results of numerical simulations shown: (a) thin struts on a slice of perlite-SMF sample presented as dark blue areas by BoneJ plug-in [34]; and (b) a single strut local buckling magnified in the designated square. (For interpretation of the references to colour in this figure legend, the reader is referred to the web version of this article.)

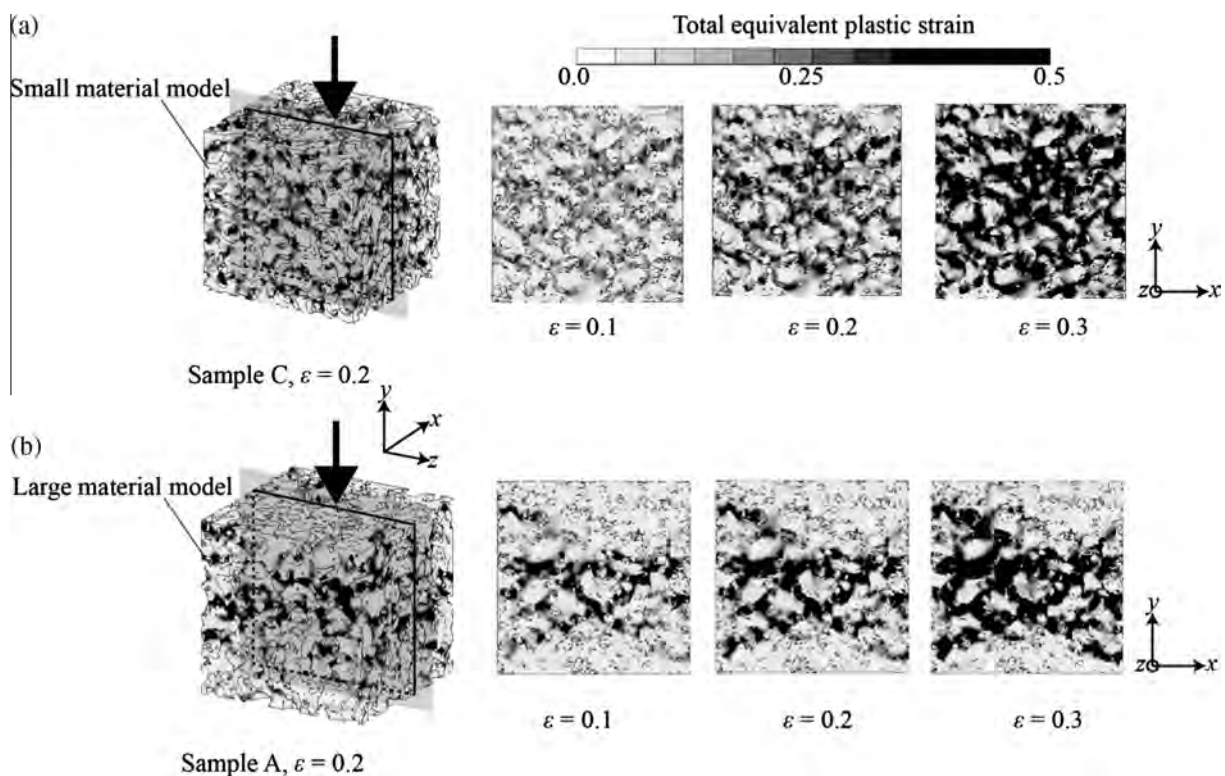


Fig. 10. Total equivalent plastic strain distribution of numerical models using (a) small (S) presented by sample C and (b) large (L) material model presented by sample A.

for all samples (A, B and C). The explanation is the strain hardening defined in the M and, in particular, S material models (see Fig. 6). The strain hardening effect increases the local yield stress and thus plasticity is more likely to spread to a neighbouring weak feature. As shown in Fig. 6 this effect is strongest for the syntactic foam with small particles and lowest for the large particle model where ideal plasticity (i.e. no strain hardening) is assumed.

In all simulations, a layer-wise collapse mechanism is observed. Due to strain hardening, the plastic collapse may temporarily stop within a layer until increasing stresses reach the new yield stress level. The syntactic foam in the present work starts to show localised plastic deformation band at macroscopic compression strain $\varepsilon \approx 0.1$. At higher compression strain ($\varepsilon = 0.2 \dots 0.3$), additional collapse bands form as more thin struts and cell walls are deformed. A similar mode of plastic deformation was also observed for closed-cell [35,36] and open-cell [37] metallic foams.

4. Conclusions

The compressive properties of perlite-MSF have been addressed with computational simulations. Calculation models were based on micro computed tomography data of actual samples in order to capture the complex material geometry. An iterative calibration of the material model then allowed the characterisation of the plastic hardening behaviour by the comparison with experimental data. The filler particle size was found to have a profound impact on the hardening behaviour. Near ideal plasticity was found for large particles whereas strong strain hardening was observed in the case of small filler particles. Next, directional analysis was performed by compressing virtual models in three perpendicular loading directions. The investigation revealed weak anisotropy of the perlite-MSF mechanical properties. The effective material properties were slightly higher if the material was loaded parallel to

the casting direction. Finally, a detailed deformation analysis of the cellular material was carried out by post-processing the numerical calculation data. Analysis of the deformation mechanism revealed concentrations of plastic deformation in thin struts that are parallel to the loading direction. On a macroscopic scale a layer-wise collapse mechanism was found which is in good agreement with experimental observations. The number of collapse bands was found to vary with the filler particle size. Strong strain hardening in the case of small filler particles caused the formation of multiple simultaneous collapse bands whereas a relatively low number of collapse bands were observed in the case of the large filler particles.

Acknowledgement

One author (MA Sulong) would like to acknowledge Mr. Dipendra Shastri for sharing his insight and knowledge on perlite particles.

References

- [1] D.D. Luong, O.M. Strbik Iii, V.H. Hammond, N. Gupta, K. Cho, J. Alloy. Compd. 550 (2013) 412–422.
- [2] M.F. Ashby, A. Evans, N.A. Fleck, L.J. Gibson, J.W. Hutchinson, H.N.G. Wadley, Metal Foams: A Design Guide: Butterworth-Heinemann, 2000.
- [3] J. Banhart, Prog. Mater. Sci. 46 (2001) 559–632.
- [4] A. Öchsner, C. Augustin, Multifunctional Metallic Hollow Sphere Structures, Multifunctional Metallic Hollow Sphere Structures: Manufacturing, Properties and Application, Engineering Materials, vol. 1, 2009.
- [5] W. Pannert, R. Winkler, M. Merkel, Mater. Lett. 63 (2009) 1121–1124.
- [6] E. Solórzano, M.A. Rodríguez-Perez, J.A. de Saja, Mater. Lett. 63 (2009) 1128–1130.
- [7] G. Castro, S.R. Nutt, X. Wenchen, Mater. Sci. Eng., A 578 (2013) 222–229.
- [8] M. Kiser, M. He, F. Zok, Acta Mater. 47 (1999) 2685–2694.
- [9] Y. Mu, G. Yao, J. Mater. Eng. Perform. 19 (2010) 995–997.
- [10] Z. Dou, L. Jiang, G. Wu, Q. Zhang, Z. Xiu, G. Chen, Scripta Mater. 57 (2007) 945–948.
- [11] C. San Marchi, F. Cao, M. Kouzeli, A. Mortensen, Mater. Sci. Eng., A 337 (2002) 202–211.
- [12] L. Zhang, Y. Zhao, J. Compos. Mater. 41 (2007) 2105–2117.
- [13] M. Roulia, K. Chassapis, C. Fotinopoulos, T. Savvidis, D. Katakis, Spill Sci. Technol. Bull. 8 (2003) 425–431.
- [14] P. Rohatgi, J. Kim, N. Gupta, S. Alaraj, A. Daoud, Compos. A Appl. Sci. Manuf. 37 (2006) 430–437.
- [15] L.B. Torobin, Method for making hollow porous microspheres, ed.: Google Patents, 1987.
- [16] L.B. Torobin, Hollow microspheres made from dispersed particle compositions and their production, ed.: Google Patents, 1988.
- [17] L.B. Torobin, Hollow microspheres made from dispersed particle compositions, ed.: Google Patents, 1990.
- [18] J.K. Cochran, Curr. Opin. Solid State Mater. Sci. 3 (1998) 474–479.
- [19] M. Taherishargh, I.V. Belova, G.E. Murch, T. Fiedler, Low-density expanded perlite–aluminium syntactic foam, Mater. Sci. Eng., A 604 (2014) 127–134.
- [20] M. Taherishargh, I.V. Belova, G.E. Murch, T. Fiedler, On the mechanical properties of heat-treated expanded perlite–aluminium syntactic foam, Mater. Design 63 (2014) 375–383.
- [21] T. Fiedler et al., Dynamic compressive loading of expanded perlite/aluminum syntactic foam, Mater. Sci. Eng., A 626 (2015) 296–304.
- [22] J. Huang, J.G. Conley, T. Mori, Metall. Mater. Trans. B 29 (1998) 1249–1260.
- [23] C. Veyhl, I.V. Belova, G.E. Murch, A. Öchsner, T. Fiedler, Finite Elem. Anal. Des. 46 (2010) 371–378.
- [24] Q. Wang, M. Praud, A. Needleman, K. Kim, J. Griffiths, C. Davidson, et al., Acta Mater. 58 (2010) 3006–3013.
- [25] P.R. Raju, B. Satyanarayana, K. Ramji, K.S. Babu, Eng. Fail. Anal. 14 (2007) 791–800.
- [26] O. Caty, E. Maire, S. Youssef, R. Bouchet, Acta Mater. 56 (2008) 5524–5534.
- [27] E. Maire, O. Caty, R. Bouchet, Fatigue of metal hollow spheres structures, in: A. Öchsner, C. Augustin (Eds.), Multifunctional Metallic Hollow Sphere Structures, Springer, Berlin Heidelberg, 2009, pp. 159–182.
- [28] C. Veyhl, T. Fiedler, U. Jehring, O. Andersen, T. Bernthaler, I.V. Belova, et al., Mater. Sci. Eng., A 562 (2013) 83–88.
- [29] M. Vesenjak, C. Veyhl, T. Fiedler, Mater. Sci. Eng., A 541 (2012) 105–109. 4/15/.
- [30] ISO 13314:2011(E) Mechanical testing of metals — Ductility testing — Compression test for porous and cellular metals, 2011.
- [31] M. Taherishargh, I.V. Belova, G.E. Murch, T. Fiedler, Mater. Sci. Eng., A 604 (2014) 127–134.
- [32] S. Hyun, H. Nakajima, Mater. Sci. Eng., A 340 (2003) 258–264.
- [33] A.-H. Benouali, L. Froyen, T. Dillard, S. Forest, F. N'guyen, J. Mater. Sci. 40 (2005) 5801–5811.
- [34] M. Doube, M.M. Kłosowski, I. Arganda-Carreras, F.P. Cordelières, R.P. Dougherty, J.S. Jackson, et al., Bone 47 (2010) 1076–1079.
- [35] A. Bastawros, H. Bart-Smith, A. Evans, J. Mech. Phys. Solids 48 (2000) 301–322.
- [36] M.A. Sulong, M. Vesenjak, I.V. Belova, G.E. Murch, T. Fiedler, Mater. Sci. Eng., A (2014).
- [37] M. Vesenjak, L. Krstulović-Opara, Z. Ren, A. Öchsner, Ž. Domazet, Exp. Mech. 49 (2009) 501–509.

Chapter 6

Compressive properties of Advanced Pore Morphology (APM) foam elements

In contrast to the infiltration casting in the previous Chapters 3-5 the cellular metal considered in this Chapter was manufactured by the thermal expansion of pre-foamed elements. The resulting APM foam element has a porous internal structure and a near spherical outer skin. The similarities between APM and the previously considered foams is that they are all metallic and exhibit a porous structure. In this Chapter, we present the compressive properties of APM under dynamic loading conditions.

The present Chapter combines micro-computed tomography imaging and finite element analysis of APM foam elements. This is the first time that this approach has been used for this novel cellular material. The μ CT imaging approach provides a highly accurate representation of the complex inner foam geometry. Geometrical data from μ CT is obtained and incorporated in the numerical analysis. This Chapter addressed two compressive loading velocities (quasi-static and dynamic) of a single APM foam element. To this end, computational calculations are performed to simulate the experimental compressive test. The compressive force-displacement data are then evaluated numerically for APM foam elements with different diameters (i.e. 5 mm and 10 mm) and strain rates. For verification purposes, numerical results are compared with experimental data published in the literature and a good agreement is found. Quasi-static and dynamic analyses reveal that plastic deformation does not occur uniformly within a single sphere but is concentrated in a conical sub-volume located in between the pressure stamp and the sphere's contact area.

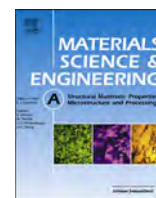
In summary, larger APM foam elements exhibit a 3.3 times higher structural stiffness compared to the smaller ones. Removing the outer skin of original APM foam elements will reduce its stiffness by 30%. Furthermore, APM foam elements show an increase of stiffness and plateau stress with increasing strain rate.

This investigation has been published online and accepted for print publication by the journal *Materials Science and Engineering: A*.

M.A. Sulong, M. Vesenjak, I.V. Belova, G.E. Murch, T. Fiedler, "Compressive properties of Advanced Pore Morphology (APM) foam elements." *Materials Science and Engineering: A* 607 (2014): 498-504.

Reprint license has been obtained from Elsevier.

Copyright © 2015 Elsevier



Compressive properties of Advanced Pore Morphology (APM) foam elements

M.A. Sulong^{a,c,*}, M. Vesenjāk^b, I.V. Belova^a, G.E. Murch^a, T. Fiedler^a

^a Centre for Mass and Thermal Transport in Engineering Materials, School of Engineering, The University of Newcastle, Callaghan 2308, Australia

^b University of Maribor, Faculty of Mechanical Engineering, Smetanova 17, SI-2000 Maribor, Slovenia

^c Department of Solid Mechanics and Design, Faculty of Mechanical Engineering, Universiti Teknologi Malaysia – UTM, 81310 UTM Skudai, Johor, Malaysia

ARTICLE INFO

Article history:

Received 30 October 2013

Received in revised form

7 April 2014

Accepted 9 April 2014

Available online 16 April 2014

Keywords:

Finite element method

Mechanical characterisation

Tomography

Aluminium alloys

Plasticity

ABSTRACT

Advanced Pore Morphology (APM) foam elements have a spherical outer skin and a porous inner structure. APM foam is a product of the improved powder metallurgy FOAMINAL[®] process. The present work investigates the mechanical properties of single APM foam elements under quasi-static and dynamic compressive loading. By means of μ CT techniques, an accurate finite element model is generated. The compressive force–displacement response of APM foam elements is numerically evaluated for different diameters and strain rates. The results of the numerical analysis are compared with experimental data. Good agreement is found. Quasi-static and dynamic loading are both investigated by making use of numerical analysis and verified by comparison with experimental results.

© 2014 Elsevier B.V. All rights reserved.

1. Introduction

Cellular materials are known for their very high porosity, high specific stiffness, acoustic damping and the ability to absorb a relatively high amount of energy at a low stress level [1,2]. Their versatile heat insulation property makes them useful for heat exchangers or thermal insulation [3]. A major limitation of conventional cellular materials is their stochastic geometry which can result in unreliable mechanical properties. Another important challenge is the reduction of their high manufacturing cost. Control of the pore structure will allow the varying of the morphology and topology (pore size distribution, pore shape and cell wall geometry), which can be expected to allow a better definition of mechanical properties [4,5]. Recently, a new concept of metal foam components production was patented by Stobener et al. [6]. Carrying the name Advanced Pore Morphology (APM, see Fig. 1) foam, this innovative cellular material has been developed on an improvement of the powder metallurgical FOAMINAL[®] process that was introduced earlier by Baumeister [7].

Several investigations have been conducted on either single or composite APM foam elements with both partial and syntactic morphology. The experiments have been carried out by Lehmhus et al. [8] to investigate the influence of APM foam density for both

quasi-static and dynamic compressive loading as well as the effect of varying the bonding agent (an epoxy-based adhesive and polyamide). They reported that the dynamic initial strength of epoxy-bonded APM foam is slightly higher than the quasi-static initial strength. A notable increase in the dynamic initial strength was observed for polyamide-bonded APM foam. Vesenjāk et al. [9] investigated the behaviour of a single APM foam element and a composite APM foam with partial and syntactic morphology under compressive loading. Two APM foam element sizes with diameters $\varnothing=5$ mm and $\varnothing=10$ mm were tested experimentally. The results indicated that the larger APM spheres exhibit a higher energy-absorption capability due to a lower densification strain. They also investigated cylinder-shaped ($d=h=30$ mm) epoxy samples with embedded APM foam elements. Experimental testing was conducted using free and confined radial boundaries. It was found that syntactic APM composites have energy absorption capacity approximately four times higher than non-bonded or partially bonded APM foam elements. Hohe et al. [10] conducted experimental and numerical tests on graded APM foams for multi-functional aerospace applications. The main focus of their investigation was perforation resistance against bird strike events. In a case study, a sandwich plate with graded APM foam core was compared with a sandwich plate with a conventional foam core. The results indicated that the use of a graded APM foam core increases the perforation resistance performance of the sandwich plate. This was achieved by dissipating the plastic energy over a larger volume. Vesenjāk et al. [11] used an infrared thermal imaging camera to enhance the usual data acquisition during compressive experimental testing of APM

* Corresponding author at: Centre for Mass and Thermal Transport in Engineering Materials, School of Engineering, The University of Newcastle, Callaghan 2308, Australia.

E-mail address: mohdayub.sulong@uon.edu.au (M.A. Sulong).



Fig. 1. Light photograph of APM foam elements.

foam elements. Infrared thermal imaging indicated that plastic yielding occurred predominantly in the outer region of the APM foam element and then propagated inwards in a shear band into the sphere. The present paper combines, for the first time, micro-computed tomography imaging and finite element analysis of APM foam elements. In contrast with earlier investigations, a highly accurate representation of the complex inner foam geometry is obtained and incorporated in the numerical analysis. As a result, detailed information on the internal deformation mechanisms is obtained. For verification purposes, numerical results are compared with experimental data published in the literature.

2. Manufacturing process of APM foam elements

The FOAMINAL[®] process is capable of successfully manufacturing near net-shaped parts and three-dimensional (3D) sandwich panels with a foamed core layer. In [10], an AlSi7 aluminium alloy was prepared in powder metallurgy precursor form with TiH₂ added as foaming agent. Foaming was activated by the heating of the precursor. This process usually takes place within a mould cavity. During the foaming process, furnace temperatures up to 800 °C are used depending on matrix alloys and the presence of stabilising ceramic particles. As a result, the foaming mould has to bear high thermal loads in each foaming cycle [8]. A new process route proposed by Stobener in APM foaming eliminates the need for expensive moulds. The manufacturing procedure consists of powder compaction (by the CONFORM[®] process) and rolling of the AlSi7 alloy with TiH₂ foaming agent to obtain expandable precursor material. The wire-shaped precursor material (diameter $\phi=3$ mm) is then cut into small granulates (length $l=2$ mm) [12], which are expanded into sphere-like foam elements (see Fig. 1) due to the thermal decomposition of the TiH₂ foaming agent in a continuous belt furnace. This is driven by internal gas pressure, surface tension and the formation of an oxide skin. So far, three sizes of APM foam elements have been manufactured with diameters of 5, 10, and 15 mm and foam element densities varying from 0.5 to 1.0 kg m⁻³ [8,13]. Structures assembled by APM foam elements exhibit two types of porosity: (i) the inner porosity in single APM foam elements and (ii) the outer porosity between many APM foam elements which depends on the size of the APM elements and their arrangement [14]. Detailed information on the automated production of APM foam elements can be found in the literature [12].

3. Model generation

Micro-computed tomography (μ CT) imaging is a non-destructive procedure that allows precise measurements on aluminium foams

[15–17] with the advantage of repetitive 3D assessment and computation of micro-structural and micro-mechanical properties. The most outstanding feature of μ CT is the ability to image the sample's interior with high spatial and contrast resolution. A thorough review of μ CT can be found in the monograph [18]. In previous analyses, sintered metallic hollow sphere structure (MHSS), sintered metallic fibre structure (SMFS), lotus-type porous material, Alporas[®] and M-Pore[®] have been characterised using μ CT technology [2,3,15–17,19,20]. The companion study [21] first addressed μ CT of APM foam elements by analysing their geometrical micro- and meso-structures. By using the voxel data from the μ CT images, geometrical properties such as the number of pores and their size distribution in the cellular materials were characterised. This novel approach can be applied to any closed-cell morphology and will be expanded to open-cell cellular materials. Results show that the deviation of the porosity and the microstructure characteristics between specimens of the same size was moderate. In the present study, μ CT scanning of small ($\phi=5$ mm) and large ($\phi=10$ mm) spherical foam elements was performed. An Xradia MicroXCT-400 machine with a Hamamatsu L8121-03 X-ray source was used. Due to the size differences of the samples, the voxel resolutions were limited to 3.61 μ m ($\phi=5$ mm sphere) and 6.28 μ m ($\phi=10$ mm sphere), respectively. A total of 1800 absorption radiographs (exposure time 16 s) was captured with a 0.2° rotation for each projection. The selected acceleration voltage was 140 kV with a current of 70 μ A. The μ CT data was first segmented by gray-value thresholding. In this step, it must be ensured that the volume of the voxels representing the metallic phase matches the volume of metal in the APM foam element. To this end, the mass of the scanned APM foam elements was measured using a precision scale. Next, the metal volume was calculated using the AlSi7 material density $\rho=2680$ kg m⁻³ [22]. The segmentation threshold was adjusted iteratively until the segmented voxel volume coincided with this calculated volume. The segmented voxels were then rendered to a 3D structure that was subsequently converted into a stereolithography (STL) surface geometry mesh. Stereolithography surface geometry is widely used in 3D model rapid prototyping. Unlike the higher-level representation such as non-uniform rational B-spline (NURBS) that contains a smooth polynomial function or spline, the created STL mesh file is not very rich in information [23]. STL meshes only describe the surface geometry of a three-dimensional object using a triangulated surface. In order to avoid the loss of geometrical detail during meshing, at least 750,000 triangles were used in the STL surface mesh. A volume mesh was then created within the bounds of the surface mesh by using the commercial automatic mesh generation software Sharc Harpoon. The small margin of error of the created model mesh volume is found for both APM foam element sizes. The small volumetric error percentages for $\phi=5$ mm and $\phi=10$ mm are 7% and 2%, respectively. A Hex-dominant mesh that contains three types of elements, namely, linear hexahedral-, linear pentahedral- and tetrahedral-elements have shown superior performance in the numerical analysis of complex geometries [16]. Accordingly, mixed meshes were used in the present analyses.

3.1. Finite element simulation

The accurate representation of the complex internal foam geometry including the micro and macro-porosity requires a high geometrical resolution. As a result, a single APM foam element is too large to be meshed (and computed) on the available large memory computers (64 GB RAM). In this work, we made use of the symmetry of the roughly spherical-shaped APM foam elements to reduce the size of the calculation model. To this end, each spherical APM element was subdivided into eight segments (see Fig. 2). For each diameter (i.e., 5 mm and 10 mm) four segments were converted into numerical calculation models.

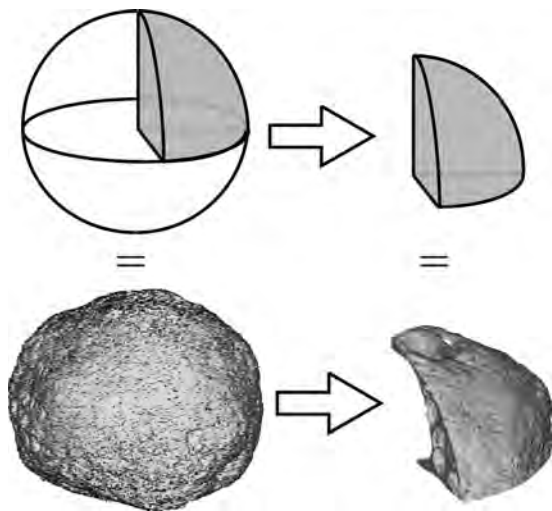


Fig. 2. Sub-division of APM foam elements.

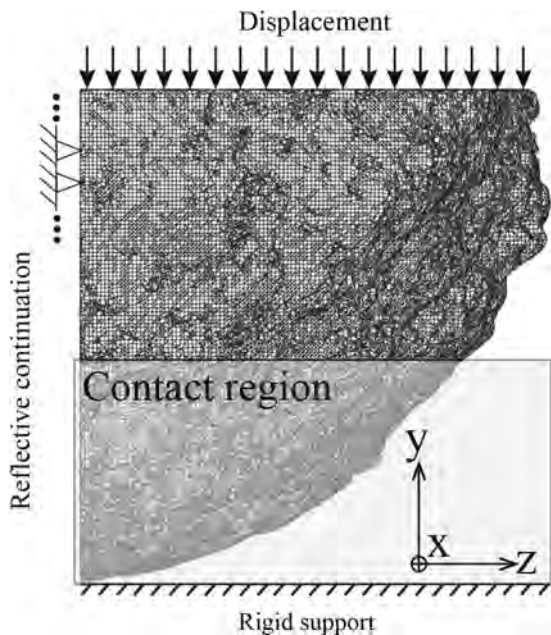


Fig. 3. Boundary conditions of the finite element analyses.

The boundary conditions of the finite element analysis are shown in Fig. 3. A rigid support was defined as part of a contact boundary condition with the deformable elements of the APM volume meshes. Quasi-static and dynamic compressive loading was introduced using a time-dependent nodal displacement boundary condition at the upper symmetry plane of the foam element. For the dynamic loading case the rate of the displacement boundary condition was adjusted to achieve a macroscopic strain rate of 100 s^{-1} . Within the remaining two symmetry planes, the normal displacement was set to zero in order to simulate the remaining APM foam element. Such boundary conditions were introduced with the assumption that the deformation propagates in an identical way at the top and the bottom of the foam elements. Nevertheless, in the actual experiment the deformation progress can only be observed and confirmed at the top of the foam elements since the moving force platen is located at the top. The maximum deformation of the model was set to 10% (quasi-static) and 70% (dynamic) of the original APM sphere's height. The smaller deformation of the quasi-static model is caused by significantly longer calculation times. Material properties of AlSi7

used in this numerical model were Young's modulus $E=72,400 \text{ MPa}$, Poisson's ratio $\nu=0.3$, yield stress $\sigma_y=120 \text{ MPa}$, density $\rho=2680 \text{ kg m}^{-3}$, and tangent modulus $T=800 \text{ MPa}$ [22]. Within the dynamic simulations the base material inertia and its strain rate effect have been accounted for [20]. The dynamic response of cellular materials is mainly influenced by (i) the micro-inertial effect and (ii) the material strain-rate sensitivity [24–26]. The micro-inertia of the individual cell walls can affect the deformation of metal foams as discussed in [27,28]. According to Tan et al. [29] the inertia effects associated with the dynamic localisation of crushing are responsible for the enhancement of the dynamic strength properties in high velocity regimes. The authors in [28] state that inertia effects contribute significantly to the rate effect, even when the strain rate sensitivity of material properties is ignored. The material rate-dependence is usually taken into account within the constitutive material model [30]. In addition, the strain-rate sensitivity of the cellular structure might be affected by the presence of a gaseous pore filler (e.g., air, H_2) [31,32]. However, the strain rate sensitivity effect is usually more apparent for structures with higher initial pore pressures or higher relative densities [33,34]. It should be noted that air compression within the cells was not considered in the scope of this work which might influence the response of the APM element subjected to dynamic loading (high strain rates). The base material strain rate sensitivity was introduced using the Cowper–Symonds constitutive model with the parameters $C=6500 \text{ s}^{-1}$ and $p=4$ [35–37]. All nodes of the aluminium foam belong to a single surface contact accounting also for friction with a coefficient of friction of 0.5 [38]. A user-defined subroutine was used to extract force–displacement data. To this end, the sum of nodal reaction forces and the average displacement of these nodes selected on the upper plane were recorded. The computational models were analysed using the commercial finite element codes MSC.Marc for the quasi-static loading case and LS-DYNA for the dynamic loading case [37].

It should be mentioned here that the simulation of a complete APM foam element will serve better results. The simulation of a full sphere with an adequate geometrical resolution that captures the internal pore structure requires extremely long computation times (> 4 months) and large random access memory ($> 128 \text{ GB}$). This obstacle is overcome by considering only a segment (one-eighth of an APM foam element) for the numerical simulation. However, this simplification introduces a number of shortcomings that should be considered during the result interpretation. First, the size and shape of pores that intersect a symmetry plane are going to be altered. Second, the boundary conditions may affect local bending and buckling of the solid phase. However, this effect seems to be limited since the analysis of stress and strain distributions in the vicinity of and away from the boundary condition showed no significant deviation. Third, the boundary conditions affect the stress wave propagation through the foam structure and influence the dynamic response. However, considering the high porosity of the structure and moderate loading velocities the influence of the symmetrical boundary is not significant. This has also been confirmed by validation of the computational results with experimental tests.

Prior to the mechanical characterisation of APM foam elements, the mesh independence of the solution was addressed. The results of the mesh refinement study are illustrated in Fig. 4. The boundary conditions described above were used and the initial gradient dF/dy of the force–displacement curve was calculated. Fig. 4 shows that 640,000 nodes ($\phi=5 \text{ mm}$) and 550,000 nodes ($\phi=10 \text{ mm}$) yielded satisfactory numerical convergence. The corresponding average element sizes were 0.014 mm for $\phi=5 \text{ mm}$ and 0.035 mm for $\phi=10 \text{ mm}$ APM foam elements. In addition, for the dynamic simulations, the time step sensitivity analysis had to

be performed in order to satisfy the Courant–Friedrichs–Lewy condition for the explicit integration scheme. Based on the smallest finite element edge length it was confirmed that the time step of $0.39 \mu\text{s}$ provides stable convergence [36].

4. Results and discussion

Fig. 5 shows the quasi-static force–displacement response of APM foam elements with $\phi=5 \text{ mm}$ and $\phi=10 \text{ mm}$ diameters. Numerical simulations of APM foam elements are denoted by thin

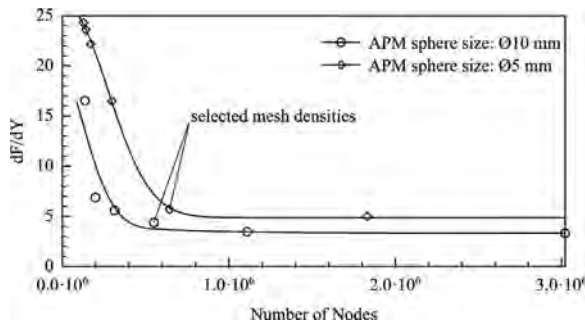


Fig. 4. Convergence analysis on APM foam elements.

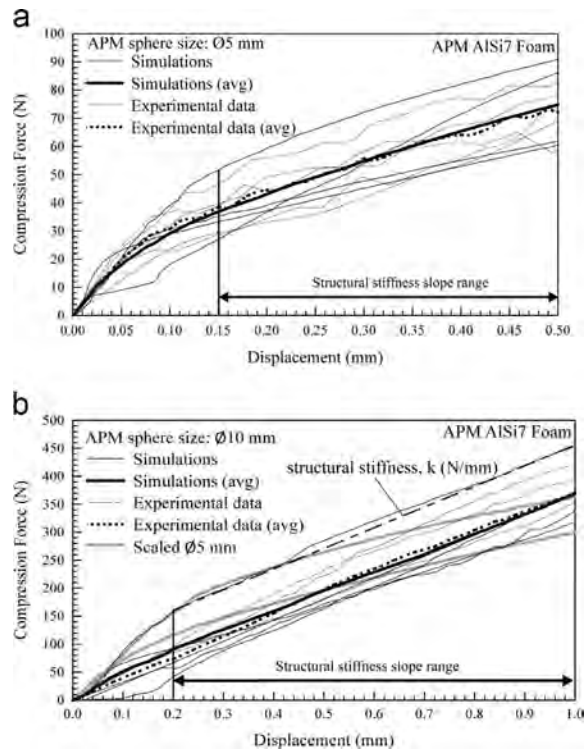


Fig. 5. Quasi-static response for (a) $\phi=5 \text{ mm}$ APM foam and (b) $\phi=10 \text{ mm}$ APM foam elements.

continuous lines and their average value is represented by a thick continuous line. The experimental data taken from [9] and the corresponding average are denoted by the thin and thick dotted lines, respectively. It can be observed that absolute values as well as the scattering of numerical and experimental results are consistent. In particular, good agreement is found in their averaged values. The comparison of large ($\phi=10 \text{ mm}$) and small ($\phi=5 \text{ mm}$) foam elements clearly indicates higher compressive force values for the large APM element. This result is expected since (unlike stress–strain data) force–displacement data are not normalised by the sample size. Accordingly, the larger ($\phi=10 \text{ mm}$) foam elements provide more resistance to compressive loading. To enable a direct comparison between the two foam element sizes, additional numerical simulations are conducted. To this end, two of the 3D segments from the $\phi=5 \text{ mm}$ APM elements are scaled in size by a factor of two (i.e., their diameter is increased to 10 mm). This scaling process does not change the geometry of the microstructure of the ‘small’ APM spheres. It can be observed that the force–displacement curves from the “scaled $\phi=5 \text{ mm}$ ” APM foam elements are different from the $\phi=10 \text{ mm}$ APM spheres. The “scaled $\phi=5 \text{ mm}$ ” curves exhibit a reduction in structural stiffness between displacements of 0.2 – 1.0 mm . The most likely explanation for this deviation is differences in the internal microstructure and outer particle shape between “scaled $\phi=5 \text{ mm}$ ” and 10 mm APM foam elements.

The structural stiffness, k of $\phi=5 \text{ mm}$ and $\phi=10 \text{ mm}$ APM foam elements is shown in Table 1. It can be seen from Fig. 5 that APM foam elements with different diameters exhibit different stiffnesses. The structural stiffness is the change in compression force divided by the difference in displacement, e.g., the slope of the dot-dashed line in Fig. 5b. For the $\phi=10 \text{ mm}$ APM foam elements, the displacement range between 0.2 mm and 1.0 mm was considered. Low displacements are disregarded in order to eliminate initial effects due to the establishment of contact between the foam element and contact plane. In the case of the $\phi=5 \text{ mm}$ APM foam elements, the selected range is 0.15 – 0.5 mm . The average structural stiffness of $\phi=10 \text{ mm}$ APM foam elements is 3.3 times higher in comparison to $\phi=5 \text{ mm}$ APM foam elements. In addition, the relative variability value was calculated by dividing the standard deviation of the structural stiffness by the corresponding average value. Comparing the relative variability of both diameters, it can be seen that the structural stiffness of the larger foam elements is more consistent. The variability of the stiffnesses is probably linked to the relative size of the pores with respect to the diameter of the foam elements. A study has been conducted in [21] to investigate the number of pores in one $\phi=5 \text{ mm}$ and one $\phi=10 \text{ mm}$ APM element with respect to their pore radius. It has been found that the number of pores per APM element for $\phi=5 \text{ mm}$ and $\phi=10 \text{ mm}$ is 4363 and $13,797$, respectively. Furthermore, the study conducted in [21] also counted the number of large pores in $\phi=5 \text{ mm}$ and $\phi=10 \text{ mm}$ APM foam elements. These largest pores in the APM (with radius of about 20% or larger of the foam elements’ diameter) are likely to strongly affect the mechanical properties of APM foam elements. Referring to the data reported in [21], there are more than 10 pores larger than 2 mm in radius for the $\phi=10 \text{ mm}$ APM foam element.

Table 1

Structural stiffness of $\phi=5 \text{ mm}$ and $\phi=10 \text{ mm}$ APM foam elements determined by the slope of their respective graphs.

APM sphere size (mm)	Effective stiffness, k (N/mm)				Simulations	
	Segment #1	Segment #2	Segment #3	Segment #4	Average	Relative variability
$\phi=5$	107.4	166.6	76.6	77.6	107.0	0.39
$\phi=10$	370.0	412.2	328.7	280.9	348.0	0.16

Furthermore, there are more than 120 pores larger than 1 mm in radius distributed in the $\varnothing=10$ mm APM sphere. It should also be noted that the largest pores (radius $\geq 20\%$ of the foam elements' diameters) shown in Figs. 1, 2, 6, 7 and 9 are non-homogeneously distributed compared to the more evenly distributed pores of size 1 mm in radius. Investigation done in [21] also found more than 10 pores (with a radius of about 20% or larger of the foam elements' diameter) in a $\varnothing=5$ mm APM sphere, but the number of pores with radius of about 10% of the foam elements' diameters is much lower (fewer than 20 pores). The higher number of more evenly distributed pores (pores with radius $\geq 10\%$ of the foam elements' diameters) in $\varnothing=10$ mm APM sphere results in more consistent results. On the other hand, a significant reduction of the number of pores with radius attaining more than 10% of the foam elements' diameters in a $\varnothing=5$ mm APM foam element has some effect in representing an adequate RVE and this resulted in inhomogeneity of the stiffnesses.

The scatter of the structural stiffness for $\varnothing=5$ mm APM sphere was also possibly caused by the irregular outer shape of the simulated segments. Comparing all the segments from $\varnothing=5$ mm to $\varnothing=10$ mm APM foam elements, the outer shape of $\varnothing=10$ mm APM segments is closer to a perfect sphere. In contrast, the smaller

APM foam elements exhibit a more irregular outer shape potentially causing scatter of their mechanical properties.

An additional numerical simulation was conducted to investigate the effect of the skin on the APM foam sample. To this end, the skin has been virtually removed from segment #2 of the $\varnothing=10$ mm APM foam sphere. This reduced the sphere volume by 13%. The structural stiffness of both APM foam elements with and without skin was then calculated. The results of 412.2 N/mm for the original sphere and 290 N/mm for the sphere without the skin reveal that a significant reduction of structural stiffness has occurred. The structural stiffness of the sphere without the skin is reduced by a factor of 1.4 compared to the original APM sphere elements. The skin thickness is more for diameter 5 mm APM foam elements compared to the diameter 10 mm APM foam element.

Fig. 6 shows the distribution of equivalent plastic strain for quasi-static loading for segment #1 of $\varnothing=5$ mm and $\varnothing=10$ mm diameter APM foam spheres. The maximum displacement applied is limited to 10% of the sample height. This displacement was chosen in order to achieve an adequate calculation time. Thus, for the APM foam element with $\varnothing=5$ mm and $\varnothing=10$ mm, the applied displacement is 0.25 mm and 0.5 mm, respectively. It can be observed that the upper part of the foam element is flattened by the simulated compressive plate. This is more likely due to minimum cross section. A similar observation has been reported by Stobener et al. [39] who conducted an experimental compression test of $\varnothing=10$ mm APM foam elements. Fig. 6 further shows that plastic deformation is not uniformly distributed over the complete foam element but occurs predominantly in proximity of the contact area. Vesenjaj et al. [11] studied the propagation of the plastic yielding within the APM foam element using infrared measurements. They too observed that the yielding originates from the contact area between the APM foam and the rigid support and spreads in a shear band with an angle of 45° towards the lower part of the foam element. Fig. 6 clearly supports this observation and demonstrates that plasticisation is not limited to the immediate surface area. A line with a distance of 2.5 mm from the initial contact point is drawn in Fig. 6a and b. It can be seen that independent of the foam element size a similar depth is affected by high levels of plastic deformation at the same macroscopic deformation of $u=0.25$ mm. However, in the case of the larger foam elements the affected volume is larger.

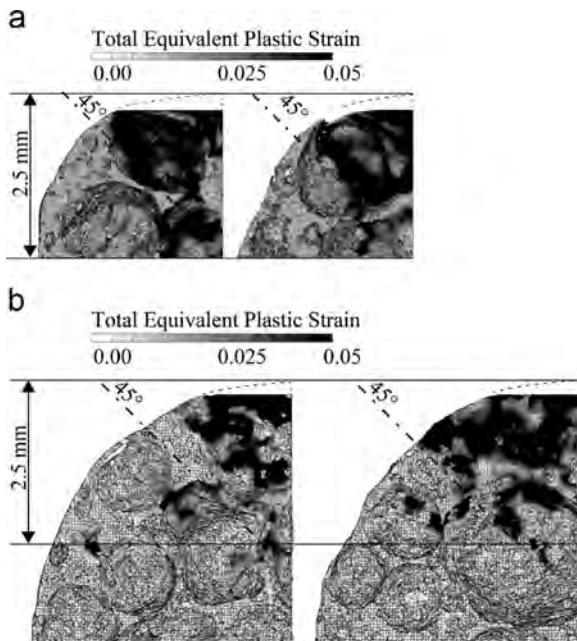


Fig. 6. Distribution of total equivalent plastic strain for macroscopic deformation of $u=0.25$ mm: (a) APM foam element with $\varnothing=5$ mm, and (b) APM foam element with $\varnothing=10$ mm (contours represent the total equivalent plastic strain).

4.1. Internal deformation analysis

The internal deformation characteristics of APM foam elements under quasi-static loading are elaborated here. Localised concentrations of equivalent plastic strain are shown in Fig. 7. The distribution of plastic strain validates the shear band premise made earlier in this section. During compression, a shear cone

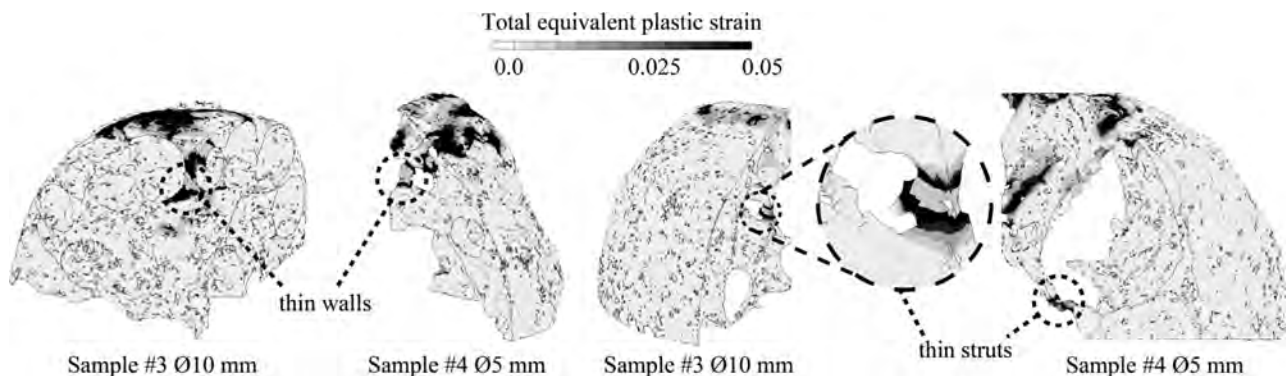


Fig. 7. Common features of internal distortion under compressive load.

with an angle of 45° (generated by revolving the 45° line about the vertical axis in Fig. 6) with respect to the loading axis was formed. Whenever features like thin walls and thin struts are located within the shear cone, they will be among the first to experience high levels of plastic deformation. In addition, high levels of plasticity occur near the contact area of the external load. In quasi-static analysis, this phenomenon is caused by the high contact stresses (contact force divided by contact area) due to the small initial contact area of the sphere. However, in dynamic analysis the flattening of the top part of the model is (regardless to the loading velocity) a result of the distribution of cross sectional areas in sphere-like bodies. Such behaviour is different from the uni-axial compression observed in hexahedral shape cellular material (e.g., Alporas[®]), wherein the incremental deformation maps show collapse bands originating from neighbouring previous bands [40].

Next, the dynamic behaviour of APM foam elements is considered. The time step increment in these direct finite element simulations is based on the size of the shortest finite element edge, i.e., 0.0093 mm for $\varnothing=5$ mm foam and 0.0109 mm for

$\varnothing=10$ mm foam. These small lengths put extreme demands on computational time. As a result, dynamic analyses were limited to $\varnothing=10$ mm foam elements. Fig. 8 shows the dynamic force–displacement response of $\varnothing=10$ mm APM foam elements. Numerical simulations of APM foam elements were conducted at a macroscopic strain rate of 100 s^{-1} and are denoted by thin continuous lines. Their average value is represented by a thick continuous line. In addition, experimental data taken from [11] are shown. The thick dotted line shows the results of experimental testing with a macroscopic strain rate of 20 s^{-1} . For comparison, results of quasi-static testing are plotted as a dashed line. The compressive response of APM foam elements shows the typical behaviour of porous materials. Following the initial elastic response one can observe the onset of an elastic–plastic transition zone that is then manifested as a plateau followed by the final densification [41]. The averaged numerical results are in good agreement with the experimental measurements. The numerical results correspond to a compressive strain rate 100 s^{-1} . In contrast, experimental results were obtained at lower strain rates (i.e., 20 s^{-1}) and quasi-static conditions. Numerical tests had to be performed at the higher strain rate since a transition to 20 s^{-1} would have caused unreasonably long calculation times. As a result, the numerical results exhibit an increased plateau stress and slightly decreased densification strain. Furthermore, it can be observed that the stiffness of the structure increases at high loading rates.

Fig. 9 shows the distribution of total equivalent plastic strain in the $\varnothing=10$ mm APM foam element at different displacement increments. As already observed in experiments and quasi-static numerical results, the local deformation originates at the contact between the APM foam element and the loading/support plate due to the lowest load bearing cross section of the spherical-shaped object. Again we can note that the propagation of the plastic strain spreads in a shear band towards the centre of the foam element in agreement with previous observations [11]. The numerical investigations conducted within this paper only focus on a single APM sphere rather than on a more complex structure made up of

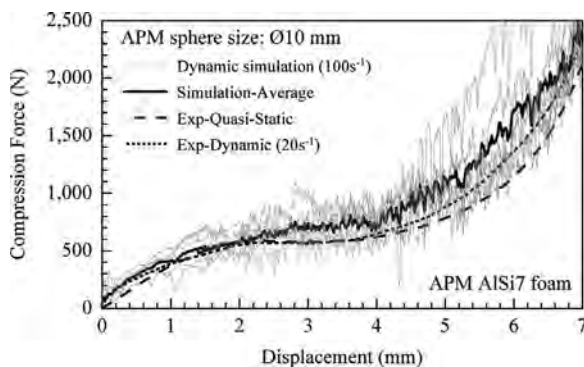


Fig. 8. Numerical simulations and experimental results for $\varnothing=10$ mm APM foam element.

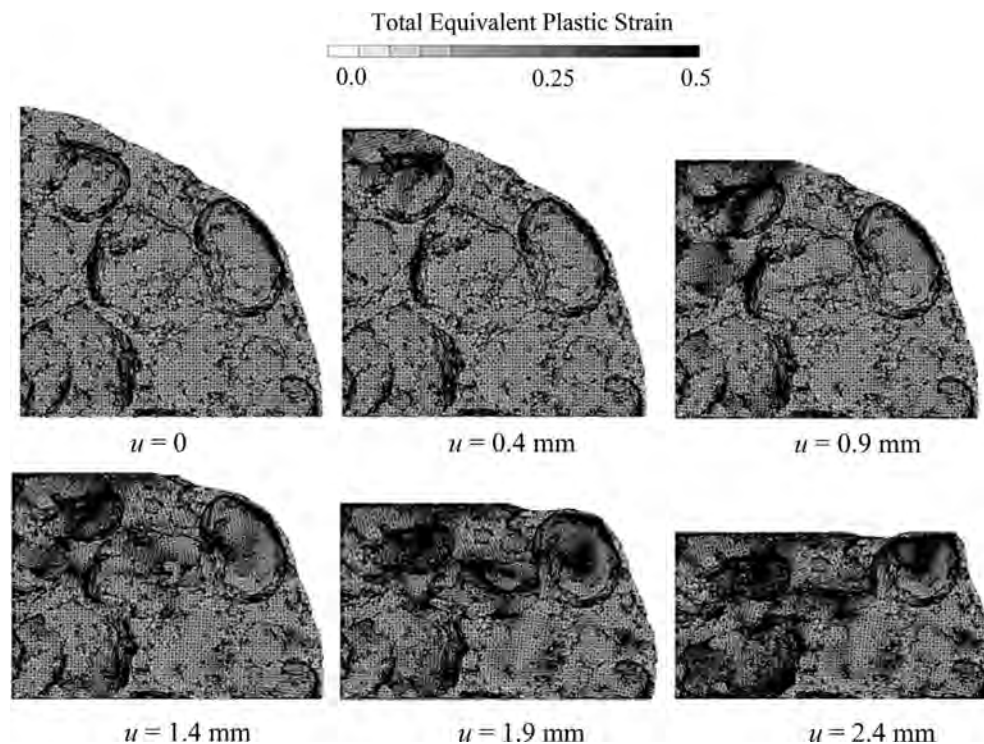


Fig. 9. Distribution of total equivalent plastic strain for the $\varnothing=10$ mm APM foam element with contours (contours represent total equivalent plastic strain).

several APM spheres. Assuming that one APM sphere can be considered as a representative volumetric element (RVE) of a structure formed by these elements, the findings presented in this work can to some extent be used to predict the mechanical properties of this material.

5. Conclusions

This paper has addressed the compressive properties of spherical APM foam elements. Two different sphere sizes, i.e., $\varnothing = 5$ mm and $\varnothing = 10$ mm were investigated. Numerical finite element analyses were conducted for quasi-static and dynamic loading. To account for the complex interior foam geometry, calculation models were directly derived from micro-computed tomography data. Results were compared with experimental measurements conducted on similar samples. Good agreement was found. Single APM foam elements demonstrated typical cellular material behaviour, i.e., an extended stress plateau followed by densification at high macroscopic strains. Numerical analyses of the APM meso-structure showed that plastic deformation does not occur uniformly but is concentrated in a relatively small sub-volume. This deformation is not limited to the surface of the spherical element but continues within the interior foam structure. More specifically, plasticity originates from the contact area of pressure stamp and sphere and propagates in a 45° shear cone towards the interior of the samples. As expected, larger APM foam elements were able to support higher compressive loads, i.e., $\varnothing = 10$ mm APM foam elements exhibit a 3.3 times higher structural stiffness. The investigation on the skin effect shows that the skin significantly contributes to the mechanical strength of APM foam elements. The single APM foam elements with removed skin have a reduction in structural stiffness by a factor of 1.4 from the original APM foam counterpart. Internal microstructure deformation analysis reveals that weak structures like thin walls and thin struts within the 45° shear cone are likely to experience high levels of plastic deformation. Finally, dynamic compression simulation indicates an increase of stiffness and plateau stress with increasing macroscopic strain rate.

References

- [1] M.F. Ashby, A. Evans, N.A. Fleck, L.J. Gibson, J.W. Hutchinson, H.N.G. Wadley, *Metal Foams: A Design Guide*, Butterworth-Heinemann, Burlington, MA 01803, USA, 2000.
- [2] T. Fiedler, C. Veyhl, I.V. Belova, M. Tane, H. Nakajima, T. Bernthaler, et al., *Adv. Eng. Mater.* 14 (2011) 144–152.
- [3] I.V. Belova, C. Veyhl, T. Fiedler, G.E. Murch, *Scr. Mater.* 65 (2011) 436–439.
- [4] M. Vesenjak, T. Fiedler, Z. Ren, A. Öchsner, *Adv. Eng. Mater.* 10 (2008) 185–191.
- [5] A. Markaki, T. Clyne, *Acta Mater.* 49 (2001) 1677–1686.
- [6] K. Stobener, D. Lehmhus, N. Zimmer, J. Baumeister, German Patent, 2005.
- [7] J. Baumeister, *Verfahren zur Herstellung poröser Metallkörper*, German Patent, 1990.
- [8] D. Lehmhus, J. Baumeister, L. Stutz, E. Schneider, K. Stobener, M. Avasse, et al., *Adv. Eng. Mater.* 12 (2009) 596–603.
- [9] M. Vesenjak, F. Gačnik, L. Krstulović-Opara, Z. Ren, *J. Compos. Mater.* 45 (2011) 2823–2831.
- [10] J. Hohe, V. Hardenacke, Y. Fascio, Y. Girard, J. Baumeister, K. Stobener, et al., *Mater. Des.* 39 (2012) 20–32.
- [11] M. Vesenjak, F. Gačnik, L. Krstulović-Opara, Z. Ren, *Mech. Adv. Mater. Struct.* (2014), <http://dx.doi.org/10.1080/15376494.2012.736059>.
- [12] K. Stobener, G. Rausch, *J. Mater. Sci.* 44 (2009) 1506–1511.
- [13] Fraunhofer IFAM, *Advanced Pore Morphology (APM) Metal Foams*, Fraunhofer IFAM, Bremen, Germany, 2007.
- [14] K. Stobener, J. Baumeister, G. Rausch, *Met. Powder Rep.* 60 (2005) 12–16.
- [15] C. Veyhl, I. Belova, G. Murch, T. Fiedler, *Mater. Sci. Eng.: A* 528 (2011) 4550–4555.
- [16] C. Veyhl, I.V. Belova, G.E. Murch, A. Öchsner, T. Fiedler, *Finite Elem. Anal. Des.* 46 (2010) 371–378.
- [17] C. Veyhl, T. Fiedler, T. Herzig, A. Öchsner, T. Bernthaler, I. Belova, et al., *Metals* 2 (2012) 113–121.
- [18] S.R. Stock, *MicroComputed Tomography: Methodology and Applications*, CRC Press, Boca Raton, FL, 2008.
- [19] C. Veyhl, T. Fiedler, O. Andersen, J. Meinert, T. Bernthaler, I.V. Belova, et al., *Int. J. Heat Mass Transf.* 55 (2012) 2440–2448.
- [20] M. Vesenjak, C. Veyhl, T. Fiedler, *Mater. Sci. Eng.: A* 541 (2012) 105–109.
- [21] M. Vesenjak, M. Borovinšek, T. Fiedler, Y. Higa, Z. Ren, *Mater. Lett.* 110 (2013) 201–203.
- [22] J. Dagner, J. Friedrich, G. Müller, *Comput. Mater. Sci.* 43 (2008) 872–885.
- [23] C. Kai, G.K. Jacob, T. Mei, *Int. J. Adv. Manuf. Technol.* 13 (1997) 566–570.
- [24] M. Vesenjak, Z. Ren, T. Fiedler, A. Öchsner, *J. Compos. Mater.* 43 (2009) 2491–2505.
- [25] V.S. Deshpande, N.A. Fleck, *Int. J. Impact Eng.* 24 (2000) 277–298.
- [26] M. Vesenjak, C. Veyhl, T. Fiedler, *Mater. Sci. Eng. A* 541 (2012) 105–109.
- [27] P.J. Tan, S.R. Reid, J.J. Harrigan, Z. Zou, S. Li, *J. Mech. Phys. Solids* 53 (2005) 2174–2205.
- [28] X.Y. Su, T.X. Yu, S.R. Reid, *Int. J. Impact Eng.* 16 (1995) 673–689.
- [29] P.J. Tan, S.R. Reid, J.J. Harrigan, Z. Zou, S. Li, *J. Mech. Phys. Solids* 53 (2005) 2206–2230.
- [30] Z. Xue, A. Vaziri, J.W. Hutchinson, *Comput. Model. Eng. Appl. Sci.* 10 (2005) 79–95.
- [31] A. Ohrndorf, P. Schmidt, U. Krupp, H.J. Christ, *Mechanische Untersuchungen eines geschlossenporigen Aluminiumschaums*, in: *Werkstoffprüfung 2000*, Bad Nauheim, 2000.
- [32] K.A. Dannemann, J. Lankford, *Mater. Sci. Eng. A* 293 (2000) 157–164.
- [33] M. Vesenjak, Z. Ren, A. Öchsner, *Int. J. Mater. Eng. Innov.* 1 (2009) 175–196.
- [34] M. Vesenjak, A. Öchsner, Z. Ren, *Mater. Lett.* 62 (2008) 3250–3253.
- [35] S.R. Bodner, P.S. Symonds, *J. Appl. Mech.* 29 (1962) 719–728.
- [36] P. Jacob, L. Goulding, *An Explicit Finite Element Primer*, NAFEMS, Glasgow, 2002.
- [37] J. Hallquist, *LS-DYNA Keyword User's Manual*, Livermore Software Technology Corporation, Livermore, California, 2007.
- [38] R. Ramsdale, *Mechanical Engineering Handbook*. Available from: <http://www.engineershandbook.com>.
- [39] K. Stobener, D. Lehmhus, M. Avasse, L. Peroni, M. Busse, *Int. J. Solids Struct.* 45 (2008) 5627–5641.
- [40] A. Bastawros, H. Bart-Smith, A. Evans, *J. Mech. Phys. Solids* 48 (2000) 301–322.
- [41] M. Vesenjak, L. Krstulović-Opara, Z. Ren, A. Öchsner, Ž. Domazet, *Exp. Mech.* 49 (2009) 501–509.

Chapter 7

Dynamic compression of aluminium foam derived from infiltration casting of salt dough

Building on Chapter 6, the present Chapter extends the analysis of the *dynamic* compressive properties of metallic foam. In this Chapter, Corevo[®] aluminium foam is considered. This metallic foam has been previously discussed in Chapter 3 but limited to quasi-static loading. Now, the investigation covers compressive properties of the samples under dynamic loading conditions. Quasi-static and dynamic loading primarily differs in terms of speed and inertia effects.

This is the first attempt to study the influence of strain rate sensitivity on Corevo[®] aluminium foam. Experimental and numerical analysis are carried out in order to determine the compressive stress-strain response, effective material properties and deformation mechanisms. Foam samples are manufactured by combining ASG06 aluminum alloy with salt dough that introduces 70-80% porosity. Impact compression loading is applied with a range of strain rates. A μ CT imaging approach is adopted to build a computational model and ensures the geometrical accuracy of the complex structure. The effective mechanical properties are analysed from the stress-strain results obtained from both the experiment and numerical tests. Furthermore, the deformation mechanism was thoroughly investigated by making use of IR thermograph technology and data from numerical simulation.

In summary, impact loading on Corevo[®] foam reveals a deformation behaviour that is different from quasi-static loading markedly in terms of major plasticity concentration areas. Due to inertia, dynamic loading tends to concentrate plasticity towards the surface in contact with the moving pressure stamp. In contrast, quasi-static loading is characterised by randomly distributed plastic deformation throughout the entire sample.

Results reported in this Chapter give an important insight in the dynamic mechanical properties of cellular metals derived from infiltration casting and their strain rate sensitivity. This crucial information is needed before aluminium foam can be used in applications such as automotive impact absorbers.

This has been published online and accepted for print publication by the journal of Mechanics of Materials.

M Vesenjak, MA Sulong, L Krstulović-Opara, V Mathier, T Fiedler, “Dynamic compression of aluminium foam derived from infiltration casting of salt dough.” *Mechanics of Materials* (2015).

Accepted Manuscript

Dynamic compression of aluminium foam derived from infiltration casting of salt dough

Matej Vesenjak , Mohd Ayub Sulong , Lovre Krstulović-Opara ,
Matej Borovinšek , Vincent Mathier , Thomas Fiedler

PII: S0167-6636(15)00221-5
DOI: [10.1016/j.mechmat.2015.10.012](https://doi.org/10.1016/j.mechmat.2015.10.012)
Reference: MECMAT 2497



To appear in: *Mechanics of Materials*

Received date: 15 January 2015
Revised date: 16 July 2015
Accepted date: 16 October 2015

Please cite this article as: Matej Vesenjak , Mohd Ayub Sulong , Lovre Krstulović-Opara ,
Matej Borovinšek , Vincent Mathier , Thomas Fiedler , Dynamic compression of aluminium
foam derived from infiltration casting of salt dough, *Mechanics of Materials* (2015), doi:
[10.1016/j.mechmat.2015.10.012](https://doi.org/10.1016/j.mechmat.2015.10.012)

This is a PDF file of an unedited manuscript that has been accepted for publication. As a service to our customers we are providing this early version of the manuscript. The manuscript will undergo copyediting, typesetting, and review of the resulting proof before it is published in its final form. Please note that during the production process errors may be discovered which could affect the content, and all legal disclaimers that apply to the journal pertain.

Highlights

- First dynamic mechanical characterisation of infiltration-cast aluminium foam.
- Properties and deformation mechanisms observed by experiments and FE analyses.
- Numerical finite element analyses were based on micro-computed tomography.
- Numerical results and infrared imaging indicate layer-wise collapse.
- Insight in the micro-deformation behaviour and anisotropy has been provided.

Dynamic compression of aluminium foam derived from infiltration casting of salt dough

Matej Vesenjak¹, Mohd Ayub Sulong², Lovre Krstulović-Opara³,
Matej Borovinšek¹, Vincent Mathier⁴, Thomas Fiedler²

¹ Faculty of Mechanical Engineering, University of Maribor, Maribor, Slovenia

² School of Engineering, The University of Newcastle, Callaghan, Australia

³ Faculty of Electrical Eng., Mech. Eng. and Naval Arch., University of Split, Split, Croatia

⁴ Constellium Innovation Cells, EPFL Quartier de l'Innovation E, Lausanne, Switzerland

Corresponding author: Matej Vesenjak, e-mail: matej.vesenjak@um.si,
phone: +386 2 220 7717, fax: +386 2 220 7994

Abstract:

This paper addresses the dynamic mechanical characterisation of infiltration-cast aluminium foam. The material is produced by combining melt aluminium with salt precursors which are removed after solidification. The resulting aluminium foam allows controlled energy absorption and hence is of high interest for impact engineering applications at high strain rates. In this study, experimental and numerical analyses are combined to quantify its effective material properties and investigate relevant deformation mechanisms. First, uniaxial compression tests are conducted for both quasi-static and dynamic loading velocities. The comparison of the test results permits a direct evaluation of property changes due to the loading velocity. Under dynamic loading conditions, infrared imaging enables the localisation of concentrated plastification and provides important insight into the dominant deformation mechanism. Additional numerical finite element analyses were based on micro-computed tomography imaging of actual samples to accurately capture the complex foam geometry. Whenever possible, numerical findings were verified by comparison with experimental data. Both numerical results and infrared imaging indicate layer-wise collapse as the main deformation mode. Furthermore, the numerical results provide insight in the micro-deformation behaviour of analysed foam and allow additional evaluation of the strain rate sensitivity and the anisotropy of mechanical properties.

Keywords: aluminium foam, salt dough infiltration casting, Corevo, compressive tests, infrared thermography, micro computed tomography, finite element method, mechanical properties

1 Introduction

Cellular metals are formed by a metallic matrix containing multiple voids usually called pores. The internal porosity allows the design of lightweight materials with unique properties. First, cellular metals have versatile thermal properties that enable their use as compact heat exchangers [1, 2] or for thermal conductivity enhancement [3]. Furthermore, they are used for structural damping [4, 5] and as core materials in sandwich panels [6, 7]. However, their most remarkable feature is the orderly collapse of pores under compressive loading. This allows the controlled conversion of impact energy in plastic deformation whilst the material compresses up to very high strains [8-10]. The result is a material that safely absorbs energy and simultaneously limits deceleration under impact conditions. Hence, the dynamic properties of cellular metals are of particular interest for a wide range of applications in impact protection. Examples include road safety barrier systems [11], battery housings in electric vehicles [12] or motorcycle helmets [13]. The current paper investigates the dynamic properties of aluminium foam derived by a low cost process from infiltration casting of salt dough (Corevo) using combined experimental and numerical analyses.

The mechanical properties of most cellular metals are known to be affected by strain rate. The main causes are strain rate sensitivity of the base material (the micro-inertial effect and the material strain-rate sensitivity) [8, 14, 15], entrapment of a filler (solid or gas) [16-20] and change of deformation mode from uniform deformation (quasi-static) to shockwave propagation [10, 21, 22]. Impact is often categorized relative to the velocity of sound as high and low velocity. Lopatnikov et al. [23] used analytical and numerical analysis to describe energy absorption of metal foams in plane-strain plate impact conditions for various velocity regimes. Low velocity impact on metal foam sandwich beams was considered in [24]. Again, analytical and experimental analysis was conducted. For an indentation body of finite dimensions local denting was found to distinctly decrease the load-carrying capacity. Unfortunately, none of the aforementioned studies used experimental testing for the verification of the results. A study by Rajaneesh et al. [25] combined experimental and numerical analysis to study the low velocity impact on foam cored (Alporas) sandwich panels. Energy absorption behaviour was found to depend both on core thickness and the type of faceplates. The results suggest using a strain based failure criterion for the foam core instead of the more widely used stress limit.

A previous study addressed the mechanical properties of Corevo aluminium foam with an average pore size of 1.9 mm under quasi-static loading conditions [26]. Combined numerical and experimental analysis indicated an offset yield stress exceeding 11 MPa and weak elastic

anisotropy. Plastic deformation was found to concentrate within thin struts parallel to the macroscopic loading direction. This study was extended in [27] where the additional larger pore size 5.6 mm was investigated, although still under quasi-static loading conditions. The results showed a distinct (up to 30%) decrease of the offset yield stress for the larger pore size.

The current study analyses for the first time Corevo aluminium foam (pore size approx. 3 mm) under dynamic loading. To this end, experimental compression testing is conducted for both quasi-static and dynamic loading conditions. During testing, infra-red (IR) thermography is used to observe the evolution of sample surface temperature. Temperature increase can be attributed to high levels of plastic deformation. In addition, numerical analyses are conducted to better understand the dominant deformation mechanism, strain rate sensitivity and material anisotropy. In order to accurately capture the complex network formed by aluminium struts micro-computed tomography (μ CT) scans of actual samples were converted into numerical calculation models. Accordingly, virtual compression tests of these models allowed the identification of plasticity concentrations, deformation bands and strut failure throughout the complete sample volume. Numerical findings are verified by comparison with macroscopic stress-strain data and IR thermographies of the experiment.

2 Sample preparation

The Corevo foam is manufactured by a replication process based on salt dough as a spacer material [28]. Salt dough pellets are manufactured with sizes ranging from 2 to 10mm (dictating the final pore size of the foam) and compressed into a preform (the compression step dictates the final foam porosity ranging from 70% to 80%). Aluminium is then infiltrated inside the preform by a low pressure die casting process. After this step, the salt is rinsed away to obtain the final foam. This process is quite versatile, allowing for foam parts with various shapes and sizes as well as the integration (one shot during casting or by integration of external elements at the preform stage) of dense metal parts.

In this study, the Corevo foam structure has cylindrical pores with $d = 2.8$ mm in diameter and $l = 3$ mm in height (Fig. 1). The aluminium alloy A357 (Al / 7% Si / 0.6% Mg) has been used as the base material in the as-cast state and occupies a fraction of 25%vol. Twenty samples of 30×30×30 mm have been cut from a single block by classical sawing and milling with physical properties given in Table 1.

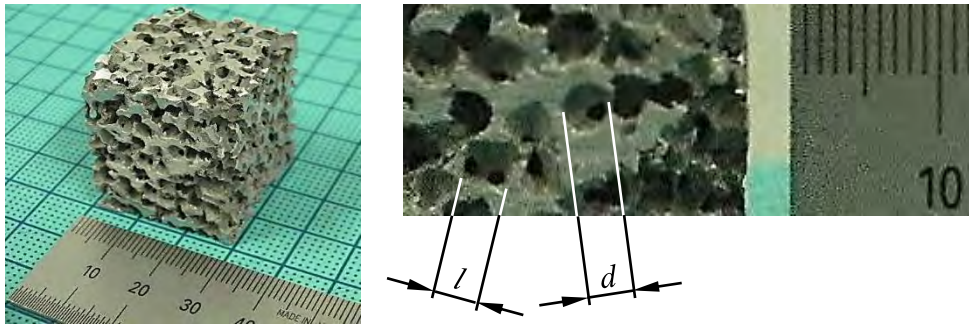


Figure 1. Testing sample

Table 1. Physical properties of tested samples

No.	Mass	Density	No.	Mass	Density
[-]	[g]	[g/dm ³]	[-]	[g]	[g/dm ³]
#E1	17.01	630.0	#E11	18.00	666.7
#E2	17.64	653.3	#E12	18.41	681.9
#E3	21.97	813.7	#E13	19.93	738.2
#E4	22.79	844.1	#E14	19.40	718.5
#E5	18.83	697.4	#E15	18.53	686.3
#E6	19.08	706.7	#E16	20.08	743.7
#E7	18.00	666.7	#E17	18.91	700.4
#E8	19.44	720.0	#E18	19.14	708.9
#E9	18.50	685.2	#E19	19.31	715.2
#E10	19.83	734.4	#E20	18.49	684.8

3 Methods

3.1 Experimental testing of Corevo specimens

The experimental testing consisted of quasi-static and dynamic compressive loading of Corevo specimens. For that purpose the servo-hydraulic testing machine INSTRON 8801 has been used according to the standard ISO 13314: 2011 [29, 30]. The experiments were monitored with two digital video cameras, both supporting recording at 100 frames per second, and an IR thermal camera. The specimens have been subjected to quasi-static loading velocity of 0.1 mm/s (specimens #E1-#E10) and dynamic loading velocity of 284 mm/s (specimens #E11-#E20). The dynamic loading resulted in a macroscopic engineering strain rate of approx. 10 s^{-1} . The testing machine support plates were lubricated with the graphite based silicone grease to minimize the friction between the specimens and the support plates.

During the tests the force and cross-head displacement have been recorded to evaluate the engineering mechanical properties. The engineering values for result evaluation were determined according to the initial geometry of the specimens. The engineering strain has been determined as the cross-head displacement divided by the initial specimen's height ($h = 30$ mm), while the engineering stress has been determined as the experimentally measured force divided by initial specimen's cross-section ($A_0 = 900$ mm²).

3.2 *IR thermography*

During dynamic compressive testing the specimens (#E11-#E20) were also monitored by IR thermography [31] using the high speed cooled middle-wave IR thermal camera Flir SC 5000 at 314 frames per second. The capture of thermal images is based on an InSb detector operating at cryogenic temperatures of -200 °C. Thermal imaging at high frame rates allows acquisition of noise free thermal images indirectly visualising irreversible deformation and its front waves, plastification slide lines, failure mechanisms, crack propagation and fracture process [32] during the mechanical loading. This method has been already proved as a reliable tool in case of several porous materials types, e.g. open-cell aluminium foams with and without silicone foam filler [29], advanced pore morphology (APM) foam elements [33], aluminium tubes filled with close-cell aluminium alloy foam [7, 34] and expanded perlite/aluminium syntactic foam [19]. In our recent research it has been also proven that the thermal images are equivalent to the strain field on the specimen's surface where IR method has been compared to three-dimensional (3D) optical Digital Image Correlation (DIC) method (e.g. ARAMIS system) [35, 36]. As the DIC is limited to the speed of charge-coupled device (CCD) cameras (frame rates up to 700 Hz) and the light source, this makes the IR approach one of the most effective methods capable of visualising plastic deformations at higher strain rates which is the case in this study. Quasi-static tests (specimens #E1-#E10) were not evaluated with IR thermography due to the rapid heat conduction in aluminium alloy that prevents clear thermal images.

3.3 *Computational models and numerical simulations*

The irregular and complex 3D geometry of the fabricated Corevo foam specimens has been taken into account by using μ CT imaging. This has already proven to be an efficient tool for geometrical characterisation [37, 38] and preparation of computational models of other porous materials like Alporas® [39], M-Pore® [8, 40], APM foam [41, 42], sintered metallic fibre

structures [43] and expanded perlite/aluminium syntactic foam [19]. The results of μ CT imaging of the Corevo samples are grey level image stacks with a voxel length of 51.92 μm . In the first step, these voxels are segmented into metallic phase and pores of the cellular structure. The segmentation threshold is iteratively calibrated until the mass of the virtual model coincides with the scanned sample. The segmented data is then converted into a closed triangulated STL surface mesh which bounds the solid volume of the structure. In the final meshing step, these surface meshes are transformed into volume meshes using the automated meshing algorithm of the Harpoon software. To achieve realistic calculation times the size of the computational model was truncated to approx. $15 \times 15 \times 15$ mm. Geometrical convergence of the numerical model requires a sufficient number of finite elements to accurately represent the complex foam geometry. Furthermore, the calculation models must contain a sufficient number of integration points to accurately capture the calculated displacement field. To ensure both geometrical and numerical convergence a preliminary study was conducted for sample #C1. To this end, six meshes containing 660k, 671k, 965, 1036k, 1187k and 1267k elements were generated. The volume deviation with respect to the segmented voxel data is less than 0.1% for all meshes and thus considered acceptable for geometrical convergence. For the numerical convergence analysis Young's modulus and the offset yield stress were determined. The medium sized mesh containing 1036k elements showed good convergence for both material parameters ($\leq 4.3\%$ deviation with respect to the highest mesh density). Accordingly, meshes with approx. 1 million fully integrated tetrahedron elements have been chosen for subsequent simulations (Table 2). It should be mentioned here that the element number in the mesh #C2 is slightly lower due to the decreased density of the sample.

Table 2. Properties of computational models

Model number	Density [g/dm ³]	Number of FE [-]
#C1	730.4	1.036.476
#C2	650.5	935.785

The mechanical properties of the base material (aluminium alloy A357) have been determined by quasi-static and dynamic experimental tensile tests on solid aluminium alloy samples according to ISO 6892-1:2010 [44].

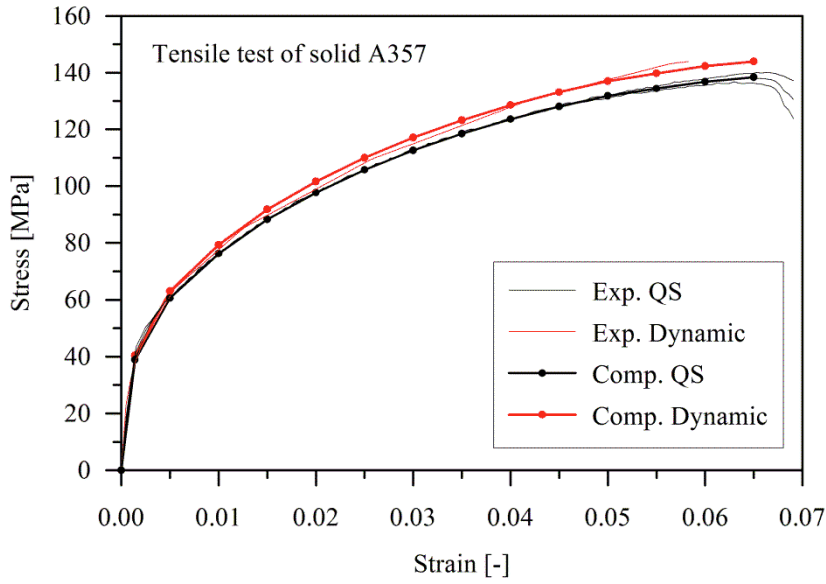


Figure 2. Stress-strain data of the base material

From these tests the stress-strain data (Fig. 2) have been used as an input for the material model in numerical simulations. A piece-wise linear elastic-plastic constitutive model accounting for strain rate sensitivity and failure has been chosen in this respect [45]. When the plastic strain in a finite element develops and exceeds the prescribed failure plastic strain (set according to the measurements given in Fig. 2), the finite element is effectively removed from the finite element model. Since fully integrated quadratic finite elements were used, the average plastic strain was considered as a failure measure, which was computed from the plastic strain in integration points [45]. The material rate-dependence is usually taken into account with straightforward incorporation into the constitutive material model [46]. For this purpose the base material strain rate sensitivity was introduced using the Cowper-Symonds constitutive model:

$$\sigma = \sigma_{stat} \cdot \left[1 + \left(\frac{\dot{\epsilon}}{C} \right)^{1/p} \right], \quad (1)$$

where σ corresponds to the stress at the strain rate $\dot{\epsilon}$ and σ_{stat} is the quasi-static response. The strain rate sensitivity parameters of the aluminium alloy are $C = 3818 \text{ s}^{-1}$ and $p = 1.723$ [47-49]. The boundary conditions of the finite element analysis combine displacement controlled loading and a fixed planar rigid wall at the opposite specimen's surface simulating uniaxial compressive loading (Fig. 3). The strain rate sensitivity of the Corevo foam has been

determined based on three constant loading velocities 0.3, 3 and 30 m/s, resulting in macroscopic engineering strain rates of 10, 100 and 1000 s⁻¹, respectively. Additionally, the computational simulations allowed to precisely study the anisotropy of Corevo foams. To this end, the computational models have been subjected to the compressive loading in three orthogonal directions (in x , y and z axis). All nodes of the foam models were included in an automatic single surface contact accounting for friction (friction coefficient of 0.5). From the forces recorded at the rigid support plane and the displacements of the loading plane, the engineering stress-strain data of the foam models have been evaluated.

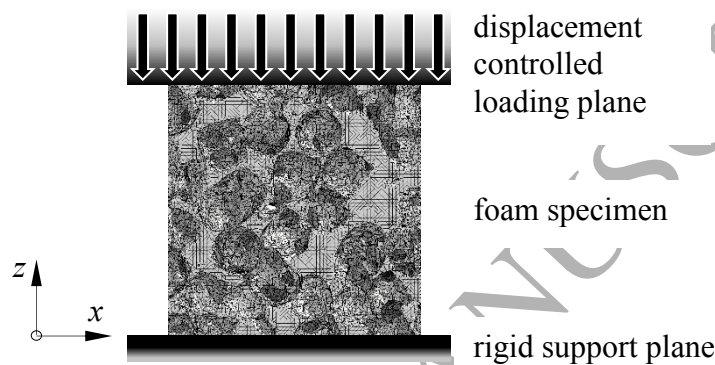


Figure 3. Boundary conditions.

The computational model has been analysed using the commercial engineering software LS-DYNA MPP R7 (single precision) based on the explicit integration scheme [45, 48]. With the sensitivity analysis of the time discretization it was confirmed that the time step of 10⁻⁹ s provides stable convergence. Computational analyses have been performed using the HP ProLiant DL380p cluster with Intel Xeon E5-2670 processors and 128 GB of RAM per processor. From 32 to 64 processor cores have been used per simulation, resulting in computational times from 50 up to 200 (for lower velocity loading cases) wall-clock hours.

4 Results and discussion

4.1 Experimental results

The characteristic compressive behaviour of Corevo specimens under quasi-static and dynamic (strain rate 10 s⁻¹) loading conditions is represented in Fig. 4. By visual observation of the specimens during experimental testing the deformation mechanisms have been studied. The specimens subjected to quasi-static loading (Fig. 4a) experienced already at lower strains (< 10%) deformation bands which are in most cases parallel to the loading/support plates

indicating a layer-wise collapse mechanism, typical for regular [20, 50, 51] but also for irregular foams with random topology [19, 52]. Due to the randomly distributed weak regions inclined deformation bands can be observed. The individually initiated collapse bands propagate further with the strain increase and eventually merge in one large horizontal deformation band (area marked with black colour) until a complete densification is being reached. The images showing the deformation during the dynamic loading (Fig. 4b) exhibit some motion blurring due to the high loading velocity (recording with 100 frames per second was not sufficient). Nevertheless, the main deformation mechanism can still be observed. The images show that parallel (horizontal) and inclined deformation bands are being formed. This indicates that the loading velocity (corresponding to a strain rate of 10 s^{-1}) is insufficient to change the deformation mechanism in the observed porous structure. As observed in case of quasi-static loading, single deformation bands are being joined at larger strains in one large collapse band.

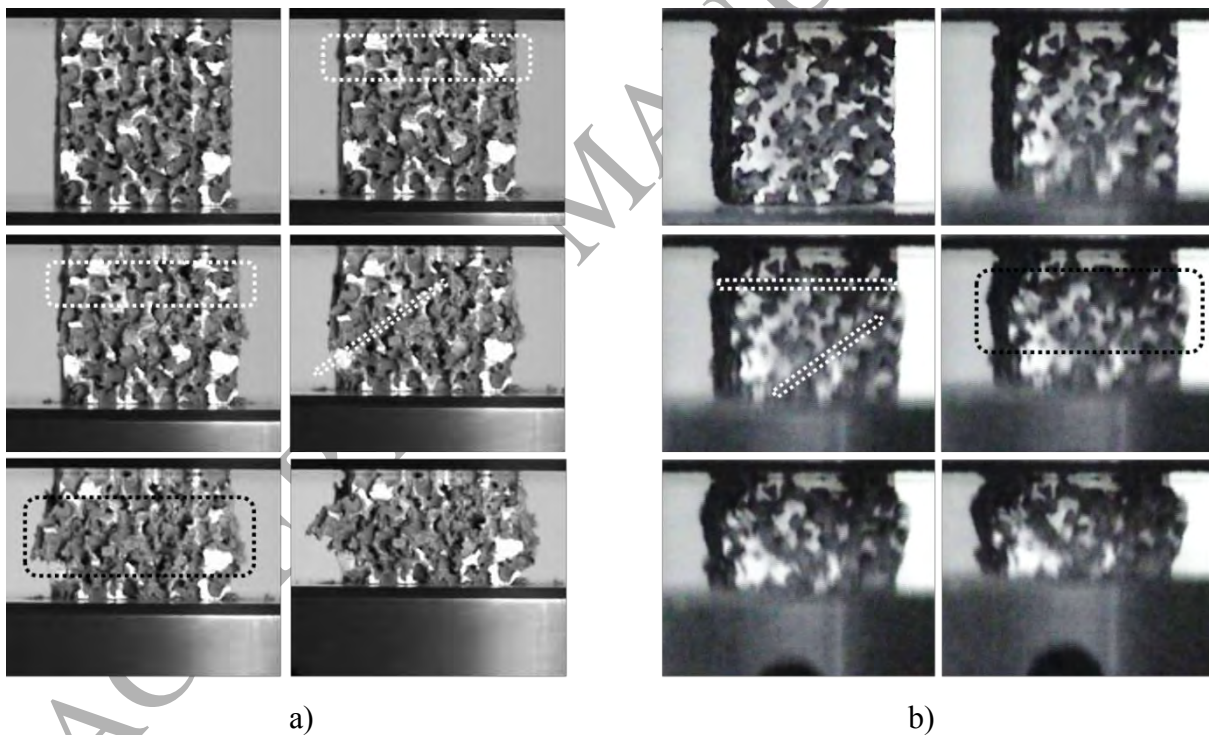


Figure 4. Compressive behaviour of Corevo specimens subjected to quasi-static (a) and dynamic (b) loading (strain increment $\Delta\epsilon \approx 10\%$)

In order to study the deformation mechanics and plastic deformation of base material in more detail IR thermography has been employed during dynamic tests (in case of quasi-static loading the generated heat indicating the plastification zones is dissipated too quickly to

provide conclusive data). Fig. 5 shows the deformation behaviour of two specimens during dynamic compression. The observed temperature increase is caused by irreversible plastification and is equivalent to the Von Mises strain field on the specimen's surface [35].

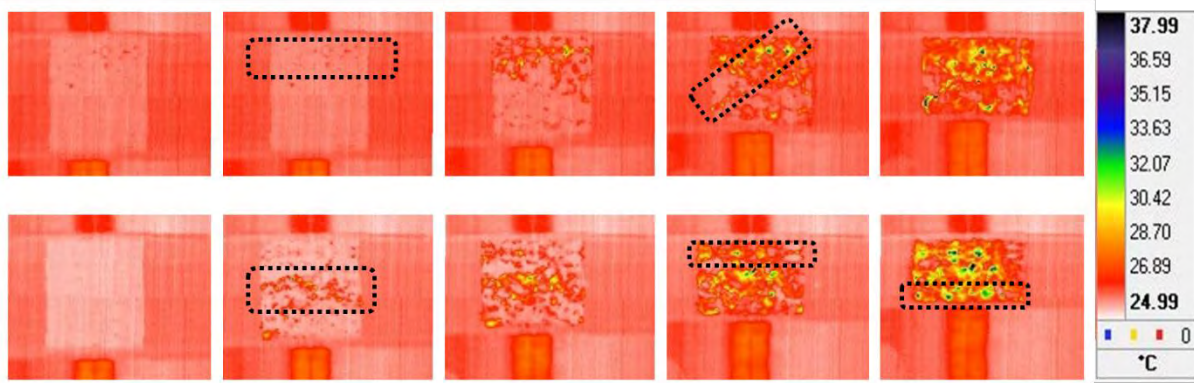


Figure 5. Compressive behaviour of two Corevo specimens subjected to dynamic loading (strain increment $\Delta\epsilon \approx 10\%$)

The first specimen (upper line in Fig. 5) shows the initiation of a horizontal collapse band (the increase in temperatures caused by plastic deformation), while the remaining visible part of the specimen still deforms elastically. At larger strain a second inclined deformation band is formed which after further deformation merges with the horizontal one. The plastification then continuously spreads through the complete specimen. The second specimen (lower line in Fig. 5) shows the typical layer-wise collapse mechanism. In total three horizontal plastification bands are gradually formed. From these bands the plastic deformation spreads through the whole porous structure.

The maximum sample temperature on the captured sample surface has been monitored during each dynamic test. The average of all measurements together with its deviations is represented from beginning of loading ($\epsilon = 0$ at $t = 0$) up to densification ($\epsilon \approx 0.8$ at $t = 0.086$ s) in Fig. 6. After an abrupt initial temperature increase (coinciding with formation of the first deformation band, region I.) the maximum temperature gradually increases up to $t \approx 0.04$ s (region II.) and then at a slower rate further increases (coincides with merging of single deformation bands) up to densification (region III.).

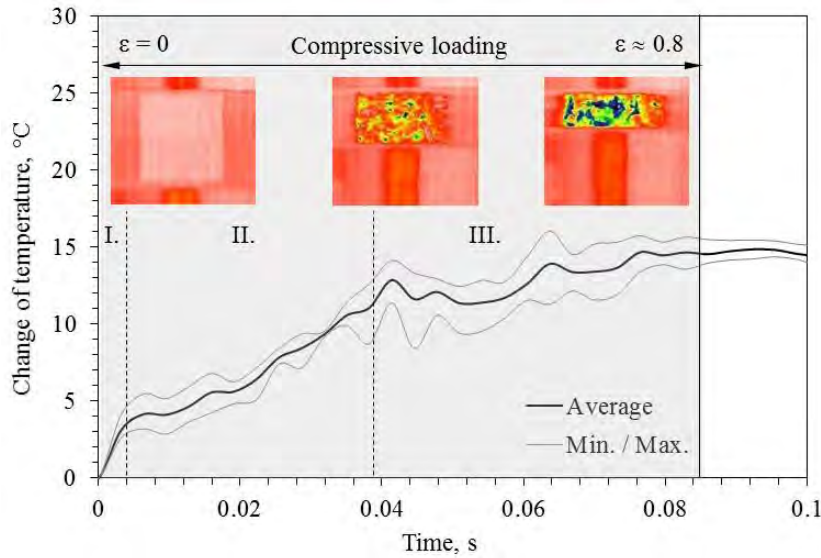


Figure 6. Trace of the maximal temperature change through time/deformation.

The response in terms of engineering stress vs. engineering strain for all tested specimens is shown in Fig. 7. The stress-strain curves show a typical compressive behaviour for porous materials that consists of the: (i) initial quasi-linear-elastic region, (ii) transition zone where the base material starts plastically to deform, (iii) plateau region with almost constant stress up to large strains and (iv) densification where the stiffness drastically increases [8, 53, 54]. The diagram shows considerable scatter of the mechanical properties which is mostly attributed to density (porosity) variation of the tested specimens. However, it should be noted that the stiffness of the specimens clearly increases with their increasing density.

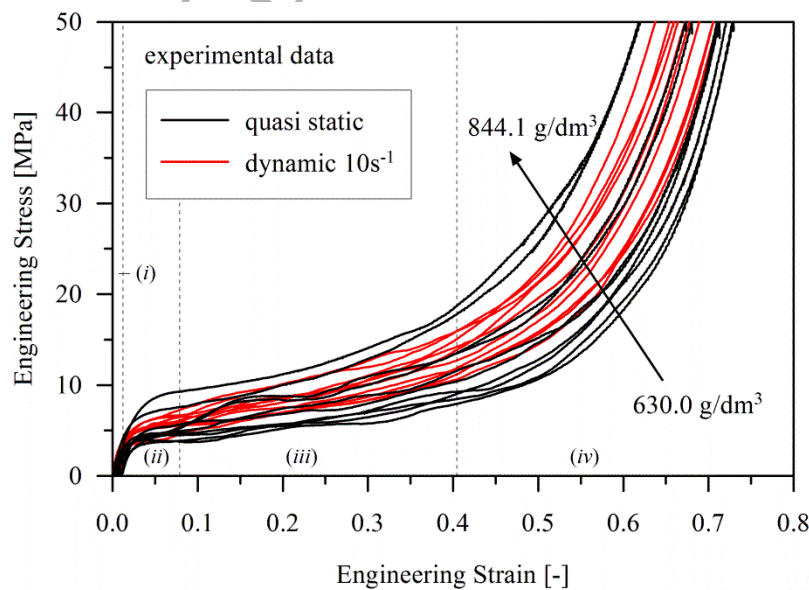


Figure 7. Stress-strain data for all specimens subjected quasi-static and dynamic compressive loading

Due to the variation of specimens densities the strain rate sensitivity cannot be clearly observed in Fig. 7. Accordingly, only the response of specimens with approximately same density ($\rho \approx 700 \text{ g/dm}^3$) have been depicted in Fig. 8. The results indicate a positive strain rate sensitivity of the Corevo foam. With increasing loading velocity the global stiffness of the structure increases, while the densification strain is slightly shifted to lower strains. Fig. 8 also contains quasi-static stress-strain data of Corevo samples with different pore sizes taken from [27]. All samples of the current study (see Table 1) exhibit an average pore size of 3 mm. It can be seen that the pore size of 5.6 mm yields almost identical results, whereas distinctly higher stresses are observed for the smaller pores size of 1.9 mm.

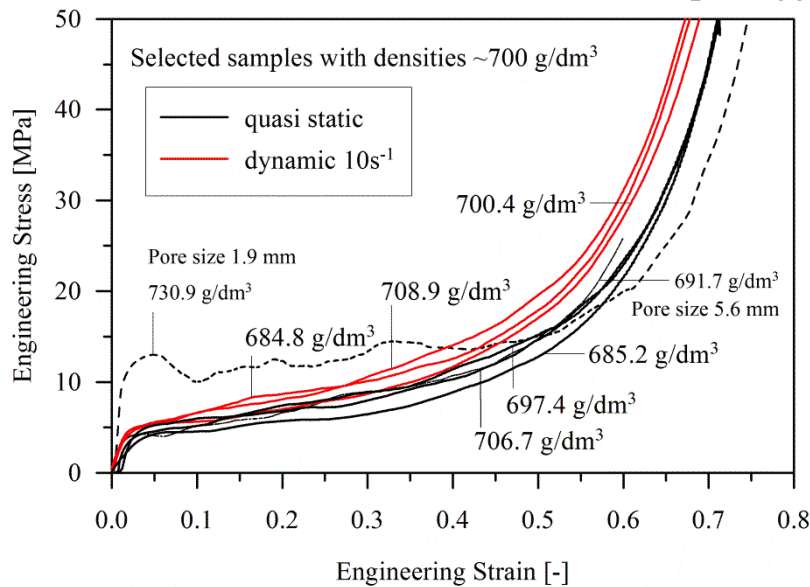


Figure 8. Stress-strain data of specimens with approximately same density ($\sim 700 \text{ g/dm}^3$) subjected quasi-static and dynamic compressive loading

4.2 Computational results

Computational simulations offer further insight in the global and local deformation behaviour, strain rate sensitivity and anisotropy of Corevo foam specimens. Initially, the computational models and their results have been compared to the experimental test data. Their response is validated with the experimental measurements (for the same loading rate) in Fig. 9. Throughout the complete strain range a very good agreement can be observed which confirms the suitability of the used computational models.

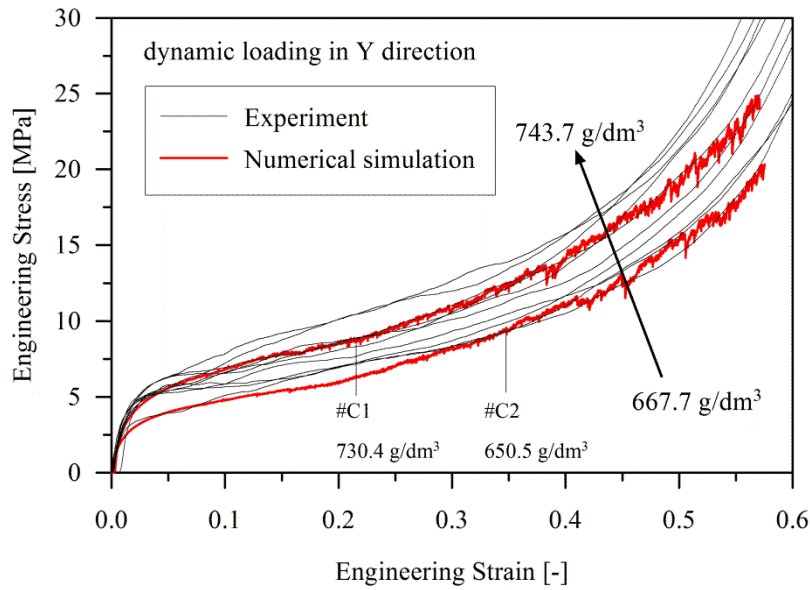


Figure 9. Comparison between the experimental and numerical results (strain rate 10 s^{-1})

Fig. 10 shows the computational deformation behaviour and plastification distribution in Corevo specimens. As discussed above, the formation of several independent deformation bands is clearly visible. The plastic deformation of the base material is mostly concentrated within these deformation bands, while other regions are being deformed only elastically.

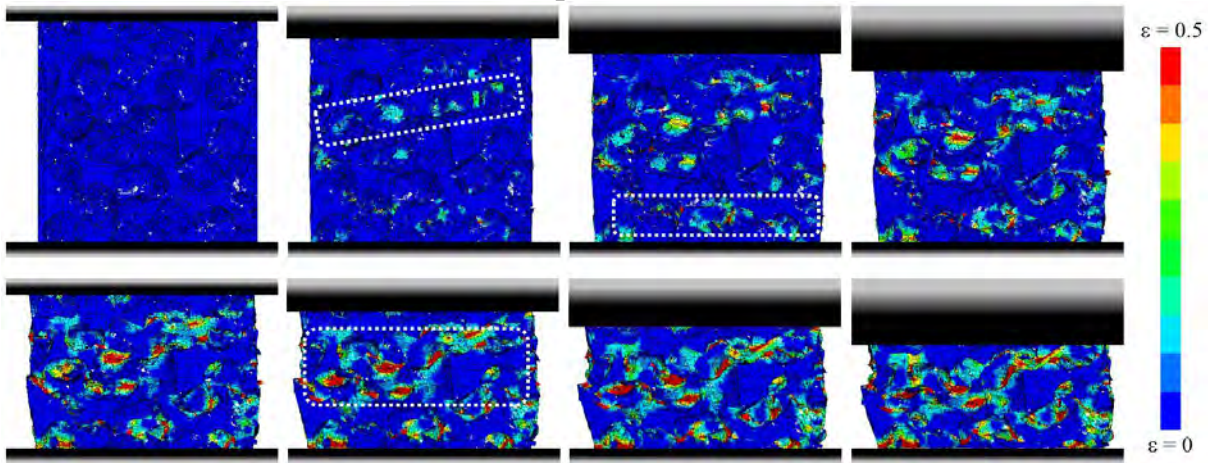


Figure 10. Computational results of Corevo specimens subjected to compressive behaviour (strain increment $\Delta\epsilon \approx 10\%$, loading direction as shown in Fig. 3)

The computational simulations show the collapse mechanics with deformation bands which are not necessarily constant through the complete specimen's thickness. Representative examples are depicted in Fig. 11. In agreement with the experimental IR observations up to three deformation bands can be observed. The orientation of those deformation bands can be horizontal, inclined or a combination of horizontal and inclined bands.

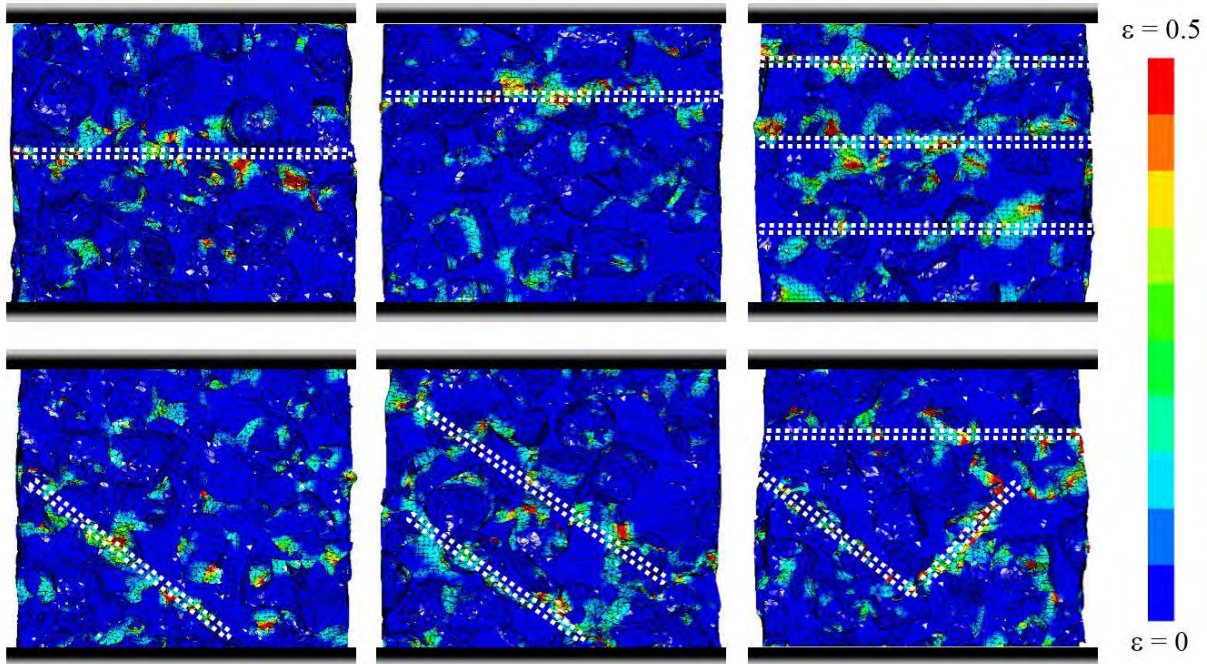


Figure 11. Representative deformation bands in various specimens (strain $\varepsilon \approx 10\%$, loading direction as shown in Fig. 3)

Another advantage of computational simulations is the availability of results in almost any point (depending on the discretisation) of the analysed model. Unlike the experimental tests, plasticity data is not limited to a single outer surface of the specimens but provides insight in the local behaviour inside the porous structure. The most common local micro-deformation mechanisms are shown in Fig. 12 and are highlighted by arrows and a letter denoting the deformation mechanism. Initially (strains up to approx. 15%) the plastic concentrations predominantly appear within thin struts that are parallel to the loading direction, as it was also observed in [19, 26]. Further deformation of the structure results in bending, crushing and stretching of aluminium struts and eventually in their failure and collapse.

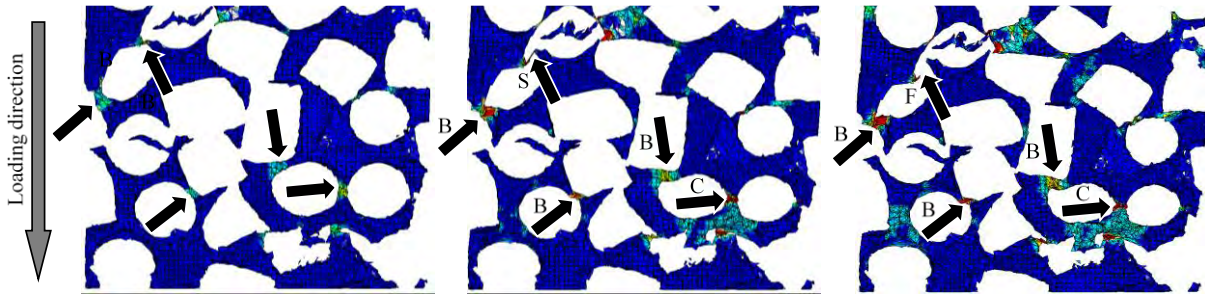


Figure 12. Local deformation mechanisms observed in computational simulations
(bending – B, crushing – C, stretching – S, failure or collapse – F)

By means of computational simulations, the strain rate sensitivity (achieving strain rates higher than the capability of the used testing machine, i.e. $> 10 \text{ s}^{-1}$) and anisotropy of Corevo specimens have been further analysed. The stress-strain data of both computational models (#C1 and #C2) are shown in Fig. 13.

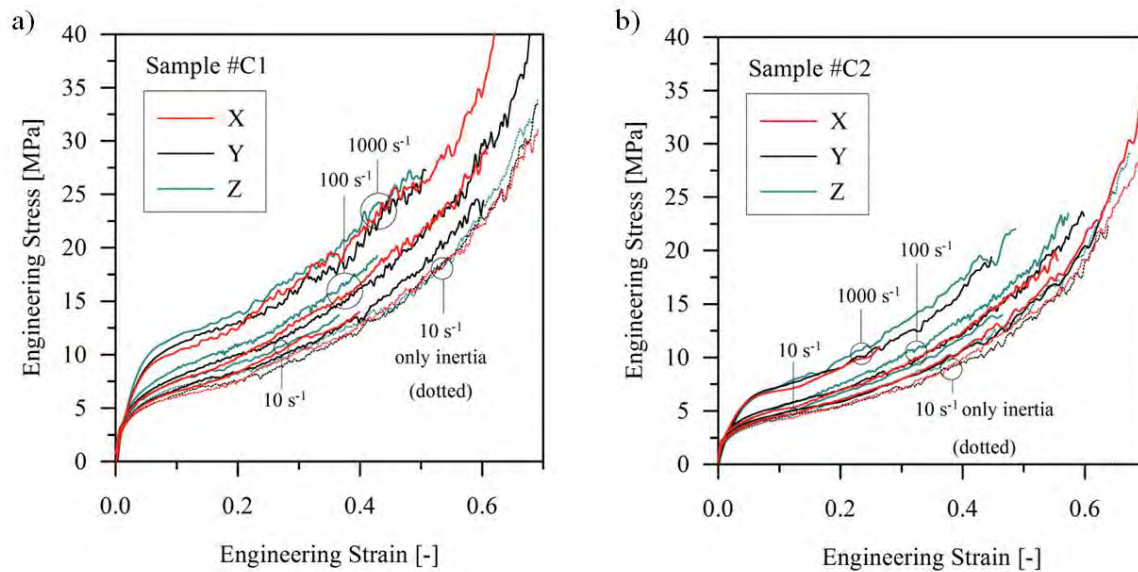


Figure 13. Stress-strain response of the computational model #C1 (a) and #C2 (b) in different loading directions and different loading velocities

The diagrams represent three different loading velocities (corresponding to strain rates 10, 100 and 1000 s^{-1}) and three orthogonal loading directions (x , y and z). In order to better understand the dynamic behaviour of Corevo foam, the material strain rate sensitivity (Cowper-Symonds model) has not been accounted for in one set of simulations. This set of simulations is in diagrams labelled as 10 s^{-1} only inertia, as the inertia represented the only

dynamic effect. From both diagrams it can be observed that the results are clustered in four strain rate groups. Within each of these groups, the influence of the loading direction can be observed. Comparison of curves for the strain rate 10 s^{-1} with 10 s^{-1} only inertia shows the impact of the material strain rate sensitivity. A noticeable increase in stiffness is found even at this relatively low strain rate. The stiffness of specimens further increases by increasing the strain rate up to 100 s^{-1} . A more significant difference can be observed at the strain rate 1000 s^{-1} which is most likely, besides to the inertia and base material strain rate sensitivity, attributed also to the change of the deformation mechanics. The influence of the loading velocity on the deformation mechanics is presented in Fig. 14. At lower strain rates, local deformations start to form randomly through the structure (depending on the weakest points). Contrary, at higher loading rates the deformation mode changes and the local deformation is due to the inertia effects mostly concentrated within the region where loading occurs and not at the weakest region, thus providing higher load carrying capacity [10, 22].

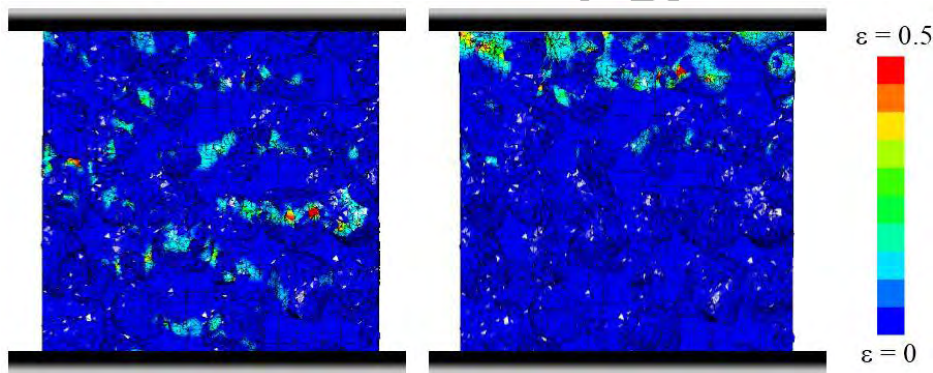


Figure 14. Comparison of strain propagation at low (10 s^{-1} , left) and high (1000 s^{-1} , right) strain rate (strain $\varepsilon \approx 5\%$, loading direction as shown in Fig. 3)

4.3 Mechanical properties of Corevo foam

The quasi-static and dynamic mechanical properties of Corevo foam specimens were determined in accordance with the ISO 13314: 2011 [30, 55] based on experimental and computational results. The 1% offset yield stress, plateau modulus, plateau stress and specific energy absorption ($0.2 < \varepsilon < 0.4$) are plotted *versus* density in Fig. 15. Thus, the influence of the density and the strain rate sensitivity can clearly be observed. Random variation of the results is most likely to be attributed to the complex foam structure and highly irregular pore topology, as it was already observed in [52]. A clear tendency that the mechanical properties increase with the foam density can be noted. The influence of the density is strongest in the

case of plateau stress (Fig. 15b) and plateau modulus (inclination of the plateau region, Fig. 15c), followed by specific energy absorption (Fig. 15d) and offset yield stress (Fig. 15a). It was observed that the offset yield stress is less affected at lower densities ($< 750 \text{ g/dm}^3$). The plateau values and specific energy absorption increase almost linearly with density increase. The results show again a positive strain rate sensitivity of the analysed specimens which is consistent with our previous studies [8, 19, 52] and also confirmed by other authors [21, 56]. Nevertheless, results contradicting this observation were also published. Some studies on the behaviour of aluminium foams reported their insensitivity to strain rate [57, 58], while others have shown that the foams with lower porosity experience a higher strain rate sensitivity which diminishes by increase of porosity [17, 59, 60]. Hence, understanding of the mechanisms contributing to the influence of strain rate sensitivity for foams are still subject to discussion.

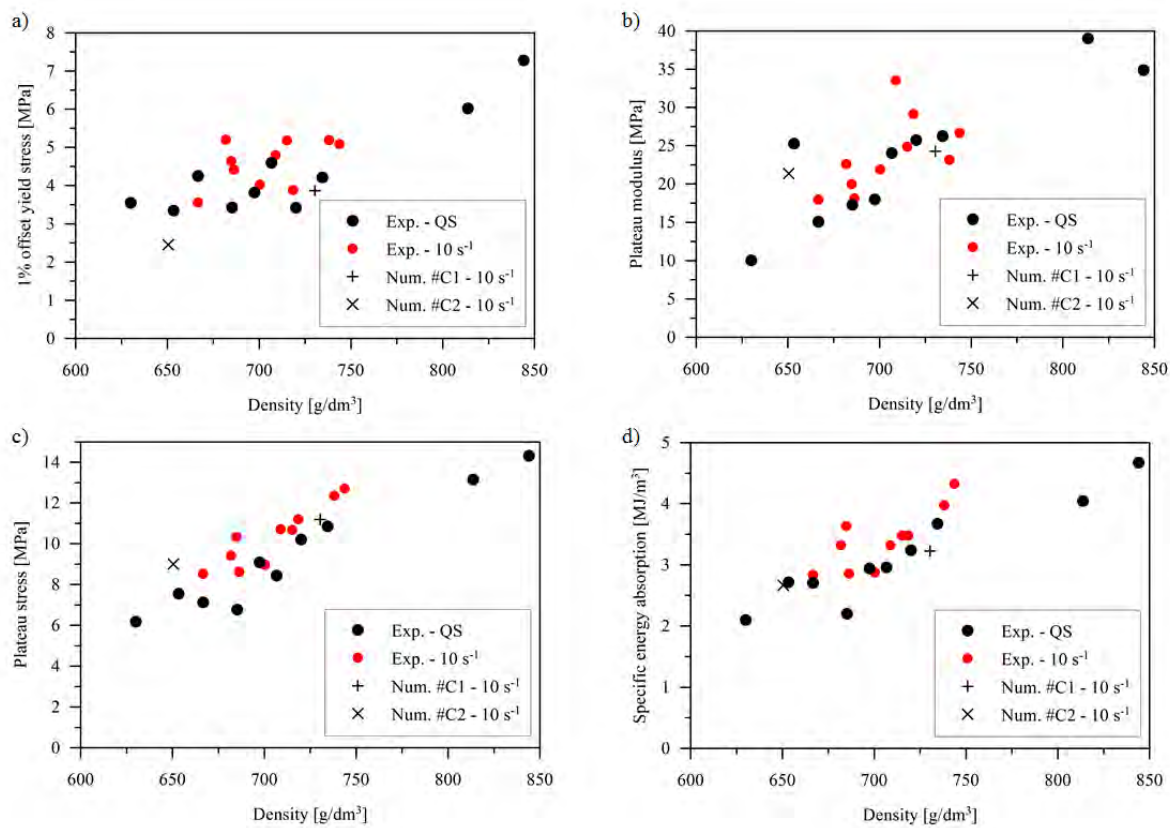


Figure 15. Experimental and computational mechanical results: 1% offset yield stress (a), plateau modulus (b), plateau stress (c) and specific energy absorption (d)

The anisotropy of the Corevo foam specimens was observed (due to the limited number of available μCT data sets) using the already validated numerical models. The influence of the

loading direction on the 1% offset yield stress and plateau stress can be observed in Figs. 16 and 17, respectively.

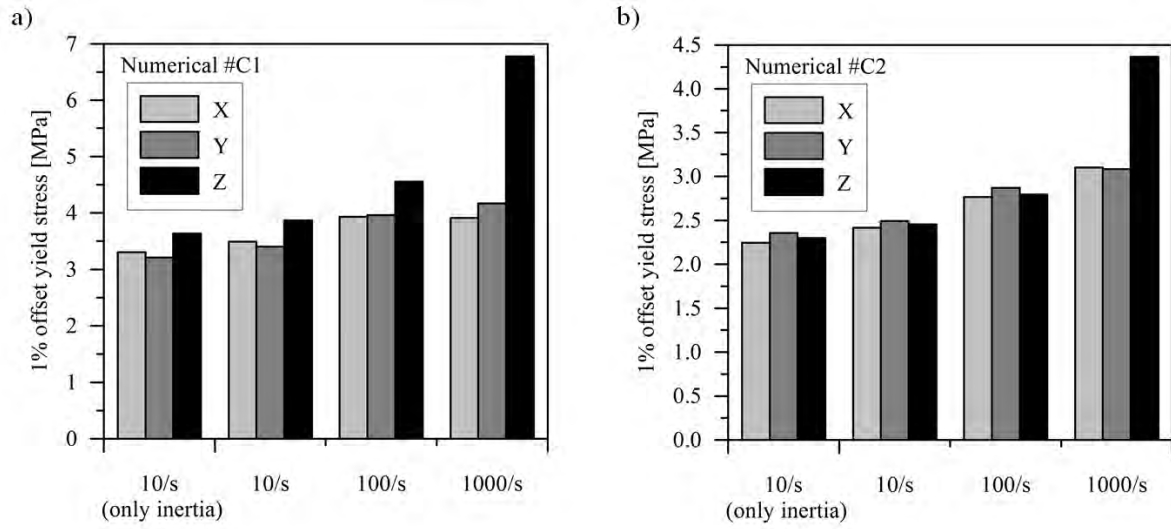


Figure 16. Influence of the anisotropy on the 1% offset yield stress for #C1 (a) and #C2 (b)

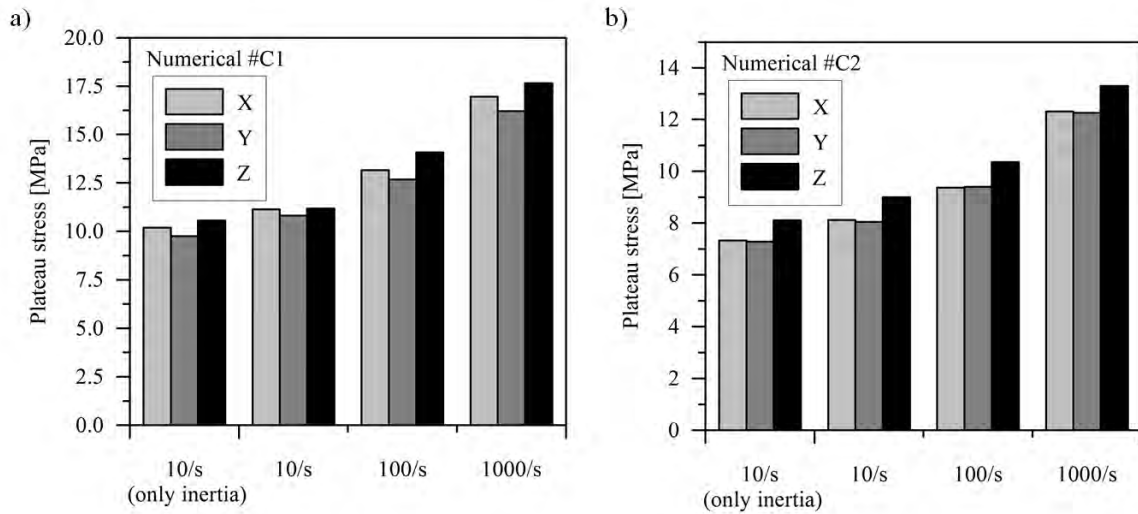


Figure 17. Influence of the anisotropy on the plateau stress for #C1 (a) and #C2 (b)

For lower strain rates ($\leq 100 \text{ s}^{-1}$) only a moderate anisotropy can be noted. This indicates that the aluminium alloy infiltration direction during specimens' fabrication does not considerably affect the mechanical properties. Furthermore, the distribution and orientation of salt pallets appear to be random (no preferred alignments) and therefore the stochastic internal foam structure does not systematically influence the mechanical properties in respect to the loading direction. Both samples show a stronger anisotropy for z-direction at the maximum strain rate

in case of yield stress. This effect is associated with the change of the deformation mode (Fig. 14) at higher strain rates and coincides with the aluminium alloy infiltration direction. Anisotropy appears to be less pronounced for the case of plateau stress, in particular at the highest strain rate. It should be noted that plateau stress is an averaged value at high strains and therefore the influence of the deformation mode change is not as prominent.

The 10 s^{-1} (only inertia) results indicate that the base material strain rate sensitivity increases the effective material properties in average by 6.7% (offset yield stress) and 10.8% (plateau stress). This additionally emphasises the need for accounting the base material strain rate sensitivity with appropriate constitutive material models in computational simulations.

5 Conclusions

The manuscript presents for the first time a detailed study of compressive mechanical properties, including the strain rate sensitivity and anisotropy, of Corevo aluminium foam. For this purpose extensive experimental tests and computational simulations have been performed. The study of deformation mechanisms during compressive tests has been additionally supported by IR thermography. Computational simulations have been based on numerical models with precisely reconstructed models replicating complex irregular 3D geometry of the fabricated specimens by using μ CT data. The suitability of computational models has been thoroughly validated by comparison with experimental tests. Collapse mechanisms have been observed by IR thermography and computational simulations, both indicating formation of deformation bands during the loading process. These bands can be parallel or inclined regarding to the loading/support plates, indicating a layer-wise collapse mechanism. Multiple collapse bands merge into one large crush band before densification. By means of computational simulations, the most common micro-deformation mechanisms were identified, showing plastic concentrations predominantly within the struts that are parallel to the loading direction at lower strains. Upon further loading struts start to bend, crush and stretch, up to their failure and collapse. The results of the experimental tests and simulations have clearly shown the influence of the loading velocity. The results indicate a positive strain rate sensitivity of the mechanical properties of the Corevo foams. Additionally, the computational simulations show moderate mechanical anisotropy. Accordingly, it can be concluded that the aluminium infiltration direction and pore topology do not significantly influence the mechanical properties in respect to the loading direction. Finally, such combined experimental and numerical investigation showed to be necessary when evaluating complex material structure, such as Corevo foam.

Acknowledgments

The paper was produced within the framework of research programme P2-063 entitled "Design of Porous Structures", which is financed by the Slovenian Research Agency "ARRS". This work was also performed within the framework of the operation entitled "Centre for Open Innovation and Research of the University of Maribor". The operation is co-funded by the European Regional Development Fund and conducted within the framework of the Operational Programme for Strengthening Regional Development Potentials for the period 2007 – 2013, development priority 1: "Competitiveness of companies and research excellence", priority axis 1.1: "Encouraging competitive potential of enterprises and research excellence", contract No. 3330-13-500032. Support of bilateral project (Slovenia – Croatia) BI-HR/012-13-042 is also acknowledged.

References

- [1] J. Tian, T.J. Lu, H.P. Hodson, D.T. Queheillalt, H.N.G. Wadley, *International Journal of Heat and Mass Transfer*, 50 (2007) 2521-2536.
- [2] D. Veyret, G. Tsotridis, *Journal of Power Sources*, 195 (2010) 1302-1307.
- [3] T. Fiedler, G.E. Murch, T. Bernthaler, I.V. Belova, in: Cairns, QLD, 2010, pp. 1500-1503.
- [4] I.S. Golovin, H.R. Sinning, *J Alloy. Compd.*, 355 (2003) 8.
- [5] Z.Xie, M.Tane, S..K.Hyun, Y.Okuda, H.Nakajima, *Mater. Sci. Eng. A*, 417 (2006) 129-133.
- [6] S. Günter, Q. Peter, A. Olaf, *Journal of Physics: Conference Series*, 165 (2009) 012061.
- [7] I. Duarte, M. Vesenjaj, L. Krstulović-Opara, I. Anžel, J.M.F. Ferreira, *Mater. Design*, 66 (2015) 532-544.
- [8] M. Vesenjaj, C. Veyhl, T. Fiedler, *Mater. Sci. Eng. A*, 541 (2012) 105-109.
- [9] X.Y. Su, T.X. Yu, S.R. Reid, *Int.J. Impact Eng.*, 16 (1995) 673-689.
- [10] S. Tanaka, K. Hokamoto, S. Irie, T. Okano, Z. Ren, M. Vesenjaj, S. Itoh, *Measurement*, 44 (2011) 2185-2189.
- [11] M.I. Thiyahuddin, Y.T. Gu, D.P. Thambiratnam, H.M. Thilakarathna, *International Journal of Impact Engineering*, 72 (2014) 26-39.
- [12] J. Baumeister, J. Weise, E. Hirtz, K. Höhne, J. Hohe, *Procedia Materials Science*, 4 (2014) 317-321.
- [13] P.K. Pinnoji, P. Mahajan, N. Bourdet, C. Deck, R. Willinger, *International Journal of Impact Engineering*, 37 (2010) 274-284.
- [14] M. Vesenjaj, Z. Ren, T. Fiedler, A. Öchsner, *J. Compos. Mater.*, 43 (2009) 2491-2505.
- [15] V.S. Deshpande, N.A. Fleck, *Int. J. Impact Eng.*, 24 (2000) 277-298.
- [16] A. Ohrndorf, P. Schmidt, U. Krupp, H.J. Christ, in: *Werkstoffprüfung 2000*, Deutscher Verband für Materialforschung und-prüfung e.V., Bad Nauheim, 2000.
- [17] K.A. Dannemann, J. Lankford, *Mater. Sci. Eng. A*, 293 (2000) 157-164.
- [18] M. Vesenjaj, A. Öchsner, Z. Ren, *Mater. Lett.*, 62 (2008) 3250-3253.
- [19] T. Fiedler, M. Taherishargh, L. Krstulović-Opara, M. Vesenjaj, *Mater. Sci. Eng. A*, 624 (2015) 296-304.

- [20] M. Vesenjak, L. Krstulović-Opara, Z. Ren, Polym. Test., 31 (2012) 705-709.
- [21] P.J. Tan, S.R. Reid, J.J. Harrigan, Z. Zou, S. Li, J. Mech. Phys. Solids, 53 (2005) 2174-2205.
- [22] P.J. Tan, S.R. Reid, J.J. Harrigan, Z. Zou, S. Li, J. Mech. Phys. Solids, 53 (2005) 2206-2230.
- [23] S.L. Lopatnikov, B.A. Gama, M.J. Haque, C. Krauthauser, J.W. Gillespie Jr, International Journal of Impact Engineering, 30 (2004) 421-445.
- [24] Q. Qin, T.J. Wang, Composite Structures, 96 (2013) 346-356.
- [25] A. Rajaneesh, I. Sridhar, S. Rajendran, Composite Structures, 94 (2012) 1745-1754.
- [26] T. Fiedler, M.A. Sulong, V. Mathier, I.V. Belova, C. Younger, G.E. Murch, Comp. Mater. Sci., 81 (2014) 246-248.
- [27] M.A. Sulong, V. Mathier, T. Fiedler, I.V. Belova, G.E. Murch, in, Trans Tech Publications, Switzerland, 2014, pp. 121-126.
- [28] Y. Conde, J.F. Despois, R. Goodall, A. Marmottant, L. Salvo, C. San Marchi, A. Mortensen, Adv. Eng. Mater., 8 (2006) 795-803.
- [29] M. Vesenjak, L. Krstulović-Opara, Z. Ren, Polym. Test., 32 (2013) 1538-1544.
- [30] ISO, ISO 13314:2011 Mechanical testing of metals - Ductility testing - Compression test for porous and cellular metals, 2011.
- [31] S. Bagavathiappan, B.B. Lahiri, T. Saravanan, J. Philip, T. Jayakumar, Infrared Physics & Technology, 60 (2013) 35-55.
- [32] D. Wagner, N. Ranc, C. Bathias, P.C. Paris, Fatigue & Fracture of Engineering Materials & Structures, 33 (2010) 12-21.
- [33] M. Vesenjak, F. Gačnik, L. Krstulović-Opara, Z. Ren, Mech. Adv. Mater. Struc., 22 (2015) 359-366.
- [34] I. Duarte, M. Vesenjak, L. Krstulović-Opara, Compos. Struct., 109 (2014) 48-56.
- [35] L. Krstulović-Opara, M. Surjak, M. Vesenjak, Z. Tonković, J. Kodvanj, Ž. Domazet, in, Proceedings of 31th Danubia-Adria Symposium on Advances in Experimental Mechanics, Kempten, Germany, 2014, pp. 232-233.
- [36] M.L. Pastor, X. Balandraud, M. Grédiac, J.L. Robert, Infrared Physics & Technology, 51 (2008) 505-515.
- [37] M. Ulbin, M. Borovinšek, Y. Higa, K. Shimojima, M. Vesenjak, Z. Ren, Mater. Lett., 136 (2014) 416-419.
- [38] M. Vesenjak, M. Borovinšek, T. Fiedler, Y. Higa, Z. Ren, Mater. Lett., 110 (2013) 201-203.
- [39] C. Veyhl, I.V. Belova, G.E. Murch, T. Fiedler, Mater. Sci. Eng. A, 528 (2011) 4550-4555.
- [40] I.V. Belova, C. Veyhl, T. Fiedler, G.E. Murch, Scripta Mater., 65 (2011) 436-439.
- [41] T. Fiedler, M.A. Sulong, M. Vesenjak, Y. Higa, I.V. Belova, A. Öchsner, G.E. Murch, Int. J. Heat Mass Trans., 73 (2014) 826-833.
- [42] M.A. Sulong, M. Vesenjak, I.V. Belova, G.E. Murch, T. Fiedler, Mater. Sci. Eng. A, 607 (2014) 498-504.
- [43] C. Veyhl, T. Fiedler, O. Andersen, J. Meinert, T. Bernthaler, I.V. Belova, G.E. Murch, Int. J. Heat Mass Trans., 55 (2012) 2440-2448.
- [44] ISO, ISO 6892-1:2010 Metallic materials - Tensile testing - Part 1: Method of test at room temperature, 2010.
- [45] J. Hallquist, LS-DYNA Keyword User's Manual, Livermore Software Technology Corporation, Livermore, California, 2007.
- [46] Z. Xue, A. Vaziri, J.W. Hutchinson, CMES - Comp. Model. Eng., 10 (2005) 79-95.
- [47] S.R. Bodner, P.S. Symonds, Journal of Applied Mechanics, 29 (1962) 719-728.
- [48] P. Jacob, L. Goulding, An Explicit Finite Element Primer, NAFEMS, Glasgow, 2002.

- [49] J. Hallquist, LS-DYNA Keyword User's Manual, Livermore Software Technology Corporation, Livermore, California, 2007.
- [50] M. Vesenjak, L. Krstulović-Opara, Z. Ren, Ž. Domazet, Polym. Test., 29 (2010) 991-994.
- [51] M. Vesenjak, L. Krstulović-Opara, Z. Ren, A. Öchsner, Ž. Domazet, Exp. Mech., 49 (2009) 501-509.
- [52] I. Duarte, M. Vesenjak, L. Krstulović-Opara, Mater. Sci. Eng. A, 616 (2014) 171-182.
- [53] M.F. Ashby, A. Evans, N.A. Fleck, L.J. Gibson, J.W. Hutchinson, H.N.G. Wadley, Metal foams: a design guide, Elsevier Science, Burlington, Massachusetts, 2000.
- [54] J. Banhart, Prog. Mater. Sci., 46 (2001) 559-632.
- [55] T. Hipke, G. Lange, R. Poss, Taschenbuch für Aluminiumschäume, Alu Media, Düsseldorf, 2007.
- [56] R. Edwin Raj, V. Parameswaran, B.S.S. Daniel, Mater. Sci. Eng. A, 526 (2009) 11-15.
- [57] D. Ruan, G. Lu, F.L. Chen, E. Siores, Compos. Struct., 57 (2002) 331-336.
- [58] I.W. Hall, M. Guden, C.J. Yu, Scripta Mater., 43 (2000) 515-521.
- [59] T. Mukai, H. Kanahashi, T. Miyoshi, M. Mabuchi, T.G. Nieh, K. Higashi, Scripta Mater., 40 (1999) 921-927.
- [60] T. Mukai, T. Miyoshi, S. Nakano, H. Somekawa, K. Higashi, Scripta Mater., 54 (2006) 533-537.

Graphical abstract

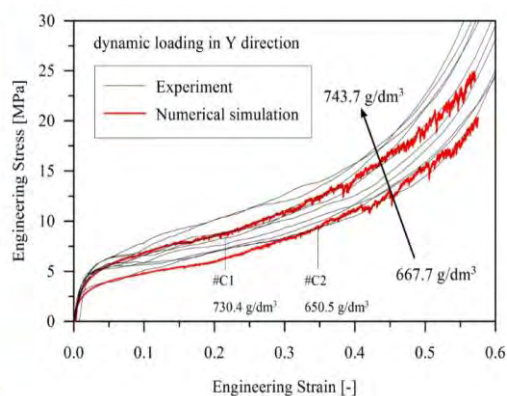
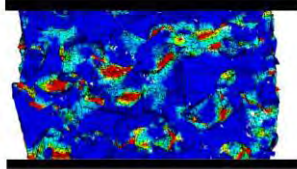
Aluminium foam derived
from infiltration casting
of salt dough



Experiments



Simulations



Chapter 8

A model of the mechanical degradation of foam replicated scaffolds

The previous Chapters 3-7 addressed the mechanical characterisations of metallic foams. In contrast, this Chapter deals with the mechanical properties of tissue engineering scaffolds, i.e. a *ceramic* porous structure. The considered biomaterial scaffold is similar to the previously investigated metallic foam materials in terms of geometry (they all have a complex internal morphology and are porous) and stress-strain behaviour. Thus the tissue engineering scaffolds are investigated using the same methods applied in previous Chapters for quasi-static loading. The biomaterial is synthesised from titania powder using the foam replication technique.

Image-based modelling from high resolution sources such as μ CT opens a wider window to explore the properties of tissue engineering scaffolds. In this Chapter, accurate predictions of the transformation of scaffold geometry caused by surface erosion and the resulting change in its mechanical response are presented. The geometrical degradation of the foam structure is simulated using a phenomenological method to mimic the surface erosion in body fluids. However, this investigation does not attempt to apply the complex diffusion-chemical reaction system into the degradation model. Instead, the models reported in the literature are used in the scope of this work to connect the relation between the implantation times to mass loss of the biomaterial scaffold. Micro-computed tomography (μ CT) images of foam replicated scaffolds are processed and partially resorbed three-dimensional (3D) geometries are re-generated herein. The virtual geometries obtained are then used for mechanical finite element analysis in order to assess the decrease of the elastic stiffness and degradation of material strength. The compressive properties of the titania scaffolds are assessed by imposing quasi-static loading. Results show the systematic decrease of the quasi-elastic gradient, 0.2% offset yield stress and the plateau stress during a ten-week (74 days) period of immersion time.

In summary, the mechanical properties of the titania scaffolds studied in this Chapter can be accurately represented using an exponential decay function of the immersion time. More importantly, this function scales the mechanical property of the original titania foam according based on its immersion time. Results obtained from this investigation reveal the great potential of numerical analysis for accurate modelling and prediction of the mechanical properties of tissue engineering scaffolds.

The latest version of the submitted paper is presented here.

M.A. Sulong, I.V. Belova, A.R. Boccaccini, G.E. Murch, T. Fiedler, "A model of the mechanical degradation of foam replicated scaffolds." *Under review in Journals of Materials Science*

Journal of Materials Science

A model of the mechanical degradation of foam replicated scaffolds

--Manuscript Draft--

Manuscript Number:	JMSC-D-15-03116R1		
Full Title:	A model of the mechanical degradation of foam replicated scaffolds		
Article Type:	Manuscript (Regular Article)		
Keywords:	Tissue engineering scaffold; bone resorption; surface erosion; Mechanical properties; finite element method		
Corresponding Author:	Mohd Ayub Sulong, M.Eng. The University of Newcastle Newcastle, NSW, NSW AUSTRALIA		
Corresponding Author Secondary Information:			
Corresponding Author's Institution:	The University of Newcastle		
Corresponding Author's Secondary Institution:			
First Author:	Mohd Ayub Sulong, M.Eng.		
First Author Secondary Information:			
Order of Authors:	Mohd Ayub Sulong, M.Eng. Irina V Belova, PhD Aldo R Boccaccini, PhD Graeme E Murch, PhD Thomas Fiedler, PhD		
Order of Authors Secondary Information:			
Abstract:	Tissue engineering scaffolds are implants that actively support tissue growth whilst providing mechanical support. For optimum functionality, they are designed to slowly dissolve in vivo so that no foreign material remains permanently implanted inside the body. The current study uses a simple degradation model that estimates the change of scaffold geometry due to surface erosion. This model is applied on scaffolds that have been manufactured using the foam replication method. In order to capture their complex geometry micro-computed tomography scans of samples are obtained. Their change in geometry and degradation of mechanical properties are evaluated using computational analysis. The present investigation found that the mechanical properties such as the quasi-elastic gradient, 0.2% offset yield stress and the plateau stress are decreased systematically over a ten week period of immersion time. Deformation analysis on the titania foam scaffold is performed by means of the deformed model obtained from finite element calculations.		
Funding Information:	<table border="1"> <tr> <td>Australian Research Council through its Discovery Project (DP130101377)</td> <td>Prof. Dr. Graeme E Murch</td> </tr> </table>	Australian Research Council through its Discovery Project (DP130101377)	Prof. Dr. Graeme E Murch
Australian Research Council through its Discovery Project (DP130101377)	Prof. Dr. Graeme E Murch		

[Click here to view linked References](#)

A model of the mechanical degradation of foam replicated scaffolds

M.A. Sulong^{*, 1, 3}, I.V. Belova¹, A.R. Boccaccini², G.E. Murch¹, T. Fiedler¹

¹Centre for Mass and Thermal Transport in Engineering Materials, School of Engineering, The University of Newcastle, Callaghan 2308, Australia

²Institute of Biomaterials, Department of Materials Science and Engineering, University of Erlangen-Nuremberg, 91058 Erlangen, Germany

³Universiti Teknologi Malaysia, Faculty of Mechanical Engineering, 81310 Skudai, Johor, Malaysia

Abstract Tissue engineering scaffolds are implants that actively support tissue growth whilst providing mechanical support. For optimum functionality, they are designed to slowly dissolve *in vivo* so that no foreign material remains permanently implanted inside the body. The current study uses a simple degradation model that estimates the change of scaffold geometry due to surface erosion. This model is applied on scaffolds that have been manufactured using the foam replication method. In order to capture their complex geometry micro-computed tomography scans of samples are obtained. Their change in geometry and degradation of mechanical properties are evaluated using computational analysis. The present investigation found that the mechanical properties such as the quasi-elastic gradient, 0.2% offset yield stress and the plateau stress are decreased systematically over a ten week period of immersion time. Deformation analysis on the titania foam scaffold is performed by means of the deformed model obtained from finite element calculations.

Keywords: Tissue engineering scaffold, bone resorption, surface erosion, mechanical properties, finite element method.

Introduction

Tissue engineering scaffolds are advanced biomaterials that aim to support self-healing mechanisms of the body. The underlying philosophy is the regrowth of damaged tissue that naturally has the ability to react to biochemical stimuli [1]. The scaffolds themselves should slowly dissolve in contact with body fluid due to a controlled resorption reaction. Benefits include possible time-delayed release of drugs, nutrients or growth factors stored within the scaffold matrix. The frequency of revision surgery can be reduced or can be avoided altogether by using this advanced biomaterial. Furthermore, no permanent implant remains inside the human body thereby decreasing the risk of an adverse host reaction.

Over the past ten years a variety of tissue engineering scaffolds have been created using numerous biomaterials. The most successful approaches include the robocasting [2], rapid prototyping [3, 4], sol-gel foaming [5] and foam replication methods[6, 7]. Robocasting is a technique which is used to manufacture an object layer-by-layer, often with the help of computer-aided design (CAD) [8]. In this technique, the so-called three-dimensional (3D) printer's inkjet in the form of aqueous paste is deposited on top of the previous layer through a tiny orifice of a nozzle [9]. Recently, bioactive glasses from the 6P53B group have been used in

the robocasting method to produce glass scaffolds that exhibit a compressive strength comparable to human cortical bone (~ 136 MPa) [10]. Sol-gel processing is another technique to fabricate bioactive glass scaffolds. This method has several advantages such as a hierarchical pore morphology, good process control and a yield of highly pure powder [11–13]. In spite of many good characteristics found in scaffolds derived from the sol-gel method, the structure has a relatively low strength (0.3–2.3 MPa) [14] and consequently this scaffold material can only be exploited in low-load bearing bone areas.

The foam replication method was first used to produce macroporous ceramics [15] before it was adapted to successfully create porous glass scaffolds [16]. The chief advantage of the foam replication method is its ability to produce highly porous glass scaffolds with open and interconnected porosity up to 95% [16]. Scaffolds that can be produced by using the foam replication method include a wide range of materials such as silicate [16], borosilicate [17] and borate bioactive glass [18]. However the challenge of biomaterials produced by this technique is the relatively low mechanical strength in the range of trabecular bone. Post-processing of glass scaffolds produced by foam replication such as coating with porous poly(D,L-lactide) PDLA [6] or carbon nanotube [19] can be used to improve the strength of the glass scaffold. It has been reported that PDLA coated glass scaffold is seven times stronger than the uncoated counterpart [6]. This strengthening mechanism could be attributed to the filling of microcracks in the thin struts by the PDLA slurry and this hypothesis is supported by numerical simulation results [20]. The present study focuses on scaffolds manufactured using the foam replication method. The resulting scaffolds exhibit porosities of $p > 90\%$ and an average pore size of $300\text{ }\mu\text{m}$.

Tissue engineering scaffold degradation has been addressed in previous research. Experimental studies have used magnetic resonance and computed tomography imaging to monitor *in vivo* implant resorption [21, 22]. However, the high cost and time requirements associated with these techniques limit their applicability for extensive studies. These drawbacks can be overcome by the additional use of numerical models. Han and Pan [23] developed a mathematical model of the simultaneous crystallization and biodegradation of biopolymers such as PGA and PLA. They extended a previous phenomenological model due to Wang *et al.* [24] by considering the formation of a crystalline phase that retards the reaction. The models combine a set of coupled reaction-diffusion equations that were solved for simple geometries using a finite element method. A polymeric biomaterials degradation simulation based on the Voxel Finite Element Method has been developed by Adachi *et al.* [25]. The investigation in [25] addresses the surface erosion of the scaffold and new bone formation in the same time frame. The proposed simulation method is promising for use in porous scaffold microstructure design. However, the coupling effects of two phenomena during regeneration were found to be very complex despite simple rate equations for the decomposition of scaffold and bone formation being used. In another study, Sanz-Herrera and Boccaccini [26] addressed the degradation of bioactive glasses for tissue engineering scaffolds. The reaction of bioactive glasses with body fluid results in hydroxyapatite being formed on the surface of the scaffold. The growing hydroxyapatite layer introduces a diffusion barrier that decreases the reaction rate over time. The set of equations forming their model was solved using a finite element method representing the geometry as voxels.

The focus of the present paper is the accurate prediction of scaffold geometry change due to surface erosion and its impact on mechanical properties. To this end, micro-computed tomography (μCT) images of foam replicated scaffolds are processed and partially resorbed

geometries are calculated. The geometries obtained are then used for mechanical finite element analysis in order to assess the degradation of the elastic stiffness and material strength. It should be emphasized here that the authors do not attempt to implement a detailed model of the complex diffusion-chemical reaction system. However, the models presented in the literatures [23], [24], [26] can be used to link implantation time to mass loss (e.g. the resorbed volume fraction) of the scaffolds.

Resorption Model

Two basic degradation mechanisms are usually distinguished: surface erosion and bulk degradation [27]. Polymers that are permeable to water (e.g. polylactic acid) are most likely to undergo bulk degradation [28, 29]. Water penetrates the polymer and subsequent hydrolysis generates carboxylic acids within the scaffold. This causes a decrease of the pH that is most pronounced away from the scaffold surfaces (at the surfaces the pH is stabilized due to mixing with surrounding body fluid). As a result, the reaction tends to form acid filled cavities within the material. When the polymer eventually breaks apart these acids are released and can cause inflammation of the surrounding tissue [30]. In contrast, hydrophobic materials undergo surface erosion which is manifested in the gradual thinning of the scaffolds. The present paper considers surface erosion which is better suited to describe the resorption behaviour of bioactive glasses.

A phenomenological model is used to predict surface erosion. In the first step, the stochastic scaffold geometry is captured using micro-computed tomography with a voxel resolution of 13.97 μm . As a result, detailed three-dimensional voxel data are obtained that represent the scaffold geometry in the form of 16 bit grey-level data. The grey-level of each voxel corresponds to the measured material density inside its volume and is used to segment the data set into scaffold (high density) and pore space (low density). To this end, the segmentation threshold is iteratively adjusted until the mass of scanned scaffold and virtual 3D model coincide.

For simplicity, the resorption reaction is assumed to occur at a constant rate for a given interface area between the reactants (i.e. scaffold and body fluid). As a result, the local reaction rate of a voxel is directly proportional to its surface area. The functionality of the algorithm is visualized in Figure 1 using a simple two-dimensional example. In most cases, the degradation rate of tissue engineering scaffold can be represented as an exponential function of time [31-32]. Initially, all pixels in the scaffold surface (grey pixels) are identified and their reaction counter is set to zero. At $t = 1$ the reaction counter of each surface pixel is incremented by its surface area (i.e. the number of interfaces with the pore space). In the example shown in Figure 1, a surface pixel is dissolved after the reaction counter has reached a value of 5 or greater. Accordingly, the protruding pixel on the left side is removed at $t = 2$. Newly exposed surface pixels are updated and their reaction counter is set to 0. This procedure is continued until the desired dissolved volume fraction is reached. In the case of the tissue engineering scaffold, the algorithm is applied to three-dimensional voxel data instead. Furthermore, the reaction counter value for voxel removal is increased to 1000 for improved accuracy. It must be highlighted here that the algorithm does not attempt to capture the reaction dynamics, i.e. it is not suitable for determining the mass loss after a certain time period. However, as mentioned above additional knowledge of the reaction dynamics can be used to relate scaffold geometry to the time the scaffold has been implanted in the body.

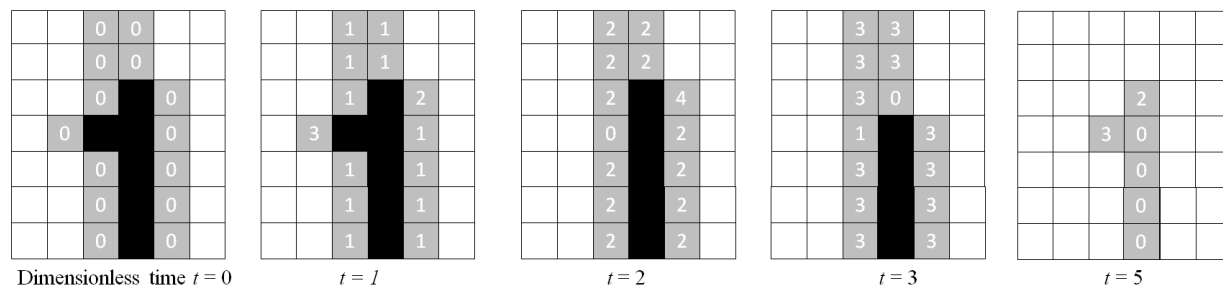


Fig. 1 Resorption model (pixels are removed at local values of 5)

Figure 2 shows results of the resorption algorithm applied to one of the μ CT data sets. Images are shown for different stages that are identified by their resorbed volume fraction Φ_{Res} , (i.e. the decrease in volume relative to the initial solid scaffold volume). Three different volume fractions are presented: the scanned μ CT model ($\Phi_{\text{Res}} = 0$ vol. %) and $\Phi_{\text{Res}} = 12$ vol. % and 30 vol. %. It can be seen that at $\Phi_{\text{Res}} = 30$ vol. % fragments start to separate from the main scaffold (disconnected fragments such as in the magnified circle are shown using a light grey colour).

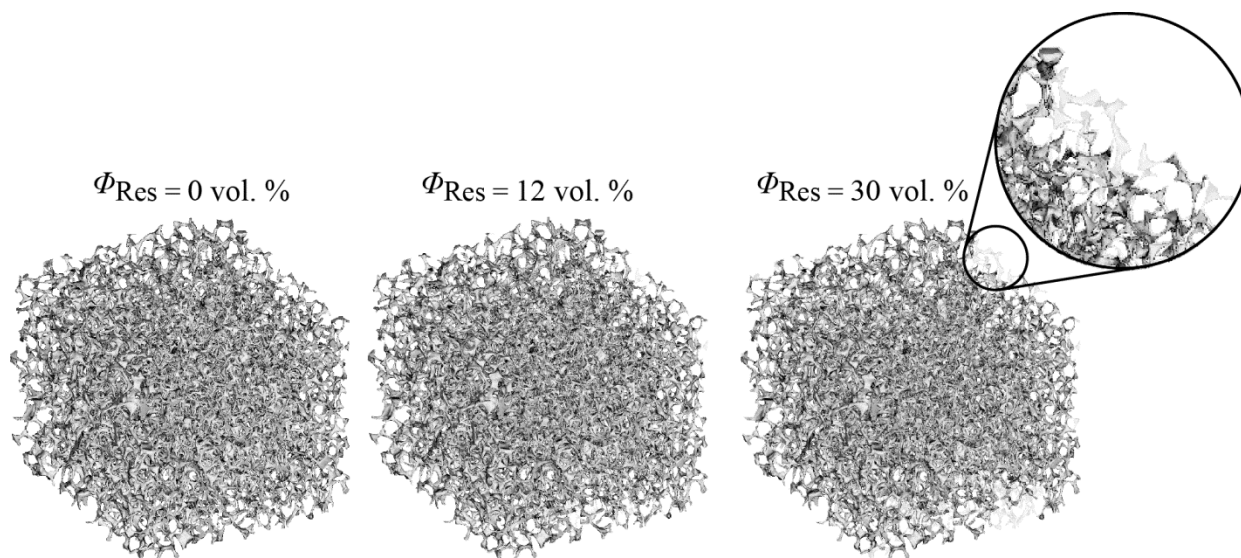


Fig. 2 Resorption of Sample #2 (areas shown in light grey are not percolating)

Finite Element Analysis

Finite element (FE) analysis is a numerical approach to mechanically characterize a sample by using a virtual model. The FE method allows the computation of mechanical properties such as reaction force, displacement, stress distribution, equivalent plastic strain and deformation analysis of a sample. The versatility of FE analysis includes the ability to repetitively test the same sample which is impossible in a destructive experimental test. This can be used to optimize a virtual sample by modifying its geometrical parameters and to consider different materials. Furthermore, FE analysis can be integrated with numerical models from micro-computed

tomography (μ CT) images. The μ CT imaging approach is well known to approximate the real structure regardless of geometrical complexity [33].

Geometric Discretisation

In the present study, the three-dimensional (3D) numerical calculation models are generated from the μ CT data of actual samples. Three different samples have been scanned and their geometric properties are shown in Table 1. The complex geometry of the samples was captured using a high resolution scan with a voxel length of 13.97 μ m. The raw μ CT data obtained are segmented using the ImageJ [34] image processing software. Using the volume fraction of titania $\Phi_{\text{TiO}_2}^*$ as the reference, the μ CT data is segmented using grey-value thresholding. To this end, the grey-value threshold is iteratively adjusted until the titania volume fraction $\Phi_{\text{TiO}_2}^*$ of the virtual model coincides with the scanned sample. The superscript * indicates that a variable refers to the original scaffold geometry (i.e. prior to resorption). The target volume fraction $\Phi_{\text{TiO}_2}^*$ of the scanned sample is obtained by dividing the titania volume V_{TiO_2} by the smallest rectangular prismatic volume V_{Prism} that encloses the sample, i.e. $\Phi_{\text{TiO}_2}^* = V_{\text{TiO}_2}/V_{\text{Prism}}$. The volume V_{Prism} is calculated by multiplication of sample height, length, and width. All dimensions (i.e.: height, length, and width) are taken as the averaged values measured at three different locations. This is done to minimise the error that may arise from minor deviation between the samples' outer shapes and the perfect rectangular prism. The titania volume V_{TiO_2} is calculated using $V_{\text{TiO}_2} = m_s/\rho_{\text{TiO}_2}$, where the sample mass m_s is obtained by weighing the samples on a digital precision scale and the density of titania TiO_2 is taken from the literature as $\rho_{\text{TiO}_2} = 3800 \text{ kg/m}^3$ [35].

To describe the resorption of models, we will use the resorbed titania volume fraction which is introduced as:

$$\Phi_{\text{Res}} = 1 - V_{\text{TiO}_2}/V_{\text{TiO}_2}^*$$

where $V_{\text{TiO}_2}^*$ is the original and V_{TiO_2} the current (i.e. after partial resorption) titania volume of a sample. Assuming a constant density of titania, this resorbed volume fraction is equivalent to the relative mass loss of the scaffold. The 'inverse' of the titania volume fraction is the porosity p of the sample, i.e. $p = 1 - \Phi_{\text{TiO}_2}$. Accordingly, the resorbed volume fraction and the scaffold porosity are simply linked by the relation:

$$p = 1 - (1 - \Phi_{\text{Res}})\Phi_{\text{TiO}_2}^*$$

Using the above equations, the porosity of samples #1, #2 and #3 at the initial stage ($\Phi_{\text{Res}} = 0\%$) are 93.31%, 93.79% and 94.34% respectively. The partially resorbed models are generated by applying the Resorption Model (see the previous Section) on the segmented data until the desired resorbed volume fraction (mass loss) is reached.

The processed μ CT data is then converted into a Stereolithography (STL) surface mesh. The STL surface mesh contains a large number of triangles (>1.3 million) to avoid the loss of geometric details. In the next step, the commercial meshing software, Sharc Harpoon is used to transform the surface mesh into a volume mesh. The resulting numerical 3D model contains a mix of hexahedral, pentahedral and tetrahedral elements. The usage of mixed meshes has been shown to produce better numerical accuracy due to decreased element distortion [36]. All FE simulations were done using the commercial finite element software, MSC.Marc[®]. The element types 7, 136

and 134 were used which corresponds to hexahedral, pentahedral and tetrahedral elements, respectively.

The geometrical parameters of the original scaffold models are listed in Table 1. The initial surface area of the samples was estimated using the Materialise Mimics software after the removal of floating pixels and has been normalized by the cuboid sample volume. Due to the high porosity relatively high values 2.78-3.05 mm²/mm³ are obtained. The mean strut thickness (MST) and its standard deviation are calculated using the open source analysis tool BoneJ [35] and the ImageJ image processing software [34]. The coefficient of variation (CoV) is obtained by the division of the standard deviation with the corresponding average MST value. The values indicate a variation of the mean strut thickness by approximately 30% which can be attributed to a thickness variation between struts and vertices. Comparing the scanned samples similar geometric parameters are obtained. This can be explained by the usage of polyurethane foam precursors in the replication method that enables close control of the scaffold geometry.

Table 1 Physical parameters of scaffold numerical samples initial state ($\Phi_{\text{Res}} = 0$ vol. %)

Samples	#1	#2	#3
Height, h (mm)	5.70	5.56	5.57
Length, l (mm)	3.62	4.66	4.65
Width, w (mm)	5.68	5.16	5.15
Porosity p^* (%)	93.31	93.79	94.34
Normalised surface area (mm ² /mm ³)	3.05	2.78	2.80
Mean strut thickness, MST (mm)	0.0777	0.0751	0.0746
MST Std. Dev. (mm)	0.0248	0.0250	0.0249
MST CoV	0.32	0.33	0.33

Material model

The investigated titania foam samples are sintered from titanium oxide nano-powder (mean particle size 23 nm) using the foam replication method [6]. The result is a foam containing relatively large meso-pores between struts and micro-pores inside the sintered titania struts. The micro-pores are too small to be captured in a μ CT scan (voxel resolution 13.97 μ m) and are therefore not included in the geometrical model. Instead, an improved material model is used for sintered bulk titania that considers this micro-porosity. This improved material model for sintered titania is based on the work by Menon [11]. They investigated the bulk erosion of sintered titania samples that were immersed in simulated body fluid (SBF) for 42 days. The titania foam of the current study was sintered at a temperature of 1300 °C which is comparable with the conditions (1400 °C) in Menon's study [11]. Relevant results of that study are summarized in Table 2 where the immersion time is shown together with the resorbed volume fraction Φ_{Res} and the Vickers hardness (HV). The yield stress σ_0 has been estimated in the present study using the Vickers hardness, i.e. $HV = 3.0 \sigma_0$ [37, 38]. The constant value of 3.0 in the equation assumes a material without significant strain hardening. Ideal plasticity of the sintered titania is assumed at all times.

Table 2 Menon study on sintered bulk titania [11]

Immersion time (days)	Volume fraction Φ_{Res} (%)	Bulk density (kg/m ³)	Vickers hardness (kgf/mm ²)	Yield stress σ_0 (MPa)
0	0	3800	404.1	134.7
14	5	3600	363.0	121.0
28	7	3540	265.5	88.5
42	12	3525	179.1	59.7
56	20	3504	114.3*	38.1
74	30	3360	33.3*	11.1

* extrapolated

Following the study by Menon numerical simulations were conducted for partially resorbed scaffolds at six stages of immersion in simulated body fluid (SBF): 0 days (original scaffold), 14 days, 28 days, 42 days, 56 days and 74 days. These immersion periods correspond to resorbed volume fractions of 0, 5, 7, 12, 20 and 30%. It should be noted that for an immersion time of 56 and 74 days the Vickers hardness was extrapolated from the data reported in [11]. For the partially resorbed models of this study the segmented μ CT geometry data was modified to the desired resorbed volume fraction using the resorption algorithm and the corresponding yield stress was used for the material model. Young's modulus E was assumed to be 6.2 GPa [39] and Poisson's ratio was defined as $\nu = 0.27$ [40] irrespective of the immersion time.

Boundary conditions and evaluation

Quasi-static mechanical compression was simulated by the finite element method in order to determine the effective mechanical properties of the original and resorbed titania scaffolds. The boundary conditions used in all simulations are shown in Fig. 3a. A time-dependent displacement boundary condition is defined on the top surface to simulate the moving platen of an experimental test rig. In addition, a zero displacement boundary condition is assigned to the opposite surface in its normal direction simulating a stationary compression platen. Nodes included in this boundary condition are confined only in the z -direction but are allowed to move freely inside the x - y plane. Fig. 3b shows the macroscopic compression strain limit $\varepsilon = 0.3$ of the computational tests.

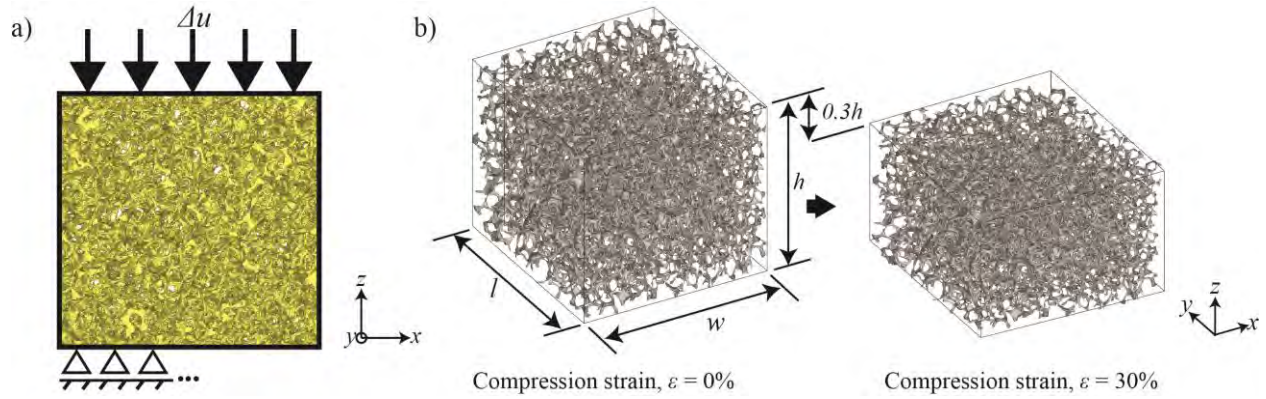


Fig. 3 a) Boundary conditions schematic diagram, b) μ CT model dimensions and compression strain limit applied in the numerical analysis

A user subroutine was applied to record the computed nodal reaction forces F and nodal displacements Δu . Based on this data, the engineering stress σ was calculated as the sum of nodal reaction forces F_N on the top surface (where the time-dependent displacement boundary condition is prescribed) divided by the initial surface area A_0 of the cubic model ($\sigma = \sum F_N/A_0$). Analogously, the engineering strain was calculated by dividing the nodal displacements by the initial height of the numerical model ($\varepsilon = \Delta u/h$). From the technical stress-strain curves the quasi-elastic gradient E , 0.2% offset yield stress $\sigma_{0.2}$ and the plateau stress σ_{Pl} were evaluated following the standard ISO 13314 (E) [41]. The quasi-elastic gradient was determined as the slope of the straight line within the linear deformation region at small strains (see curve labelled with I in Fig. 4). The 0.2% offset yield stress is determined as the compressive stress at the plastic strain of 0.2% (see label II in Fig. 4). The plateau stress has been defined as the average stress in the range of 20-30 % of compressive strain.

Mesh independence study

A mesh sensitivity study was conducted by computing six preliminary compression tests. For time-efficiency, the final compression was limited to 10% macroscopic engineering strain. Six meshes of the same geometry (based on the original μ CT data of Sample #1) with increasing elements numbers of 47k, 64k, 91k, 124k, 161k and 190 k elements respectively were tested. The obtained stress-strain curves are shown in Fig. 4. It can be observed that numerical convergence is reached for a numerical model with 161k elements, i.e. a further increase of the element number to 190k does not significantly alter the results. The average FE size that corresponds to this chosen model is 28 μm . Due to the similar geometry, the results of the mesh refinement study of Sample #1 were applied to Samples #2 and #3 and the resulting meshes (with a slightly increased mesh density) contain 166k and 164k elements, respectively.

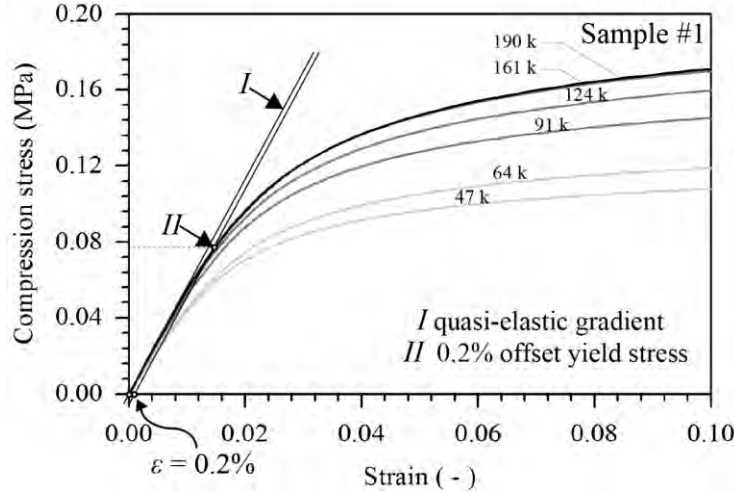


Fig. 4 Mesh sensitivity analysis on Sample #1

Results and Discussion

In order to quantify the change of effective mechanical properties due to resorption, the quasi-elastic gradient E , the 0.2% offset yield stress $\sigma_{0.2}$ and the plateau stress σ_{Pl} were determined for the resorbed volume fractions $\Phi_{res} = 0\%$ (initial scaffolds), 5%, 7%, 12%, 20%, and 30%. Starting at the volume fraction $\Phi_{res} = 12\%$ a small number of struts become disconnected from the main scaffold. This effect increases for higher resorbed volume fractions and models for $\Phi_{res} > 30\%$ are disregarded since the structure breaks into disconnected fragments that are unable to support an external load.

The stress-strain curves obtained from numerical simulations are shown in Fig. 5. The dark blue solid lines, magenta dashed lines and cyan dotted lines represent samples #1, #2 and #3 respectively. The six groups of stress-strain curves correspond to the increasing immersion time between 0 and 74 days. It can be observed that the stresses gradually decrease as the immersion time increases. A comparison of the initial scaffolds ($\Phi_{res} = 0\%$) shows a systematic deviation between samples #1-3. The higher stress values for sample #1 can be explained by the lowest porosity of this scaffold (see Table 1), followed by samples #2 and #3. The porosity dependence of mechanical properties is well documented in the literature for metallic foams [42, 43] and porous biomaterials [44–46].

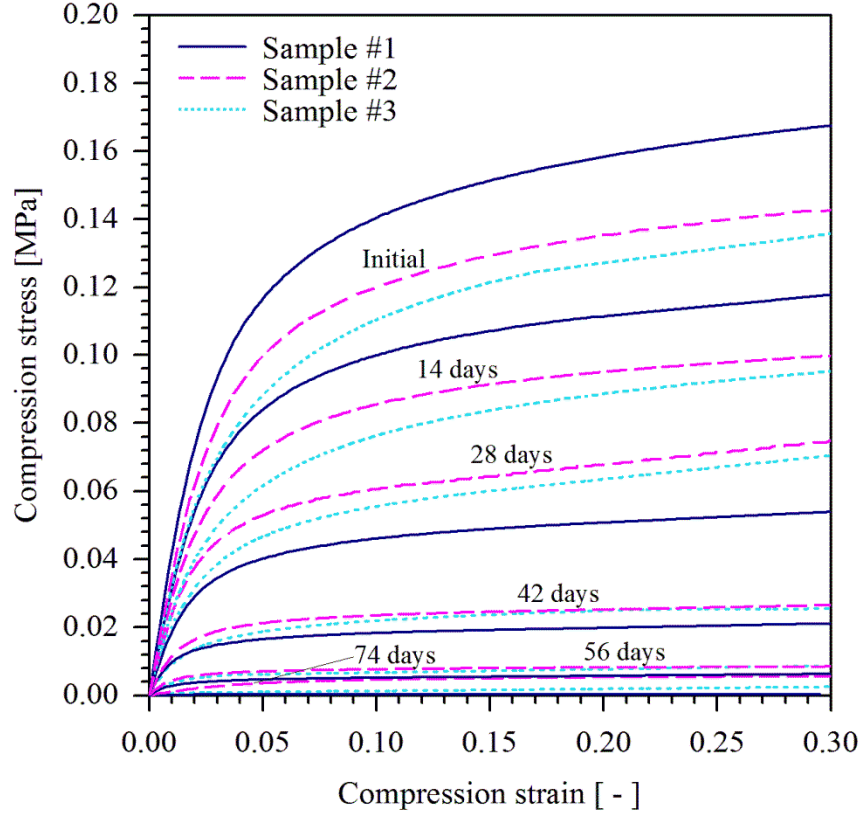


Fig. 5 Stress-strain curves from numerical simulations under a compression stress

Using the stress-strain data from Fig. 5, the quasi-elastic gradient E , the 0.2% offset yield stress $\sigma_{0.2}$ and the plateau stress σ_{PI} were determined. In Fig. 6 these effective material properties are plotted versus the immersion time in SBF solution. The quasi-elastic gradient shows initial values of $E^* = 3.4 - 4.1$ MPa. The maximum initial value belongs to the sample #1 (4.1 MPa) and the minimum value corresponds to sample #3 (3.4 MPa). As briefly discussed above, this deviation is due to porosity variations of the original samples. After immersion in SBF for 28 days ($\Phi_{res} = 7$ vol. %) the elastic gradient reduced to almost half of its initial value (~ 2.1 MPa). At an immersion time of 74 days ($\Phi_{res} = 30$ vol. %) the scaffolds begin to lose structural integrity (i.e. multiple struts become disconnected from the lattice structure) and the elastic gradient converges to zero. This loss of connectivity is shown in Fig. 7 for a thin slice of sample #1 at 0 (original), 28 and 74 days of immersion.

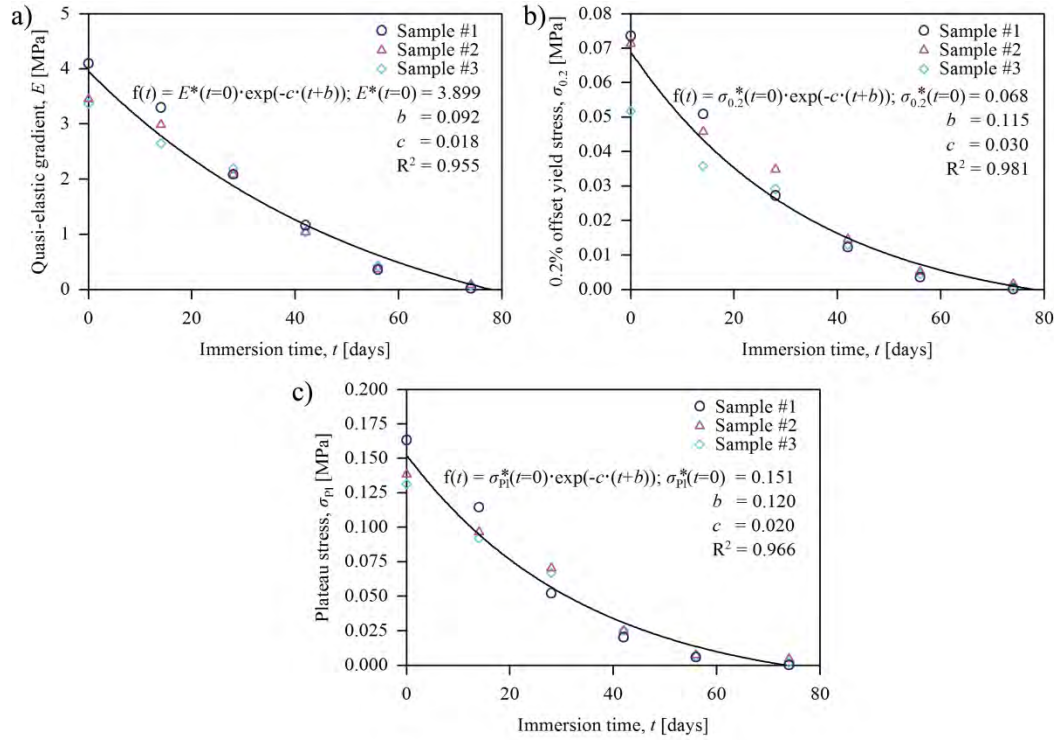


Fig. 6 a) Quasi-elastic gradient, E b) 0.2% offset yield stress, $\sigma_{0.2}$ and c) Plateau stress, σ_{p1} (20-30% strain)

The 0.2% offset yield stress and plateau stress are shown in Figs. 6 b-c. The values gradually decrease in a similar pattern to the quasi-elastic gradient. For the 0.2% offset yield stress the values of the initial scaffolds are in the range of 0.052 - 0.070 MPa and the plateau stresses are between 0.067 - 0.131 MPa. Analogous to the elastic gradient, both properties converge towards zero due to the loss of strut connectivity at 74 days (see Fig. 7). The results of the quasi-elastic gradient E , the 0.2% offset yield stress $\sigma_{0.2}$ and the plateau stress σ_{p1} can be interpolated using an exponential decay function $f(t) = a \cdot \exp(-c \cdot (t+b))$ where t is the immersion time and variables b , c are fitting parameters. The parameter a is the corresponding material property of the original scaffold, i.e. for the quasi-elastic gradient $a = E^*(t=0)$, for the 0.2% offset yield stress $a = \sigma_{0.2}^*(t=0)$, and for the plateau stress $a = \sigma_{p1}^*(t=0)$. The goodness of fit is indicated by R^2 and all values exceed 0.95. It is interesting to compare the deviations of the three tested samples #1-3. Initially, the stress-strain data (see Fig. 5) and effective material properties (see Fig. 6) exhibit a distinct deviation between samples. However, increasing immersion time in SBF appears to reduce the differences in their mechanical properties. A possible explanation is a more uniform strut thickness of the scaffolds due to immersion in SBF solutions. The average strut thickness of the models was calculated using the BoneJ plugin [35] in ImageJ. The average strut thicknesses for models #1-3 prior to immersion in SBF are 0.0777 mm, 0.0751 mm and 0.0729 mm respectively. This corresponds to a scatter of 6 % between maximum and minimum values. Immersion in SBF for 74 days yields strut thickness of 0.0651 mm, 0.0637 mm and 0.0658 mm which is equivalent to a decreased scatter of 3 %.

Furthermore, localized plastic buckling can be found in many places within the deformed computational model. At a macroscopic compressive strain of $\varepsilon = 10\%$, the plasticity

concentrates at weak features, i.e. mostly thin struts within the structure. The thin struts that are parallel to the loading direction are more prone to exhibit high stresses (indicated by black arrows in Fig. 7 at the original stage) as opposed to struts normal to the loading direction.

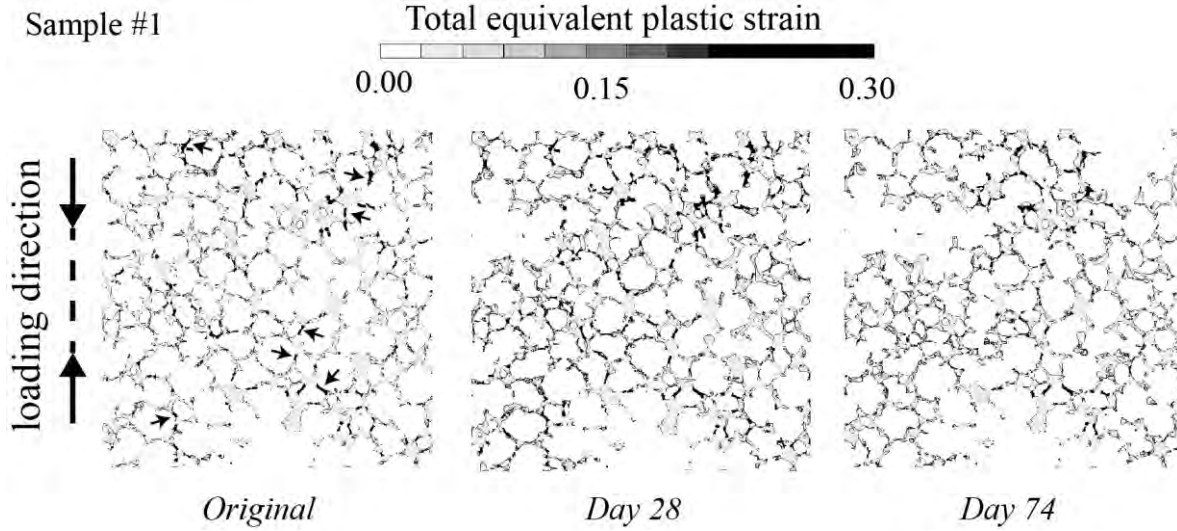


Fig. 7 Plasticity distribution map on a thin slice of titania foam sample #1 for the condition at 0, 28 and 74 days of immersion

Two characteristic geometric features can be identified in the foam structure: ‘ellipsoidal’ and vertical ‘column’ struts (see Fig. 8). Both features are found to buckle under compressive loading. After buckling of a single feature, plastic failure is likely to spread to an adjacent feature resulting in failure bands propagating through the structure. This deformation mechanism is typical for open-cell foams such as aluminium replicated foam [46] or open-cell nickel foam [47].

The buckling of the two features was further investigated with respect to their compressive strength. To this end, the strut shapes were analysed using simplified FE models based on direct measurements on the μ CT data. In the case of the ellipsoid the aspect ratio, strut diameter and length are determined. The column strut model requires the knowledge of the strut length and the minimum and maximum strut diameters (see Fig. 8). The measurements were taken randomly at 20 different features to obtain representative values. The average aspect ratio of the ellipsoid is $m/n = 1.4$ and its average strut thickness is 0.035 mm with standard deviations of 0.26 and 0.02 respectively. The column strut length l_{col} measurement is illustrated using a scaled-up strut image in Fig. 8. The mean value of the column strut’s length is 0.41 mm with a standard deviation of 0.1. The maximum (d_{max}) and minimum (d_{min}) diameters are also determined from direct measurement with the values of 0.035 mm and 0.0175 mm respectively. The obtained FE models are then compressed in the negative z -direction with time-dependent point load boundary condition on the nodes of the top surface(s) as indicated in Fig. 8. The displacement in the z -direction of all nodes contained within the bottom surface(s) is set to zero. For the ellipsoidal strut model, the surface nodes of the horizontal struts are ‘tied’, i.e. they must exhibit an identical

displacement in the x -direction. These ties approximate the presence of the neighbouring foam structure that provides some support to the sides of the ellipsoidal strut.

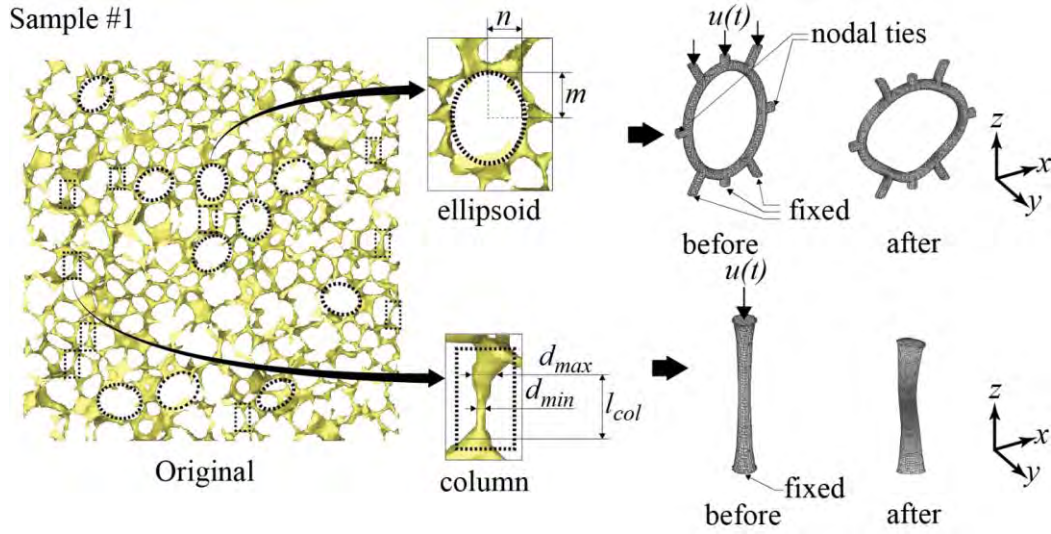


Fig. 8 Finite element (FE) modelling of simplified ellipsoidal and column struts

The compressive force-displacement data are then obtained from the numerical simulations. The force data is defined by the boundary condition and displacement has been obtained as the average nodal displacement of all nodes contained in the point force boundary condition. The linear slopes at the beginning of both force-displacement diagrams are the stiffness of the strut configurations. The FE results reveal that the ellipsoid strut has an effective gradient of 8 N/mm, whereas the column strut effective gradient is 12 N/mm. Accordingly, a column is 1.5 times stiffer than an ellipsoid strut. In contrast, the strength (i.e. the maximum load before buckling) of an ellipsoidal strut is 2.5 times higher compared with a column strut (0.25 N and 0.1 N respectively). As a result, column struts are likely to experience higher loads due to their higher stiffness but buckle prior to ellipsoidal struts due to their lower strength. Images of the progressive plasticity sequence are shown in Fig. 9. These results reinforce the findings in previous FE simulations [48, 49] that localised buckling is likely to initiate in vertical column struts (pointed by black arrows) which are parallel to the loading direction.

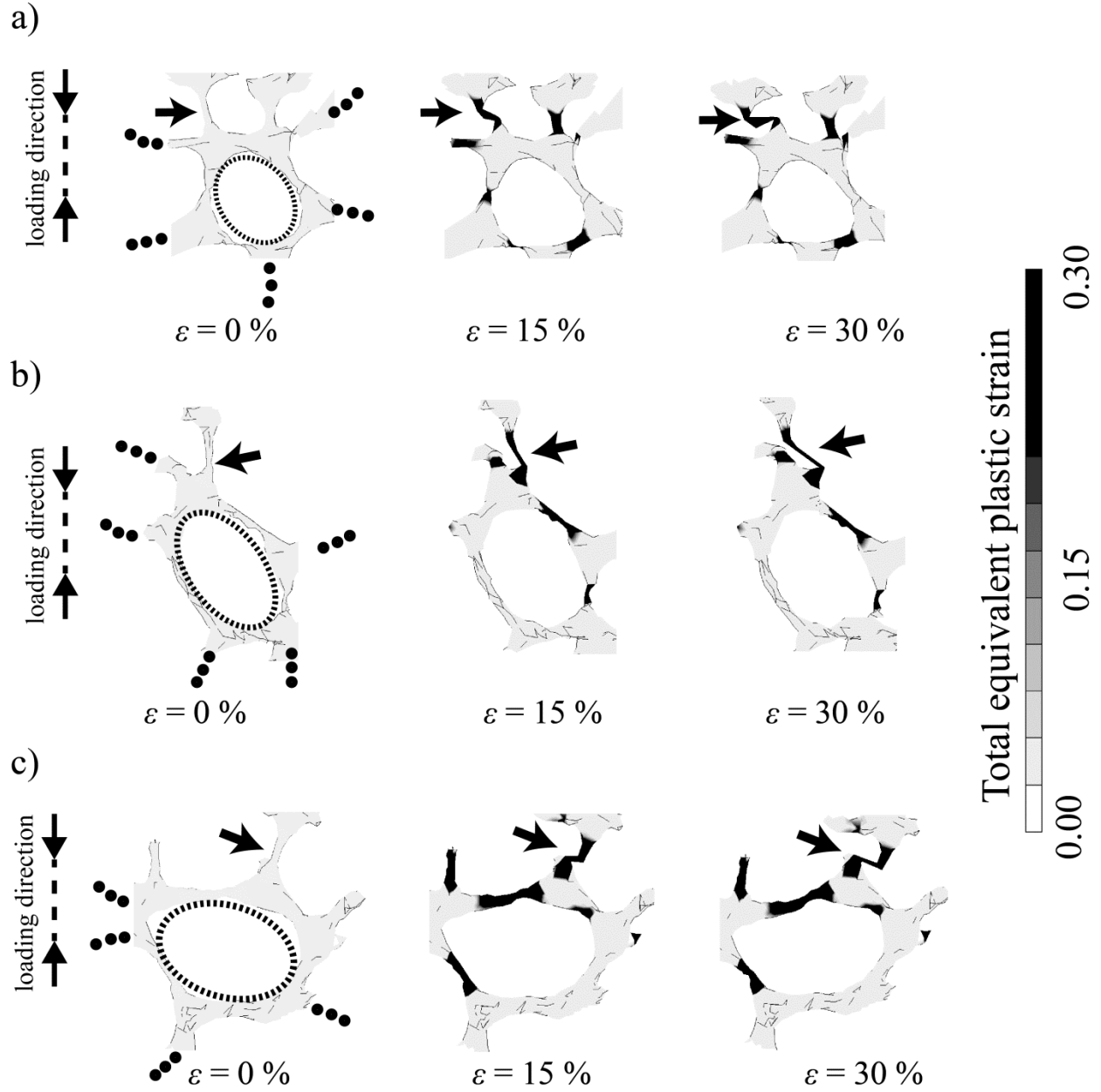


Fig. 9 Localised plastic buckling (picked at random from Samples #1-3)

Conclusions

The mechanical degradation of titania foam due to immersion in simulated body fluid has been addressed in this paper. The degradation mechanism has been simulated using a phenomenological method to predict the surface erosion at different stages due to immersion in the body fluids. Subsequent mechanical characterization of the partially resorbed scaffolds was done by making use of finite element analysis. The numerical models of the scaffolds were based on micro computed tomography data of three titania foam samples in order to accurately capture the complex material geometry. The investigation revealed a systematic decrease of the quasi-elastic gradient, 0.2% offset yield stress and plateau stress. The degradation of these mechanical

properties can be accurately expressed using an exponential decay function. This function scales the mechanical property of the original titania foam according to its immersion time. A detailed deformation analysis was performed on the numerical samples based on the results of the finite element analysis. The investigation revealed that plastic deformations tend to originate from thin struts that are parallel to the compressive loading direction. At strains above 10%, failure of some of these struts occurs in the form of buckling where they reached plasticity limit. When an individual strut has buckled it can no longer support the compressive load and additional force is transferred to adjacent struts. Some of these struts will buckle under the additional load causing the formation of collapse bands within the structure. Buckling analysis was conducted on two characteristic strut configurations (column and ellipsoid) of the titania foam. The results revealed that localised buckling is likely to initiate on a column struts that are 60% weaker compared to ellipsoidal strut configurations.

Acknowledgement

This research was supported by the Australian Research Council through its Discovery Project DP130101377 “Structural design of third generation biomaterials”.

References

- [1] L. L. Hench and J. M. Polak, “Third-generation biomedical materials,” *Science* (80)., vol. 295, no. 5557, pp. 1014–1017, 2002.
- [2] S. Eqtesadi, A. Motealleh, P. Miranda, A. Pajares, A. Lemos, and J. M. F. Ferreira, “Robocasting of 45S5 bioactive glass scaffolds for bone tissue engineering,” *J. Eur. Ceram. Soc.*, vol. 34, no. 1, pp. 107–118, 2014.
- [3] T. H. Ang, F. S. A. Sultana, D. W. Hutmacher, Y. S. Wong, J. Y. H. Fuh, X. M. Mo, H. T. Loh, E. Burdet, and S.-H. Teoh, “Fabrication of 3D chitosan–hydroxyapatite scaffolds using a robotic dispensing system,” *Mater. Sci. Eng. C*, vol. 20, no. 1, pp. 35–42, 2002.
- [4] A. Pfister, R. Landers, A. Laib, U. Hübner, R. Schmelzeisen, and R. Mülhaupt, “Biofunctional rapid prototyping for tissue-engineering applications: 3D bioplotting versus 3D printing,” *J. Polym. Sci. Part A Polym. Chem.*, vol. 42, no. 3, pp. 624–638, 2004.
- [5] S. Midha, T. B. Kim, W. van den Bergh, P. D. Lee, J. R. Jones, and C. A. Mitchell, “Preconditioned 70S30C bioactive glass foams promote osteogenesis in vivo,” *Acta Biomater.*, vol. 9, no. 11, pp. 9169–9182, 2013.
- [6] Q. Z. Chen and A. R. Boccaccini, “Poly (D, L-lactic acid) coated 45S5 Bioglass®-based scaffolds: Processing and characterization,” *J. Biomed. Mater. Res. Part A*, vol. 77, no. 3, pp. 445–457, 2006.

- [7] Q. Fu, M. N. Rahaman, B. S. Bal, R. F. Brown, and D. E. Day, "Mechanical and in vitro performance of 13–93 bioactive glass scaffolds prepared by a polymer foam replication technique," *Acta Biomater.*, vol. 4, no. 6, pp. 1854–1864, 2008.
- [8] D. W. Hutmacher, M. Sittinger, and M. V. Risbud, "Scaffold-based tissue engineering: rationale for computer-aided design and solid free-form fabrication systems," *Trends Biotechnol.*, vol. 22, no. 7, pp. 354–362, 2004.
- [9] W.-Y. Yeong, C.-K. Chua, K.-F. Leong, and M. Chandrasekaran, "Rapid prototyping in tissue engineering: challenges and potential," *Trends Biotechnol.*, vol. 22, no. 12, pp. 643–652, 2004.
- [10] Q. Fu, E. Saiz, and A. P. Tomsia, "Bioinspired strong and highly porous glass scaffolds," *Adv. Funct. Mater.*, vol. 21, no. 6, pp. 1058–1063, 2011.
- [11] A. Menon, "Sintering Additives for Nanocrystalline Titania and Processing of Porous Bone Tissue Engineering Scaffolds," University of Central Florida Orlando, Florida, 2009.
- [12] M. Uchida, H.-M. Kim, T. Kokubo, S. Fujibayashi, and T. Nakamura, "Structural dependence of apatite formation on titania gels in a simulated body fluid," *J. Biomed. Mater. Res. Part A*, vol. 64A, no. 1, pp. 164–170, 2003.
- [13] Q. Fu, E. Saiz, M. N. Rahaman, and A. P. Tomsia, "Bioactive glass scaffolds for bone tissue engineering: state of the art and future perspectives," *Mater. Sci. Eng. C*, vol. 31, no. 7, pp. 1245–1256, 2011.
- [14] J. R. Jones, L. M. Ehrenfried, and L. L. Hench, "Optimising bioactive glass scaffolds for bone tissue engineering," *Biomaterials*, vol. 27, no. 7, pp. 964–973, 2006.
- [15] S. Karl and A. V Somers, "Method of making porous ceramic articles." Google Patents, 1963.
- [16] Q. Z. Chen, I. D. Thompson, and A. R. Boccaccini, "45S5 Bioglass®-derived glass–ceramic scaffolds for bone tissue engineering," *Biomaterials*, vol. 27, no. 11, pp. 2414–2425, 2006.
- [17] Q. Fu, M. N. Rahaman, B. S. Bal, L. F. Bonewald, K. Kuroki, and R. F. Brown, "Silicate, borosilicate, and borate bioactive glass scaffolds with controllable degradation rate for bone tissue engineering applications. II. In vitro and in vivo biological evaluation," *J. Biomed. Mater. Res. - Part A*, vol. 95, no. 1, pp. 172–179, 2010.
- [18] H. Fu, Q. Fu, N. Zhou, W. Huang, M. N. Rahaman, D. Wang, and X. Liu, "In vitro evaluation of borate-based bioactive glass scaffolds prepared by a polymer foam replication method," *Mater. Sci. Eng. C*, vol. 29, no. 7, pp. 2275–2281, 2009.

- [19] D. Meng, S. N. Rath, N. Mordan, V. Salih, U. Kneser, and A. R. Boccaccini, "In vitro evaluation of 45S5 Bioglass®-derived glass-ceramic scaffolds coated with carbon nanotubes," *J. Biomed. Mater. Res. Part A*, vol. 99, no. 3, pp. 435–444, 2011.
- [20] T. Fiedler, M. Fisher, J. A. Roether, I. V Belova, T. Samtleben, T. Bernthaler, G. E. Murch, and A. R. Boccaccini, "Strengthening mechanism of PDLLA coated titania foam," *Mech. Mater.*, vol. 69, no. 1, pp. 35–40, 2014.
- [21] N. Torio-Padron, D. Paul, D. von Elverfeldt, G. B. Stark, and A. M. Huotari, "Resorption rate assessment of adipose tissue-engineered constructs by intravital magnetic resonance imaging," *J. Plast. Reconstr. Aesthetic Surg.*, vol. 64, no. 1, pp. 117–122, 2011.
- [22] K. Kłodowski, J. Kamiński, K. Nowicka, J. Tarasiuk, S. Wroński, M. Świętek, M. Błażewicz, H. Figiel, K. Turek, and T. Szponder, "Micro-imaging of implanted scaffolds using combined MRI and micro-CT," *Comput. Med. Imaging Graph.*, vol. 38, no. 6, pp. 458–468, 2014.
- [23] X. Han and J. Pan, "A model for simultaneous crystallisation and biodegradation of biodegradable polymers," *Biomaterials*, vol. 30, no. 3, pp. 423–30, Jan. 2009.
- [24] Y. Wang, J. Pan, X. Han, C. Sinka, and L. Ding, "A phenomenological model for the degradation of biodegradable polymers," *Biomaterials*, vol. 29, no. 23, pp. 3393–3401, 2008.
- [25] T. Adachi, Y. Osako, M. Tanaka, M. Hojo, and S. J. Hollister, "Framework for optimal design of porous scaffold microstructure by computational simulation of bone regeneration," *Biomaterials*, vol. 27, no. 21, pp. 3964–3972, 2006.
- [26] J. A. Sanz-Herrera and A. R. Boccaccini, "Modelling bioactivity and degradation of bioactive glass based tissue engineering scaffolds," *Int. J. Solids Struct.*, vol. 48, no. 2, pp. 257–268, Jan. 2011.
- [27] B. A. Winkelstein, *Orthopaedic biomechanics*. CRC Press, 2012.
- [28] A. Göpferich, "Mechanisms of polymer degradation and erosion," *Biomaterials*, vol. 17, no. 2, pp. 103–114, 1996.
- [29] M. A. Attawia, K. M. Herbert, K. E. Uhrich, R. Langer, and C. T. Laurencin, "Proliferation, morphology, and protein expression by osteoblasts cultured on poly (anhydride-co-imides)," *J. Biomed. Mater. Res.*, vol. 48, no. 3, pp. 322–327, 1999.
- [30] J. C. Middleton and A. J. Tipton, "Synthetic biodegradable polymers as orthopedic devices," *Biomaterials*, vol. 21, no. 23, pp. 2335–2346, Dec. 2000.
- [31] D. W. Hutmacher, "Scaffolds in tissue engineering bone and cartilage," *Biomaterials*, vol. 21, no. 24, pp. 2529–2543, Dec. 2000.

- [32] L. Wu and J. Ding, "In vitro degradation of three-dimensional porous poly(D,L-lactide-co-glycolide) scaffolds for tissue engineering," *Biomaterials*, vol. 25, no. 27, pp. 5821–30, Dec. 2004.
- [33] O. Caty, E. Maire, S. Youssef, and R. Bouchet, "Modeling the properties of closed-cell cellular materials from tomography images using finite shell elements," *Acta Mater.*, vol. 56, no. 19, pp. 5524–5534, 2008.
- [34] C. A. Schneider, W. S. Rasband, and K. W. Eliceiri, "NIH Image to ImageJ: 25 years of image analysis," *Nat Meth*, vol. 9, no. 7, pp. 671–675, 2012.
- [35] N. A. Kotov, F. C. Meldrum, and J. H. Fendler, "Monoparticulate layers of titanium dioxide nanocrystallites with controllable interparticle distances," *J. Phys. Chem.*, vol. 98, no. 36, pp. 8827–8830, 1994.
- [36] C. Veyhl, I. V. Belova, G. E. Murch, A. Öchsner, and T. Fiedler, "On the mesh dependence of non-linear mechanical finite element analysis," *Finite Elem. Anal. Des.*, vol. 46, no. 5, pp. 371–378, 2010.
- [37] A. E. Tekkaya, "Relationship between Vickers Hardness and Yield Stress for Cold Formed Materials," *steel Res.*, vol. 71, no. 1, 2000.
- [38] D. Tabor, *The hardness of metals*, vol. 10. ClarendonP, 1951.
- [39] Z. Li, Y. Qu, X. Zhang, and B. Yang, "Bioactive nano-titania ceramics with biomechanical compatibility prepared by doping with piezoelectric BaTiO₃," *Acta Biomater.*, vol. 5, no. 6, pp. 2189–2195, 2009.
- [40] S. J. Kalita, S. Qiu, and S. Verma, "A quantitative study of the calcination and sintering of nanocrystalline titanium dioxide and its flexural strength properties," *Mater. Chem. Phys.*, vol. 109, no. 2–3, pp. 392–398, 2008.
- [41] I. Standard, "ISO 13314:2011(E) Mechanical testing of metals — ductility testing — compression test for porous and cellular metals," *Reference number ISO*, vol. 13314, no. 13314. pp. 1–7, 2011.
- [42] C. San Marchi and A. Mortensen, "Deformation of open-cell aluminum foam," *Acta Mater.*, vol. 49, no. 19, pp. 3959–3969, 2001.
- [43] Y. Conde, J. Despois, R. Goodall, A. Marmottant, L. Salvo, C. San Marchi, and A. Mortensen, "Replication processing of highly porous materials," *Adv. Eng. Mater.*, vol. 8, no. 9, pp. 795–803, 2006.
- [44] K. Rezwan, Q. Z. Chen, J. J. Blaker, and A. R. Boccaccini, "Biodegradable and bioactive porous polymer/inorganic composite scaffolds for bone tissue engineering," *Biomaterials*, vol. 27, no. 18, pp. 3413–3431, 2006.

- 1
2
3
4 [45] F. G. Torres, S. N. Nazhat, S. H. Sheikh Md Fadzullah, V. Maquet, and A. R. Boccaccini,
5 "Mechanical properties and bioactivity of porous PLGA/TiO₂ nanoparticle-filled
6 composites for tissue engineering scaffolds," *Compos. Sci. Technol.*, vol. 67, no. 6, pp.
7 1139–1147, 2007.
8
9
10 [46] S. C. Baker, G. Rohman, J. Southgate, and N. R. Cameron, "The relationship between the
11 mechanical properties and cell behaviour on PLGA and PCL scaffolds for bladder tissue
12 engineering," *Biomaterials*, vol. 30, no. 7, pp. 1321–1328, 2009.
13
14
15
16
17
18
19
20
21
22
23
24
25
26
27
28
29
30
31
32
33
34
35
36
37
38
39
40
41
42
43
44
45
46
47
48
49
50
51
52
53
54
55
56
57
58
59
60
61
62
63
64
65

Chapter 9

Conclusions and outlook

In this thesis, the characterisation of advanced porous materials including cellular metals and tissue engineering scaffolds was addressed. Mechanical properties of these two types of foam materials were investigated using experimental and virtual compressive loading tests. The thesis further covers the mechanical characterisation of syntactic foam morphology, open-type and closed-type cellular metals under dynamic loading.

Where possible, a combination of experimental test and numerical simulation was employed to perform an in-depth analysis of the foam materials. Moreover, data was obtained from high definition CT images in order to generate accurate 3D models of all the samples used for computational simulations.

9.1 Engineering material charts

Together with other engineering materials, advanced porous structures fall in the attainable material space. The following engineering material charts include data points for Corevo[®] foam, perlite-metallic syntactic foam (MSF), advanced pore morphology (APM) structures and titania biomaterial scaffolds. The original chart was developed by (Gibson *et al.*, 2010) and allows the comparison of foam materials with other engineering materials as well as natural structures such as Balsa and cork wood products. In Figs. 9.1 and 9.2 materials are compared in terms of their Young's modulus and yield strengths. The charts use logarithmic scale on both axes to capture the wide range of existing materials.

In Figure 9.1, the Young's moduli of the materials investigated in this thesis are indicated as black filled ovals. For the APM structure the values for Young's modulus are taken from the literatures (Stöbener *et al.*, 2008, Stöbener and Rausch, 2009) since the investigation in this work is only dealing with a single APM foam element. In the literature, several APM foam elements are bonded together to form a cylindrical shape sample either with epoxy or polyamide. The Young's modulus of Corevo[®] foam, perlite-MSF, and titania biomaterial scaffold are in close proximity to each other and the top range of polymers and elastomers. Perlite-MSF's modulus lies in between carbon fibre composites and titanium monofilaments lattice structures or TMCs. The Young's moduli for cellular metals considered in this thesis are located outside the 'metallic foam' area (i.e. light pink with white dots). This difference may be attributed to higher density and at least partially an improved metallic foam property since the creation of the original image.

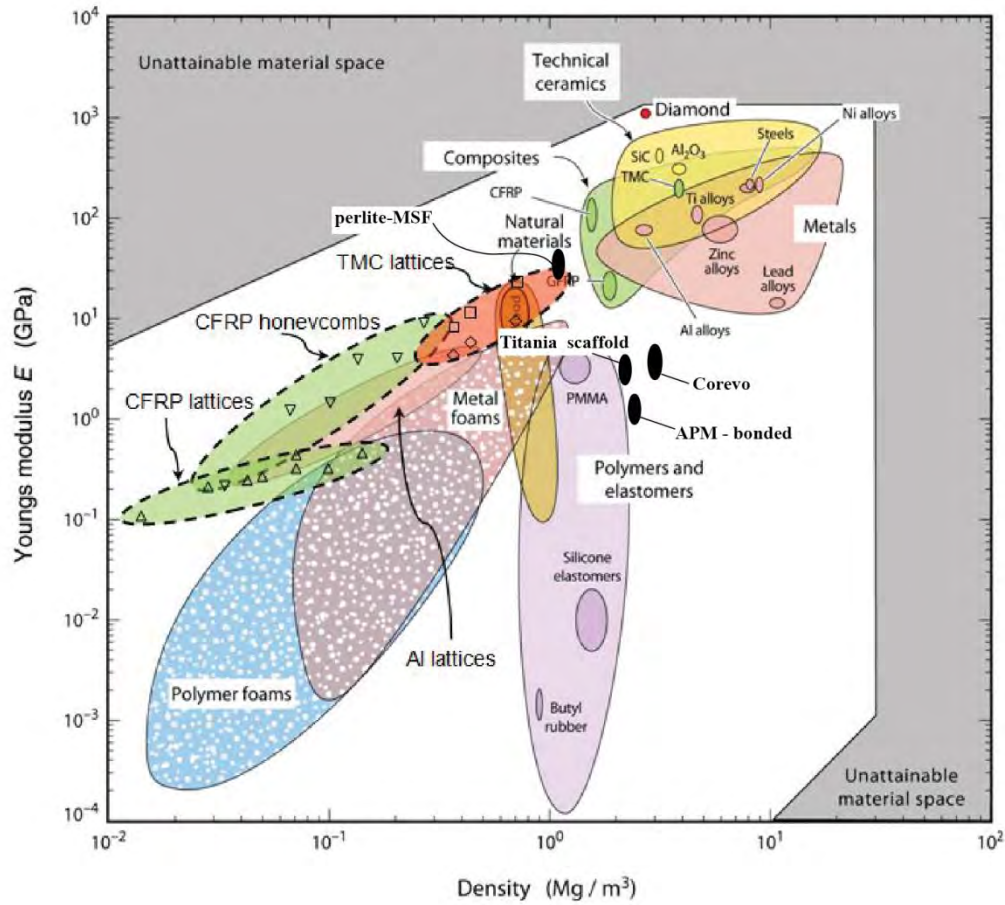


Fig. 9.1: Engineering material property charts showing the Young's modulus plotted against density (Image adapted from (Gibson *et al.*, 2010)).

The yield strengths of foam materials investigated in the scope of this thesis are shown in Figure 9.2. The position of data points is different from the ones found for Young's modulus and this may be attributed to a stronger sensitivity to differences in porosity, base material and the pore geometry. It should be further highlighted that the yield strength values for the foam materials of the current study were obtained under compressive loading. In Figure 9.2 several 'building blocks' are presented for material groups such as composites, ceramics, glasses, and polymers. By observing Figure 9.2, it becomes obvious that the challenge for future porous material development is to have lighter and stronger characteristics.

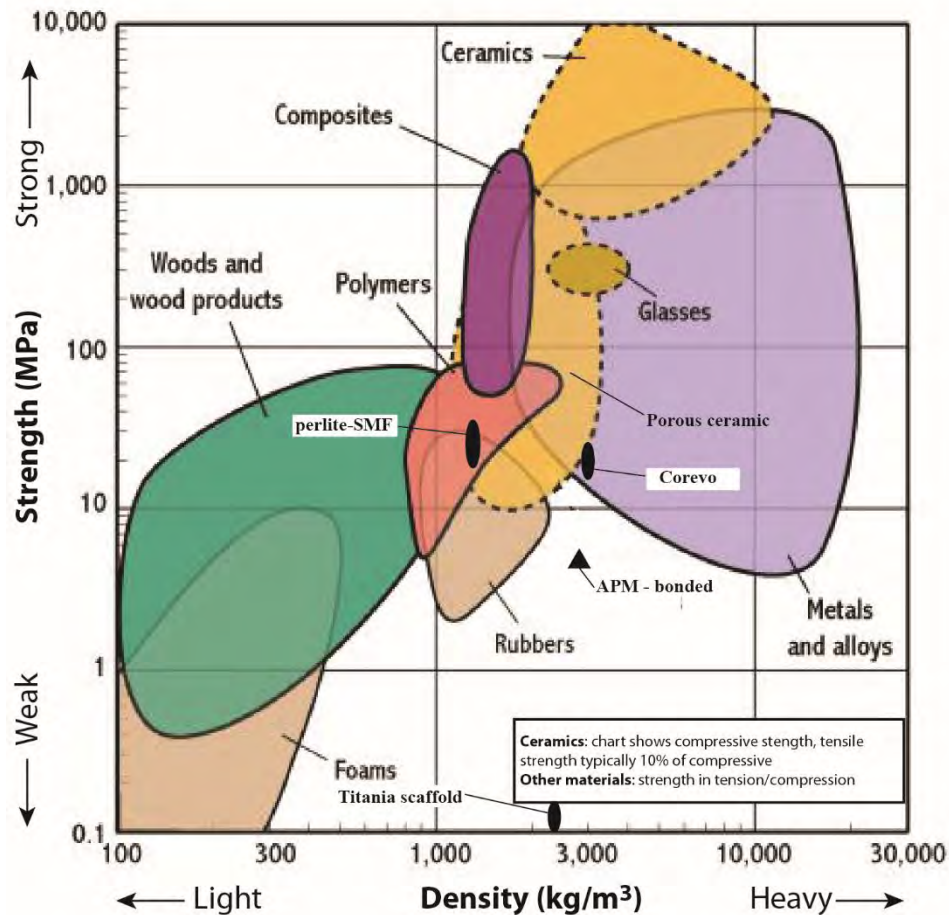


Fig. 9.2: Identifiable building blocks (denoted by random shapes of various colours) which are adjacent shown (porous ceramics, glasses, composites, polymers) (Image adapted from (Ashby *et al.*, 2000)).

9.2 Discussions

In this section, the results obtained within the scope of this thesis are interpreted with regard to the hypotheses proposed in Chapter 1.

Our investigation on the open-cell type cellular metals in Chapter 3 reveals a characteristic failure mechanism. The plastic failure observed within the structure (i.e. Corevo[®]) is found to be concentrated at weak features such as thin struts and fragile cell walls which are parallel to the loading direction. The plastification then propagates to the next weak features and subsequently forms a visible collapse band. Thus our hypothesis on the characteristic collapse mechanism is confirmed with the relevant explanation elaborated above. In addition, the parameters studied (i.e. the effective elastic gradient and initial yield stress) exhibit an anisotropic behaviour. Superior elastic properties are found along the loading direction parallel to the casting direction.

The findings in Chapter 4 show the effect of different filler particle sizes on the geometry of the syntactic foam and its mechanical properties. In order to assess the degree of this effect, elastic gradient, yield stress, plateau stress and energy absorption were computed from the numerical and experimental results. The results indicate that the perlite particle size affects

the homogeneity of the internal structure of the foam. Syntactic foams with smaller filler particles exhibit superior mechanical properties with a higher stress-strain slope and visibly less jagged curves. Foams with smaller filler particles also have a higher plateau stress and subsequently improved energy absorption capability. This constitutes the answer to our research question for this study. Furthermore better mechanical properties for smaller filler particles foam may be explained by a more refined grain structure with small dendritic arms as observed under the electron microscope.

In Chapter 5 the proposition was that there is a significant difference between the amount of load that can be supported by thin struts or weak cell walls parallel to the loading direction compared with other directions. This was not confirmed. Only a weak mechanical anisotropy of perlite-MSF samples was found. Nevertheless, the effective material properties are found to be only slightly better if the loading direction is parallel to the casting direction. Therefore the research proposition was not confirmed. The findings in this Chapter are consistent with the results obtained for Corevo[®] foam in terms of the collapse mechanism. In agreement with the experimental test, layer-wise plastification is also observed in our numerical simulations in which highly accurate 3D models are used. Moreover, foam samples with small filler particles exhibit denser collapse bands compared to medium and large filler particles syntactic foams. This is likely due to strain hardening that increases the local yield stress and consequently spread to the neighbouring fragile struts and cell walls.

Results from Chapter 6 verify that plastic deformation of single APM foam is not uniform throughout the structure (our research question for this study). The plasticity is concentrated in a conical sub-volume with a 45° angle of the APM sphere. This cone is located immediately under the loading plate for both quasi-static and dynamic tests. Such plastic deformation is reported for the first time. Furthermore, APM foam elements with a larger diameter exhibit 3.3 times higher compressive force as compared to smaller diameter foam elements. It is also concluded from our numerical simulations that the APM foam elements skin play an important role in improving its mechanical properties. The stiffness of the structure without the skin is reduced to 30% of the foam elements structure with the skin intact.

In Chapter 7, our hypothesis on the difference between the mechanical response of quasi-static and dynamic loadings was tested. The dynamic mechanical properties are found to be significantly different from the quasi-static counterparts. In the dynamic loading test, the major plastification areas are concentrated towards the surface in contact with the moving pressure stamp. These observations are obtained by means of numerical analysis and IR thermal camera images. A likely explanation of this plastification behaviour is due to inertia effects resulted from the dynamic loading.

In Chapter 8, it was clearly shown that the mechanical properties of titania scaffold structure disintegrate gradually when eroded in body fluid solutions. By using several samples synthesised from replication casting method, parameters such as elastic gradient, 0.2% offset yield stress and plateau stress were characterised. The changes of these parameters were also observed for an implantation period of 0 up to 10 weeks. As was stated in our hypothesis, the mechanical properties of tissue engineering scaffold studied in this chapter can be accurately modelled using an exponential decay function of the immersion time. This function scales the mechanical property of the original titania scaffold with respect to an implantation period of 10 weeks where the structure completely loses its mechanical integrity. From the post-script file retrieved from numerical analysis, localised plastic buckling is observed for thin struts that are parallel to the loading direction throughout the scaffold structures.

9.3 Conclusions

The key conclusions from the conducted investigations can be summarised as follows:

1. Fragile features in cellular metals such as weak cell walls and thin struts that are parallel to the macroscopic loading direction are prone to reach early plastification and failure.
2. Some mechanical anisotropy is commonly found in cellular metals made by investment casting in the direction that is parallel to the casting direction. However, the degree of the anisotropy varies on parameters such as pore geometry and pore spatial distribution.
3. APM foam elements with larger diameter exhibit higher support and can tolerate maximum compressive force by a factor of 3.3 of the maximum compressive force for APM elements with smaller diameter.
4. For a single APM foam element, plasticity is concentrated immediately under the pressure stamp during the quasi-static and dynamic loading tests. The region deformed by the compressive force is localised in upside down conical sub-volume with a 45° angle.
5. For other foam materials (i.e. Corevo[®], perlite-MSF), a so-called layer wise plastic collapse is observed and they are mostly parallel to the force platen.
6. Micro-inertial effect triggered by dynamic loadings causes the occurrence of plastification in the area of contact between the exerted force and the cellular metal sample's surface.
7. The general mechanical properties of the ceramic-based (i.e. titania) tissue engineering scaffolds are similar to cellular metals which is demonstrated by an extended stress plateau followed by densification at high deformation strains.
8. The controlled surface degradation and material properties changes of biomaterial scaffolds considered in this thesis can be characterised using an exponential decay function. The surface degradation is controlled to match the experimental degradation performed *in vitro* taken from literature.
9. The degradation of titania scaffolds can be scaled based on the respective mechanical properties of the original foam according to its immersion time.

9.4 Outlook

For the purpose of future development of this area, the following suggestions can be outlined:

- Investigation by means of experimental and numerical analysis can be extended to engineering elements such as foam-filled tubes or sandwich foam structure.
- In future research, the mechanical properties and deformation mechanism of APMs or stack of APM foam elements can be investigated. This research should also include metallic sphere arrangement analysis (i.e.: FCC, BCC and Hexagonal) of the APM foam elements.

- Compressive loading can be further studied in multiple directions of a single APM foam elements to assess a possible anisotropy of the material.
- Research on MSFs can be further extended by studying the effect of sphericity of the filler particles towards the stiffness and strength of syntactic foams.

References

- ADACHI, T., OSAKO, Y., TANAKA, M., HOJO, M. and HOLLISTER, S. J. 2006. Framework for optimal design of porous scaffold microstructure by computational simulation of bone regeneration. *Biomaterials*, 27, 3964-3972.
- AMSTERDAM, E., DE HOSSON, J. T. M. and ONCK, P. R. 2008. On the plastic collapse stress of open-cell aluminum foam. *Scripta Materialia*, 59, 653-656.
- ASHBY, M. F., EVANS, A., FLECK, N. A., GIBSON, L. J., HUTCHINSON, J. W. and WADLEY, H. N. G. 2000. *Metal Foams: A Design Guide*, Butterworth-Heinemann.
- ASHBY, M. F. and MEDALIST, R. M. 1983. The mechanical properties of cellular solids. *Metallurgical Transactions A*, 14, 1755-1769.
- AUGUSTIN, C. and HUNGERBACH, W. 2009. Production of hollow spheres (HS) and hollow sphere structures (HSS). *Materials Letters*, 63, 1109-1112.
- BABSCÁN, N., MÉSZÁROS, I. and HEGMAN, N. 2003. Thermal and Electrical Conductivity Measurements on Aluminium Foams. *Materialwissenschaften und Werkstofftechnik*, Volume 34.
- BADICHE, X., FOREST, S., GUIBERT, T., BIENVENU, Y., BARTOUT, J. D., IENNY, P., CROSET, M. and BERNET, H. 2000. Mechanical properties and non-homogeneous deformation of open-cell nickel foams: application of the mechanics of cellular solids and of porous materials. *Materials Science and Engineering: A*, 289, 276-288.
- BAKER, S. C., ROHMAN, G., SOUTHGATE, J. and CAMERON, N. R. 2009. The relationship between the mechanical properties and cell behaviour on PLGA and PCL scaffolds for bladder tissue engineering. *Biomaterials*, 30, 1321-1328.
- BANHART, J. 2001. Manufacture, characterisation and application of cellular metals and metal foams. *Progress in Materials Science*, 46, 559-632.
- BANHART, J. and WEAIRE, D. 2002. On the road again: metal foams find favor. *Physics Today*, 55, 37-42.
- BART-SMITH, H., BASTAWROS, A.-F., MUMM, D., EVANS, A., SYPECK, D. and WADLEY, H. 1998. Compressive deformation and yielding mechanisms in cellular Al alloys determined using X-ray tomography and surface strain mapping. *Acta Materialia*, 46, 3583-3592.
- BASTAWROS, A., BART-SMITH, H. and EVANS, A. 2000. Experimental analysis of deformation mechanisms in a closed-cell aluminum alloy foam. *Journal of the Mechanics and Physics of Solids*, 48, 301-322.
- BAUMEISTER, E., KLAEGER, S. and KALDOS, A. 2004. Lightweight, hollow-sphere-composite (HSC) materials for mechanical engineering applications. *Journal of materials processing technology*, 155, 1839-1846.
- BAUMEISTER, E. and MOLITOR, M. 2009. Hollow Spheres in Composite Materials and Metallic Hollow Sphere Composites (MHSC). *Multifunctional Metallic Hollow Sphere Structures*. Springer.
- BAUMEISTER, J. 1990. *Verfahren zur Herstellung poröser Metallkörper*. German patent application.
- BAUMEISTER, J., BANHART, J. and WEBER, M. 1997. Aluminium foams for transport industry. *Materials and Design*, 18, 217-220.
- BAUMEISTER, J., RAUSCH, G., STÖBENER, K., LEHMHUS, D. and BUSSE, M. 2007. Verbundwerkstoffe mit Aluminiumschaum – Anwendungen im Schienenfahrzeugbau. *Materialwissenschaft und Werkstofftechnik*, 38, 939-942.
- BAUMEISTER, J. and WEISE, J. 2000. Metallic Foams. *Ullmann's Encyclopedia of Industrial Chemistry*. Wiley-VCH Verlag GmbH and Co. KGaA.
- BOCCACCINI, A., BLAKER, J., MAQUET, V., CHUNG, W., JÉRÔME, R. and NAZHAT, S. 2006. Poly(D,L-lactide) (PDLLA) foams with TiO₂ nanoparticles and

- PDLLA/TiO₂-Bioglass® foam composites for tissue engineering scaffolds. *Journal of Materials Science*, 41, 3999-4008.
- BOCCACCINI, A. R., GERHARDT, L. C., REBELING, S. and BLAKER, J. J. 2005. Fabrication, characterisation and assessment of bioactivity of poly(D,L lactid acid) (PDLLA)/TiO₂ nanocomposite films. *Composites Part A: Applied Science and Manufacturing*, 36, 721-727.
- BOOMSMA, K. and POULIKAKOS, D. 2001. The Effects of Compression and Pore Size Variations on the Liquid Flow Characteristics in Metal Foams. *Journal of Fluids Engineering*, 124, 263-272.
- CATY, O., MAIRE, E., YOUSSEF, S. and BOUCHET, R. 2008. Modeling the properties of closed-cell cellular materials from tomography images using finite shell elements. *Acta materialia*, 56, 5524-5534.
- CHEN, Q. and BOCCACCINI, A. 2006. Poly (D, L-lactic acid) coated 45S5 Bioglass®-based scaffolds: Processing and characterization. *Journal of Biomedical Materials Research Part A*, 77, 445-457.
- CHO, J., JOSHI, M. S., and SUN, C. T. (2006). Effect of inclusion size on mechanical properties of polymeric composites with micro and nano particles. *Composites Science and Technology*, 66(13)
- COUTEAU, O. AND DUNAND, D. 2008. Creep of aluminum syntactic foams. *Materials Science and Engineering: A*, 488, 573-579
- DEGISCHER, H. and KRISZT, B. (eds.) 2002. *Handbook of Cellular Metals - Production, Processing, Applications*: Wiley-VCH.
- EVANS, A. G., HUTCHINSON, J. and ASHBY, M. 1998. Multifunctionality of cellular metal systems. *Progress in Materials Science*, 43, 171-221.
- FIEDLER, T., FISHER, M., ROETHER, J. A., BELOVA, I. V., SAMTLEBEN, T., BERNTHALER, T., MURCH, G. E. and BOCCACCINI, A. R. 2014. Strengthening mechanism of PDLLA coated titania foam. *Mechanics of Materials*, 69, 35-40.
- FU, H., FU, Q., ZHOU, N., HUANG, W., RAHAMAN, M. N., WANG, D. and LIU, X. 2009. In vitro evaluation of borate-based bioactive glass scaffolds prepared by a polymer foam replication method. *Materials Science and Engineering C*, 29, 2275-2281.
- FU, Q., RAHAMAN, M. N., BAL, B. S., BONEWALD, L. F., KUROKI, K. and BROWN, R. F. 2010. Silicate, borosilicate, and borate bioactive glass scaffolds with controllable degradation rate for bone tissue engineering applications. II. In vitro and in vivo biological evaluation. *Journal of Biomedical Materials Research - Part A*, 95, 172-179.
- FU, Q., RAHAMAN, M. N., BAL, B. S., BROWN, R. F. and DAY, D. E. 2008. Mechanical and in vitro performance of 13–93 bioactive glass scaffolds prepared by a polymer foam replication technique. *Acta Biomaterialia*, 4, 1854-1864.
- FU, Q., SAI, Z., E., RAHAMAN, M. N. and TOMSIA, A. P. 2011a. Bioactive glass scaffolds for bone tissue engineering: state of the art and future perspectives. *Materials Science and Engineering: C*, 31, 1245-1256.
- FU, Q., SAI, Z., E. and TOMSIA, A. P. 2011b. Bioinspired strong and highly porous glass scaffolds. *Advanced Functional Materials*, 21, 1058-1063.
- GERHARDT, L.-C., JELL, G. and BOCCACCINI, A. 2007. Titanium dioxide (TiO₂) nanoparticles filled poly (D, L lactid acid)(PDLLA) matrix composites for bone tissue engineering. *Journal of Materials Science: Materials in Medicine*, 18, 1287-1298.
- GIBSON, L. J. and ASHBY, M. F. 1997. *Cellular Solids: Structures and Properties* Cambridge, New York, Cambridge University Press.

- GIBSON, L. J. and ASHBY, M. F. 2001. *Cellular solids - Structure and properties*, Second Edition, Cambridge University Press.
- GIBSON, L. J., ASHBY, M. F. and HARLEY, A. B. 2010. *Cellular Materials in Nature and Medicine*, New York, Cambridge University Press.
- GLORIUS, S., NIES, B., FARACK, J., QUADBECK, P., HAUSER, R., STANDKE, G., RÖBLER, S., SCHARNWEBER, D. and STEPHANI, G. 2011. Metal Foam – Bone Cement Composites: Mechanical and Biological Properties and Perspectives for Bone Implant Design. *Advanced Engineering Materials*, 13, 1019-1023.
- GUTWEIN, L. and WEBSTER, T. 2002. Osteoblast and Chondrocyte Proliferation in the Presence of Alumina And Titania Nanoparticles. *Journal of Nanoparticle Research*, 4, 231-238.
- HAN, X. and PAN, J. 2009. A model for simultaneous crystallisation and biodegradation of biodegradable polymers. *Biomaterials*, 30, 423-430.
- HIPKE, T., LANGE, G. and POSS, R. 2007. *Taschenbuch für Aluminium-schäume*, Aluminium Verlag.
- HOHE, J., HARDENACKE, V., FASCIO, V., GIRARD, Y., BAUMEISTER, J., STÖBENER, K., WEISE, J., LEHMHUS, D., PATTOFATTO, S., ZENG, H., ZHAO, H., CALBUCCI, V., RUSTICHELLI, F. and FIORI, F. 2012. Numerical and experimental design of graded cellular sandwich cores for multi-functional aerospace applications. *Materials and Design*, 39, 20-32.
- HOLLISTER, S. J. 2005. Porous scaffold design for tissue engineering. *Nature materials*, 4, 518-524.
- HOSSEINI, S. M. H., MERKEL, M. and ÖCHSNER, A. 2009. Finite element simulation of the thermal conductivity of perforated hollow sphere structures (PHSS): Parametric study. *Materials Letters*, 63, 1135-1137.
- HUTMACHER, D. W., SITTINGER, M. and RISBUD, M. V. 2004. Scaffold-based tissue engineering: rationale for computer-aided design and solid free-form fabrication systems. *Trends in Biotechnology*, 22, 354-362.
- IFAM 2007. Advanced Pore Morphology (APM) Metal Foams. In: (IFAM), F. I. F. M. (ed.). Bremen.
- JEE, C. S. Y., GUO, Z. X., EVANS, J. R. G. and ÖZGÜVEN, N. 2000. Preparation of high porosity metal foams. *Metallurgical and Materials Transactions B*, 31, 1345-1352.
- JONES, J. R., EHRENFRIED, L. M. and HENCH, L. L. 2006. Optimising bioactive glass scaffolds for bone tissue engineering. *Biomaterials*, 27, 964-973.
- JUHASZ, J. (2004). Mechanical properties of glass-ceramic A-W-polyethylene composites: effect of filler content and particle size. *Biomaterials*, 25(6), 949-955.
- KARL, S. and SOMERS, A. V. 1963. Method of making porous ceramic articles. Google Patents.
- KŁODOWSKI, K., KAMIŃSKI, J., NOWICKA, K., TARASIUK, J., WRÓŃSKI, S., ŚWIĘTEK, M., BŁAŻEWICZ, M., FIGIEL, H., TUREK, K. and SZPONDER, T. 2014. Micro-imaging of implanted scaffolds using combined MRI and micro-CT. *Computerized Medical Imaging and Graphics*, 38, 458-468.
- KOKUBO, T. and TAKADAMA, H. 2006. How useful is SBF in predicting in vivo bone bioactivity? *Biomaterials*, 27, 2907-2915.
- LEHMHUS, D., BAUMEISTER, J., STUTZ, L., SCHNEIDER, E., STÖBENER, K., AVALLE, M., PERONI, L. and PERONI, M. 2009. Mechanical Characterization of Particulate Aluminum Foams—Strain-Rate, Density and Matrix Alloy versus Adhesive Effects. *Advanced Engineering Materials*, 12, 596-603.

- LI, Z., QU, Y., ZHANG, X. and YANG, B. 2009. Bioactive nano-titania ceramics with biomechanical compatibility prepared by doping with piezoelectric BaTiO₃. *Acta Biomaterialia*, 5, 2189-2195.
- LIU, X., CHU, P. K. and DING, C. 2004. Surface modification of titanium, titanium alloys, and related materials for biomedical applications. *Materials Science and Engineering: R: Reports*, 47, 49-121.
- LU, T. J., STONE, H. A. and ASHBY, M. F. 1998. Heat transfer in open-cell metal foams. *Acta Materialia*, 46, 3619-3635.
- MARKAKI, A. and CLYNE, T. 2001. The effect of cell wall microstructure on the deformation and fracture of aluminium-based foams. *Acta materialia*, 49, 1677-1686.
- MENG, D., IOANNOU, J. and BOCCACCINI, A. 2009. Bioglass®-based scaffolds with carbon nanotube coating for bone tissue engineering. *Journal of Materials Science: Materials in Medicine*, 20, 2139-2144.
- MENON, A. 2009. *Sintering Additives for Nanocrystalline Titania and Processing of Porous Bone Tissue Engineering Scaffolds*. University of Central Florida Orlando, Florida.
- MERETOJA, V. V., TIRRI, T., ÄÄRITALO, V., WALBOOMERS, X. F., JANSEN, J. A. and NÄRHI, T. O. 2007. Titania and titania-silica coatings for titanium: comparison of ectopic bone formation within cell-seeded scaffolds. *Tissue engineering*, 13, 855-863.
- MERKEL, M., PANNERT, W. and WINKLER, R. 2009. On the Vibroacoustic Behaviour of HSS. In: ÖECHSNER, A. and AUGUSTIN, C. (eds.) *Multifunctional Metallic Hollow Sphere Structures*. Springer Berlin Heidelberg.
- MIDHA, S., KIM, T. B., VAN DEN BERGH, W., LEE, P. D., JONES, J. R. and MITCHELL, C. A. 2013. Preconditioned 70S30C bioactive glass foams promote osteogenesis in vivo. *Acta biomaterialia*, 9, 9169-9182.
- MOHAMAD YUNOS, D., BRETCANU, O. and BOCCACCINI, A. 2008. Polymer-bioceramic composites for tissue engineering scaffolds. *Journal of Materials Science*, 43, 4433-4442.
- MUÑOZ-BONILLA, A., CERRADA, M. L., FERNÁNDEZ-GARCÍA, M., KUBACKA, A., FERRER, M. and FERNÁNDEZ-GARCÍA, M. 2013. Biodegradable Polycaprolactone-Titania Nanocomposites: Preparation, Characterization and Antimicrobial Properties. *International Journal of Molecular Sciences*, 14, 9249-9266.
- NOVAK, S., DRUCE, J., CHEN, Q. Z. and BOCCACCINI, A. R. 2009. TiO₂ foams with poly(D,L-lactic acid) (PDLLA) and PDLLA/Bioglass coatings for bone tissue engineering scaffolds. *J. Mater. Sci.*, 44, 1442-1448.
- ÖCHSNER, A. and AUGUSTIN, C. 2009. Introduction: Multifunctional Metallic Hollow Sphere Structures. Springer Berlin Heidelberg.
- ÖECHSNER, A. and AUGUSTIN, C. 2009. Multifunctional Metallic Hollow Sphere Structures. *Multifunctional Metallic Hollow Sphere Structures: Manufacturing, Properties and Application, Engineering Materials*, 1.
- PANNERT, W., WINKLER, R. and MERKEL, M. 2009. On the acoustical properties of metallic hollow sphere structures (MHSS). *Materials Letters*, 63, 1121-1124.
- QUADBECK, P., HAUSER, R., KÜMMEL, K., STANDKE, G., STEPHANI, G., NIES, B., RÖBLER, S. and WEGENER, B. Iron based cellular metals for degradable synthetic bone replacement. PM2010 World Congress, Florenz, Italy, 2010.
- RAJU, P. R., SATYANARAYANA, B., RAMJI, K. and BABU, K. S. 2007. Evaluation of fatigue life of aluminum alloy wheels under radial loads. *Engineering Failure Analysis*, 14, 791-800.

- REZWAN, K., CHEN, Q. Z., BLAKER, J. J. and BOCCACCINI, A. R. 2006. Biodegradable and bioactive porous polymer/inorganic composite scaffolds for bone tissue engineering. *Biomaterials*, 27, 3413-3431.
- ROHANOVÁ, D., BOCCACCINI, A. R., YUNOS, D. M., HORKAVCOVÁ, D., BŘEZOVSKÁ, I. and HELEBRANT, A. 2011. TRIS buffer in simulated body fluid distorts the assessment of glass–ceramic scaffold bioactivity. *Acta biomaterialia*, 7, 2623-2630.
- RUSSIAS, J., SAIZ, E., DEVILLE, S., GRYN, K., LIU, G., NALLA, R. and TOMSIA, A. P. 2007. Fabrication and in vitro characterization of three-dimensional organic/inorganic scaffolds by robocasting. *Journal of Biomedical Materials Research Part A*, 83, 434-445.
- SAVAIANO, J. K. and WEBSTER, T. J. 2004. Altered responses of chondrocytes to nanophase PLGA/nanophase titania composites. *Biomaterials*, 25, 1205-1213.
- SCHWINGEL, D., SEELIGER, H.-W., VECCHIONACCI, C., ALWES, D. and DITTRICH, J. 2007. Aluminium foam sandwich structures for space applications. *Acta Astronautica*, 61, 326-330.
- SOLÓRZANO, E., RODRÍGUEZ-PEREZ, M. A. and DE SAJA, J. A. 2009. Thermal conductivity of metallic hollow sphere structures: An experimental, analytical and comparative study. *Materials Letters*, 63, 1128-1130.
- STEPHANI, G. 2010. Titanium with bioanalogues structure for use in orthopaedic implants. *Cellmet News*.
- STÖBENER, K., BAUMEISTER, J., LEHMHUS, D., RAUSCH, G., STANZICK, H. and ZÖLLMER, V. Composites based on metallic foams: phenomenology; production; properties and principles. International conference in Advanced Metallic Materials”, Smolenice, Slovakia, 2003. 281-286.
- STÖBENER, K., BAUMEISTER, J., RAUSCH, G. and RAUSCH, M. 2005a. Forming metal foams by simpler methods for cheaper solutions. *Metal Powder Report*, 60, 12-16.
- STÖBENER, K., LEHMHUS, D., AVALLE, M., PERONI, L. and BUSSE, M. 2008. Aluminum foam-polymer hybrid structures (APM aluminum foam) in compression testing. *International Journal of Solids and Structures*, 45, 5627-5641.
- STÖBENER, K., LEHMHUS, D., ZIMMER, N. and J. BAUMEISTER. 2005b. German patent application.
- STÖBENER, K. and RAUSCH, G. 2009. Aluminium foam-polymer composites: processing and characteristics. *Journal of materials science*, 44, 1506-1511.
- TAHERISHARGH, M., BELOVA, I. V., MURCH, G. E. and FIEDLER, T. 2014. Low-density expanded perlite–aluminium syntactic foam. *Materials Science and Engineering: A*, 604, 127-134.
- TIAINEN, H., WOHLFAHRT, J. C., VERKET, A., LYGSTADAAS, S. P. and HAUGEN, H. J. 2012. Bone formation in TiO₂ bone scaffolds in extraction sockets of minipigs. *Acta Biomaterialia*, 8, 2384-2391.
- TORIO-PADRON, N., PAUL, D., VON ELVERFELDT, D., STARK, G. B. and HUOTARI, A. M. 2011. Resorption rate assessment of adipose tissue-engineered constructs by intravital magnetic resonance imaging. *Journal of Plastic, Reconstructive and Aesthetic Surgery*, 64, 117-122.
- TORRES, F. G., NAZHAT, S. N., SHEIKH MD FADZULLAH, S. H., MAQUET, V. and BOCCACCINI, A. R. 2007. Mechanical properties and bioactivity of porous PLGA/TiO₂ nanoparticle-filled composites for tissue engineering scaffolds. *Composites Science and Technology*, 67, 1139-1147.
- TRITT, T. (ed.) 2004. *Thermal conductivity: theory, properties, and applications*: Kluwer Academics / Plenum Publishers.

- UCHIDA, M., KIM, H.-M., KOKUBO, T., FUJIBAYASHI, S. and NAKAMURA, T. 2003. Structural dependence of apatite formation on titania gels in a simulated body fluid. *Journal of Biomedical Materials Research Part A*, 64A, 164-170.
- VESENJAK, M., BOROVINŠEK, M., FIEDLER, T., HIGA, Y. and REN, Z. 2013. Structural Characterisation of Advanced Pore Morphology (APM) Foam Elements. *Materials Letters*.
- VESENJAK, M., FIEDLER, T., REN, Z. and ÖCHSNER, A. 2008. Behaviour of Syntactic and Partial Hollow Sphere Structures under Dynamic Loading. *Advanced Engineering Materials*, 10, 185-191.
- VESENJAK, M., GAČNIK, F., KRSTULOVIĆ-OPARA, L. and REN, Z. 2011. Behavior of composite advanced pore morphology foam. *Journal of Composite Materials*, 45, 2823-2831.
- VESENJAK, M., VEYHL, C. and FIEDLER, T. 2012. Analysis of anisotropy and strain rate sensitivity of open-cell metal foam. *Materials Science and Engineering: A*, 541, 105-109.
- VITALE-BROVARONE, C., BAINO, F. and VERNÉ, E. 2009. High strength bioactive glass-ceramic scaffolds for bone regeneration. *Journal of Materials Science: Materials in Medicine*, 20, 643-653.
- WANG, Y., PAN, J., HAN, X., SINKA, C. and DING, L. 2008. A phenomenological model for the degradation of biodegradable polymers. *Biomaterials*, 29, 3393-3401.
- WEBSTER, T. J., SIEGEL, R. W. and BIZIOS, R. 2001. Nanoceramic surface roughness enhances osteoblast and osteoclast functions for improved orthopaedic/dental implant efficacy. *Scripta Materialia*, 44, 1639-1642.
- XIE, X.-H., WANG, X.-L., ZHANG, G., HE, Y.-X., WANG, X.-H., LIU, Z., HE, K., PENG, J., LENG, Y. and QIN, L. 2010. Structural and degradation characteristics of an innovative porous PLGA/TCP scaffold incorporated with bioactive molecular icaritin. *Biomedical Materials*, 5, 054109.
- YEONG, W.-Y., CHUA, C.-K., LEONG, K.-F. and CHANDRASEKARAN, M. 2004. Rapid prototyping in tissue engineering: challenges and potential. *Trends in Biotechnology*, 22, 643-652.
- YU, M., ZHU, P. and MA, Y. 2012. Global sensitivity analysis for the elastic properties of hollow spheres filled syntactic foams using high dimensional model representation method. *Computational Materials Science*, 61, 89-98.

Appendix

Determination of the thermal conductivity of periodic APM foam models

In this section, the thermal properties of APM foam elements are investigated for the first time. Numerical models of metallic foam assembled by APM foam elements of two different diameter sizes (i.e. 5 mm and 10 mm) are considered. The foam elements are identical to the ones investigated in Chapter 5 for mechanical characterisation. In the case of APM foam elements, the material can absorb a substantial amount of compressive stress whilst being lightweight and having adjustable effective thermal conductivity when different morphological arrangements (i.e. syntactic or sintered) are chosen.

Syntactic and partial morphologies are considered in this thermal conductivity simulation. The complex internal structure of a single APM foam element is captured by means of a high resolution micro-computed tomography (μ CT) imaging approach. The obtained three-dimensional (3D) geometry data is directly converted into Lattice Monte Carlo (LMC) calculation models. In the numerical simulations, symmetric boundary conditions are used and APM foam elements are arranged in a primitive cubic pattern to mimic an infinite APM foam element structure. The effective thermal conductivity tensor is obtained for different scans of APM foam elements. Furthermore, partial APM foams obtained e.g. by sintering or adhesive bonding and syntactic (infiltration casting using a metallic phase) morphology are distinguished. The average thermal conductivity is found to be 6.4 (ϕ 5 mm) and 7.4 (ϕ 10 mm) times higher for syntactic compared to sintered APM foam. For sintered APM foam element arrangement, the absolute value of thermal conductivity ranges 3.7 – 6.3 W/mK. The thermal conductivity can be adjusted between 32.5 – 40.0 W/mK for the thermal conductivity of syntactic APM foam element structures.

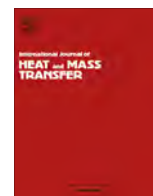
In summary, the effective thermal conductivity can be tailored according to the desired application whether the foam structure needed to be a thermal insulator or thermal conductor by switching the spatial assembly from syntactic to sintered arrangement.

This investigation has been published online and accepted for print publication by the journal International Journal of Heat and Mass Transfer.

T Fiedler, MA Sulong, M Vesenjak, Y Higa, IV Belova, A Öchsner, GE Murch, "Determination of the thermal conductivity of periodic APM foam models." *International Journal of Heat and Mass Transfer* 73 (2014): 826-833.

Reprint license has been obtained from Elsevier.

Copyright © 2015 Elsevier



Determination of the thermal conductivity of periodic APM foam models



T. Fiedler^{a,*}, M.A. Sulong^a, M. Vesenjak^b, Y. Higa^c, I.V. Belova^a, A. Öchsner^{d,a}, G.E. Murch^a

^a Centre for Mass and Thermal Transport in Engineering Materials, University of Newcastle, School of Engineering, Callaghan, NSW 2308, Australia

^b University of Maribor, Faculty of Mechanical Engineering, 2000 Maribor, Slovenia

^c Okinawa National College of Technology, Department of Mechanical Systems Engineering, 905-2192 Nago, Okinawa, Japan

^d Discipline of Mechanical Engineering, Griffith University (Gold Coast Campus), Parklands Drive, Southport, Queensland 4214, Australia

ARTICLE INFO

Article history:

Received 20 September 2013

Received in revised form 20 February 2014

Accepted 20 February 2014

Available online 21 March 2014

Keywords:

Cellular metal

Advanced pore morphology foam

Thermal conductivity

Lattice Monte Carlo

Analytical analysis

ABSTRACT

Advanced pore morphology (APM) foam elements have a spherical outer skin and a porous inner structure. In this study, the method of Lattice Monte Carlo is applied to determining the thermal characterisation of periodic structures formed by spherical APM foam elements. Two diameters, i.e. 5 mm and 10 mm spheres, are considered. To this end, micro-computed tomography data of real samples is converted into numerical calculation models. This procedure allows the accurate geometric representation of the complex internal foam geometry. Lattice Monte Carlo is then used to obtain the effective thermal conductivity of partial and syntactic structures made up of APM foam elements. Samples are analysed for variation in absolute and directional (anisotropy) thermal conductivity.

© 2014 Elsevier Ltd. All rights reserved.

1. Introduction

This work addresses the determination of the effective thermal conductivity of a periodic model of cellular metal assembled from advanced pore morphology (APM) foam elements. Cellular metals exhibit a number of attractive properties such as high specific strength [1], controlled energy absorption [2], damping [3] and versatile thermal properties [4,5]. Furthermore, large specific internal surface areas make them attractive candidates for application as heat exchanger or catalysts [6,7]. Cellular metals are formed from a metallic matrix with internal porosity. Structures with interconnected and mutually insulated pores are called open-celled and closed-celled, respectively. A major challenge that impedes the large scale industrial application of cellular metals is the inconsistency of physical properties [8]. Previous analyses have shown that changes in porosity [9,10], pore size and shapes [11] or even minor geometrical defects [12] can cause a significant variation in the effective properties. A promising solution is the assembly of cellular metals using pre-manufactured building elements. As an example, metallic hollow sphere structures [13] are made up from hollow spherical shells of sintered metal. More recently, APM foam elements have been introduced [14]. These are (approximately) spherical particles with a metallic skin and a stochastic

internal foam structure. As such, they combine the controlled geometry of hollow sphere structures with the stochastic foam geometry of 'classical' cellular metals. APM foam elements are manufactured using a powder compaction process. AlSi7 powder and TiH₂ foaming agent are rolled into wire-shaped precursor material. This precursor is then cut into small granulates that are expanded into sphere-like foam elements (see Fig. 1). Advanced pore morphology structures (APMS) are formed by joining APM foam elements using suitable joining technologies such as sintering, soldering or adhesive bonding.

Previous analyses of APMS have focused on their mechanical properties. Lehmhus et al. [15] investigated the influence of APM foam density in quasi-static and dynamic compressive testing. Vesnjak et al. [16] addressed the compressive behaviour of single APM foam elements and composite APM foam. They further introduced infrared thermal imaging to identify areas of plasticisation in experimental testing [17]. Hohe et al. [18] conducted experimental and numerical tests on graded APM foams for multi-functional aerospace applications. Their main focus of investigation was perforation resistance against bird strike events.

For the first time, the present paper investigates the thermal properties of APMS. Two different types of APM foam elements with diameters 5 mm and 10 mm are considered. Furthermore, two different morphologies (partial and syntactic APMS) are addressed. To this end, the complex geometry of single APM foam elements is captured using micro-computed tomography (μ CT) imaging. Geometric data are then converted directly into Lattice

* Corresponding author. Tel.: +61 02 4921 6188.

E-mail address: Thomas.Fiedler@newcastle.edu.au (T. Fiedler).



Fig. 1. Light photograph of APM foam elements.

Monte Carlo (LMC) calculation models. Symmetric boundary conditions are used in the simulations and mimic an infinite APMS structure with foam elements arranged in a primitive cubic pattern. For each sample, the effective thermal conductivity tensor is obtained. APMS are tested for directional variation (anisotropy) and sample variation of their effective thermal conductivity.

2. APMS geometry

The APMS geometry is captured using micro-computed tomography imaging. An Xradia MicroXCT-400 machine with a Hamamatsu L8121-03 X-ray source was used for the scanning. Due to the size differences of the samples, the voxel resolutions were limited to 5.61 μm and 11.08 μm , respectively. A total of 1800 absorption radiographs (exposure time 16 s) was captured with 0.2° rotation for each projection. The selected acceleration voltage was 140 kV with a current of 70 μA . Segmentation of the μCT data allows material identification (in the case of APM foam elements this is either AlSi7 aluminium alloy or air). This material data is then mapped onto lattice models (see below *Lattice Monte Carlo Analysis*) where each lattice node corresponds to a voxel of the μCT data. A three-dimensional μCT reconstruction of a 10 mm APMS foam element is shown in Fig. 2. In order to visualise the internal pore structure, the foam element is cropped along one of its central planes.

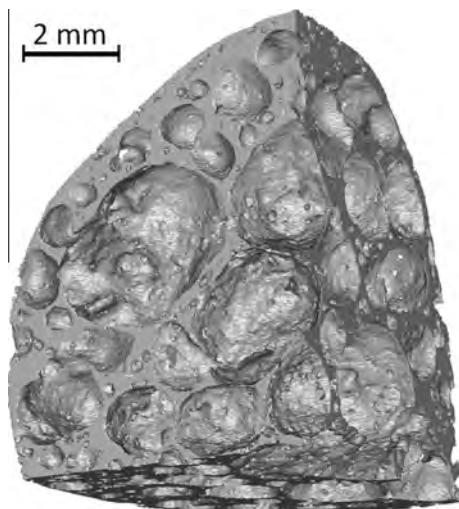


Fig. 2. Micro-computed CT data: three-dimensional reconstruction (cropped to 1/8 of the spherical element).

The internal pores of APMS foam elements are predominantly closed, i.e. enclosed by a solid cell wall. However, the micro-computed tomography data indicates small openings within these cell walls connecting the majority of neighbouring pores. This observation can be confirmed using electron-beam microscopy of the same material. Fig. 3 shows a micrograph of an APM foam element cross section and small holes within the cell walls can easily be identified.

The geometric properties of the scanned foam elements #1–10 are summarized in Table 1.

3. Lattice Monte Carlo analysis

Numerical analysis of the effective thermal conductivity of APMS is performed using Lattice Monte Carlo (LMC) analysis. This versatile finite difference method has been successfully applied to determine the effective thermal conductivity of cellular metals such as sintered fibre structures [19], hollow sphere structures [20], Alporas® aluminium foam and M-Pore® metal sponge [21]. The LMC method is based on probing particles that are inserted into a lattice model to explore the effective diffusivity of composite materials. Geometry data is usually derived from μCT imaging. Alternatively simplified model structures can also be utilised.

Probing particles perform random walks within the primitive cubic lattice model and are directed by jump probabilities. These probabilities are the thermal diffusivities of each material (normalised by the maximum thermal diffusivity of all components present in the model). Whilst simulating APMS, the effective thermal conductivity of the cell wall material AlSi7 is 167 W/(m K) [22]. The thermal conductivity of air enclosed within the pores is only 0.027 W/(m K) [23] and thus can be assumed to be zero to a good approximation. This minor simplification allows decreasing the required computation times for each calculation. The accuracy of LMC analyses is determined by the number n of probing particles

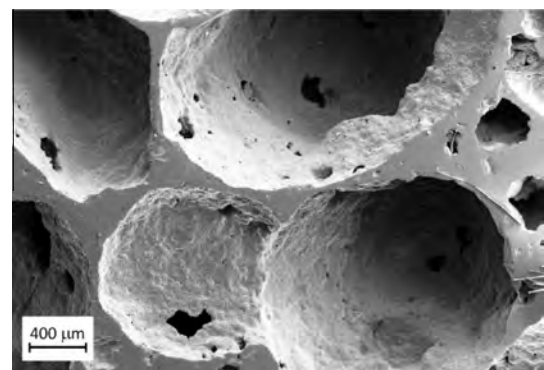


Fig. 3. Electron beam microscopy of APM foam element.

Table 1

Geometric properties of APM foam elements.

Sample	Nominal outer diameter (mm)	Porosity (%)	Mass (g)
#1	5	81.0	0.064
#2	5	85.3	0.050
#3	5	80.5	0.066
#4	5	82.0	0.061
#5	5	83.7	0.055
#6	10	84.1	0.43
#7	10	84.6	0.42
#8	10	82.3	0.48
#9	10	81.6	0.50
#10	10	82.3	0.48

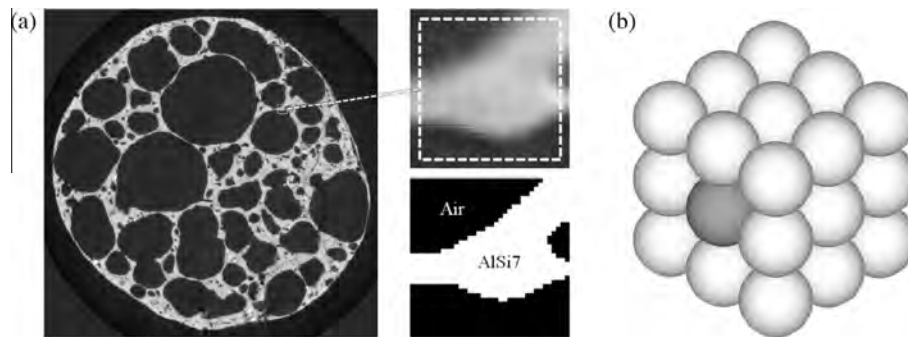


Fig. 4. Model generation of APMS: (a) segmentation of APM foam element, (b) primitive cubic assembly of APMS.

and can be estimated according to $\varepsilon \approx 1/n^{0.5}$. Within all analyses $n = 10^5$ particles were used resulting in $\varepsilon \approx 0.32\%$. Each particle needs to explore a representative volume of the geometry, i.e. a sufficient number of successful jump attempts is required. In the current simulations 10^6 jump attempts per particle were defined resulting in a mean diffusion length $\langle |R| \rangle = 1365$ voxels. Since this number exceeds the model resolution (i.e. 900 voxels per edge) the condition of representative random walks is satisfied. A detailed description of the LMC algorithm can be found in the literature [24].

Fig. 4(a) shows the segmentation of an APM foam element cross section. The magnification shows that geometry data is assembled by multiple voxels with varying grey levels. Light voxels correspond to volumes with strong X-ray attenuation, i.e. the higher density AlSi7 in APM foam elements. Dark voxels indicate the lower density air that fills internal and external pores. For the segmentation, i.e. the distinction between air and AlSi7 a critical grey level needs to be defined. Any voxels with a higher brightness are then assigned to the metallic AlSi7 phase. The mass of the resulting virtual APM foam element is the product of the combined metallic voxel volume and AlSi7 density $\rho = 2680 \text{ kg/m}^3$ [22]. The calculated mass is compared to measurements on the scanned sample and the segmentation threshold is iteratively adjusted until the two masses coincide. The final calculation models contain symmetric boundary conditions. This means that each APM foam element is mirrored in three perpendicular planes. As a result, single APM foam elements are expanded into infinite APMS with a primitive cubic structure (see Fig. 4(b)). Within their contact planes, all spheres are truncated by 1% of their radius in order to establish thermal contact with the mirrored neighbouring spheres. It should be mentioned here that thermal properties of single APM foam elements are not that useful since the thermal properties of structure formed by these units will be governed by the thermal contact between adjacent spheres.

The symmetric boundary condition is a simplification that has been introduced since no actual sintered or syntactic APM structures were available. In addition, due to the requirement of capturing small geometric features of the foam inside the APM elements, the limited resolution of micro-computed tomography imaging permits the scan of larger samples. The symmetric boundary condition is schematically shown in Fig. 5(a), where arrows indicate the direction of the maximum thermal conductivity of the mirrored foam element. The resulting structure is in fact periodic (white dashed box). In the case of the three-dimensional model considered, the periodic unit cell contains 8 spheres. However, the symmetric boundary condition introduces two simplifications. First, APM foam elements in a real structure are most likely not arranged in a perfect primitive cubic pattern. This will increase their packing density and thus change their thermal conductivity. Thus, the calculated values for the effective thermal conductivity are a lower bound for partial and an upper bound for syntactic APM structures. Second, the vector indicating the direction of the maximum thermal conductivity is likely to be randomly oriented in an APM structure as schematically shown in Fig. 5(b). As a result, the anisotropy of a single foam element is going to be diminished in the overall structure. In contrast, symmetric boundary conditions preserve the anisotropy in the normal directions of the symmetry planes. This can be easily verified using theoretical results of [25]. Therefore, the anisotropy study given in this paper is presenting an upper bound of thermal anisotropy in APM structures. It should be clarified here that the current study calculates the effective thermal conductivity of APM foam structures assembled by APM foam elements. Whilst the geometrical model of the foam element is highly accurate (i.e. obtained by micro-computed tomography imaging), the model of the structure is simplified due to the necessary use of symmetric boundary conditions.

4. Partial APMS

First, partial APMS are considered. In these structures, APM foam elements are joined using sintering or adhesive bonding (resulting in additional thermal resistance). As a result, these materials exhibit internal porosity within the APM foam and interconnected external porosity between the foam elements. The result of a LMC simulation is the complete thermal conductivity tensor of an APMS. A total of 5 APM foam elements each for the sphere diameters 5 mm and 10 mm have been scanned using μCT imaging. As discussed above, the presented effective thermal conductivities form a lower bound for randomly packed APM foams.

Fig. 6 shows the effective thermal conductivity of 5 mm sintered APMS. Three values are indicated for each structure, i.e. the minimum, average and maximum thermal conductivities. The average thermal conductivity of 5 mm APMS is between 5.0 and 5.8 W/(m K). The standard deviation of the five samples is

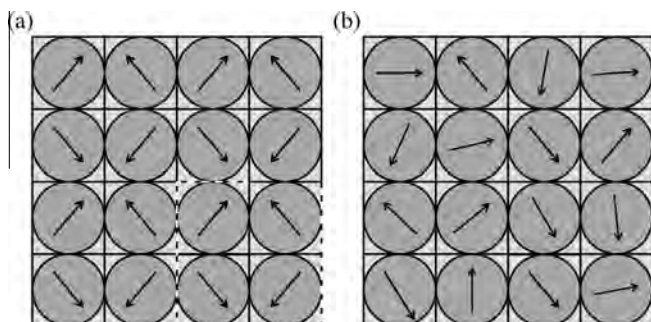


Fig. 5. Model of primitive cubic APM structures: (a) symmetric BC, (b) random orientation.

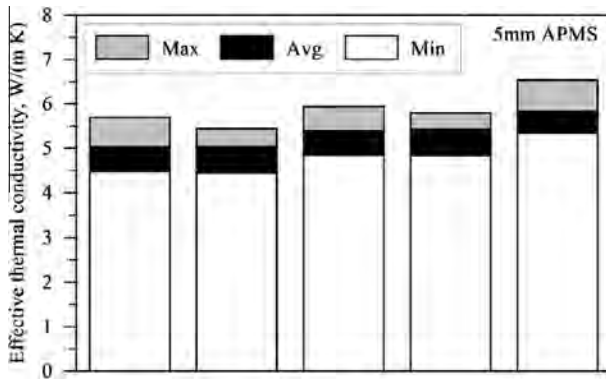


Fig. 6. Effective thermal conductivity of 5 mm sintered APMS.

0.33 W/(m K). The minimum and maximum thermal conductivities are directional values and thus indicate some material anisotropy. The corresponding minimum and maximum values (sample #1) are 4.5 W/(m K) and 6.5 W/(m K).

Fig. 7 shows the corresponding results for 10 mm sintered APMS. A strong variation of the average thermal conductivity between samples can be observed. The averages range from 3.7 W/(m K) to 6.6 W/(m K). As a result, the standard deviation of the average thermal conductivity is 1.27 W/(m K) thus clearly exceeding the value of 5 mm APMS (0.33 W/(m K)). In addition, 10 mm APMS exhibit a slightly lower thermal conductivity than 5 mm APMS. This can be partially explained by the higher porosity of 10 mm APM foam elements (see Table 1). It should be highlighted here that 10 mm APMS exhibit a very small directional variation of thermal conductivity, i.e. their minimum and maximum thermal conductivities are similar.

Fig. 8 is a plot of the effective thermal conductivities of 5 mm and 10 mm sintered APMS versus their relative density, i.e. the amount of AlSi7 voxels divided by the total number of voxels contained in each model. In addition, a linear regression (based on all data points) is plotted as dashed line. As expected, the average thermal conductivity increases with the relative density. However, a poor correlation (the squared correlation coefficient $R^2 = 0.47$) between the data points and the linear regression is observed. This indicates that the thermal conductivity of APMS is not governed by the relative density alone. Contributing factors are most likely the spatial and size distribution of internal pores and the contact between the approximately spherical APMS foam elements. Thus, a single APM foam element should not be considered a representative volume element of sintered APM foam. The effective thermal conductivity of APM foam is more likely to exhibit an averaged value in proximity to the linear regression line.

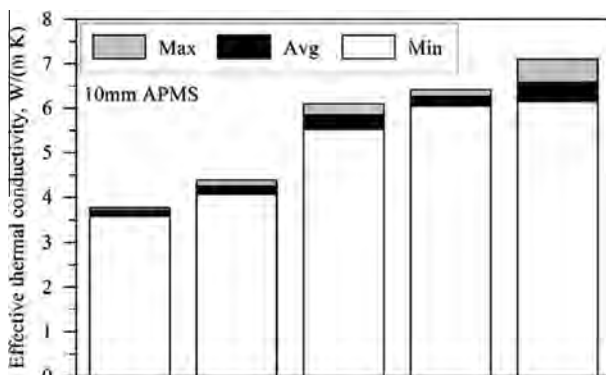


Fig. 7. Effective thermal conductivity of 10 mm sintered APMS.

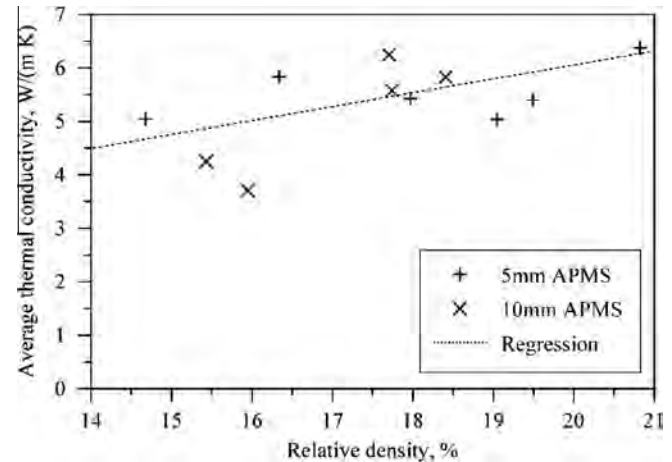


Fig. 8. Effective thermal conductivity of sintered APMS plotted vs relative density.

In the following, the anisotropy of the thermal conductivity of APMS is considered. It should be noted that the use of symmetric boundary conditions preserves the thermal anisotropy of an individual APM chosen to be the elementary block of the APM structure (see above). Figs. 9 and 10 show polar plots of the effective thermal conductivity of 5 mm and 10 mm APMS, respectively. For each sample, three curves are plotted. These three curves correspond to three arbitrary perpendicular planes of the APMS. For better comparability, all curves are rotated in such a way that the maximum conductivity direction coincides with the y axis of the plots. The 5 mm APMS show very consistent conductivity curves for all samples and planes. This reflects the close clustering of the average thermal conductivities shown in Fig. 7. In addition, a small but distinct thermal anisotropy can be observed. The average ratio of maximum and minimum thermal conductivity of each sample is 1.29.

Fig. 10 shows the conductivity polar plots of 10 mm sintered APMS. In contrast to the 5 mm APMS the curves exhibit an approximately circular shape indicating thermal isotropy, i.e. there is no clear directional variation of the effective thermal conductivity. The corresponding average ratio of maximum and minimum thermal conductivities is 1.13. However, the radius of these circles distinctly varies with the sample reflecting the changes in average thermal conductivities shown in Fig. 6. It can be concluded that 5 mm APMS exhibit thermal anisotropy whereas 10 mm APMS exhibit a strong variation of the thermal conductivity depending on single APM foam elements.

Previous tests assumed a perfect thermal contact between neighbouring spheres as may be obtained in soldered or diffusion bonded structures. However, competing joining techniques such as adhesive bonding will introduce additional thermal contact resistance R_c between spheres. Fig. 11 shows the model structure used for the study of the change in effective APMS conductivity and its dependence on the thermal contact resistance between neighbouring spheres. The model is assembled from cubes that exhibit the effective thermal conductivity of APM foam elements presented above. Between these cubes, a thin layer of thermal insulator is added that introduces the thermal contact resistance R_c .

Let us assume that the width of the resistance layers δ (shown in the darker colour in Fig. 11) is 1% of the sphere radius, then their volume $\phi = 1.5\%$ of the total volume; and we assume that its thermal conductivity is $\lambda_{res} = \epsilon \lambda_{eff}$. Then for the analytical expression of the total effective thermal conductivity λ_{eff}^{total} of the structure shown in Fig. 11 we have following options:

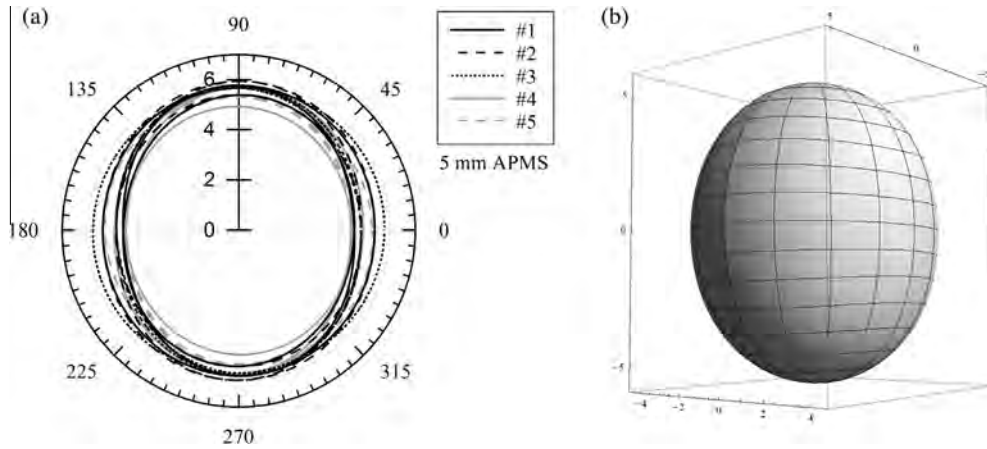


Fig. 9. (a) Polar plot of the effective thermal conductivity in W/(m K) of 5 mm sintered APMS in three perpendicular planes. (b) 3D plot of the (averaged) thermal conductivity tensor of sample #1 in three main directions.

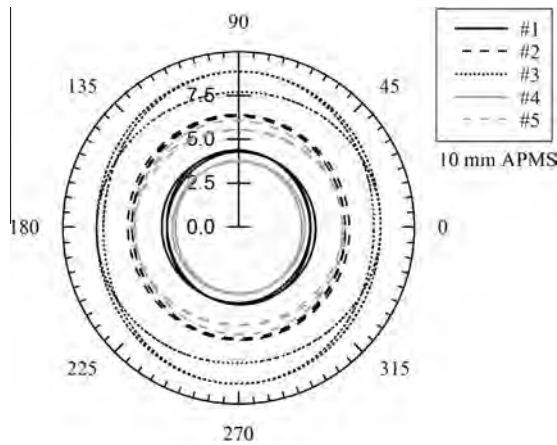


Fig. 10. Polar plot of the effective thermal conductivity in W/(m K) of 10 mm sintered APMS in three perpendicular planes.

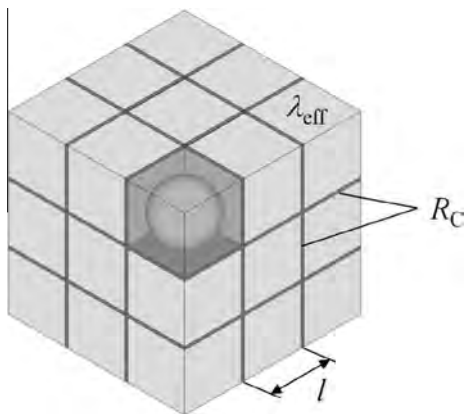


Fig. 11. Thermal resistance model.

1. Maxwell expression [26]:

$$\begin{aligned}\lambda_{eff}^{total} &= \lambda_{res} \left(1 + \frac{3(1-\phi)(\lambda_{eff} - \lambda_{res})}{\phi\lambda_{eff} + (3-\phi)\lambda_{res}} \right) \\ &= \lambda_{res} \left(\frac{2.97\lambda_{eff} + 0.03\lambda_{res}}{0.015\lambda_{eff} + 2.985\lambda_{res}} \right)\end{aligned}\quad (1)$$

2. Series-Parallel method [19,27] for the 3D, closed cell structure case:

$$\begin{aligned}\lambda_{eff}^{total} &= \left(2\frac{\delta}{l} - \frac{\delta^2}{l^2} \right) \lambda_{res} + \left(1 - \frac{\delta}{l} \right)^2 \frac{\lambda_{eff} \lambda_{res}}{\frac{\delta}{l} \lambda_{eff} + (1 - \frac{\delta}{l}) \lambda_{res}} \\ &\approx 0.01 \lambda_{res} + 0.99 \frac{\lambda_{eff} \lambda_{res}}{0.005\lambda_{eff} + 0.995\lambda_{res}} \\ &\approx \lambda_{res} \left(\frac{0.99\lambda_{eff} + 0.01\lambda_{res}}{0.005\lambda_{eff} + 0.995\lambda_{res}} \right)\end{aligned}\quad (2)$$

It is easy to see that for the given conditions this expression is the same as the Maxwell equation (1).

3. Parallel-Series method [19,27] for the 3D, closed cell structure case:

$$\begin{aligned}\lambda_{eff}^{total} &= \frac{\lambda_{res} \left((1 - \frac{\delta}{l})^2 \lambda_{eff} + \left(2\frac{\delta}{l} - \frac{\delta^2}{l^2} \right) \lambda_{res} \right)}{\frac{\delta}{l} \left((1 - \frac{\delta}{l})^2 \lambda_{eff} + \left(2\frac{\delta}{l} - \frac{\delta^2}{l^2} \right) \lambda_{res} \right) + (1 - \frac{\delta}{l}) \lambda_{res}} \\ &\approx \lambda_{res} \left(\frac{0.99\lambda_{eff} + 0.01\lambda_{res}}{0.005\lambda_{eff} + 0.995\lambda_{res}} \right)\end{aligned}\quad (3)$$

It is easy to see that for the given conditions this expression is the same as the Maxwell equation (1).

4. The Bruggemann model [28] requires solving the following equation:

$$1 - \left(1 - \frac{\delta}{l} \right)^3 = 0.015 = \left(\frac{\lambda_{eff} - \lambda_{eff}^{total}}{\lambda_{eff} - \lambda_{res}} \right) \left(\frac{\lambda_{res}}{\lambda_{eff}^{total}} \right)^{1/3}\quad (4)$$

5. Russel equation [29]:

$$\begin{aligned}\lambda_{eff}^{total} &= \lambda_{res} \frac{(1 - \frac{\delta}{l})^2 \lambda_{eff} + (1 - (1 - \frac{\delta}{l})^2) \lambda_{res}}{\left((1 - \frac{\delta}{l})^2 - (1 - \frac{\delta}{l})^3 \right) \lambda_{eff} + \left(1 - (1 - \frac{\delta}{l})^2 + (1 - \frac{\delta}{l})^3 \right) \lambda_{res}} \\ &\approx \lambda_{res} \left(\frac{0.99\lambda_{eff} + 0.01\lambda_{res}}{0.005\lambda_{eff} + 0.995\lambda_{res}} \right)\end{aligned}\quad (5)$$

It is easy to show that for the given conditions this expression is the same as the Maxwell equation (1).

6. Misnar equation [30]:

$$\begin{aligned}\lambda_{eff}^{total} &= \lambda_{res} \left(1 + \frac{\lambda_{eff} - \lambda_{res}}{\frac{\delta}{l} \lambda_{eff} + (1 - \frac{\delta}{l}) \lambda_{res}} \right) \\ &= \lambda_{res} \left(1 + \frac{\lambda_{eff} - \lambda_{res}}{0.005\lambda_{eff} + 0.995\lambda_{res}} \right)\end{aligned}\quad (6)$$

7. Ashby equation [31]:

$$\lambda_{\text{eff}}^{\text{total}} = \phi^{\xi} \lambda_{\text{res}} = 0.015^{\xi} \lambda_{\text{res}} \quad (7)$$

where ξ ranges between 1/3 and 2/3.

8. Progellhoff's expression [32]:

$$\lambda_{\text{eff}}^{\text{total}} = \lambda_{\text{res}} \left(1 + \frac{\lambda_{\text{eff}}}{\lambda_{\text{res}}} \phi^n \right) = \lambda_{\text{res}} \left(1 + \frac{\lambda_{\text{eff}}}{\lambda_{\text{res}}} 0.015^n \right) \quad (8)$$

where n is a fitting parameter.

9. Scaling relation [27]:

$$\lambda_{\text{eff}}^{\text{total}} = \lambda_{\text{res}} \phi^n = \lambda_{\text{res}} 0.015^n \quad (9)$$

where n is a fitting parameter and usually $n \in [1.65, 1.85]$.

In Fig. 12 we have plotted all the expressions for the total effective thermal conductivity. The solid line corresponds to Bruggemann's expression (4), the long dashed line corresponds to Maxwell's expression (1), the long-short dashed line corresponds to Misnar's expression (6), the short dashed lines correspond to Progellhoff's expression with $n = 1.0$ for the line marked 8_2 , $n = 0.5$ for line marked 8_1 , and expressions (7) and (9) give lines that are very close to 0 on this scale.

It is clear that relations (7) and (9) both give very low values. On the other hand, the solution to Bruggemann's equation for the total effective conductivity is probably too high. This can be explained by noting that in the derivation of Bruggemann's equation the volume of inclusions are incrementally increased by replacing the corresponding volume of the initial composite structure (therefore the differential limit is applied from above). Progellhoff's expression (8) at the limit $\varepsilon \rightarrow 0$ gives an unrealistic high value.

Therefore the most reasonable expression for the total effective thermal conductivity is the relation 1 – the Maxwell equation. We will analyse this expression further by varying the thickness δ of the insulating layer (i.e. the adhesive joining the APM foam elements) as a fraction of the sphere radius (or length l). In Fig. 13 we plot $\lambda_{\text{eff}}^{\text{total}}$ as a function of ε for the following values of δ : 0.1% of l , 0.25% of l , 0.5% of l , 1.0% of l , and 2.5% of l . It is obvious that $\lambda_{\text{eff}}^{\text{total}}$ depends strongly on δ (as well as ε). An increase of thickness δ distinctly decreases the effective thermal conductivity for a given value of ε .

5. Syntactic APMS

In the following, syntactic APMS are considered. In syntactic structures, the space between the spherical foam elements is

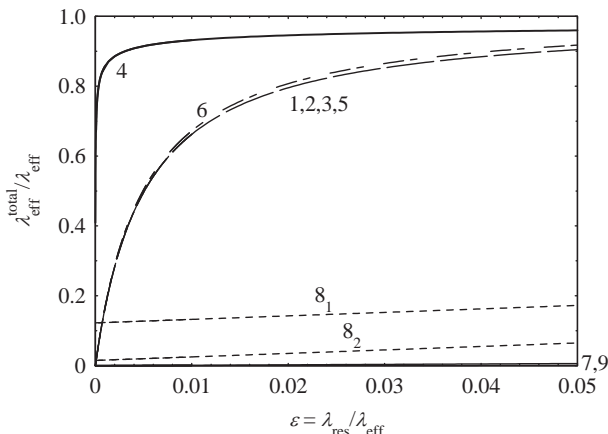


Fig. 12. Total effective thermal conductivity as a function of ε .

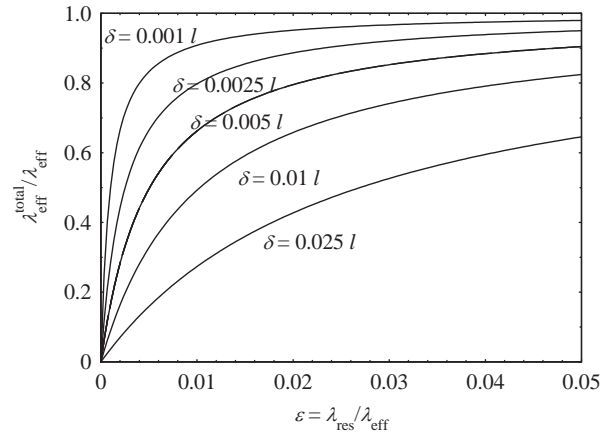


Fig. 13. Total effective thermal conductivity (Maxwell expression (1)) as a function of ε .

completely occupied by aluminium. This is achieved by filling APM foam elements into a mould and insert molten aluminium that fills the interstitial space. As a result, contact resistance between the APM foam elements is negligible and thermal conduction occurs predominantly within the space *outside* the APM foam elements. In addition, the porosity of these structures is distinctly decreased resulting in a higher relative density. It has been discussed earlier that the use of symmetric boundary conditions underestimates the packing density of APM foam elements. Thus, the following results can be considered as an upper bound for the effective thermal conductivity of randomly packed syntactic APM structures.

Analogous to Figs. 6 and 7 the minimum, average, and maximum syntactic APM foam conductivities are shown below. Fig. 14 displays the effective thermal conductivities of 5 mm syntactic APMS. Values of the average thermal conductivity range from 32.1 W/(m K) to 41.0 W/(m K). It should be highlighted here that the variation in conductivity is due differences between samples. Directional variations (i.e. thermal anisotropy) are small as discussed below.

Fig. 15 shows the effective thermal conductivities of 10 mm syntactic APMS. In contrast to Fig. 14, the effective thermal conductivity is relatively consistent among the considered samples and ranges between 36.3 W/(m K) and 38.7 W/(m K). Again, differences between maximum and minimum conductivity of each sample are low indicating thermal isotropy. Comparing the overall averages of 5 mm (35.5 W/(m K)) and 10 mm (37.9 W/(m K)), a slightly higher concavity is found for the 10 mm samples. As

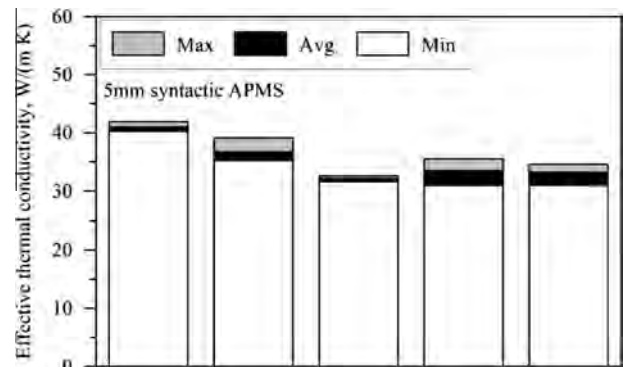


Fig. 14. Effective thermal conductivity of 5 mm syntactic APMS.

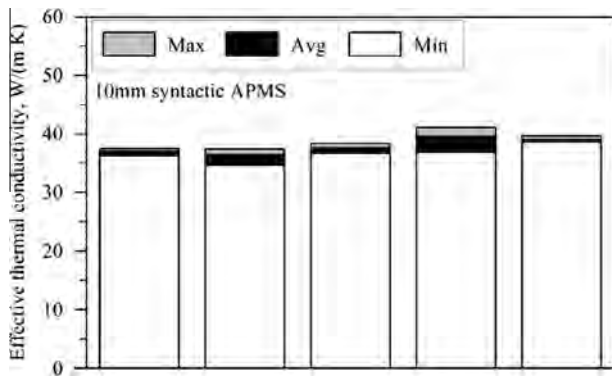


Fig. 15. Effective thermal conductivity of 10 mm syntactic APMS.

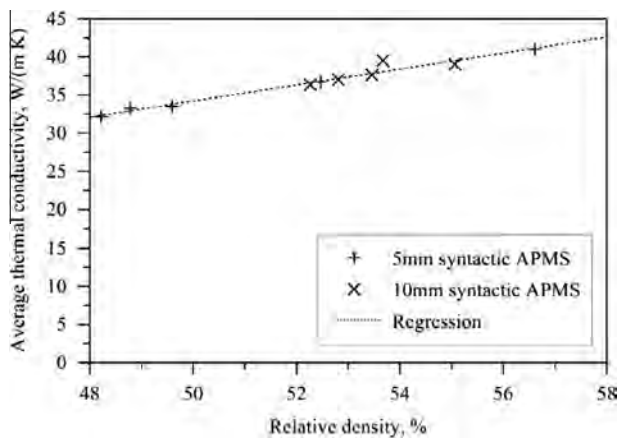


Fig. 16. Effective thermal conductivity of syntactic APMS plotted vs relative density.

shown in Fig. 17, this can be explained by differences in relative density.

It is interesting to note that *sintered* 5 mm APMS (see Fig. 6) exhibit consistent conductivities. In contrast, the *syntactic* 5 mm APMS (see Fig. 14) show a distinct scattering between different samples. A likely explanation is that in syntactic APMS thermal conduction is governed by metallic phase within the former void space between APM foam elements. Shape deviations of the outer

APM foam element surface (which is approximately spherical) will then cause a distinct change in relative density and thus its effective thermal conductivity. This supposition is supported by Fig. 16 where the effective thermal conductivity of syntactic APMS is plotted versus their relative density. It can be seen that a linear regression fit accurately describes the dependence of the effective thermal conductivity on relative density. Scattering in thermal conductivity can thus be explained by variations in relative density (i.e. porosity).

Fig. 17 shows polar plots of the effective thermal conductivity of 5 mm and 10 mm syntactic APMS. In contrast to sintered APMS (see Figs. 9 and 10) near-circular shapes are obtained. This indicates thermal isotropy, i.e. the thermal conductivity is widely independent of direction. This can again be explained by the additional conducting phase in the space between the spherical APM foam elements. Thermal conduction now occurs predominantly within this volume and thus is less dependent on the internal foam geometry of the APM elements. As a result, their anisotropic contribution to thermal conduction is decreased resulting in macroscopic thermal isotropy. The thermal anisotropy can be quantified by calculating the average ratio of maximum and minimum thermal conductivities. The corresponding averaged values are 1.09 for 5 mm syntactic APMS and 1.06 for 10 mm syntactic APMS.

6. Conclusions

This work addressed the effective thermal conductivity of periodic models of advanced pore morphology structures (APMS). The complex geometry of 5 mm and 10 mm APM foam elements (5 samples per size) was captured using micro computed tomography analysis. Symmetric boundary conditions were used in order to combine single foam elements into infinite primitive cubic foam structures. Numerical Lattice Monte Carlo analyses were conducted on the resulting three dimensional models that accurately represent the real sample geometry.

Different joining technologies of APM foam elements were considered. Sintered APMS exhibit an average thermal conductivity of 5.5 W/(m K) (5 mm sintered APMS) and 5.1 W/(m K) (10 mm sintered APMS). A distinct scattering of the effective thermal conductivity of 10 mm APMS was observed. In contrast, the effective thermal conductivity of 5 mm APMS was found to be consistent among the investigated samples. Both structures showed some degree of thermal anisotropy. The ratio of maximum and minimum thermal conductivity is 1.29 (5 mm APMS) and 1.13 (10 mm APMS). A thermal resistance model was introduced to investigate

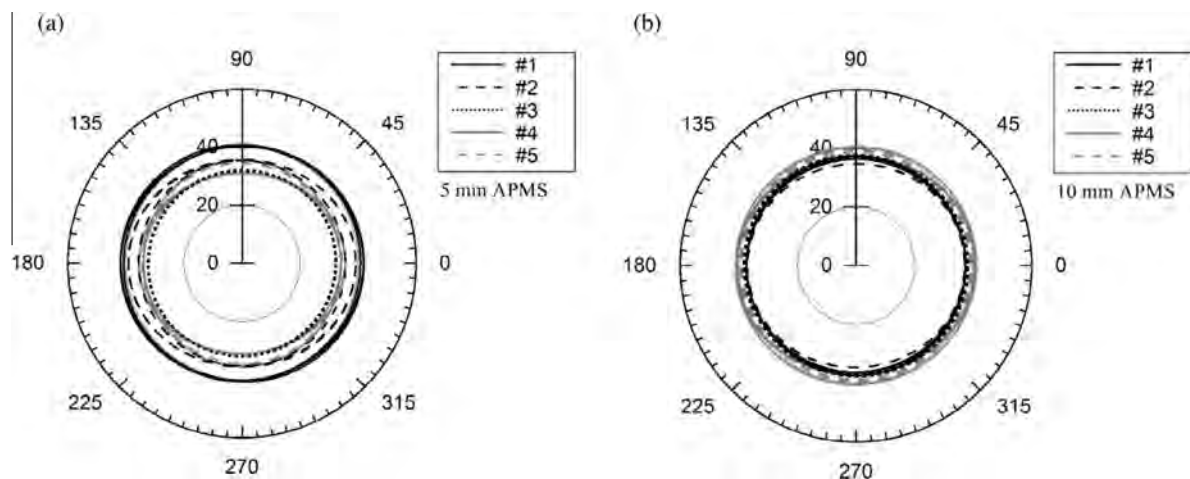


Fig. 17. Polar plot of the effective thermal conductivity in W/(m K) of syntactic APMS in three perpendicular planes: (a) 5 mm syntactic APMS, (b) 10 mm syntactic APMS.

the effective thermal conductivity of adhesively bonded APMS. Adhesives exhibit a low thermal conductivity and thus form thermal barriers between APM foam elements. As a result, a distinct decrease of the thermal conductivity of adhesively bonded APMS was found.

Finally, syntactic APMS were considered where the porosity outside the APM foam elements is completely filled by the metallic phase (e.g. by casting). As expected, a distinct increase of the effective thermal conductivity was found. The average values are 35.3 W/(m K) for 5 mm APMS and 37.9 W/(m K) for 10 mm APMS. Furthermore, isotropic behaviour was observed with the following low ratios of maximum and minimum thermal conductivity: 1.09 (5 mm APMS) and 1.06 (10 mm APMS).

Acknowledgements

The authors acknowledge the financial support of under the Australian Research Council Discovery Projects funding scheme (project number DP1094696). The authors also thank Prof Erich Kisi from the University of Newcastle, Australia, for help with the EBM testing instrument. Financial support of the Slovenian Research Agency and the Japan Society for the Promotion of Science under the project BI-JP/12-14-002 is kindly acknowledged.

References

- [1] L.J. Gibson, M.F. Ashby, *Cellular Solids – Structure and Properties*, second ed., Cambridge University Press, 2001.
- [2] S. Tanaka, K. Hokamoto, S. Irie, T. Okano, Z. Ren, M. Vesenjak, S. Itoh, High-velocity impact experiment of aluminum foam sample using powder gun, *Measurement* 44 (10) (2011) 2185–2189.
- [3] I.S. Golovin, H.R. Sinning, Damping in some cellular metallic materials, *J. Alloy. Compd.* 355 (1–2) (2003) 8.
- [4] T. Fiedler, I.V. Belova, G.E. Murch, Theoretical and Lattice Monte Carlo analyses on thermal conduction in cellular metals, *Comput. Mater. Sci.* 50 (2010) 503–509.
- [5] M. Vesenjak, Z. Žunič, Z. Ren, A. Öchsner, Computational study of heat transfer in honeycomb structures accounting for gaseous pore filler, *Defect Diffus. Forum* 273–276 (2008) 669–706.
- [6] J. Tian, T.J. Lu, H.P. Hodson, D.T. Queheillalt, H.N.G. Wadley, Cross flow heat exchange of textile cellular metal core sandwich panels, *Int. J. Heat Mass Transfer* 50 (13–14) (2007) 2521–2536.
- [7] S. Günter, Q. Peter, A. Olaf, New multifunctional lightweight materials based on cellular metals – manufacturing, properties and applications, *J. Phys.: Conf. Ser.* 165 (1) (2009) 012061.
- [8] U. Ramamurty, A. Paul, Variability in mechanical properties of a metal foam, *Acta Mater.* 52 (4) (2004) 869–876.
- [9] C. Veyhl, I.V. Belova, G.E. Murch, T. Fiedler, Finite element analysis of the mechanical properties of cellular aluminium based on micro-computed tomography, *Mater. Sci. Eng. A* 528 (2011) 4550–4555.
- [10] H.P. Degischer, *Handbook of Cellular Metals*, Wiley-VCH, Weinheim, 2002.
- [11] Y. An, C.e. Wen, P.D. Hodgson, C. Yang, Investigation of cell shape effect on the mechanical behaviour of open-cell metal foams, *Comput. Mater. Sci.* 55 (2012) 1–9.
- [12] T. Fiedler, I.V. Belova, G.E. Murch, μ -CT-based finite element analysis on imperfections in open-celled metal foam: mechanical properties, *Scr. Mater.* 67 (5) (2012) 455–458.
- [13] T. Fiedler, H.S. Richards, I.V. Belova, A. Öchsner, G.E. Murch, Experimental analysis on the thermal anisotropy of syntactic hollow sphere structures, *Exp. Therm. Fluid Sci.* 44 (2013) 637–641.
- [14] K. Stöbener, G. Rausch, Aluminium foam-polymer composites: processing and characteristics, *J. Mater. Sci.* 44 (2009) 1506–1511.
- [15] D. Lehmhus, J. Baumeister, L. Stutz, E. Schneider, K. Stöbener, M. Avasle, L. Peroni, M. Peroni, Mechanical characterization of particulate aluminum foams-strain-rate, density and matrix alloy versus adhesive effects, *Adv. Eng. Mater.* 12 (7) (2009) 596–603.
- [16] M. Vesenjak, F. Gačnik, L. Krstulović-Opara, Z. Ren, Behavior of composite advanced pore morphology foam, *J. Compos. Mater.* 45 (26) (2011) 2823–2831.
- [17] M. Vesenjak, F. Gačnik, L. Krstulović-Opara, Z. Ren, Mechanical properties of advanced pore morphology foam element, *Mech. Adv. Mater. Struct.*, in press.
- [18] J. Hohe, V. Hardenacke, V. Fascio, Y. Girard, J. Baumeister, K. Stöbener, J. Weise, D. Lehmhus, S. Pattofatto, H. Zeng, H. Zhao, V. Calbucci, F. Rustichelli, F. Fiori, Numerical and experimental design of graded cellular sandwich cores for multi-functional aerospace applications, *Mater. Des.* 39 (2012) 20–32.
- [19] C. Veyhl, I.V. Belova, G.E. Murch, T. Fiedler, On the thermal conductivity of sintered metallic fibre structures, *Int. J. Heat Mass Transfer* 55 (2012) 2440–2448.
- [20] J. Farnsworth, G.E. Murch, I.V. Belova, A. Öchsner, T. Fiedler, A Lattice Monte Carlo analysis on thermal diffusion in syntactic hollow-sphere structures, *Mater. Sci. Eng. Technol.* 41 (2010) 283–286.
- [21] T. Fiedler, E. Solórzano, F. Garcia-Moreno, A. Öchsner, I.V. Belova, G.E. Murch, Lattice Monte Carlo and experimental analyses of the thermal conductivity of random shaped cellular aluminium, *Adv. Eng. Mater.* 11 (2009) 843–847.
- [22] J. Holt, *Structural Alloys Handbook*, CINDAS, Purdue University, West Lafayette, 1996.
- [23] K. Kadoya, N. Matsunaga, A. Nagashima, Viscosity and thermal conductivity of dry air in the gaseous phase, *J. Phys. Chem. Ref. Data* 14 (4) (1985) 947–970.
- [24] I.V. Belova, G.E. Murch, T. Fiedler, A. Öchsner, Lattice-based walks and the Monte Carlo method for addressing mass, thermal and elasticity problems, *Defect Diffus. Forum* 283–286 (2009) 13–23.
- [25] I.V. Belova, C. Veyhl, T. Fiedler, G.E. Murch, Analysis of anisotropic behaviour of thermal conductivity in cellular metals, *Scr. Mater.* 65 (5) (2011) 436–439.
- [26] J.C. Maxwell-Garnett, Colours in metal glasses and in metallic films, *Philos. Trans. R. Soc. Lond.* 203 (1904) 385–420.
- [27] E. Solorzano, J.A. Reglero, A. Rodríguez-Pérez, D. Lehmhus, M. Wichmann, J.A.d. Saja, An experimental study on the thermal conductivity of aluminium foams by using the transient plane source method, *Int. J. Heat Mass Transfer* 51 (25–26) (2008) 6259–6267.
- [28] D.A.G. Bruggeman, Dielectric constant and conductivity of mixtures of isotropic materials, *Ann. Phys.* 24 (7) (1934). 9p.
- [29] L.R. Glicksman, Heat transfer in foams, in: N.C. Hilyard, A. Cunningham (Eds.), *Low Density Cellular Plastics – Physical Basis of Behaviour*, Chapman and Hall, London, 1994, pp. 107–111.
- [30] A.N. Abramenko, A.S. Kalinichenko, Y. Burtser, V.A. Kalinichenko, S.A. Tanaeva, I.P. Vasilenko, Determination of the thermal conductivity of foam aluminum, *J. Eng. Phys. Thermophys.* 72 (369–373) (1999).
- [31] M.F. Ashby, A. Evans, N.A. Fleck, L.J. Gibson, J.W. Hutchinson, H.N.G. Wadley, *Metal Foams: A Design Guide*, Elsevier Science, Burlington, 2000.
- [32] R.C. Progelhof, J.L. Throne, Cooling of structural foams, *J. Cell. Plast.* 11 (1975) 152–163.

Co-author statements

Co-author statement

I, Thomas Fiedler, attest that Research Higher Degree candidate Mohd Ayub Sulong contributed with obtaining stress-strain data and carried out the experimental test of the paper below:

T Fiedler, MA Sulong, V Mathier, IV Belova, C Younger, GE Murch, "Mechanical properties of aluminium foam derived from infiltration casting of salt dough." *Computational Materials Science* 81 (2014): 246-248.

Thomas Fiedler

(Signature of Co-author)
(Full name of Co-author)

Date: 14/7/2015

MOHD AYUB SULONG

(Signature of Candidate)
(Full name of Candidate)

Date: 14/7/2015

(Signature of Assistant Dean Research Training [ADRT])

(Full name of ADRT)

Date:

Co-author statement

I, Thomas Fiedler, attest that Research Higher Degree candidate Mohd Ayub Sulong contributed with segmentation and extracted strut thickness data from micro-computed tomography images of the paper below:

M. Taherishargh, MA Sulong, IV Belova, GE Murch, T Fiedler, "On the particle size effect in expanded perlite aluminium syntactic foam." *Materials & Design* 66 (2015): 294-303.

Thomas Fiedler

(Signature of Co-author)
(Full name of Co-author)

Date: 14/7/2015

Mohd Ayub Sulong

(Signature of Candidate)
(Full name of Candidate)

Date: 14/7/2015

(Signature of Assistant Dean Research Training [ADRT])

(Full name of ADRT)

Date:

Co-author statement

I, Thomas Fiedler, attest that Research Higher Degree candidate Mohd Ayub Sulong contributed with preparing the first draft, performed the numerical analysis and analysed the results of the paper below:

M.A. Sulong, M. Taherishargh, I.V. Belova, G.E. Murch, T. Fiedler, "On the mechanical anisotropy of aluminium perlite syntactic foam." *Submitted to Computational Materials Science*

Thomas Fiedler

(Signature of Co-author)

(Full name of Co-author)

Date: 4/7/2015

MOHD AYUB SULONG

(Signature of Candidate)

(Full name of Candidate)

Date: 4/7/2015

(Signature of Assistant Dean Research Training [ADRT])

(Full name of ADRT)

Date:

Co-author statement

I, Thomas Fiedler, attest that Research Higher Degree candidate Mohd Ayub Sulong contributed with preparing the first draft, performed the quasi-static numerical analysis and reviewed the final version of the paper below:

M.A. Sulong, M. Vesenjak, I.V. Belova, G.E. Murch, T. Fiedler, "Compressive properties of Advanced Pore Morphology (APM) foam elements." *Materials Science and Engineering: A* 607 (2014): 498-504.

Thomas Fiedler

(Signature of Co-author)

(Full name of Co-author)

Date: 14/7/2015

MOHD AYUB SULONG

(Signature of Candidate)

(Full name of Candidate)

Date: 14/7/2015

(Signature of Assistant Dean Research Training [ADRT])

(Full name of ADRT)

Date:

Co-author statement

I, Thomas Fiedler, attest that Research Higher Degree candidate Mohd Ayub Sulong contributed with three dimensional mesh model generation from micro-computed tomography images of the paper below:

M Vesenjak, MA Sulong, L Krstulović-Opara, V Mathier, T Fiedler, "Dynamic compression of aluminium foam derived from infiltration casting of salt dough." *Submitted to Mechanics of Material*

Thomas Fiedler

(Signature of Co-author)

(Full name of Co-author)

Date:

14/7/2015

(Signature of Candidate)

MOHD AYUB SULONG

(Full name of Candidate)

Date:

14/7/2015

(Signature of Assistant Dean Research Training [ADRT])

(Full name of ADRT)

Date:

Co-author statement

I, Thomas Fiedler, attest that Research Higher Degree candidate Mohd Ayub Sulong contributed with preparing the draft, extracting the stress-strain data according to ISO 13314 and performed the numerical analysis of the paper below:

M.A. Sulong, I.V. Belova, A. Boccaccini, G.E. Murch, T. Fiedler, "A model of the mechanical degradation of foam replicated scaffolds." *Submitted to Computational Materials Science*

Thomas Fiedler

(Signature of Co-author)
(Full name of Co-author)

Date: 14/7/2015

Mohd Ayub Sulong

(Signature of Candidate)
(Full name of Candidate)

Date: 14/7/2015

(Signature of Assistant Dean Research Training [ADRT])

(Full name of ADRT)

Date:

Co-author statement

I, Thomas Fiedler, attest that Research Higher Degree candidate Mohd Ayub Sulong contributed with converting micro-computed tomography into numerical models, performing Lattice Monte Carlo (LMC) analysis, extracted the effective thermal conductivity and results discussion of the paper below:

T Fiedler, MA Sulong, M Vesenjak, Y Higa, IV Belova, A Öchsner, GE Murch, "Determination of the thermal conductivity of periodic APM foam models." *International Journal of Heat and Mass Transfer* 73 (2014): 826-833.

Thomas Fiedler

(Signature of Co-author)

(Full name of Co-author)

Date: 14/7/2015

MOHD AYUB SULONG

(Signature of Candidate)

(Full name of Candidate)

Date: 14/7/2015

(Signature of Assistant Dean Research Training [ADRT])

(Full name of ADRT)

Date:

Co-author statement

I, Irina Belova, attest that Research Higher Degree candidate Mohd Ayub Sulong contributed with obtaining stress-strain data and carried out the experimental test of the paper below:

T Fiedler, MA Sulong, V Mathier, IV Belova, C Younger, GE Murch, "Mechanical properties of aluminium foam derived from infiltration casting of salt dough." *Computational Materials Science* 81 (2014): 246-248.

Prof. I. V. Belova

(Signature of Co-author)
(Full name of Co-author)

Date: 13/7/2015

13/7/2015

(Signature of Candidate)
(Full name of Candidate)

MOHD AYUB SULONG
Date:

(Signature of Assistant Dean Research Training [ADRT])

(Full name of ADRT)

Date:

Co-author statement

I, Irina Belova, attest that Research Higher Degree candidate Mohd Ayub Sulong contributed with segmentation and extracted strut thickness data from micro-computed tomography images of the paper below:

M. Taherishargh, MA Sulong, IV Belova, GE Murch, T Fiedler, "On the particle size effect in expanded perlite aluminium syntactic foam." *Materials & Design* 66 (2015): 294-303.

Prof. I. V. Belova

(Signature of Co-author)

(Full name of Co-author)

Date:

13/7/2015

(Signature of Candidate)

MOHD AYUB SULONG

(Full name of Candidate)

Date:

13/7/2015

(Signature of Assistant Dean Research Training [ADRT])

(Full name of ADRT)

Date:

Co-author statement

I, Irina Belova, attest that Research Higher Degree candidate Mohd Ayub Sulong contributed with preparing the first draft, performed the numerical analysis and analysed the results of the paper below:

M.A. Sulong, M. Taherishargh, I.V. Belova, G.E. Murch, T. Fiedler, "On the mechanical anisotropy of aluminium perlite syntactic foam." *Submitted to Computational Materials Science*

Prof. I.V. Belova

(Signature of Co-author)

(Full name of Co-author)

Date: 13/7/2015

Mohd Ayub Sulong

(Signature of Candidate)

(Full name of Candidate)

Date: 13/7/2015

(Signature of Assistant Dean Research Training [ADRT])

(Full name of ADRT)

Date:

Co-author statement

I, Irina Belova, attest that Research Higher Degree candidate Mohd Ayub Sulong contributed with preparing the first draft, performed the quasi-static numerical analysis and reviewed the final version of the paper below:

M.A. Sulong, M. Vesenjak, I.V. Belova, G.E. Murch, T. Fiedler, "Compressive properties of Advanced Pore Morphology (APM) foam elements." *Materials Science and Engineering: A* 607 (2014): 498-504.

Prof I.V. Belova

(Signature of Co-author)

(Full name of Co-author)

Date: 13/7/2015

(Signature of Candidate)

MOHD AYUB SULONG

(Full name of Candidate)

Date: 13/7/2015

(Signature of Assistant Dean Research Training [ADRT])

(Full name of ADRT)

Date:

Co-author statement

I, Irina Belova, attest that Research Higher Degree candidate Mohd Ayub Sulong contributed with preparing the draft, extracting the stress-strain data according to ISO 13314 and performed the numerical analysis of the paper below:

M.A. Sulong, I.V. Belova, A. Boccaccini, G.E. Murch, T. Fiedler, "A model of the mechanical degradation of foam replicated scaffolds." *Submitted to Computational Materials Science*

Prof. I. V. Belova

(Signature of Co-author)

(Full name of Co-author)

Date: 13/7/2015

Mohd Ayub Sulong

(Signature of Candidate)

(Full name of Candidate)

Date: 13/7/2015

(Signature of Assistant Dean Research Training [ADRT])

(Full name of ADRT)

Date:

Co-author statement

I, Irina Belova, attest that Research Higher Degree candidate Mohd Ayub Sulong contributed with converting micro-computed tomography into numerical models, performing Lattice Monte Carlo (LMC) analysis, extracted the effective thermal conductivity and results discussion of the paper below:

T Fiedler, MA Sulong, M Vesenjak, Y Higa, IV Belova, A Öchsner, GE Murch, "Determination of the thermal conductivity of periodic APM foam models." *International Journal of Heat and Mass Transfer* 73 (2014): 826-833.

Prof. I. V. Belova

(Signature of Co-author)

(Full name of Co-author)

Date: 13/7/2015

(Signature of Candidate)

MOHD AYUB SULONG

(Full name of Candidate)

Date: 13/7/2015

(Signature of Assistant Dean Research Training [ADRT])

(Full name of ADRT)

Date:

Co-author statement

I, Graeme Murch, attest that Research Higher Degree candidate Mohd Ayub Sulong contributed with obtaining stress-strain data and carried out the experimental test of the paper below:

T Fiedler, MA Sulong, V Mathier, IV Belova, C Younger, GE Murch, "Mechanical properties of aluminium foam derived from infiltration casting of salt dough." *Computational Materials Science* 81 (2014): 246-248.

(Signature of Co-author)

Prof. Graeme E. Murch

(Full name of Co-author)

Date: July 10, 2015

(Signature of Candidate)

MOHD AYUB SULONG

(Full name of Candidate)

Date: 10/7/2015

(Signature of Assistant Dean Research Training [ADRT])

(Full name of ADRT)

Date:

Co-author statement

I, Graeme Murch, attest that Research Higher Degree candidate Mohd Ayub Sulong contributed with segmentation and extracted strut thickness data from micro-computed tomography images of the paper below:

M. Taherishargh, MA Sulong, IV Belova, GE Murch, T Fiedler, "On the particle size effect in expanded perlite aluminium syntactic foam." *Materials & Design* 66 (2015): 294-303.

(Signature of Co-author)

Prof Graeme E. Murch

(Full name of Co-author)

Date: July 10, 2015

(Signature of Candidate)

Mohd Ayub Sulong

(Full name of Candidate)

Date: 10/7/2015

(Signature of Assistant Dean Research Training [ADRT])

----- (Full name of ADRT)

Date:

Co-author statement

I, Graeme Murch, attest that Research Higher Degree candidate Mohd Ayub Sulong contributed with preparing the first draft, performed the numerical analysis and analysed the results of the paper below:

M.A. Sulong, M. Taherishargh, I.V. Belova, G.E. Murch, T. Fiedler, "On the mechanical anisotropy of aluminium perlite syntactic foam." *Submitted to Computational Materials Science*

(Signature of Co-author)

Prof. Graeme E. Murch

(Full name of Co-author)

Date: July 10, 2015

(Signature of Candidate)

Mohd Ayub Sulong

(Full name of Candidate)

Date: 10/7/2015

(Signature of Assistant Dean Research Training [ADRT])

(Full name of ADRT)

Date:

Co-author statement

I, Graeme Murch, attest that Research Higher Degree candidate Mohd Ayub Sulong contributed with preparing the first draft, performed the quasi-static numerical analysis and reviewed the final version of the paper below:

M.A. Sulong, M. Vesenjak, I.V. Belova, G.E. Murch, T. Fiedler, "Compressive properties of Advanced Pore Morphology (APM) foam elements." *Materials Science and Engineering: A* 607 (2014): 498-504.

(Signature of Co-author)

Prof Graeme E Murch.

(Full name of Co-author)

Date: July 10, 2015

(Signature of Candidate)

MOHD AYUB SULONG

(Full name of Candidate)

Date: 10/7/2015

(Signature of Assistant Dean Research Training [ADRT])

(Full name of ADRT)

Date:

Co-author statement

I, Graeme Murch, attest that Research Higher Degree candidate Mohd Ayub Sulong contributed with preparing the draft, extracting the stress-strain data according to ISO 13314 and performed the numerical analysis of the paper below:

M.A. Sulong, I.V. Belova, A. Boccaccini, G.E. Murch, T. Fiedler, "A model of the mechanical degradation of foam replicated scaffolds." *Submitted to Computational Materials Science*

(Signature of Co-author)

Prof Graeme E Murch

(Full name of Co-author)

Date: *July 10, 2015*

(Signature of Candidate)

MOHD AYUB SULONG

(Full name of Candidate)

Date: *10/7/2015*

(Signature of Assistant Dean Research Training [ADRT])

(Full name of ADRT)

Date:

Co-author statement

I, Graeme Murch, attest that Research Higher Degree candidate Mohd Ayub Sulong contributed with converting micro-computed tomography into numerical models, performing Lattice Monte Carlo (LMC) analysis, extracted the effective thermal conductivity and results discussion of the paper below:

T Fiedler, MA Sulong, M Vesenjak, Y Higa, IV Belova, A Öchsner, GE Murch, "Determination of the thermal conductivity of periodic APM foam models." *International Journal of Heat and Mass Transfer* 73 (2014): 826-833.

(Signature of Co-author)

Prof Graeme E Murch

(Full name of Co-author)

Date: July 10, 2015

(Signature of Candidate)

Mohd Ayub Sulong

(Full name of Candidate)

Date: 10/7/2015

(Signature of Assistant Dean Research Training [ADRT])

(Full name of ADRT)

Date:

Co-author statement

I, Matej Vesenjak, attest that Research Higher Degree candidate Mohd Ayub Sulong contributed with preparing the first draft, performed the quasi-static numerical analysis and reviewed the final version of the paper below:

M.A. Sulong, M. Vesenjak, I.V. Belova, G.E. Murch, T. Fiedler, "Compressive properties of Advanced Pore Morphology (APM) foam elements." *Materials Science and Engineering: A* 607 (2014): 498-504.

(Signature of Co-author)

Matej VESENJAK

(Full name of Co-author)

Date: 22. June 2015

(Signature of Candidate)

MOHD AYUB SULONG

(Full name of Candidate)

Date: 9/7/2015

(Signature of Assistant Dean Research Training [ADRT])

(Full name of ADRT)

Date:

Co-author statement

I, Matej Vesenjak, attest that Research Higher Degree candidate Mohd Ayub Sulong contributed with three dimensional mesh model generation from micro-computed tomography images of the paper below:

M Vesenjak, MA Sulong, L Krstulović-Opara, V Mathier, T Fiedler, "Dynamic compression of aluminium foam derived from infiltration casting of salt dough." *Submitted to Mechanics of Material*

(Signature of Co-author)

Matej VESENJAK

(Full name of Co-author)

Date: 22 June 2015

(Signature of Candidate)

MOHD AYUB SULONG

(Full name of Candidate)

Date: 9/7/2015

(Signature of Assistant Dean Research Training [ADRT])

----- (Full name of ADRT)

Date:

Co-author statement

I, Matej Vesenjak, attest that Research Higher Degree candidate Mohd Ayub Sulong contributed with converting micro-computed tomography into numerical models, performing Lattice Monte Carlo (LMC) analysis, extracted the effective thermal conductivity and results discussion of the paper below:

T Fiedler, MA Sulong, M Vesenjak, Y Higa, IV Belova, A Öchsner, GE Murch, "Determination of the thermal conductivity of periodic APM foam models." *International Journal of Heat and Mass Transfer* 73 (2014): 826-833.

(Signature of Co-author)

Matej VESENJAK

(Full name of Co-author)

Date: 22 June 2015

(Signature of Candidate)

MOHD AYUB SULONG

(Full name of Candidate)

Date: 9/7/2015

(Signature of Assistant Dean Research Training [ADRT])

(Full name of ADRT)

Date:

Co-author statement

I, Vincent Mathier, attest that Research Higher Degree candidate Mohd Ayub Sulong contributed with obtaining stress-strain data and carried out the experimental test of the paper below:

T Fiedler, MA Sulong, V Mathier, IV Belova, C Younger, GE Murch, "Mechanical properties of aluminium foam derived from infiltration casting of salt dough." *Computational Materials Science* 81 (2014): 246-248.

(Signature of Co-author)

Vincent MATHIER

(Full name of Co-author)

Date: 15.06.2015

(Signature of Candidate)

MOHD AYUB SULONG

(Full name of Candidate)

Date: 9/7/2015

(Signature of Assistant Dean Research Training [ADRT])

(Full name of ADRT)

Date:

Co-author statement

I, Vincent Mathier, attest that Research Higher Degree candidate Mohd Ayub Sulong contributed with three dimensional mesh model generation from micro-computed tomography images of the paper below:

M Vesenjak, MA Sulong, L Krstulović-Opara, V Mathier, T Fiedler, "Dynamic compression of aluminium foam derived from infiltration casting of salt dough." *Submitted to Mechanics of Material*

(Signature of Co-author)

Vincent MATHIER

(Full name of Co-author)

Date: 15.06.2015

(Signature of Candidate)

MOHD AYUB SULONG

(Full name of Candidate)

Date: 9/07/2015

(Signature of Assistant Dean Research Training [ADRT])

(Full name of ADRT)

Date:

Co-author statement

I, Lovre Krstulović-Opara, attest that Research Higher Degree candidate Mohd Ayub Sulong contributed with three dimensional mesh model generation from micro-computed tomography images of the paper below:

M Vesenjāk, MA Sulong, L Krstulović-Opara, V Mathier, T Fiedler, "Dynamic compression of aluminium foam derived from infiltration casting of salt dough." *Submitted to Mechanics of Material*

(Signature of Co-author)

Prof. Dr.-Ing. Lovre Krstulović-Opara (Full name of Co-author)

Date: 11. June 2015

(Signature of Candidate)

MOHD AYUB SULONG (Full name of Candidate)

Date: 9/7/2015

(Signature of Assistant Dean Research Training [ADRT])

----- (Full name of ADRT)

Date:

Co-author statement

As communicated by his PhD supervisor and co-author of this paper, Dr. T. Fiedler I, Aldo R. Boccaccini, confirm that Research Higher Degree candidate Mohd Ayub Sulong contributed with preparing the draft, extracting the stress-strain data according to ISO 13314 and performed the numerical analysis of the paper below:

M.A. Sulong, I.V. Belova, A.R. Boccaccini, G.E. Murch, T. Fiedler, "A model of the mechanical degradation of foam replicated scaffolds." *Submitted to Computational Materials Science*

(Signature of Co-author)

Prof. Aldo R. Boccaccini

(Full name of Co-author)

Date: 13/6/2015

(Signature of Candidate)

MOHD AYUB SULONG

(Full name of Candidate)

Date: 9/7/2015

(Signature of Assistant Dean Research Training [ADRT])

(Full name of ADRT)

Date:

Co-author statement

I, Andreas Öchsner, attest that Research Higher Degree candidate Mohd Ayub Sulong contributed with converting micro-computed tomography into numerical models, performing Lattice Monte Carlo (LMC) analysis, extracted the effective thermal conductivity and results discussion of the paper below:

T Fiedler, MA Sulong, M Vesenjak, Y Higa, IV Belova, A Öchsner, GE Murch, "Determination of the thermal conductivity of periodic APM foam models." *International Journal of Heat and Mass Transfer* 73 (2014): 826-833.

----- (Signature of Co-author)

Prof. Dr.-Ing. Andreas Öchsner, DSc (Full name of Co-author)

Date: 11/6/2015

(Signature of Candidate)

MOHD AYUB SULONG

(Full name of Candidate)

Date: 9/7/2015

(Signature of Assistant Dean Research Training [ADRT])

----- (Full name of ADRT)

Date:

Co-author statement

I, Yoshikazu Higa, attest that Research Higher Degree candidate Mohd Ayub Sulong contributed with converting micro-computed tomography into numerical models, performing Lattice Monte Carlo (LMC) analysis, extracted the effective thermal conductivity and results discussion of the paper below:

T Fiedler, MA Sulong, M Vesenjak, Y Higa, IV Belova, A Öchsner, GE Murch, "Determination of the thermal conductivity of periodic APM foam models." *International Journal of Heat and Mass Transfer* 73 (2014): 826-833.

----- (Signature of Co-author)

YOSHIKAZU HIGA
----- (Full name of Co-author)

Date: 2015/06/13

----- (Signature of Candidate)

MOHD AYUB SULONG
----- (Full name of Candidate)

Date: 9/7/2015

(Signature of Assistant Dean Research Training [ADRT])

----- (Full name of ADRT)

Date:

Co-author statement

I, Mehdi Taherishargh, attest that Research Higher Degree candidate Mohd Ayub Sulong contributed with segmentation and extracted strut thickness data from micro-computed tomography images of the paper below:

M. Taherishargh, MA Sulong, IV Belova, GE Murch, T Fiedler, "On the particle size effect in expanded perlite aluminium syntactic foam." *Materials & Design* 66 (2015): 294-303.

(Signature of Co-author)

(Full name of Co-author)

Date:

16 / 06 / 2015

(Signature of Candidate)

(Full name of Candidate)

Date:

16 / 06 / 2015

(Signature of Assistant Dean Research Training [ADRT])

(Full name of ADRT)

Date:

Co-author statement

I, Mehdi Taherishargh, attest that Research Higher Degree candidate Mohd Ayub Sulong contributed with preparing the first draft, performed the numerical analysis and analysed the results of the paper below:

M.A. Sulong, M. Taherishargh, I.V. Belova, G.E. Murch, T. Fiedler, "On the mechanical anisotropy of aluminium perlite syntactic foam." *Submitted to Computational Materials Science*

(Signature of Co-author)

Mehdi Taherishargh

(Full name of Co-author)

Date: 16/06/2015

(Signature of Candidate)

MOHD AYUB SULONG

(Full name of Candidate)

Date: 16/06/2015

(Signature of Assistant Dean Research Training [ADRT])

(Full name of ADRT)

Date:

Co-author statement

I, Chris Younger, attest that Research Higher Degree candidate Mohd Ayub Sulong contributed with obtaining stress-strain data and carried out the experimental test of the paper below:

T Fiedler, MA Sulong, V Mathier, IV Belova, C Younger, GE Murch, "Mechanical properties of aluminium foam derived from infiltration casting of salt dough." *Computational Materials Science* 81 (2014): 246-248.

(Signature of Co-author)

Chris Younger

(Full name of Co-author)

Date: 9/6/15

(Signature of Candidate)

MOHD AYUB SULONG

(Full name of Candidate)

Date: 9/7/2015

(Signature of Assistant Dean Research Training [ADRT])

----- (Full name of ADRT)

Journal reprint license

ELSEVIER LICENSE
TERMS AND CONDITIONS

Jun 08, 2015

This is a License Agreement between Mohd Ayub Sulong ("You") and Elsevier ("Elsevier") provided by Copyright Clearance Center ("CCC"). The license consists of your order details, the terms and conditions provided by Elsevier, and the payment terms and conditions.

All payments must be made in full to CCC. For payment instructions, please see information listed at the bottom of this form.

Supplier	Elsevier Limited The Boulevard, Langford Lane Kidlington, Oxford, OX5 1GB, UK
Registered Company Number	1982084
Customer name	Mohd Ayub Sulong
Customer address	12 Albert St MAYFIELD, NSW 2304
License number	3644520960232
License date	Jun 08, 2015
Licensed content publisher	Elsevier
Licensed content publication	Materials Science and Engineering: A
Licensed content title	Compressive properties of Advanced Pore Morphology (APM) foam elements
Licensed content author	M.A. Sulong, M. Vesenjaj, I.V. Belova, G.E. Murch, T. Fiedler
Licensed content date	23 June 2014
Licensed content volume number	607
Licensed content issue number	n/a
Number of pages	7
Start Page	498
End Page	504
Type of Use	reuse in a thesis/dissertation
Portion	full article
Format	both print and electronic
Are you the author of this Elsevier article?	Yes
Will you be translating?	No
Title of your thesis/dissertation	Characterisation of Advanced Porous Materials
Expected completion date	Aug 2015
Estimated size (number of pages)	150

Elsevier VAT number	GB 494 6272 12
Permissions price	0.00 AUD
VAT/Local Sales Tax	0.00 AUD / 0.00 GBP
Total	0.00 AUD
Terms and Conditions	

INTRODUCTION

1. The publisher for this copyrighted material is Elsevier. By clicking "accept" in connection with completing this licensing transaction, you agree that the following terms and conditions apply to this transaction (along with the Billing and Payment terms and conditions established by Copyright Clearance Center, Inc. ("CCC"), at the time that you opened your Rightslink account and that are available at any time at <http://myaccount.copyright.com>).

GENERAL TERMS

2. Elsevier hereby grants you permission to reproduce the aforementioned material subject to the terms and conditions indicated.

3. Acknowledgement: If any part of the material to be used (for example, figures) has appeared in our publication with credit or acknowledgement to another source, permission must also be sought from that source. If such permission is not obtained then that material may not be included in your publication/copies. Suitable acknowledgement to the source must be made, either as a footnote or in a reference list at the end of your publication, as follows:

"Reprinted from Publication title, Vol /edition number, Author(s), Title of article / title of chapter, Pages No., Copyright (Year), with permission from Elsevier [OR APPLICABLE SOCIETY COPYRIGHT OWNER]." Also Lancet special credit - "Reprinted from The Lancet, Vol. number, Author(s), Title of article, Pages No., Copyright (Year), with permission from Elsevier."

4. Reproduction of this material is confined to the purpose and/or media for which permission is hereby given.

5. Altering/Modifying Material: Not Permitted. However figures and illustrations may be altered/adapted minimally to serve your work. Any other abbreviations, additions, deletions and/or any other alterations shall be made only with prior written authorization of Elsevier Ltd. (Please contact Elsevier at permissions@elsevier.com)

6. If the permission fee for the requested use of our material is waived in this instance, please be advised that your future requests for Elsevier materials may attract a fee.

7. Reservation of Rights: Publisher reserves all rights not specifically granted in the combination of (i) the license details provided by you and accepted in the course of this licensing transaction, (ii) these terms and conditions and (iii) CCC's Billing and Payment terms and conditions.

8. License Contingent Upon Payment: While you may exercise the rights licensed immediately upon issuance of the license at the end of the licensing process for the transaction, provided that you have disclosed complete and accurate details of your proposed use, no license is finally effective unless and until full payment is received from you (either by publisher or by CCC) as provided in CCC's Billing and Payment terms and conditions. If

full payment is not received on a timely basis, then any license preliminarily granted shall be deemed automatically revoked and shall be void as if never granted. Further, in the event that you breach any of these terms and conditions or any of CCC's Billing and Payment terms and conditions, the license is automatically revoked and shall be void as if never granted. Use of materials as described in a revoked license, as well as any use of the materials beyond the scope of an unrevoked license, may constitute copyright infringement and publisher reserves the right to take any and all action to protect its copyright in the materials.

9. Warranties: Publisher makes no representations or warranties with respect to the licensed material.

10. Indemnity: You hereby indemnify and agree to hold harmless publisher and CCC, and their respective officers, directors, employees and agents, from and against any and all claims arising out of your use of the licensed material other than as specifically authorized pursuant to this license.

11. No Transfer of License: This license is personal to you and may not be sublicensed, assigned, or transferred by you to any other person without publisher's written permission.

12. No Amendment Except in Writing: This license may not be amended except in a writing signed by both parties (or, in the case of publisher, by CCC on publisher's behalf).

13. Objection to Contrary Terms: Publisher hereby objects to any terms contained in any purchase order, acknowledgment, check endorsement or other writing prepared by you, which terms are inconsistent with these terms and conditions or CCC's Billing and Payment terms and conditions. These terms and conditions, together with CCC's Billing and Payment terms and conditions (which are incorporated herein), comprise the entire agreement between you and publisher (and CCC) concerning this licensing transaction. In the event of any conflict between your obligations established by these terms and conditions and those established by CCC's Billing and Payment terms and conditions, these terms and conditions shall control.

14. Revocation: Elsevier or Copyright Clearance Center may deny the permissions described in this License at their sole discretion, for any reason or no reason, with a full refund payable to you. Notice of such denial will be made using the contact information provided by you. Failure to receive such notice will not alter or invalidate the denial. In no event will Elsevier or Copyright Clearance Center be responsible or liable for any costs, expenses or damage incurred by you as a result of a denial of your permission request, other than a refund of the amount(s) paid by you to Elsevier and/or Copyright Clearance Center for denied permissions.

LIMITED LICENSE

The following terms and conditions apply only to specific license types:

15. Translation : This permission is granted for non-exclusive world English rights only unless your license was granted for translation rights. If you licensed translation rights you may only translate this content into the languages you requested. A professional translator must perform all translations and reproduce the content word for word preserving the integrity of the article. If this license is to re-use 1 or 2 figures then permission is granted for non-exclusive world rights in all languages.

16. **Posting licensed content on any Website:** The following terms and conditions apply as follows: Licensing material from an Elsevier journal: All content posted to the web site must

maintain the copyright information line on the bottom of each image; A hyper-text must be included to the Homepage of the journal from which you are licensing at <http://www.sciencedirect.com/science/journal/xxxxx> or the Elsevier homepage for books at <http://www.elsevier.com>; Central Storage: This license does not include permission for a scanned version of the material to be stored in a central repository such as that provided by Heron/XanEdu.

Licensing material from an Elsevier book: A hyper-text link must be included to the Elsevier homepage at <http://www.elsevier.com> . All content posted to the web site must maintain the copyright information line on the bottom of each image.

Posting licensed content on Electronic reserve: In addition to the above the following clauses are applicable: The web site must be password-protected and made available only to bona fide students registered on a relevant course. This permission is granted for 1 year only. You may obtain a new license for future website posting.

17. For journal authors: the following clauses are applicable in addition to the above:

Preprints:

A preprint is an author's own write-up of research results and analysis, it has not been peer-reviewed, nor has it had any other value added to it by a publisher (such as formatting, copyright, technical enhancement etc.).

Authors can share their preprints anywhere at any time. Preprints should not be added to or enhanced in any way in order to appear more like, or to substitute for, the final versions of articles however authors can update their preprints on arXiv or RePEc with their Accepted Author Manuscript (see below).

If accepted for publication, we encourage authors to link from the preprint to their formal publication via its DOI. Millions of researchers have access to the formal publications on ScienceDirect, and so links will help users to find, access, cite and use the best available version. Please note that Cell Press, The Lancet and some society-owned have different preprint policies. Information on these policies is available on the journal homepage.

Accepted Author Manuscripts: An accepted author manuscript is the manuscript of an article that has been accepted for publication and which typically includes author-incorporated changes suggested during submission, peer review and editor-author communications.

Authors can share their accepted author manuscript:

- immediately
 - via their non-commercial person homepage or blog
 - by updating a preprint in arXiv or RePEc with the accepted manuscript
 - via their research institute or institutional repository for internal institutional uses or as part of an invitation-only research collaboration work-group
 - directly by providing copies to their students or to research collaborators for their personal use
 - for private scholarly sharing as part of an invitation-only work group on

commercial sites with which Elsevier has an agreement

- after the embargo period
 - via non-commercial hosting platforms such as their institutional repository
 - via commercial sites with which Elsevier has an agreement

In all cases accepted manuscripts should:

- link to the formal publication via its DOI
- bear a CC-BY-NC-ND license - this is easy to do
- if aggregated with other manuscripts, for example in a repository or other site, be shared in alignment with our hosting policy not be added to or enhanced in any way to appear more like, or to substitute for, the published journal article.

Published journal article (JPA): A published journal article (PJA) is the definitive final record of published research that appears or will appear in the journal and embodies all value-adding publishing activities including peer review co-ordination, copy-editing, formatting, (if relevant) pagination and online enrichment.

Policies for sharing publishing journal articles differ for subscription and gold open access articles:

Subscription Articles: If you are an author, please share a link to your article rather than the full-text. Millions of researchers have access to the formal publications on ScienceDirect, and so links will help your users to find, access, cite, and use the best available version.

Theses and dissertations which contain embedded PJAs as part of the formal submission can be posted publicly by the awarding institution with DOI links back to the formal publications on ScienceDirect.

If you are affiliated with a library that subscribes to ScienceDirect you have additional private sharing rights for others' research accessed under that agreement. This includes use for classroom teaching and internal training at the institution (including use in course packs and courseware programs), and inclusion of the article for grant funding purposes.

Gold Open Access Articles: May be shared according to the author-selected end-user license and should contain a [CrossMark logo](#), the end user license, and a DOI link to the formal publication on ScienceDirect.

Please refer to Elsevier's [posting policy](#) for further information.

18. For book authors the following clauses are applicable in addition to the above: Authors are permitted to place a brief summary of their work online only. You are not allowed to download and post the published electronic version of your chapter, nor may you scan the printed edition to create an electronic version. Posting to a repository: Authors are permitted to post a summary of their chapter only in their institution's repository.

19. Thesis/Dissertation: If your license is for use in a thesis/dissertation your thesis may be submitted to your institution in either print or electronic form. Should your thesis be published commercially, please reapply for permission. These requirements include permission for the Library and Archives of Canada to supply single copies, on demand, of

the complete thesis and include permission for Proquest/UMI to supply single copies, on demand, of the complete thesis. Should your thesis be published commercially, please reapply for permission. Theses and dissertations which contain embedded PJAs as part of the formal submission can be posted publicly by the awarding institution with DOI links back to the formal publications on ScienceDirect.

Elsevier Open Access Terms and Conditions

You can publish open access with Elsevier in hundreds of open access journals or in nearly 2000 established subscription journals that support open access publishing. Permitted third party re-use of these open access articles is defined by the author's choice of Creative Commons user license. See our [open access license policy](#) for more information.

Terms & Conditions applicable to all Open Access articles published with Elsevier:

Any reuse of the article must not represent the author as endorsing the adaptation of the article nor should the article be modified in such a way as to damage the author's honour or reputation. If any changes have been made, such changes must be clearly indicated.

The author(s) must be appropriately credited and we ask that you include the end user license and a DOI link to the formal publication on ScienceDirect.

If any part of the material to be used (for example, figures) has appeared in our publication with credit or acknowledgement to another source it is the responsibility of the user to ensure their reuse complies with the terms and conditions determined by the rights holder.

Additional Terms & Conditions applicable to each Creative Commons user license:

CC BY: The CC-BY license allows users to copy, to create extracts, abstracts and new works from the Article, to alter and revise the Article and to make commercial use of the Article (including reuse and/or resale of the Article by commercial entities), provided the user gives appropriate credit (with a link to the formal publication through the relevant DOI), provides a link to the license, indicates if changes were made and the licensor is not represented as endorsing the use made of the work. The full details of the license are available at <http://creativecommons.org/licenses/by/4.0>.

CC BY NC SA: The CC BY-NC-SA license allows users to copy, to create extracts, abstracts and new works from the Article, to alter and revise the Article, provided this is not done for commercial purposes, and that the user gives appropriate credit (with a link to the formal publication through the relevant DOI), provides a link to the license, indicates if changes were made and the licensor is not represented as endorsing the use made of the work. Further, any new works must be made available on the same conditions. The full details of the license are available at <http://creativecommons.org/licenses/by-nc-sa/4.0>.

CC BY NC ND: The CC BY-NC-ND license allows users to copy and distribute the Article, provided this is not done for commercial purposes and further does not permit distribution of the Article if it is changed or edited in any way, and provided the user gives appropriate credit (with a link to the formal publication through the relevant DOI), provides a link to the license, and that the licensor is not represented as endorsing the use made of the work. The full details of the license are available at <http://creativecommons.org/licenses/by-nc-nd/4.0>. Any commercial reuse of Open Access articles published with a CC BY NC SA or CC BY NC ND license requires permission from Elsevier and will be subject to a fee.

Commercial reuse includes:

- Associating advertising with the full text of the Article
- Charging fees for document delivery or access
- Article aggregation
- Systematic distribution via e-mail lists or share buttons

Posting or linking by commercial companies for use by customers of those companies.

20. Other Conditions:

v1.7

Questions? customercare@copyright.com or +1-855-239-3415 (toll free in the US) or +1-978-646-2777.

ELSEVIER LICENSE
TERMS AND CONDITIONS

Jun 08, 2015

This is a License Agreement between Mohd Ayub Sulong ("You") and Elsevier ("Elsevier") provided by Copyright Clearance Center ("CCC"). The license consists of your order details, the terms and conditions provided by Elsevier, and the payment terms and conditions.

All payments must be made in full to CCC. For payment instructions, please see information listed at the bottom of this form.

Supplier	Elsevier Limited The Boulevard, Langford Lane Kidlington, Oxford, OX5 1GB, UK
Registered Company Number	1982084
Customer name	Mohd Ayub Sulong
Customer address	12 Albert St MAYFIELD, NSW 2304
License number	3644521268885
License date	Jun 08, 2015
Licensed content publisher	Elsevier
Licensed content publication	International Journal of Heat and Mass Transfer
Licensed content title	Determination of the thermal conductivity of periodic APM foam models
Licensed content author	T. Fiedler, M.A. Sulong, M. Vesenjak, Y. Higa, I.V. Belova, A. Öchsner, G.E. Murch
Licensed content date	June 2014
Licensed content volume number	73
Licensed content issue number	n/a
Number of pages	8
Start Page	826
End Page	833
Type of Use	reuse in a thesis/dissertation
Intended publisher of new work	other
Portion	full article
Format	both print and electronic
Are you the author of this Elsevier article?	Yes
Will you be translating?	No
Title of your thesis/dissertation	Characterisation of Advanced Porous Materials
Expected completion date	Aug 2015

Estimated size (number of pages)	150
Elsevier VAT number	GB 494 6272 12
Permissions price	0.00 USD
VAT/Local Sales Tax	0.00 USD / 0.00 GBP
Total	0.00 USD
Terms and Conditions	

INTRODUCTION

1. The publisher for this copyrighted material is Elsevier. By clicking "accept" in connection with completing this licensing transaction, you agree that the following terms and conditions apply to this transaction (along with the Billing and Payment terms and conditions established by Copyright Clearance Center, Inc. ("CCC"), at the time that you opened your Rightslink account and that are available at any time at <http://myaccount.copyright.com>).

GENERAL TERMS

2. Elsevier hereby grants you permission to reproduce the aforementioned material subject to the terms and conditions indicated.

3. Acknowledgement: If any part of the material to be used (for example, figures) has appeared in our publication with credit or acknowledgement to another source, permission must also be sought from that source. If such permission is not obtained then that material may not be included in your publication/copies. Suitable acknowledgement to the source must be made, either as a footnote or in a reference list at the end of your publication, as follows:

"Reprinted from Publication title, Vol /edition number, Author(s), Title of article / title of chapter, Pages No., Copyright (Year), with permission from Elsevier [OR APPLICABLE SOCIETY COPYRIGHT OWNER]." Also Lancet special credit - "Reprinted from The Lancet, Vol. number, Author(s), Title of article, Pages No., Copyright (Year), with permission from Elsevier."

4. Reproduction of this material is confined to the purpose and/or media for which permission is hereby given.

5. Altering/Modifying Material: Not Permitted. However figures and illustrations may be altered/adapted minimally to serve your work. Any other abbreviations, additions, deletions and/or any other alterations shall be made only with prior written authorization of Elsevier Ltd. (Please contact Elsevier at permissions@elsevier.com)

6. If the permission fee for the requested use of our material is waived in this instance, please be advised that your future requests for Elsevier materials may attract a fee.

7. Reservation of Rights: Publisher reserves all rights not specifically granted in the combination of (i) the license details provided by you and accepted in the course of this licensing transaction, (ii) these terms and conditions and (iii) CCC's Billing and Payment terms and conditions.

8. License Contingent Upon Payment: While you may exercise the rights licensed immediately upon issuance of the license at the end of the licensing process for the transaction, provided that you have disclosed complete and accurate details of your proposed

use, no license is finally effective unless and until full payment is received from you (either by publisher or by CCC) as provided in CCC's Billing and Payment terms and conditions. If full payment is not received on a timely basis, then any license preliminarily granted shall be deemed automatically revoked and shall be void as if never granted. Further, in the event that you breach any of these terms and conditions or any of CCC's Billing and Payment terms and conditions, the license is automatically revoked and shall be void as if never granted. Use of materials as described in a revoked license, as well as any use of the materials beyond the scope of an unrevoked license, may constitute copyright infringement and publisher reserves the right to take any and all action to protect its copyright in the materials.

9. Warranties: Publisher makes no representations or warranties with respect to the licensed material.

10. Indemnity: You hereby indemnify and agree to hold harmless publisher and CCC, and their respective officers, directors, employees and agents, from and against any and all claims arising out of your use of the licensed material other than as specifically authorized pursuant to this license.

11. No Transfer of License: This license is personal to you and may not be sublicensed, assigned, or transferred by you to any other person without publisher's written permission.

12. No Amendment Except in Writing: This license may not be amended except in a writing signed by both parties (or, in the case of publisher, by CCC on publisher's behalf).

13. Objection to Contrary Terms: Publisher hereby objects to any terms contained in any purchase order, acknowledgment, check endorsement or other writing prepared by you, which terms are inconsistent with these terms and conditions or CCC's Billing and Payment terms and conditions. These terms and conditions, together with CCC's Billing and Payment terms and conditions (which are incorporated herein), comprise the entire agreement between you and publisher (and CCC) concerning this licensing transaction. In the event of any conflict between your obligations established by these terms and conditions and those established by CCC's Billing and Payment terms and conditions, these terms and conditions shall control.

14. Revocation: Elsevier or Copyright Clearance Center may deny the permissions described in this License at their sole discretion, for any reason or no reason, with a full refund payable to you. Notice of such denial will be made using the contact information provided by you. Failure to receive such notice will not alter or invalidate the denial. In no event will Elsevier or Copyright Clearance Center be responsible or liable for any costs, expenses or damage incurred by you as a result of a denial of your permission request, other than a refund of the amount(s) paid by you to Elsevier and/or Copyright Clearance Center for denied permissions.

LIMITED LICENSE

The following terms and conditions apply only to specific license types:

15. Translation : This permission is granted for non-exclusive world English rights only unless your license was granted for translation rights. If you licensed translation rights you may only translate this content into the languages you requested. A professional translator must perform all translations and reproduce the content word for word preserving the integrity of the article. If this license is to re-use 1 or 2 figures then permission is granted for non-exclusive world rights in all languages.

16. Posting licensed content on any Website: The following terms and conditions apply as follows: Licensing material from an Elsevier journal: All content posted to the web site must maintain the copyright information line on the bottom of each image; A hyper-text must be included to the Homepage of the journal from which you are licensing at <http://www.sciencedirect.com/science/journal/xxxxx> or the Elsevier homepage for books at <http://www.elsevier.com>; Central Storage: This license does not include permission for a scanned version of the material to be stored in a central repository such as that provided by Heron/XanEdu.

Licensing material from an Elsevier book: A hyper-text link must be included to the Elsevier homepage at <http://www.elsevier.com> . All content posted to the web site must maintain the copyright information line on the bottom of each image.

Posting licensed content on Electronic reserve: In addition to the above the following clauses are applicable: The web site must be password-protected and made available only to bona fide students registered on a relevant course. This permission is granted for 1 year only. You may obtain a new license for future website posting.

17. For journal authors: the following clauses are applicable in addition to the above:

Preprints:

A preprint is an author's own write-up of research results and analysis, it has not been peer-reviewed, nor has it had any other value added to it by a publisher (such as formatting, copyright, technical enhancement etc.).

Authors can share their preprints anywhere at any time. Preprints should not be added to or enhanced in any way in order to appear more like, or to substitute for, the final versions of articles however authors can update their preprints on arXiv or RePEc with their Accepted Author Manuscript (see below).

If accepted for publication, we encourage authors to link from the preprint to their formal publication via its DOI. Millions of researchers have access to the formal publications on ScienceDirect, and so links will help users to find, access, cite and use the best available version. Please note that Cell Press, The Lancet and some society-owned have different preprint policies. Information on these policies is available on the journal homepage.

Accepted Author Manuscripts: An accepted author manuscript is the manuscript of an article that has been accepted for publication and which typically includes author-incorporated changes suggested during submission, peer review and editor-author communications.

Authors can share their accepted author manuscript:

- immediately
 - via their non-commercial person homepage or blog
 - by updating a preprint in arXiv or RePEc with the accepted manuscript
 - via their research institute or institutional repository for internal institutional uses or as part of an invitation-only research collaboration work-group
 - directly by providing copies to their students or to research collaborators for

their personal use

- for private scholarly sharing as part of an invitation-only work group on commercial sites with which Elsevier has an agreement
- after the embargo period
 - via non-commercial hosting platforms such as their institutional repository
 - via commercial sites with which Elsevier has an agreement

In all cases accepted manuscripts should:

- link to the formal publication via its DOI
- bear a CC-BY-NC-ND license - this is easy to do
- if aggregated with other manuscripts, for example in a repository or other site, be shared in alignment with our hosting policy not be added to or enhanced in any way to appear more like, or to substitute for, the published journal article.

Published journal article (JPA): A published journal article (PJA) is the definitive final record of published research that appears or will appear in the journal and embodies all value-adding publishing activities including peer review co-ordination, copy-editing, formatting, (if relevant) pagination and online enrichment.

Policies for sharing publishing journal articles differ for subscription and gold open access articles:

Subscription Articles: If you are an author, please share a link to your article rather than the full-text. Millions of researchers have access to the formal publications on ScienceDirect, and so links will help your users to find, access, cite, and use the best available version.

Theses and dissertations which contain embedded PJAs as part of the formal submission can be posted publicly by the awarding institution with DOI links back to the formal publications on ScienceDirect.

If you are affiliated with a library that subscribes to ScienceDirect you have additional private sharing rights for others' research accessed under that agreement. This includes use for classroom teaching and internal training at the institution (including use in course packs and courseware programs), and inclusion of the article for grant funding purposes.

Gold Open Access Articles: May be shared according to the author-selected end-user license and should contain a [CrossMark logo](#), the end user license, and a DOI link to the formal publication on ScienceDirect.

Please refer to Elsevier's [posting policy](#) for further information.

18. For book authors the following clauses are applicable in addition to the above: Authors are permitted to place a brief summary of their work online only. You are not allowed to download and post the published electronic version of your chapter, nor may you scan the printed edition to create an electronic version. Posting to a repository: Authors are permitted to post a summary of their chapter only in their institution's repository.

19. Thesis/Dissertation: If your license is for use in a thesis/dissertation your thesis may be

submitted to your institution in either print or electronic form. Should your thesis be published commercially, please reapply for permission. These requirements include permission for the Library and Archives of Canada to supply single copies, on demand, of the complete thesis and include permission for Proquest/UMI to supply single copies, on demand, of the complete thesis. Should your thesis be published commercially, please reapply for permission. Theses and dissertations which contain embedded PJAs as part of the formal submission can be posted publicly by the awarding institution with DOI links back to the formal publications on ScienceDirect.

Elsevier Open Access Terms and Conditions

You can publish open access with Elsevier in hundreds of open access journals or in nearly 2000 established subscription journals that support open access publishing. Permitted third party re-use of these open access articles is defined by the author's choice of Creative Commons user license. See our [open access license policy](#) for more information.

Terms & Conditions applicable to all Open Access articles published with Elsevier:

Any reuse of the article must not represent the author as endorsing the adaptation of the article nor should the article be modified in such a way as to damage the author's honour or reputation. If any changes have been made, such changes must be clearly indicated.

The author(s) must be appropriately credited and we ask that you include the end user license and a DOI link to the formal publication on ScienceDirect.

If any part of the material to be used (for example, figures) has appeared in our publication with credit or acknowledgement to another source it is the responsibility of the user to ensure their reuse complies with the terms and conditions determined by the rights holder.

Additional Terms & Conditions applicable to each Creative Commons user license:

CC BY: The CC-BY license allows users to copy, to create extracts, abstracts and new works from the Article, to alter and revise the Article and to make commercial use of the Article (including reuse and/or resale of the Article by commercial entities), provided the user gives appropriate credit (with a link to the formal publication through the relevant DOI), provides a link to the license, indicates if changes were made and the licensor is not represented as endorsing the use made of the work. The full details of the license are available at <http://creativecommons.org/licenses/by/4.0>.

CC BY NC SA: The CC BY-NC-SA license allows users to copy, to create extracts, abstracts and new works from the Article, to alter and revise the Article, provided this is not done for commercial purposes, and that the user gives appropriate credit (with a link to the formal publication through the relevant DOI), provides a link to the license, indicates if changes were made and the licensor is not represented as endorsing the use made of the work. Further, any new works must be made available on the same conditions. The full details of the license are available at <http://creativecommons.org/licenses/by-nc-sa/4.0>.

CC BY NC ND: The CC BY-NC-ND license allows users to copy and distribute the Article, provided this is not done for commercial purposes and further does not permit distribution of the Article if it is changed or edited in any way, and provided the user gives appropriate credit (with a link to the formal publication through the relevant DOI), provides a link to the license, and that the licensor is not represented as endorsing the use made of the work. The full details of the license are available at <http://creativecommons.org/licenses/by-nc-nd/4.0>.

Any commercial reuse of Open Access articles published with a CC BY NC SA or CC BY NC ND license requires permission from Elsevier and will be subject to a fee.

Commercial reuse includes:

- Associating advertising with the full text of the Article
- Charging fees for document delivery or access
- Article aggregation
- Systematic distribution via e-mail lists or share buttons

Posting or linking by commercial companies for use by customers of those companies.

20. Other Conditions:

v1.7

Questions? customercare@copyright.com or +1-855-239-3415 (toll free in the US) or +1-978-646-2777.

ELSEVIER LICENSE
TERMS AND CONDITIONS

Jun 08, 2015

This is a License Agreement between Mohd Ayub Sulong ("You") and Elsevier ("Elsevier") provided by Copyright Clearance Center ("CCC"). The license consists of your order details, the terms and conditions provided by Elsevier, and the payment terms and conditions.

All payments must be made in full to CCC. For payment instructions, please see information listed at the bottom of this form.

Supplier	Elsevier Limited The Boulevard, Langford Lane Kidlington, Oxford, OX5 1GB, UK
Registered Company Number	1982084
Customer name	Mohd Ayub Sulong
Customer address	12 Albert St MAYFIELD, NSW 2304
License number	3644530050292
License date	Jun 08, 2015
Licensed content publisher	Elsevier
Licensed content publication	Computational Materials Science
Licensed content title	Mechanical properties of aluminium foam derived from infiltration casting of salt dough
Licensed content author	T. Fiedler, M.A. Sulong, V. Mathier, I.V. Belova, C. Younger, G.E. Murch
Licensed content date	January 2014
Licensed content volume number	81
Licensed content issue number	n/a
Number of pages	3
Start Page	246
End Page	248
Type of Use	reuse in a thesis/dissertation
Intended publisher of new work	other
Portion	full article
Format	both print and electronic
Are you the author of this Elsevier article?	Yes
Will you be translating?	No
Title of your thesis/dissertation	Characterisation of Advanced Porous Materials
Expected completion date	Aug 2015

Estimated size (number of pages)	150
Elsevier VAT number	GB 494 6272 12
Permissions price	0.00 USD
VAT/Local Sales Tax	0.00 USD / 0.00 GBP
Total	0.00 USD
Terms and Conditions	

INTRODUCTION

1. The publisher for this copyrighted material is Elsevier. By clicking "accept" in connection with completing this licensing transaction, you agree that the following terms and conditions apply to this transaction (along with the Billing and Payment terms and conditions established by Copyright Clearance Center, Inc. ("CCC"), at the time that you opened your Rightslink account and that are available at any time at <http://myaccount.copyright.com>).

GENERAL TERMS

2. Elsevier hereby grants you permission to reproduce the aforementioned material subject to the terms and conditions indicated.

3. Acknowledgement: If any part of the material to be used (for example, figures) has appeared in our publication with credit or acknowledgement to another source, permission must also be sought from that source. If such permission is not obtained then that material may not be included in your publication/copies. Suitable acknowledgement to the source must be made, either as a footnote or in a reference list at the end of your publication, as follows:

"Reprinted from Publication title, Vol /edition number, Author(s), Title of article / title of chapter, Pages No., Copyright (Year), with permission from Elsevier [OR APPLICABLE SOCIETY COPYRIGHT OWNER]." Also Lancet special credit - "Reprinted from The Lancet, Vol. number, Author(s), Title of article, Pages No., Copyright (Year), with permission from Elsevier."

4. Reproduction of this material is confined to the purpose and/or media for which permission is hereby given.

5. Altering/Modifying Material: Not Permitted. However figures and illustrations may be altered/adapted minimally to serve your work. Any other abbreviations, additions, deletions and/or any other alterations shall be made only with prior written authorization of Elsevier Ltd. (Please contact Elsevier at permissions@elsevier.com)

6. If the permission fee for the requested use of our material is waived in this instance, please be advised that your future requests for Elsevier materials may attract a fee.

7. Reservation of Rights: Publisher reserves all rights not specifically granted in the combination of (i) the license details provided by you and accepted in the course of this licensing transaction, (ii) these terms and conditions and (iii) CCC's Billing and Payment terms and conditions.

8. License Contingent Upon Payment: While you may exercise the rights licensed immediately upon issuance of the license at the end of the licensing process for the transaction, provided that you have disclosed complete and accurate details of your proposed

use, no license is finally effective unless and until full payment is received from you (either by publisher or by CCC) as provided in CCC's Billing and Payment terms and conditions. If full payment is not received on a timely basis, then any license preliminarily granted shall be deemed automatically revoked and shall be void as if never granted. Further, in the event that you breach any of these terms and conditions or any of CCC's Billing and Payment terms and conditions, the license is automatically revoked and shall be void as if never granted. Use of materials as described in a revoked license, as well as any use of the materials beyond the scope of an unrevoked license, may constitute copyright infringement and publisher reserves the right to take any and all action to protect its copyright in the materials.

9. Warranties: Publisher makes no representations or warranties with respect to the licensed material.

10. Indemnity: You hereby indemnify and agree to hold harmless publisher and CCC, and their respective officers, directors, employees and agents, from and against any and all claims arising out of your use of the licensed material other than as specifically authorized pursuant to this license.

11. No Transfer of License: This license is personal to you and may not be sublicensed, assigned, or transferred by you to any other person without publisher's written permission.

12. No Amendment Except in Writing: This license may not be amended except in a writing signed by both parties (or, in the case of publisher, by CCC on publisher's behalf).

13. Objection to Contrary Terms: Publisher hereby objects to any terms contained in any purchase order, acknowledgment, check endorsement or other writing prepared by you, which terms are inconsistent with these terms and conditions or CCC's Billing and Payment terms and conditions. These terms and conditions, together with CCC's Billing and Payment terms and conditions (which are incorporated herein), comprise the entire agreement between you and publisher (and CCC) concerning this licensing transaction. In the event of any conflict between your obligations established by these terms and conditions and those established by CCC's Billing and Payment terms and conditions, these terms and conditions shall control.

14. Revocation: Elsevier or Copyright Clearance Center may deny the permissions described in this License at their sole discretion, for any reason or no reason, with a full refund payable to you. Notice of such denial will be made using the contact information provided by you. Failure to receive such notice will not alter or invalidate the denial. In no event will Elsevier or Copyright Clearance Center be responsible or liable for any costs, expenses or damage incurred by you as a result of a denial of your permission request, other than a refund of the amount(s) paid by you to Elsevier and/or Copyright Clearance Center for denied permissions.

LIMITED LICENSE

The following terms and conditions apply only to specific license types:

15. Translation: This permission is granted for non-exclusive world English rights only unless your license was granted for translation rights. If you licensed translation rights you may only translate this content into the languages you requested. A professional translator must perform all translations and reproduce the content word for word preserving the integrity of the article. If this license is to re-use 1 or 2 figures then permission is granted for non-exclusive world rights in all languages.

16. Posting licensed content on any Website: The following terms and conditions apply as follows: Licensing material from an Elsevier journal: All content posted to the web site must maintain the copyright information line on the bottom of each image; A hyper-text must be included to the Homepage of the journal from which you are licensing at <http://www.sciencedirect.com/science/journal/xxxxx> or the Elsevier homepage for books at <http://www.elsevier.com>; Central Storage: This license does not include permission for a scanned version of the material to be stored in a central repository such as that provided by Heron/XanEdu.

Licensing material from an Elsevier book: A hyper-text link must be included to the Elsevier homepage at <http://www.elsevier.com> . All content posted to the web site must maintain the copyright information line on the bottom of each image.

Posting licensed content on Electronic reserve: In addition to the above the following clauses are applicable: The web site must be password-protected and made available only to bona fide students registered on a relevant course. This permission is granted for 1 year only. You may obtain a new license for future website posting.

17. For journal authors: the following clauses are applicable in addition to the above:

Preprints:

A preprint is an author's own write-up of research results and analysis, it has not been peer-reviewed, nor has it had any other value added to it by a publisher (such as formatting, copyright, technical enhancement etc.).

Authors can share their preprints anywhere at any time. Preprints should not be added to or enhanced in any way in order to appear more like, or to substitute for, the final versions of articles however authors can update their preprints on arXiv or RePEc with their Accepted Author Manuscript (see below).

If accepted for publication, we encourage authors to link from the preprint to their formal publication via its DOI. Millions of researchers have access to the formal publications on ScienceDirect, and so links will help users to find, access, cite and use the best available version. Please note that Cell Press, The Lancet and some society-owned have different preprint policies. Information on these policies is available on the journal homepage.

Accepted Author Manuscripts: An accepted author manuscript is the manuscript of an article that has been accepted for publication and which typically includes author-incorporated changes suggested during submission, peer review and editor-author communications.

Authors can share their accepted author manuscript:

- immediately
 - via their non-commercial person homepage or blog
 - by updating a preprint in arXiv or RePEc with the accepted manuscript
 - via their research institute or institutional repository for internal institutional uses or as part of an invitation-only research collaboration work-group
 - directly by providing copies to their students or to research collaborators for

their personal use

- for private scholarly sharing as part of an invitation-only work group on commercial sites with which Elsevier has an agreement
- after the embargo period
 - via non-commercial hosting platforms such as their institutional repository
 - via commercial sites with which Elsevier has an agreement

In all cases accepted manuscripts should:

- link to the formal publication via its DOI
- bear a CC-BY-NC-ND license - this is easy to do
- if aggregated with other manuscripts, for example in a repository or other site, be shared in alignment with our hosting policy not be added to or enhanced in any way to appear more like, or to substitute for, the published journal article.

Published journal article (JPA): A published journal article (PJA) is the definitive final record of published research that appears or will appear in the journal and embodies all value-adding publishing activities including peer review co-ordination, copy-editing, formatting, (if relevant) pagination and online enrichment.

Policies for sharing publishing journal articles differ for subscription and gold open access articles:

Subscription Articles: If you are an author, please share a link to your article rather than the full-text. Millions of researchers have access to the formal publications on ScienceDirect, and so links will help your users to find, access, cite, and use the best available version.

Theses and dissertations which contain embedded PJAs as part of the formal submission can be posted publicly by the awarding institution with DOI links back to the formal publications on ScienceDirect.

If you are affiliated with a library that subscribes to ScienceDirect you have additional private sharing rights for others' research accessed under that agreement. This includes use for classroom teaching and internal training at the institution (including use in course packs and courseware programs), and inclusion of the article for grant funding purposes.

Gold Open Access Articles: May be shared according to the author-selected end-user license and should contain a [CrossMark logo](#), the end user license, and a DOI link to the formal publication on ScienceDirect.

Please refer to Elsevier's [posting policy](#) for further information.

18. For book authors the following clauses are applicable in addition to the above: Authors are permitted to place a brief summary of their work online only. You are not allowed to download and post the published electronic version of your chapter, nor may you scan the printed edition to create an electronic version. Posting to a repository: Authors are permitted to post a summary of their chapter only in their institution's repository.

19. Thesis/Dissertation: If your license is for use in a thesis/dissertation your thesis may be

submitted to your institution in either print or electronic form. Should your thesis be published commercially, please reapply for permission. These requirements include permission for the Library and Archives of Canada to supply single copies, on demand, of the complete thesis and include permission for Proquest/UMI to supply single copies, on demand, of the complete thesis. Should your thesis be published commercially, please reapply for permission. Theses and dissertations which contain embedded PJAs as part of the formal submission can be posted publicly by the awarding institution with DOI links back to the formal publications on ScienceDirect.

Elsevier Open Access Terms and Conditions

You can publish open access with Elsevier in hundreds of open access journals or in nearly 2000 established subscription journals that support open access publishing. Permitted third party re-use of these open access articles is defined by the author's choice of Creative Commons user license. See our [open access license policy](#) for more information.

Terms & Conditions applicable to all Open Access articles published with Elsevier:

Any reuse of the article must not represent the author as endorsing the adaptation of the article nor should the article be modified in such a way as to damage the author's honour or reputation. If any changes have been made, such changes must be clearly indicated.

The author(s) must be appropriately credited and we ask that you include the end user license and a DOI link to the formal publication on ScienceDirect.

If any part of the material to be used (for example, figures) has appeared in our publication with credit or acknowledgement to another source it is the responsibility of the user to ensure their reuse complies with the terms and conditions determined by the rights holder.

Additional Terms & Conditions applicable to each Creative Commons user license:

CC BY: The CC-BY license allows users to copy, to create extracts, abstracts and new works from the Article, to alter and revise the Article and to make commercial use of the Article (including reuse and/or resale of the Article by commercial entities), provided the user gives appropriate credit (with a link to the formal publication through the relevant DOI), provides a link to the license, indicates if changes were made and the licensor is not represented as endorsing the use made of the work. The full details of the license are available at <http://creativecommons.org/licenses/by/4.0>.

CC BY NC SA: The CC BY-NC-SA license allows users to copy, to create extracts, abstracts and new works from the Article, to alter and revise the Article, provided this is not done for commercial purposes, and that the user gives appropriate credit (with a link to the formal publication through the relevant DOI), provides a link to the license, indicates if changes were made and the licensor is not represented as endorsing the use made of the work. Further, any new works must be made available on the same conditions. The full details of the license are available at <http://creativecommons.org/licenses/by-nc-sa/4.0>.

CC BY NC ND: The CC BY-NC-ND license allows users to copy and distribute the Article, provided this is not done for commercial purposes and further does not permit distribution of the Article if it is changed or edited in any way, and provided the user gives appropriate credit (with a link to the formal publication through the relevant DOI), provides a link to the license, and that the licensor is not represented as endorsing the use made of the work. The full details of the license are available at <http://creativecommons.org/licenses/by-nc-nd/4.0>.

Any commercial reuse of Open Access articles published with a CC BY NC SA or CC BY NC ND license requires permission from Elsevier and will be subject to a fee.

Commercial reuse includes:

- Associating advertising with the full text of the Article
- Charging fees for document delivery or access
- Article aggregation
- Systematic distribution via e-mail lists or share buttons

Posting or linking by commercial companies for use by customers of those companies.

20. Other Conditions:

v1.7

Questions? customercare@copyright.com or +1-855-239-3415 (toll free in the US) or +1-978-646-2777.

ELSEVIER LICENSE
TERMS AND CONDITIONS

Jun 08, 2015

This is a License Agreement between Mohd Ayub Sulong ("You") and Elsevier ("Elsevier") provided by Copyright Clearance Center ("CCC"). The license consists of your order details, the terms and conditions provided by Elsevier, and the payment terms and conditions.

All payments must be made in full to CCC. For payment instructions, please see information listed at the bottom of this form.

Supplier	Elsevier Limited The Boulevard, Langford Lane Kidlington, Oxford, OX5 1GB, UK
Registered Company Number	1982084
Customer name	Mohd Ayub Sulong
Customer address	12 Albert St MAYFIELD, NSW 2304
License number	3644521380167
License date	Jun 08, 2015
Licensed content publisher	Elsevier
Licensed content publication	Materials & Design
Licensed content title	On the particle size effect in expanded perlite aluminium syntactic foam
Licensed content author	M. Taherishargh, M.A. Sulong, I.V. Belova, G.E. Murch, T. Fiedler
Licensed content date	5 February 2015
Licensed content volume number	66
Licensed content issue number	n/a
Number of pages	10
Start Page	294
End Page	303
Type of Use	reuse in a thesis/dissertation
Intended publisher of new work	other
Portion	full article
Format	both print and electronic
Are you the author of this Elsevier article?	Yes
Will you be translating?	No
Title of your thesis/dissertation	Characterisation of Advanced Porous Materials
Expected completion date	Aug 2015

Estimated size (number of pages)	150
Elsevier VAT number	GB 494 6272 12
Permissions price	0.00 USD
VAT/Local Sales Tax	0.00 USD / 0.00 GBP
Total	0.00 USD
Terms and Conditions	

INTRODUCTION

1. The publisher for this copyrighted material is Elsevier. By clicking "accept" in connection with completing this licensing transaction, you agree that the following terms and conditions apply to this transaction (along with the Billing and Payment terms and conditions established by Copyright Clearance Center, Inc. ("CCC"), at the time that you opened your Rightslink account and that are available at any time at <http://myaccount.copyright.com>).

GENERAL TERMS

2. Elsevier hereby grants you permission to reproduce the aforementioned material subject to the terms and conditions indicated.

3. Acknowledgement: If any part of the material to be used (for example, figures) has appeared in our publication with credit or acknowledgement to another source, permission must also be sought from that source. If such permission is not obtained then that material may not be included in your publication/copies. Suitable acknowledgement to the source must be made, either as a footnote or in a reference list at the end of your publication, as follows:

"Reprinted from Publication title, Vol /edition number, Author(s), Title of article / title of chapter, Pages No., Copyright (Year), with permission from Elsevier [OR APPLICABLE SOCIETY COPYRIGHT OWNER]." Also Lancet special credit - "Reprinted from The Lancet, Vol. number, Author(s), Title of article, Pages No., Copyright (Year), with permission from Elsevier."

4. Reproduction of this material is confined to the purpose and/or media for which permission is hereby given.

5. Altering/Modifying Material: Not Permitted. However figures and illustrations may be altered/adapted minimally to serve your work. Any other abbreviations, additions, deletions and/or any other alterations shall be made only with prior written authorization of Elsevier Ltd. (Please contact Elsevier at permissions@elsevier.com)

6. If the permission fee for the requested use of our material is waived in this instance, please be advised that your future requests for Elsevier materials may attract a fee.

7. Reservation of Rights: Publisher reserves all rights not specifically granted in the combination of (i) the license details provided by you and accepted in the course of this licensing transaction, (ii) these terms and conditions and (iii) CCC's Billing and Payment terms and conditions.

8. License Contingent Upon Payment: While you may exercise the rights licensed immediately upon issuance of the license at the end of the licensing process for the transaction, provided that you have disclosed complete and accurate details of your proposed

use, no license is finally effective unless and until full payment is received from you (either by publisher or by CCC) as provided in CCC's Billing and Payment terms and conditions. If full payment is not received on a timely basis, then any license preliminarily granted shall be deemed automatically revoked and shall be void as if never granted. Further, in the event that you breach any of these terms and conditions or any of CCC's Billing and Payment terms and conditions, the license is automatically revoked and shall be void as if never granted. Use of materials as described in a revoked license, as well as any use of the materials beyond the scope of an unrevoked license, may constitute copyright infringement and publisher reserves the right to take any and all action to protect its copyright in the materials.

9. Warranties: Publisher makes no representations or warranties with respect to the licensed material.

10. Indemnity: You hereby indemnify and agree to hold harmless publisher and CCC, and their respective officers, directors, employees and agents, from and against any and all claims arising out of your use of the licensed material other than as specifically authorized pursuant to this license.

11. No Transfer of License: This license is personal to you and may not be sublicensed, assigned, or transferred by you to any other person without publisher's written permission.

12. No Amendment Except in Writing: This license may not be amended except in a writing signed by both parties (or, in the case of publisher, by CCC on publisher's behalf).

13. Objection to Contrary Terms: Publisher hereby objects to any terms contained in any purchase order, acknowledgment, check endorsement or other writing prepared by you, which terms are inconsistent with these terms and conditions or CCC's Billing and Payment terms and conditions. These terms and conditions, together with CCC's Billing and Payment terms and conditions (which are incorporated herein), comprise the entire agreement between you and publisher (and CCC) concerning this licensing transaction. In the event of any conflict between your obligations established by these terms and conditions and those established by CCC's Billing and Payment terms and conditions, these terms and conditions shall control.

14. Revocation: Elsevier or Copyright Clearance Center may deny the permissions described in this License at their sole discretion, for any reason or no reason, with a full refund payable to you. Notice of such denial will be made using the contact information provided by you. Failure to receive such notice will not alter or invalidate the denial. In no event will Elsevier or Copyright Clearance Center be responsible or liable for any costs, expenses or damage incurred by you as a result of a denial of your permission request, other than a refund of the amount(s) paid by you to Elsevier and/or Copyright Clearance Center for denied permissions.

LIMITED LICENSE

The following terms and conditions apply only to specific license types:

15. Translation: This permission is granted for non-exclusive world English rights only unless your license was granted for translation rights. If you licensed translation rights you may only translate this content into the languages you requested. A professional translator must perform all translations and reproduce the content word for word preserving the integrity of the article. If this license is to re-use 1 or 2 figures then permission is granted for non-exclusive world rights in all languages.

16. Posting licensed content on any Website: The following terms and conditions apply as follows: Licensing material from an Elsevier journal: All content posted to the web site must maintain the copyright information line on the bottom of each image; A hyper-text must be included to the Homepage of the journal from which you are licensing at <http://www.sciencedirect.com/science/journal/xxxxx> or the Elsevier homepage for books at <http://www.elsevier.com>; Central Storage: This license does not include permission for a scanned version of the material to be stored in a central repository such as that provided by Heron/XanEdu.

Licensing material from an Elsevier book: A hyper-text link must be included to the Elsevier homepage at <http://www.elsevier.com> . All content posted to the web site must maintain the copyright information line on the bottom of each image.

Posting licensed content on Electronic reserve: In addition to the above the following clauses are applicable: The web site must be password-protected and made available only to bona fide students registered on a relevant course. This permission is granted for 1 year only. You may obtain a new license for future website posting.

17. For journal authors: the following clauses are applicable in addition to the above:

Preprints:

A preprint is an author's own write-up of research results and analysis, it has not been peer-reviewed, nor has it had any other value added to it by a publisher (such as formatting, copyright, technical enhancement etc.).

Authors can share their preprints anywhere at any time. Preprints should not be added to or enhanced in any way in order to appear more like, or to substitute for, the final versions of articles however authors can update their preprints on arXiv or RePEc with their Accepted Author Manuscript (see below).

If accepted for publication, we encourage authors to link from the preprint to their formal publication via its DOI. Millions of researchers have access to the formal publications on ScienceDirect, and so links will help users to find, access, cite and use the best available version. Please note that Cell Press, The Lancet and some society-owned have different preprint policies. Information on these policies is available on the journal homepage.

Accepted Author Manuscripts: An accepted author manuscript is the manuscript of an article that has been accepted for publication and which typically includes author-incorporated changes suggested during submission, peer review and editor-author communications.

Authors can share their accepted author manuscript:

- immediately
 - via their non-commercial person homepage or blog
 - by updating a preprint in arXiv or RePEc with the accepted manuscript
 - via their research institute or institutional repository for internal institutional uses or as part of an invitation-only research collaboration work-group
 - directly by providing copies to their students or to research collaborators for

their personal use

- for private scholarly sharing as part of an invitation-only work group on commercial sites with which Elsevier has an agreement
- after the embargo period
 - via non-commercial hosting platforms such as their institutional repository
 - via commercial sites with which Elsevier has an agreement

In all cases accepted manuscripts should:

- link to the formal publication via its DOI
- bear a CC-BY-NC-ND license - this is easy to do
- if aggregated with other manuscripts, for example in a repository or other site, be shared in alignment with our hosting policy not be added to or enhanced in any way to appear more like, or to substitute for, the published journal article.

Published journal article (JPA): A published journal article (PJA) is the definitive final record of published research that appears or will appear in the journal and embodies all value-adding publishing activities including peer review co-ordination, copy-editing, formatting, (if relevant) pagination and online enrichment.

Policies for sharing publishing journal articles differ for subscription and gold open access articles:

Subscription Articles: If you are an author, please share a link to your article rather than the full-text. Millions of researchers have access to the formal publications on ScienceDirect, and so links will help your users to find, access, cite, and use the best available version.

Theses and dissertations which contain embedded PJAs as part of the formal submission can be posted publicly by the awarding institution with DOI links back to the formal publications on ScienceDirect.

If you are affiliated with a library that subscribes to ScienceDirect you have additional private sharing rights for others' research accessed under that agreement. This includes use for classroom teaching and internal training at the institution (including use in course packs and courseware programs), and inclusion of the article for grant funding purposes.

Gold Open Access Articles: May be shared according to the author-selected end-user license and should contain a [CrossMark logo](#), the end user license, and a DOI link to the formal publication on ScienceDirect.

Please refer to Elsevier's [posting policy](#) for further information.

18. For book authors the following clauses are applicable in addition to the above: Authors are permitted to place a brief summary of their work online only. You are not allowed to download and post the published electronic version of your chapter, nor may you scan the printed edition to create an electronic version. Posting to a repository: Authors are permitted to post a summary of their chapter only in their institution's repository.

19. Thesis/Dissertation: If your license is for use in a thesis/dissertation your thesis may be

submitted to your institution in either print or electronic form. Should your thesis be published commercially, please reapply for permission. These requirements include permission for the Library and Archives of Canada to supply single copies, on demand, of the complete thesis and include permission for Proquest/UMI to supply single copies, on demand, of the complete thesis. Should your thesis be published commercially, please reapply for permission. Theses and dissertations which contain embedded PJAs as part of the formal submission can be posted publicly by the awarding institution with DOI links back to the formal publications on ScienceDirect.

Elsevier Open Access Terms and Conditions

You can publish open access with Elsevier in hundreds of open access journals or in nearly 2000 established subscription journals that support open access publishing. Permitted third party re-use of these open access articles is defined by the author's choice of Creative Commons user license. See our [open access license policy](#) for more information.

Terms & Conditions applicable to all Open Access articles published with Elsevier:

Any reuse of the article must not represent the author as endorsing the adaptation of the article nor should the article be modified in such a way as to damage the author's honour or reputation. If any changes have been made, such changes must be clearly indicated.

The author(s) must be appropriately credited and we ask that you include the end user license and a DOI link to the formal publication on ScienceDirect.

If any part of the material to be used (for example, figures) has appeared in our publication with credit or acknowledgement to another source it is the responsibility of the user to ensure their reuse complies with the terms and conditions determined by the rights holder.

Additional Terms & Conditions applicable to each Creative Commons user license:

CC BY: The CC-BY license allows users to copy, to create extracts, abstracts and new works from the Article, to alter and revise the Article and to make commercial use of the Article (including reuse and/or resale of the Article by commercial entities), provided the user gives appropriate credit (with a link to the formal publication through the relevant DOI), provides a link to the license, indicates if changes were made and the licensor is not represented as endorsing the use made of the work. The full details of the license are available at <http://creativecommons.org/licenses/by/4.0>.

CC BY NC SA: The CC BY-NC-SA license allows users to copy, to create extracts, abstracts and new works from the Article, to alter and revise the Article, provided this is not done for commercial purposes, and that the user gives appropriate credit (with a link to the formal publication through the relevant DOI), provides a link to the license, indicates if changes were made and the licensor is not represented as endorsing the use made of the work. Further, any new works must be made available on the same conditions. The full details of the license are available at <http://creativecommons.org/licenses/by-nc-sa/4.0>.

CC BY NC ND: The CC BY-NC-ND license allows users to copy and distribute the Article, provided this is not done for commercial purposes and further does not permit distribution of the Article if it is changed or edited in any way, and provided the user gives appropriate credit (with a link to the formal publication through the relevant DOI), provides a link to the license, and that the licensor is not represented as endorsing the use made of the work. The full details of the license are available at <http://creativecommons.org/licenses/by-nc-nd/4.0>.

Any commercial reuse of Open Access articles published with a CC BY NC SA or CC BY NC ND license requires permission from Elsevier and will be subject to a fee.

Commercial reuse includes:

- Associating advertising with the full text of the Article
- Charging fees for document delivery or access
- Article aggregation
- Systematic distribution via e-mail lists or share buttons

Posting or linking by commercial companies for use by customers of those companies.

20. Other Conditions:

v1.7

Questions? customercare@copyright.com or +1-855-239-3415 (toll free in the US) or +1-978-646-2777.

ELSEVIER LICENSE
TERMS AND CONDITIONS

Aug 02, 2015

This is a License Agreement between Mohd Ayub Sulong ("You") and Elsevier ("Elsevier") provided by Copyright Clearance Center ("CCC"). The license consists of your order details, the terms and conditions provided by Elsevier, and the payment terms and conditions.

All payments must be made in full to CCC. For payment instructions, please see information listed at the bottom of this form.

Supplier	Elsevier Limited The Boulevard, Langford Lane Kidlington, Oxford, OX5 1GB, UK
Registered Company Number	1982084
Customer name	Mohd Ayub Sulong
Customer address	12 Albert St MAYFIELD, NSW 2304
License number	3680711219614
License date	Aug 02, 2015
Licensed content publisher	Elsevier
Licensed content publication	Computational Materials Science
Licensed content title	On the mechanical anisotropy of the compressive properties of aluminium perlite syntactic foam
Licensed content author	M.A. Sulong, M. Taherishargh, I.V. Belova, G.E. Murch, T. Fiedler
Licensed content date	November 2015
Licensed content volume number	109
Licensed content issue number	n/a
Number of pages	8
Start Page	258
End Page	265
Type of Use	reuse in a thesis/dissertation
Portion	full article
Format	both print and electronic
Are you the author of this Elsevier article?	Yes
Will you be translating?	No
Title of your thesis/dissertation	Characterisation of Advanced Porous Materials
Expected completion date	Aug 2015
Estimated size (number of pages)	150

Elsevier VAT number	GB 494 6272 12
Permissions price	0.00 AUD
VAT/Local Sales Tax	0.00 AUD / 0.00 GBP
Total	0.00 AUD
Terms and Conditions	

INTRODUCTION

1. The publisher for this copyrighted material is Elsevier. By clicking "accept" in connection with completing this licensing transaction, you agree that the following terms and conditions apply to this transaction (along with the Billing and Payment terms and conditions established by Copyright Clearance Center, Inc. ("CCC"), at the time that you opened your Rightslink account and that are available at any time at <http://myaccount.copyright.com>).

GENERAL TERMS

2. Elsevier hereby grants you permission to reproduce the aforementioned material subject to the terms and conditions indicated.

3. Acknowledgement: If any part of the material to be used (for example, figures) has appeared in our publication with credit or acknowledgement to another source, permission must also be sought from that source. If such permission is not obtained then that material may not be included in your publication/copies. Suitable acknowledgement to the source must be made, either as a footnote or in a reference list at the end of your publication, as follows:

"Reprinted from Publication title, Vol /edition number, Author(s), Title of article / title of chapter, Pages No., Copyright (Year), with permission from Elsevier [OR APPLICABLE SOCIETY COPYRIGHT OWNER]." Also Lancet special credit - "Reprinted from The Lancet, Vol. number, Author(s), Title of article, Pages No., Copyright (Year), with permission from Elsevier."

4. Reproduction of this material is confined to the purpose and/or media for which permission is hereby given.

5. Altering/Modifying Material: Not Permitted. However figures and illustrations may be altered/adapted minimally to serve your work. Any other abbreviations, additions, deletions and/or any other alterations shall be made only with prior written authorization of Elsevier Ltd. (Please contact Elsevier at permissions@elsevier.com)

6. If the permission fee for the requested use of our material is waived in this instance, please be advised that your future requests for Elsevier materials may attract a fee.

7. Reservation of Rights: Publisher reserves all rights not specifically granted in the combination of (i) the license details provided by you and accepted in the course of this licensing transaction, (ii) these terms and conditions and (iii) CCC's Billing and Payment terms and conditions.

8. License Contingent Upon Payment: While you may exercise the rights licensed immediately upon issuance of the license at the end of the licensing process for the transaction, provided that you have disclosed complete and accurate details of your proposed use, no license is finally effective unless and until full payment is received from you (either by publisher or by CCC) as provided in CCC's Billing and Payment terms and conditions. If

full payment is not received on a timely basis, then any license preliminarily granted shall be deemed automatically revoked and shall be void as if never granted. Further, in the event that you breach any of these terms and conditions or any of CCC's Billing and Payment terms and conditions, the license is automatically revoked and shall be void as if never granted. Use of materials as described in a revoked license, as well as any use of the materials beyond the scope of an unrevoked license, may constitute copyright infringement and publisher reserves the right to take any and all action to protect its copyright in the materials.

9. Warranties: Publisher makes no representations or warranties with respect to the licensed material.

10. Indemnity: You hereby indemnify and agree to hold harmless publisher and CCC, and their respective officers, directors, employees and agents, from and against any and all claims arising out of your use of the licensed material other than as specifically authorized pursuant to this license.

11. No Transfer of License: This license is personal to you and may not be sublicensed, assigned, or transferred by you to any other person without publisher's written permission.

12. No Amendment Except in Writing: This license may not be amended except in a writing signed by both parties (or, in the case of publisher, by CCC on publisher's behalf).

13. Objection to Contrary Terms: Publisher hereby objects to any terms contained in any purchase order, acknowledgment, check endorsement or other writing prepared by you, which terms are inconsistent with these terms and conditions or CCC's Billing and Payment terms and conditions. These terms and conditions, together with CCC's Billing and Payment terms and conditions (which are incorporated herein), comprise the entire agreement between you and publisher (and CCC) concerning this licensing transaction. In the event of any conflict between your obligations established by these terms and conditions and those established by CCC's Billing and Payment terms and conditions, these terms and conditions shall control.

14. Revocation: Elsevier or Copyright Clearance Center may deny the permissions described in this License at their sole discretion, for any reason or no reason, with a full refund payable to you. Notice of such denial will be made using the contact information provided by you. Failure to receive such notice will not alter or invalidate the denial. In no event will Elsevier or Copyright Clearance Center be responsible or liable for any costs, expenses or damage incurred by you as a result of a denial of your permission request, other than a refund of the amount(s) paid by you to Elsevier and/or Copyright Clearance Center for denied permissions.

LIMITED LICENSE

The following terms and conditions apply only to specific license types:

15. Translation: This permission is granted for non-exclusive world English rights only unless your license was granted for translation rights. If you licensed translation rights you may only translate this content into the languages you requested. A professional translator must perform all translations and reproduce the content word for word preserving the integrity of the article. If this license is to re-use 1 or 2 figures then permission is granted for non-exclusive world rights in all languages.

16. Posting licensed content on any Website: The following terms and conditions apply as follows: Licensing material from an Elsevier journal: All content posted to the web site must

maintain the copyright information line on the bottom of each image; A hyper-text must be included to the Homepage of the journal from which you are licensing at <http://www.sciencedirect.com/science/journal/xxxxx> or the Elsevier homepage for books at <http://www.elsevier.com>; Central Storage: This license does not include permission for a scanned version of the material to be stored in a central repository such as that provided by Heron/XanEdu.

Licensing material from an Elsevier book: A hyper-text link must be included to the Elsevier homepage at <http://www.elsevier.com> . All content posted to the web site must maintain the copyright information line on the bottom of each image.

Posting licensed content on Electronic reserve: In addition to the above the following clauses are applicable: The web site must be password-protected and made available only to bona fide students registered on a relevant course. This permission is granted for 1 year only. You may obtain a new license for future website posting.

17. For journal authors: the following clauses are applicable in addition to the above:

Preprints:

A preprint is an author's own write-up of research results and analysis, it has not been peer-reviewed, nor has it had any other value added to it by a publisher (such as formatting, copyright, technical enhancement etc.).

Authors can share their preprints anywhere at any time. Preprints should not be added to or enhanced in any way in order to appear more like, or to substitute for, the final versions of articles however authors can update their preprints on arXiv or RePEc with their Accepted Author Manuscript (see below).

If accepted for publication, we encourage authors to link from the preprint to their formal publication via its DOI. Millions of researchers have access to the formal publications on ScienceDirect, and so links will help users to find, access, cite and use the best available version. Please note that Cell Press, The Lancet and some society-owned have different preprint policies. Information on these policies is available on the journal homepage.

Accepted Author Manuscripts: An accepted author manuscript is the manuscript of an article that has been accepted for publication and which typically includes author-incorporated changes suggested during submission, peer review and editor-author communications.

Authors can share their accepted author manuscript:

- immediately
 - via their non-commercial person homepage or blog
 - by updating a preprint in arXiv or RePEc with the accepted manuscript
 - via their research institute or institutional repository for internal institutional uses or as part of an invitation-only research collaboration work-group
 - directly by providing copies to their students or to research collaborators for their personal use
 - for private scholarly sharing as part of an invitation-only work group on

commercial sites with which Elsevier has an agreement

- after the embargo period
 - via non-commercial hosting platforms such as their institutional repository
 - via commercial sites with which Elsevier has an agreement

In all cases accepted manuscripts should:

- link to the formal publication via its DOI
- bear a CC-BY-NC-ND license - this is easy to do
- if aggregated with other manuscripts, for example in a repository or other site, be shared in alignment with our hosting policy not be added to or enhanced in any way to appear more like, or to substitute for, the published journal article.

Published journal article (JPA): A published journal article (PJA) is the definitive final record of published research that appears or will appear in the journal and embodies all value-adding publishing activities including peer review co-ordination, copy-editing, formatting, (if relevant) pagination and online enrichment.

Policies for sharing publishing journal articles differ for subscription and gold open access articles:

Subscription Articles: If you are an author, please share a link to your article rather than the full-text. Millions of researchers have access to the formal publications on ScienceDirect, and so links will help your users to find, access, cite, and use the best available version.

Theses and dissertations which contain embedded PJAs as part of the formal submission can be posted publicly by the awarding institution with DOI links back to the formal publications on ScienceDirect.

If you are affiliated with a library that subscribes to ScienceDirect you have additional private sharing rights for others' research accessed under that agreement. This includes use for classroom teaching and internal training at the institution (including use in course packs and courseware programs), and inclusion of the article for grant funding purposes.

Gold Open Access Articles: May be shared according to the author-selected end-user license and should contain a [CrossMark logo](#), the end user license, and a DOI link to the formal publication on ScienceDirect.

Please refer to Elsevier's [posting policy](#) for further information.

18. For book authors the following clauses are applicable in addition to the above: Authors are permitted to place a brief summary of their work online only. You are not allowed to download and post the published electronic version of your chapter, nor may you scan the printed edition to create an electronic version. Posting to a repository: Authors are permitted to post a summary of their chapter only in their institution's repository.

19. Thesis/Dissertation: If your license is for use in a thesis/dissertation your thesis may be submitted to your institution in either print or electronic form. Should your thesis be published commercially, please reapply for permission. These requirements include permission for the Library and Archives of Canada to supply single copies, on demand, of

the complete thesis and include permission for Proquest/UMI to supply single copies, on demand, of the complete thesis. Should your thesis be published commercially, please reapply for permission. Theses and dissertations which contain embedded PJAs as part of the formal submission can be posted publicly by the awarding institution with DOI links back to the formal publications on ScienceDirect.

Elsevier Open Access Terms and Conditions

You can publish open access with Elsevier in hundreds of open access journals or in nearly 2000 established subscription journals that support open access publishing. Permitted third party re-use of these open access articles is defined by the author's choice of Creative Commons user license. See our [open access license policy](#) for more information.

Terms & Conditions applicable to all Open Access articles published with Elsevier:

Any reuse of the article must not represent the author as endorsing the adaptation of the article nor should the article be modified in such a way as to damage the author's honour or reputation. If any changes have been made, such changes must be clearly indicated.

The author(s) must be appropriately credited and we ask that you include the end user license and a DOI link to the formal publication on ScienceDirect.

If any part of the material to be used (for example, figures) has appeared in our publication with credit or acknowledgement to another source it is the responsibility of the user to ensure their reuse complies with the terms and conditions determined by the rights holder.

Additional Terms & Conditions applicable to each Creative Commons user license:

CC BY: The CC-BY license allows users to copy, to create extracts, abstracts and new works from the Article, to alter and revise the Article and to make commercial use of the Article (including reuse and/or resale of the Article by commercial entities), provided the user gives appropriate credit (with a link to the formal publication through the relevant DOI), provides a link to the license, indicates if changes were made and the licensor is not represented as endorsing the use made of the work. The full details of the license are available at <http://creativecommons.org/licenses/by/4.0>.

CC BY NC SA: The CC BY-NC-SA license allows users to copy, to create extracts, abstracts and new works from the Article, to alter and revise the Article, provided this is not done for commercial purposes, and that the user gives appropriate credit (with a link to the formal publication through the relevant DOI), provides a link to the license, indicates if changes were made and the licensor is not represented as endorsing the use made of the work. Further, any new works must be made available on the same conditions. The full details of the license are available at <http://creativecommons.org/licenses/by-nc-sa/4.0>.

CC BY NC ND: The CC BY-NC-ND license allows users to copy and distribute the Article, provided this is not done for commercial purposes and further does not permit distribution of the Article if it is changed or edited in any way, and provided the user gives appropriate credit (with a link to the formal publication through the relevant DOI), provides a link to the license, and that the licensor is not represented as endorsing the use made of the work. The full details of the license are available at <http://creativecommons.org/licenses/by-nc-nd/4.0>. Any commercial reuse of Open Access articles published with a CC BY NC SA or CC BY NC ND license requires permission from Elsevier and will be subject to a fee.

Commercial reuse includes:

- Associating advertising with the full text of the Article
- Charging fees for document delivery or access
- Article aggregation
- Systematic distribution via e-mail lists or share buttons

Posting or linking by commercial companies for use by customers of those companies.

20. Other Conditions:

v1.7

Questions? customercare@copyright.com or +1-855-239-3415 (toll free in the US) or +1-978-646-2777.
